Corrosion of reinforcement bars in steel ibre reinforced concrete structures

Solgaard, Anders Ole Stubbe; Stang, Henrik; Geiker, Mette Rica; Edvardsen, Carola; Larsen, Erik Stoklund

Publication date:
2014

Document Version
Publisher's PDF, also known as Version of record

Corrosion of reinforcement bars in steel fibre reinforced concrete structures

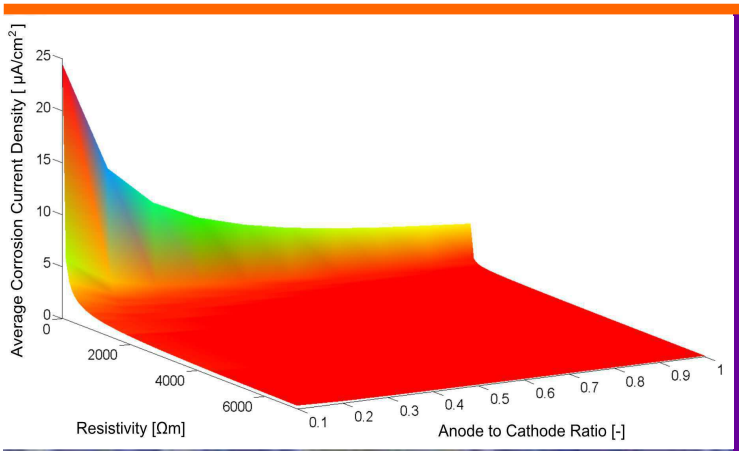

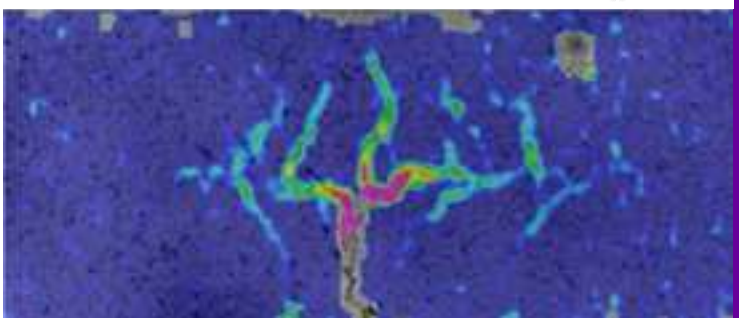

Anders Ole Stubbe Solgaard

PhD Thesis

Department of Civil Engineering

2013

DTU Civil Engineering Report R-257 (UK)
June 2013

DTU Civil Engineering
Department of Civil Engineering

Corrosion of reinforcement bars in steel fibre reinforced concrete structures

Anders Ole Stubbe Solgaard

Ph.D. Thesis

Department of Civil Engineering
Technical University of Denmark

COWI A/S
2013

Photo front page:
Top: Surface plot of results from numerical simulations showing the average corrosion current density of embedded reinforcement as function of the anode to cathode ratio and the electrical resistivity of concrete. Bottom: Photogrammetric investigations of load-induced damage along traditional reinforcement embedded in steel fibre reinforced concrete.

Corrosion of reinforcement bars in steel fibre reinforced concrete structures

Printed by Rosendahls-Schultz Grafisk
Department of Civil Engineering
Technical University of Denmark
COWI A/S
ISBN: 9788778773395
ISSN: 1601-2917
Report: BYG R-257

Preface

This thesis is submitted as a partial fulfilment of the requirements for the Danish Ph.D. degree. The thesis is based on experimental and numerical investigations conducted as part of the Ph.D. project "Application of Fibre Reinforced Concrete in Civil Infrastructure".

An external research stay at Dipartimento di Chimica, Materiali e Ingegneria Chimica "G. Natta" at Politecnico di Milano, Italy, formed part of the Ph.D. project.

The principal supervisor of this Ph.D. project was Professor Henrik Stang from DTU Byg with co-supervisors Mette Geiker also from DTU Byg, Carola Edvardsen from COWI A/S and Erik Stoklund Larsen also from COWI A/S. Experimental works were carried out at DTU Byg and in the laboratory at Dipartimento di Chimica, Materiali e Ingegneria Chimica "G. Natta" at Politecnico di Milano.

Financial support for the Ph.D. project was provided by the Danish Agency for Science, Technology and Innovation, COWI A/S, Bekaert NV, Grace and the Danish Road Directorate.

Kgs. Lyngby the 24th of June 2013

Anders Ole Stubbe Solgaard 24/6/2013

Anders Ole Stubbe Solgaard

Acknowledgments

First of all I would like to acknowledge the advices and support from my supervisors, Henrik Stang and Mette Geiker both from the Department of Civil Engineering at the Technical University of Denmark, and Carola Edvardsen and Erik Stoklund Larsen from my host company COWI A/S, Denmark during my Ph.D. study. This study has shaped me to the person I am today, not only in relation to my professional career but also with regard to my personal development, and you have a great share in this.

The full financial support for the Ph.D. project *"*Application of Fibre Reinforced Concrete in Civil Infrastructure*"* by the Danish Agency for Science, Technology and innovation, COWI A/S, DTU, Bekaert NV, Grace and the Danish Road Directorate is also highly appreciated.

Furthermore I owe my most sincere appreciations to Luca Bertolini, his research group and colleagues at Dipartimento di Chimica, Materiali e Ingegneria Chimica "G. Natta" Politecnico di Milano for welcoming me to Milano during my external research stay. Without your hospitality and helpfulness, the work concerning the susceptibility of stray-current induced corrosion of steel fibres would not have been possible.

Torben Jacobsen from the Department of Chemistry at the Technical University is acknowledged for letting me use the equipment for AC-IS analyses and for the help during interpretation of experimental data.

During the Ph.D. study, several students have been involved in the experimental investigations presented in the thesis, and I would like to thank you all for your valuable contributions to my studies.

Flemming Olsen is greatly acknowledged for linguistic proof-reading of manuscripts for papers. Moreover, I would like to acknowledge the support and fruitful discussions I have had with André Küter from COWI A/S, Bradley Justin Pease, DTU and my fellow Ph.D. students at DTU Byg. In particular I have enjoyed the professional discussions and collaboration I have had with Alexander Michel, DTU. All of you made the studies worthwhile in good as well as in bad times.

Last, but not least, I would like to thank my family and friends for the encouragements and general understanding of my absence (mentally as well as physically) every now and then during my studies. Without your constant support it would have been impossible for me to finish my studies.

Abstract

Steel fibres have been known as an alternative to traditional reinforcement bars for special applications of structural concrete for decades and the use of steel fibre reinforced concrete (SFRC) has gradually increased in recent years. Steel fibres lead to reduced crack widths in concrete formed, among other reasons, due to shrinkage and/or mechanical loading. Steel fibres are nowadays also used in combination with traditional reinforcement for structural concrete, where the role of the fibres is to minimize the crack widths whereas the traditional reinforcement bars are used for structural purpose. Although such, so-called, combined reinforcement systems, are gaining impact within the construction industry, they are only marginally covered by existing guidelines for structural design and the literature concerning their mechanical and, in particular their durability aspects, is sparse.

The aim of the work presented in this Ph.D. thesis was to quantify the influence of steel fibres on corrosion of traditional reinforcement bars embedded in uncracked concrete as well as cracked concrete. Focus of the work was set on the impact of steel fibres on corrosion propagation in uncracked concrete and the influence of steel fibres on initiation and propagation of cracks in concrete. Moreover, the impact of fibres on corrosion-induced cover cracking was covered. The impact of steel fibres on propagation of reinforcement corrosion was investigated through studies of their impact on the electrical resistivity of concrete, which is known to affect the corrosion process of embedded reinforcement. The work concerning the impact of steel fibres on initiation and propagation of cracks was linked to corrosion initiation and propagation of embedded reinforcement bars via additional studies. Cracks in the concrete cover are known to alter the ingress rate of depassivating substances and thereby influence the corrosion process. The Ph.D. study covered numerical as well as experimental studies.

Electrochemically passive steel fibres are electrically isolating thus not changing the electrical resistivity of concrete, whereas electrochemically active (depassivated/corroding) steel fibres are conducting. The impact of electrochemically active (depassivated/corroding) steel fibres on the electrical resistivity of SFRC was studied experimentally and analytically herein. Those studies showed that the addition of electrically conductive steel fibres may potentially reduce the electrical resistivity of concrete. Numerical studies of the correlation between the corrosion rate and the electrical resistivity of concrete were presented to study the impact of conductive steel fibres on the corrosion propagation phase of reinforcement bars. It was observed that under extreme conditions, viz. conductive (depassivated/corroding) steel fibres throughout the concrete volume, the reduction of the electrical resistivity caused by conductive fibres lead to a remarkable increase in the corrosion rate. However it is stressed that the case of corroding steel fibres throughout the concrete volume is somewhat hypothetical due to the very high corrosion-resistance of embedded steel fibres. Thus the investigated case refers to a worst-case scenario.

Numerical and experimental studies on the impact of steel fibres on initiation and propagation of load-induced cracks in concrete showed that the steel fibres restrained the crack width of a bending crack through the concrete cover, once the crack was formed. Moreover the numerical studies showed that the length of separation at the concrete/steel-bar interface (displacement discontinuity perpendicular to the reinforcement bar) was reduced for SFRC compared to plain concrete, whereas there was no clear impact on the slip at the concrete/steel-bar (displacement discontinuity parallel to the reinforcement bar) caused by the steel fibres. Additional experimental and numerical studies concerning corrosion of reinforcement embedded in cracked concrete (plain concrete and SFRC) showed that the time-to-corrosion-intiation was similar for plain concrete and SFRC for the same surface crack width. With regard to the corrosion propagation phase in cracked concrete the numerical studies showed that the corrosion rate and the length of the anodic surface on the reinforcement was comparable in plain concrete and SFRC for the same surface crack width. Thus, based on these observations there apperared to be no impact from steel fibres on the corrosion process of embedded reinforcement.

Finally the influence of steel fibres on. corrosion induced cracking of the concrete cover, was investigated numerically. These simulations covered traditional reinforcement embedded in either plain concrete or SFRC and it was observed that once a crack in the concrete cover was formed, the development of the crack width at the concrete surface was reduced in SFRC compared to plain concrete. This indicates that the fibres can restrain the propagation of corrosion-induced cracks and thereby reduce the detrimental impact of cracks on the corrosion process.

Resumé

Stålfibre kan til visse konstruktionstyper være et alternativ til traditionel armering og i løbet af de senere år har brugen af stålfiberarmeret beton (SFRC) været støt stigende. Stålfibre kan reducere vidden af revner i beton som f.eks. kan opstå i forbindelse med svind eller mekanisk belastning. Stålfibre benyttes også sammen med traditionelle armeringsjern hvor formålet med at benytte stålfibre er at minimere revnevidderne i betonen mens den traditionelle armering benyttes af strukturelle, bæreevnemæssige hensyn. På trods af sådanne armeringsarrangementer, såkaldt kombinerede armeringssystemer, vinder indpas i konstruktionsbranchen er de kun i begrænset omfang dækket af eksisterende standarder og guidelines for konstruktionsdesign og den dokumenterede viden omkring de mekaniske og i særdeleshed de holdbarhedsmæssige aspekter af disse armeringssystemer er begrænset.

Formålet med arbejdet rapporteret i denne Ph.D. afhandling var at undersøge indflydelsen af stålfibre på korrosion af de traditionelle armeringsjern i kombinerede armeringssystemer i urevnet såvel som revnet beton. Fokus for dette arbejde var at kvantificere stålfibrenes indflydelse på korrosions-propagering i urevnet beton samt at kvantificere stålfibrenes indflydelse på revnedannelse og revneudvikling i beton. Endvidere blev fibrenes indflydelse på korrosions-induceret revnedannelse i beton dæklag undersøgt. Fibrenes indflydelse på korrosions-propagering blev undersøgt ved at studere deres indflydelse på den elektriske resistivitet af beton, som spiller en central rolle i korrosionsprocessen. Studierne af fibrenes betydning for revnedannelse og revneudvikling i beton blev relateret til armeringskorrosion via separate studier (revner i betonen reducerer modstanden mod indtrængning af f.eks. fugt og klorider som kan føre til korrosion-initiering samt accelerere en igangværende korrosionsproces). Ph.D. studiet omfattede numeriske såvel som eksperimentelle studier.

Elektrokemisk passive stålfibre er elektrisk isolerede, og har derfor ingen indflydelse på den elektriske resistivitet af beton, hvorimod elektrokemisk aktive (depassiverede/korroderede) stål fibre er elektrisk ledende. Indflydelsen af elektrokemisk aktive stålfibre på den elektriske resistivitet af SFRC blev undersøgt eksperimentelt og analytisk. Disse studier viste, at elektrisk ledende stålfibre potentielt reducerer betons elektriske resistivitet. Numeriske studier af sammenhængen mellem korrosionshastigheden og den elektriske resistivitet af beton blev udført for at undersøge indflydelsen af elektrisk ledende stålfibre på korrosions-propageringsfasen af armeringsjern. Disse numeriske studier viste, at under ekstreme forhold, dvs. elektrisk ledende stålfibre, medførte den reducerede elektriske resistivitet af beton, som følge af stålfibrenes evne til at lede strøm, en markant forøgelse af korrosions-hastigheden. Det skal dog pointeres at en situation, hvor alle stålfibre i betonen er elektrisk ledende, dvs. depassiverede/korroderede, er højst usandsynlig idet ståfibrene er særdeles korrosionsbestandige, hvorfor denne situation svarer til et hypotetisk scenarium.

Numeriske og eksperimentelle undersøgelser af stålfibres indflydelse på revnedannelse og revneudbredelse som følge af mekanisk belastning viste at udbredelsen af en bøjningsrevne i dæklaget i SFRC var mindre end i almindelig beton (for den samme lastpåvirkning). Endvidere viste de numeriske undersøgelser, at udbredelsen af separation langs skillefladen mellem beton og armeringsjern, dvs. en deformation vinkelret på armeringsjernet, var mindre i SFRC sammenlignet med almindelig beton, hvorimod udbredelsen af slip i denne skilleflade (deformation parallelt med armeringsjernet) ikke blev ændret pga. stålfibrene. Supplerende eksperimentelle og numeriske studier af korrosion i revnet beton (almindelig beton og SFRC) viste, at korrosion blev inititeret til samme tidspunkt, når revnevidden ved betonoverfladen var ens i de to materialer. Resultater fra de numeriske undersøgelser viste også at korrosionshastigheden og anodens størrelse var sammenlignelige for almindelig beton og SFRC (for den samme revnevidde ved betonoverfladen). På baggrund af dette blev det konkluderet, at stålfibre, under disse forudsætninger, har begrænset indflydelse på korrosion af armeringsjern.

Stålfibres indflydelse på korrosions-induceret revnedannelse af dæklag blev undersøgt numerisk. Disse numeriske studier omhandlede armeringsjern i almindelig beton og SFRC, og resultaterne fra undersøgelserne viste, at revneudbredelsen var mindre i SFRC sammenlignet med almindelig beton. Således kan stålfibrene begrænse udbredelsen af korrosions-inducerede revner og dermed reducere den skadelige indvirking af revner i betondæklaget på korrosionsprocessen.

Table of Contents

Additional work of the Ph.D. study (not part of this thesis)

[1] Solgaard, A.O.S., Stang, H., Goltermann, P.: 'In-Plane Shear Test of Fibre Reinforced Concrete Panels'. In proceedings: *The 7th International RILEM Symposium (BEFIB2008), 2008, Chennai (India).*

[2] Solgaard, A.O.S., Michel, A., Stang, H., Geiker, M.R., Küter, A., Edvardsen, C.: 'Modelling the influence of steel fibres on the electrical resistivity of cementitious composites'. In proceedings: *3rd International PhD Workshop on Modelling the Durability of Reinforced Concrete*, *2009, Guimarães (Portugal).*

[3] Solgaard, A.O.S., Michel, A., Stang, H., Geiker, M.R., Edvardsen, C. and Küter, A.: 'Numerical modeling of cracking of concrete due to corrosion of reinforcement – Impact of cover thickness and concrete toughness'. In proceedings: *The 7th International Conference on Fracture Mechanics of Concrete and Concrete (FraMCos7), 2010, Jeju (Korea).*

[4] Solgaard, A.O.S., Stang, H.: 'Application of Fibre Reinforced Concrete in Civil Infrastructure'. In proceedings: *The 8th fib PhD Symposium, 2010, Kgs. Lyngby (Denmark).*

[5] Solgaard, A.O.S., Küter, A., Edvardsen, C., Stang, H., Geiker, M.: 'Durability Aspects of Steel Fibre Reinforced Concrete in Civil Infrastructure'. In proceedings: *The 2nd International Symposium on Service Life Design for Infrastructures, 2010, Delft (The Netherlands).*

[6] Michel, A., Solgaard, A.O.S., Geiker, M.R., Stang, H., Olesen, J.F.: 'Influence of resistivity on the corrosion of reinforcement in concrete'. In proceedings: *3rd International PhD Workshop on Modelling the Durability of Reinforced Concrete*, *2009, Guimarães (Portugal).*

[7] Michel, A., Solgaard, A.O.S., Geiker, M.R., Stang, H., Olesen, J.F.: 'Modeling Formation of Cracks in Concrete Cover due to Reinforcement Corrosion'. In proceedings: *The 7th International Conference on Fracture Mechanics of Concrete and Concrete (FraMCos7), 2010, Jeju (Korea).*

[8] Michel, A., Solgaard, A.O.S., Geiker, M.R., Stang, H., Olesen, J.F.: 'Modeling the Influence of Resistivity on the Corrosion of Reinforcement in Concrete'. In proceedings: *CONMOD'10 Symposium on concrete modeling, 2010, Lausanne (Switzerland).*

[9] Solgaard, A.O.S., Carsana, M., Geiker, M.R., Küter, A., Bertolini, L.: 'Experimental Observations of Stray Current Effects on Steel Fibres Embedded in Mortar', Accepted for Publication in Corrosion Science, March 2013.

[10] Solgaard, A.O.S., Michel, A., Stang, H.: 'Photogrammetric Investigations on the Debonding along the Concrete/Steel Interface in Reinforced Concrete Beams', *Technical Report*, Department of Civil Engineering at the Technical University of Denmark, http://www.byg.dtu.dk/Publikationer/Byg_rapporter.aspx, 2013.

Chapter 1
Introduction

1.1 Scope

Reinforced concrete is the most widely used man-made construction material and is used for various structural projects ranging from small concrete beams to major bridge constructions. Traditional reinforcement bars have been preferred as reinforcement system to compensate for the low tensile capacity of concrete, for more than a century. Over the past decades other types of reinforcement have gained foothold within the construction industry. One of the predominant alternatives to traditional reinforcement is steel fibres. Steel fibres are mixed-in during batching of concrete, ie the fibres are discretely dispersed throughout the concrete volume adding reinforcement in all directions.

The main favoured mechanical, material property of concrete is its compressive strength. The compressive strength of concrete is mainly determined by the water-to-cement ratio (w/c ratio), the maturity and the curing conditions of the concrete, see eg [*Metha and Monteiro, 2006*]. The addition of fibres has a beneficial effect on the mechanical performance of concrete subjected to compression. Examples of stress-strain curves for concrete (with/without fibres) subjected to compressive loading are given in Figure 1.1.

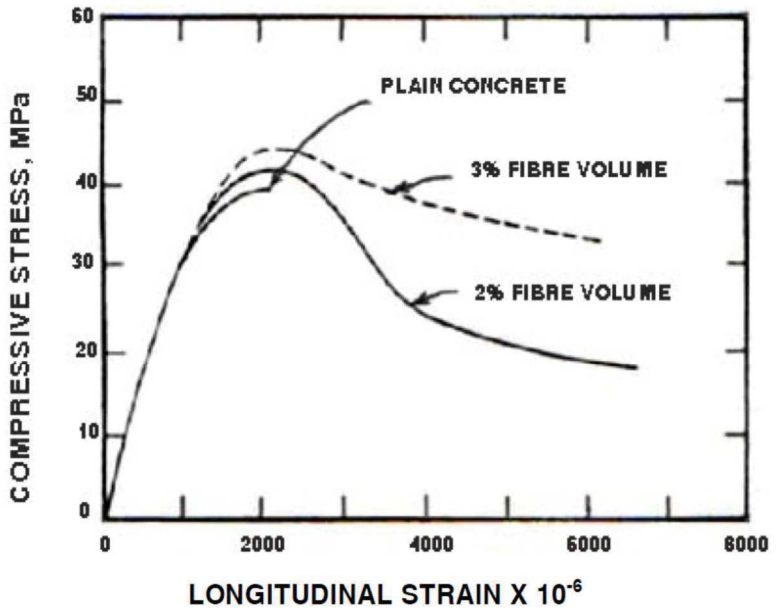

Figure 1.1 *Stress-strain curve for concrete (with/without fibres) subjected to compression. [Johnston, 1974].*

As illustrated in Figure 1.1 the compressive strength of concrete is only moderately affected by the addition of up to 3 vol.-% of steel fibres, but the failure of the concrete specimen is changed from a quasi-brittle failure mechanism to a more ductile failure when fibres are added to the concrete. The addition of fibres allow for a re-distribution of stresses as the fibres bridge the internal micro-cracks of the concrete formed during mechanical loading and thus transfer stresses across cracks, [*Maidl, 1995*]. Finally it is seen from Figure 1.1 that the Young's modulus of concrete with fibres is similar to that of concrete without fibres, ie plain concrete. This is in line with observations presented in eg [*Schnütgen, 1978*] showing that the Young's modulus of SFRC is in the same range as for plain concrete and that the Young's modulus of SFRC increases when the Young's modulus of the fibres compared to the Young's modulus of concrete increases. However, it is noted that this is a general observation, and for some (special) types of SFRC, eg ultra-high performance fibre reinforced concrete (UHPFRC) [*Graybeal, 2006*] Young's modulus is higher than for plain concrete.

The main beneficial effect on the mechanical properties of concrete caused by the addition of (steel) fibres, is their impact on the formation of cracks caused by tensile stresses. Cracks in concrete are formed, when the tensile capacity is exceeded, but stresses can still be transferred across the crack in the so-called fracture process zone. This fracture process zone consists of microcracks, aggregate bridging and other toughening mechanisms [*Shah et al., 1995*]. In SFRC the fracture process zone furthermore contains fibre bridging [*van Mier, 1997*]. An illustration of the mechanical response of plain concrete and SFRC when subjected to direct tensile loading is given in Figure 1.2.

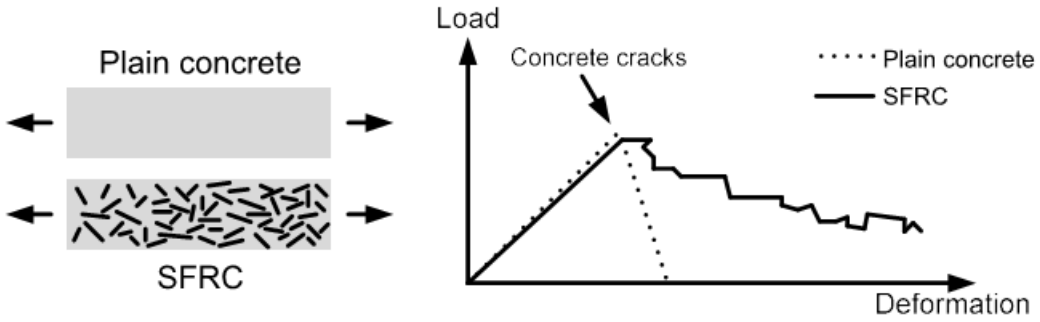

Figure 1.2 *Left: Uni-axial tensile loading of plain concrete SFRC. Right: Mechanical response of uni-axial tensile loading. The illustration is not in scale. Inspired by [Herholdt et al., 1985].*

Note: The mechanical response of SFRC as sketched in Figure 1.2 corresponds to that of a material with tension-softening properties, ie the tensile capacity decreases after a crack has been formed. On the contrary, special fibre reinforced concrete composites eg engineered cementitious composites (ECC) have strain-hardening properties ie the tensile strength in the cracked state is higher than the tensile stress when a crack is

formed. Strain-hardening materials are beyond the scope of this Ph.D. thesis and are consequently not described any further.

Figure 1.2 illustrates that the load-bearing capacity in the post-peak state, ie after a crack has been formed, is negligible for plain concrete subjected to uni-axial tensile loading, whereas the load-bearing capacity in the post-peak state of SFRC is still considerable, though decreasing. Among other factors this increased ductility of SFRC compared to that of plain concrete, is caused by redistribution of stresses by the fibres bridging the cracks. The mechanical response of SFRC in the post-peak state depends on, among other factors, the amount and geometry of the steel fibres and the bond between the concrete and the steel fibres [*Maidl, 1995*]. It will also be seen from Figure 1.2 that the peak load of SFRC is similar to that of plain concrete.

The fracture mechanical properties of plain concrete and SFRC are usually described by the fictitious crack model which was originally formulated for plain concrete by Hillerborg et al. [*Hillerborg et al., 1976*] and later developed to consider fibre reinforced concrete (FRC) [*Hillerborg, 1980*].

In summary, the compressive strength as well as the tensile strength of SFRC and plain concrete are similar, whereas the post-peak response is altered by the presence of fibres in SFRC. Hence, in general, SFRC cannot serve as a substitution for traditional reinforced concrete for structures where a high tensile capacity of the construction material is required. However, for structures mainly subjected to compressive load, SFRC is a competitive alternative to traditional reinforced concrete and examples of structures constructed from SFRC are:

- The District Heating Line in Copenhagen (Denmark), [*Kasper et al., 2008*],
- A number of rings for the 2nd Heinenoord tunnel (Netherlands) were built from precast SFRC segments [*Kooiman, 1999*],
- The baggage handling tunnel at London Heathrow airport [*Moyson, 1995*],
- The Gold Coast Desalination project (segmental lining in Australia) [*Wimpenny et al., 2009*],
- Several tunnels in Norway [*Wimpenny et al., 2009*], and
- 20 km of the Channel Tunnel Rail Link in England [*Davies et al., 2006*].

Steel fibres and traditional reinforcement have different benefits, ie the ability to limit crack widths and increase the tensile capacity, respectively, and using them simultaneously as one, so-called, combined reinforcement system has gained foothold within the past years. The phenomenon of utilizing such combined reinforcement systems is not new; Structures utilizing such combined reinforcement have been constructed worldwide in particular within the past decades, eg Barcelona Metro (Spain) [*Gettu et al., 2006*], bored tunnels for sewage and waste water part of the STEP project in Abu Dhabi [*COWI, 2013*] and Madrid Metro (Spain) [*World Tunneling, 2009*].

The utilization of SFRC for structural applications has hitherto been hindered by a general lack of standards concerning the design of such structures. A number of national guidelines for the design and application of SFRC has emerged over the past years, eg in Germany [*DBV, 2001*] and Italy [*CNR-DT 204, 2006*]. Recently, design guidelines for fibre reinforced concrete have been implemented in the latest model code from *fib*, viz. *fib* Model Code 2010 [*fib*, *2012*]. However this model code mainly concerns the mechanical properties and the identification of these properties via prescribed tests such as 3 point bending tests in accordance with standard test methods [*DS/EN 14651-A1, 2007*]. The durability of the material is not considered directly. Consequently, design-engineers may be reluctant to utilize SFRC; especially for structures with requirements for a long service life (> 50 -100 years) and located in severe environment, eg marine exposure, due to the risk of corrosion of the steel fibres, and/or the traditional reinforcement bars. Considering the use of combined reinforcement systems, some guidance on design is available in the German Guideline for SFRC (Merkblatt Stahl-faserbeton) [*DBV, 2001*]. However, the possible utilization of combined reinforcement systems is excluded from model codes, such as the *fib* model code, which hinders the utilization of combined reinforcement systems. Hence there appears to be an emerging requirement for the understanding of the properties, mechanical as well as the durability, of such combined reinforcement systems.

The studies described in this Ph.D. thesis, focused on the durability, in terms of corrosion resistance, of combined reinforcement systems.

1.2 State-of-the-Art

Corrosion of reinforcement embedded in concrete can be divided into two distinct phases, viz. corrosion initiation and corrosion propagation, as described eg by Tuutti [*Tuutti, 1982*]. These phases are schematically illustrated in Figure 1.3.

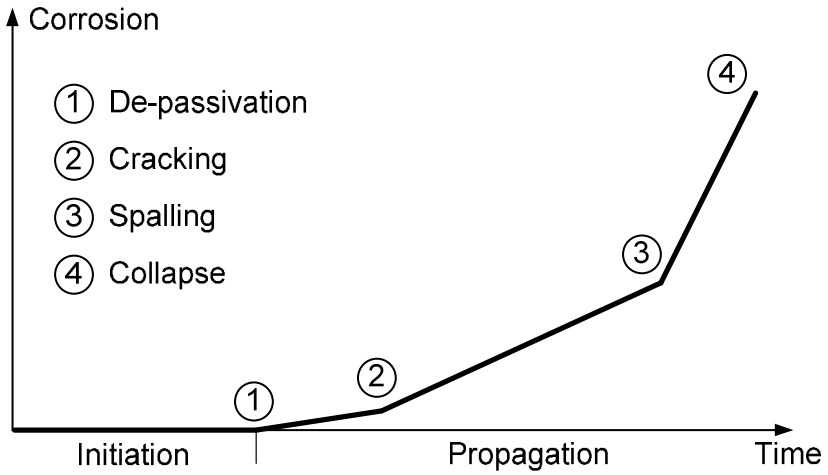

Figure 1.3 *Tuutti's model for reinforcement corrosion including events related to structural consequences. Adapted from [Duracrete, 2000].*

During the initiation phase depassivating substances, eg CO_2 and/or Cl^-, ingress through the concrete cover. The end of the initiation phase is defined as the point in time where the protecting passive layer at the reinforcement-surface, which has been formed due to the high alkalinity of the concrete, is broken down [*Tuutti, 1982*]. The depassivating substances eventually reach the reinforcement resulting in a break-down of this passive layer when a critical concentration of the depassivating substances at the level of the reinforcement occurs. The required time until the passive layer is broken down (reinforcement is depassivated) is denoted the time-to-initiation of corrosion and marks the end of the corrosion initiation phase. The end of the initiation phase is marked with (1) in Figure 1.3, and active corrosion has been initiated.

The next phase is the corrosion propagation phase, where iron-dissolution takes place. The rate of this process, ie the corrosion rate, is controlled by a number of parameters among which the most important are the availability of oxygen and moisture, transport properties of concrete, eg electrical resistivity, moisture and chloride transport, temperature, etc. [*Bertolini et al., 2004*]. The corrosion process causes cross sectional reduction of the embedded reinforcement and corrosion products are formed. Depending on the type of corrosion products formed, this may eventually lead to cracking and spalling of the concrete and finally collapse of the structure if the corrosion process continues. The consequences related to mechanical damage: cracking, damage and final collapse are marked with (2), (3) and (4), respectively, in Figure 1.3.

As already presented, the corrosion process, including initiation and propagation phases, is largely influenced by the ingress and the ingress rate of depassivating substances. The ingress rate of depassivating substances is significantly different in cracked concrete, ie cracks in the concrete cover, compared to uncracked concrete.

In uncracked concrete the concrete cover acts as a physical barrier and protects the embedded reinforcement against the surrounding environmental conditions. The time-to-corrosion-initiation is controlled by the transport rate of depassivating substances through the concrete cover towards the reinforcement. This transport rate is influenced by the concentration of depassivating substances in the surrounding environment and other ambient conditions, as well as the properties of the concrete cover, eg microstructure and w/c ratio, binding capacity, flaws in the concrete, etc. [*Bertolini et al., 2004; Metha and Monteiro, 2006*]. The time-to-corrosion-initiation is the time until a critical level of depassivating substances is reached at the level of the reinforcement. In uncracked concrete this phase may last up to several decades dependent on among others, the previously mentioned parameters as well as the thickness of the concrete cover, [*Bertolini et al., 2004*].

For cracked concrete it is generally accepted that the time-to-corrosion-initiation is much shorter compared to the uncracked state, as the cracks facilitate rapid ingress of depassivating substances towards the embedded reinforcement, eg [*Schießl and Raupach, 1997; Mohammed et al., 2001; Pease et al., 2011*]. Apart from decreasing

the time-to-corrosion-initiation the cracks and the possible associated debonding at the concrete/steel interface may also, dependent on their width and extent, have an impact on the corrosion rate during the propagation phase [*Schießl, 1976; Gautefall and Vennesland, 1983; Schießl and Raupach, 1997; Pease et al., 2011*]. This is due to the increased ingress rate of substances required for the corrosion process to continue, eg oxygen and moisture, through the crack(s) [*Schießl and Raupach, 1997*].

For concrete reinforced with a combined reinforcement system the same distinction between corrosion of reinforcement bars in uncracked and cracked concrete can be made. A brief overview of corrosion of steel fibres as well as their role on corrosion of reinforcement bars in uncracked and cracked concrete is provided below.

For uncracked concrete the impact of steel fibres on the ingress rate of chlorides, possible changes in the electrical resistivity and corrosion (chloride induced) of the steel fibres is described in the following. In uncracked SFRC, the ingress rate of chlorides is not adversely influenced by the presence of fibres compared to plain concrete. This conclusion is based on results published in [*Abrycki and Zajdzinski, 2012*] as well as experimental observations presented in [*Mangat and Gurusamy, 1987a*; *Mangat and Gurusamy, 1987b*]. Hence the susceptibility of chloride induced corrosion of traditional bar reinforcement embedded in uncracked concrete is similar when considering plain concrete and SFRC, assuming similar concrete/steel interface-conditions. With regards to the risk of corrosion of the steel fibres, a higher chloride threshold has been reported for steel fibres compared to traditional reinforcement bars, eg [*Janotka et al., 1989; Dauberschmidt, 2006*]. Possible explanations for this increased chloride threshold of steel fibres compared to traditional bar reinforcement are:

- Size-effect
    - Due to the small dimensions of a single fibre, the potential differences and the polarisation of one fibre, which is required for the formation of a corrosion cell (anode and cathode) on that fibre, are limited [*Dauberschmidt, 2002*],
    - The probability of chloride-induced (pitting) corrosion is stochastically distributed along the total steel surface [*Angst et al., 2009*], ie a small steel surface, as found on a fibre, corresponds to a small probability of pitting corrosion. Hence the probability of pitting corrosion of steel fibres is much smaller than for traditional reinforcement due to their reduced size.
- Casting conditions
    - In SFRC, the steel fibres are mixed-in during batching as opposed to casting of traditional bar reinforced concrete where the reinforcement is fixed during casting. The procedure used for batching and casting of SFRC leads to a reduction of the voids at the concrete/steel fibre inter-

face compared to the procedure used for traditionally reinforced concrete which can result in bleeding-channels at the circumference of the reinforcement. A reduction of the number of voids at the concrete/Steel interface is known to reduce the chloride threshold, as shown by eg Buenfeld et al. [*Buenfeld et al., 2004*]. Additionally, the casting procedure of SFRC leads to a dense and well-defined concrete/steel fibre interface which results in the formation of a more even passive layer (compared to traditional reinforcement bars), [*Dauberschmidt, 2006*].

Based on this information, ie the ingress rate of chlorides in uncracked SFRC and the increased chloride threshold of steel fibres compared to traditional bar reinforcement, it is concluded that the susceptibility of chloride induced corrosion initiation of steel fibres in uncracked concrete is considerably less than for traditional bar reinforcement in uncracked concrete, while the probability of corrosion initiation of traditional reinforcement bars in SFRC is the same as for reinforcement bars in plain concrete.

The electrical resistivity of concrete plays a dominant role in the corrosion propagation phase; An increased electrical resistivity of the concrete results in a reduced corrosion rate, [*Tuutti., 1982*]. While the influences of porosity and microstructure, temperature, moisture content, binder type and concrete maturity on the electrical resistivity of concrete have been studied extensively and described in the literature, eg [*Gjørv et al., 1977; Whittington et al., 1981; Hötte, 2003; Hope et al., 1985*] the knowledge concerning the possible impact of the addition of steel fibres is sparser. It is, however, generally accepted that electrochemically passive steel fibres are non-conducting due to the isolating effect of the passive surface layer, see eg [*Torrents et al., 2000; Torrents et al., 2001; Mason et al., 2000*]. Consequently electrochemically passive fibres do not alter the electrical resistivity of concrete apart from possible side-effects due to the addition of steel fibres, eg changed microstructure and air content, which may be considered subordinate. Electrochemically active fibres, ie depassivated/corroding fibres where the isolating passive layer is broken down are, however, able to conduct current, and thereby possibly change the electrical resistivity of concrete. Thus, considering combined reinforcement systems, corroding steel fibres may potentially increase the corrosion rate of the bar reinforcement due to their impact on the electrical resistivity. However, very little quantitative information is available in the literature about the reduction of the electrical resitivity of concrete caused by depassivated steel fibre systems.

In cracked concrete the ingress rate of chlorides is increased compared to uncracked concrete as presented above. Short-term experiments concerning chloride ingress in cracked plain concrete and SFRC reported by Pease [*Pease, 2010*] showed that the chloride ingress in cracked SFRC was reduced compared to the ingress in cracked, plain concrete for the same crack width (0.2 mm). Moreover, the water permeability of cracked SFRC and plain concrete was investigated by Rapoport et al. [*Rapoport et al., 2001*] showing that for crack widths larger than approx. 0.1 mm (crack width at

the surface), the permeability of SFRC was significantly less (95% confidence level) than for cracked, plain concrete with the same crack width at the surface. Rapoport et al. suggests that the reduced permeability of SFRC compared to plain concrete could be caused by more, finer cracks were formed in SFRC caused by the fibres bridging the cracks whereas few, relatively big cracks were formed in plain concrete. The impact of cracks on the susceptibility of corrosion of steel fibres in concrete has been investigated experimentally and described in the literature, eg [*Morse and Williamson, 1977; Mangat and Gurusamy, 1987a; Nemegeer et al., 2000; Granju and Balouch, 2005*]. Dependent on the exposure conditions eg chlorides, moisture availability and duration of exposure, various limits for crack widths are reported. The crack width limit for SFRC, ie the maximum allowable crack width at which corrosion of the fibres does not occur, has been reported in the range 0.1-0.5 mm, in the aforementioned literature.

The fracture mechanical properties of concrete when subjected to tensile stress, ie the tensile-deformation relationship, are significantly altered by the addition of discretely, dispersed steel fibres, cf. Section 1.1. The steel fibres bridging cracks changes the stress distribution in the concrete providing a more ductile response compared to plain concrete. Therefore steel fibres can be used to reduce crack widths in concrete. Additionally, the increased ductility caused by the steel fibres may reduce secondary types of load-induced cracking such as load-induced debonding along the concrete/reinforcement-interface, ie slip (dislocation parallel to the reinforcement) and separation (dislocation perpendicular to the reinforcement). Results presented in [*Pease et al., 2010*] showed that debonding at the concrete/steel interface results in an increased ingress of depassivating substances along the reinforcement leading to an enlarged anodic site at the reinforcement. Similar studies concerning corrosion along reinforcement bars in SFRC have, to the best of the author's knowledge, not been reported in the literature.

As seen from Figure 1.1 initiation and propagation of reinforcement corrosion, is followed by mechanical damage of the concrete, ie cracking and possible spalling of the concrete cover. This formation of cracks is caused by expansive corrosion products taking up more volume than the virgin steel, and is a well-known phenomenon observed in relation to uniform reinforcement corrosion see eg [*Bertolini et al., 2004*]. The correlation between corrosion induced concrete cover cracking and extent of corrosion has been described in the literature, eg experimental observations [*Rasheeduzzafar et al., 1992; Andrade et al., 1993; Alonso et al., 1998*] and modelling approaches [*Bazant, 1979; Suda et al., 1993; Liu and Weyers, 1998; Chernin et al., 2010*]. However, hitherto observations experimentally and/or numerically concerning corrosion-induced cover cracking in SFRC, and the possible crack width limiting effect of the steel fibres has not been addressed in the literature.

Additional information about corrosion of steel fibres in uncracked as well as cracked concrete is available in the literature, eg [*Kosa, 1988; Kosa and Naaman, 1990;*

Maidl, 1995; Hansen, 1999; Granju and Balouch, 2005; Nordstrøm, 2005; Daub-erschmidt, 2006] whereas more detailed descriptions on the phases of reinforcement corrosion and the influencing parameters can be retrieved in the literature, eg [*Tuutti, 1982*; *Bentur et al., 1998; Bertolini et al., 2004*].

1.3 Aim, Scope and Limitations of the Work

The aim of the work presented in this Ph.D. thesis was:

Quantification of the impact of steel fibres on corrosion of reinforcement bars embedded in concrete.

Based on the aforementioned state-of-the-art descriptions concerning corrosion in cracked and uncracked concrete reinforced with combined reinforcement systems it was decided to focus on:

- The impact of steel fibres on corrosion propagation in uncracked concrete, and
- The impact of steel fibres on initiation and propagation of cracks in concrete with combined reinforcement.

in relation to corrosion of the traditional reinforcement bars.

An overview of the scenarios covered by the work presented in this thesis is given in Table 1.1.

Table 1.1 *Overview of work covered by the Ph.D. thesis.*

		Concrete properties	
		Uncracked	**Cracked**
Corrosion phase	**Initiation**	-	X
	Propagation	X	X

It will be seen from Table 1.1 that corrosion initiation in uncracked concrete is not covered herein. This choice is justified as follows; As already described, corrosion initiation in uncracked concrete is controlled by the transport of depassivating substances through the concrete cover. Assuming that the ingress rate of chlorides is comparable for plain concrete and SFRC, which is justified from the discussion presented in Section 1.2, similar conditions would be expected for these materials leading to comparable time-to-initiation of corrosion.

A number of factors influence the corrosion propagation phase in uncracked concrete, as described in Section 1.2, of which the electrical resistivity has a predominant role. While the literature states that electrochemically passive steel fibres do not affect the electrical resistivity, the impact of electrochemically active (depassivated/corroding) steel fibres (conductive steel fibres) on the electrical resistivity has not been described in the literature. The impact of conductive steel fibres on the electrical resistivity is experimentally and analytically quantified and compared to the impact on the electri-

cal resistivity of moisture and temperature. Additionally, numerical studies concerning the correlation between the electrical resistivity and the corrosion rate are presented.

The influence of steel fibres on initiation and propagation of reinforcement corrosion in cracked concrete is presented in this Ph.D. thesis. The impact of the steel fibres on the mechanical properties of concrete are reported from studies of the formation of a mechanically-induced crack through the concrete cover as well as debonding along the concrete/steel (reinforcement bar) interface. These studies cover experimental observations and numerically based simulations of concrete reinforced with either traditional reinforcement bars or combined reinforcement to illustrate the impact of steel fibres. The impact of cracks and debonding on reinforcement corrosion (initiation and propagation) is investigated by experimental as well as numerical analyses for traditionally reinforced concrete and concrete containing combined reinforcement.

Fulfilling the aim of this thesis requires cross-disciplinary research, ie combining fracture mechanics, for the quantification of crack formation, with the theories of electrochemistry, for the description of reinforcement corrosion. Thus the scope of this work is potentially very broad and a number of limitations have been specified to narrow it to an operational level.

Whenever referring to SFRC in this Ph.D. thesis, only concrete containing relatively limited amounts of steel fibres, ie in the range 0-1.5 vol.-% steel fibres, is considered. This amount of steel fibres leads to tension-softening behaviour and corresponds to what is currently used within the civil infrastructure when using combined reinforcement systems.

Cracks can be formed in concrete due to a number of different mechanisms, eg early age shrinkage, settlement of the structure, corrosion of the reinforcement bars, mechanical load, etc. [*CSR, 1992; Neville, 1996*]. The work concerning corrosion in cracked concrete, which is presented in this Ph.D. thesis, relates to load-induced (bending) cracks. Cracking of the concrete cover caused by corrosion of reinforcement bars, cf. (2) in Figure 1.3 is also considered.

In general, corrosion initiation and propagation of steel fibres are not considered in this Ph.D. thesis, apart from the possible impact of corroding steel fibres on corrosion of traditional reinforcement bars embedded in SFRC.

1.4 Outline of the Thesis

This Ph.D. thesis consists of seven chapters. Experimental and theoretical/numerical studies carried out as part of the Ph.D. study to consider the role of steel fibres on the corrosion of traditional reinforcement are presented in Chapters 2-5. The chapters contain research work written in the format of journal papers. These journal papers are either submitted or accepted for publication in peer-reviewed scientific journals. Each chapter contains background information required for the understanding of the topics discussed. Since these chapters are written as stand-alone research papers, some repetition of theoretical considerations will occur. In Chapter 6 the results presented in Chapters 2-4 are put into perspective through two case studies. Numerical models for reinforcement corrosion recently developed at the Department of Civil Engineering at the Technical University of Denmark, have been applied to analyse initiation and propagation of corrosion of embedded reinforcement using the data presented in Chapters 2-4 as input for the numerical simulations. Conclusions, scientific achievements, limitations and future work are given in Chapter 7.

Chapter 2 (Paper I) concerns an experimental program for the determination of the electrical resistivity of SFRC in the worst-case scenario where the steel fibres are electrically conducting (depassivated or corroding fibres). The aim of the work presented in the chapter is to analyse the impact of various factors, such as the addition of conductive steel fibres, the amount of moisture in the concrete and the temperature, on the electrical resistivity of concrete. Moreover, an analytical model for the prediction of the correlation between the content of conductive steel fibres and the electrical resistivity of concrete is presented and tested with results from the experimental studies.

Chapter 3 (Paper II) presents a numerical, finite-element based model for the simulation of mechanically, load-induced cracking of reinforced concrete beams subjected to three-point bending. This model is based on general fracture mechanical theories, viz. the fictitious crack model. The load-induced cracking predicted by the model includes the formation of a main bending crack at the tensile surface propagating towards the reinforcement bar, as well as debonding along this concrete/reinforcement interface. Debonding is constituted of slip as well as separation at the concrete/steel interface. The capabilities of the presented model to simulate the correct physical fracture mechanisms is verified by comparing the predictions of the model with results presented in a separate technical report prepared as part of the Ph.D. study [*Solgaard et al., 2013*]. The experimental and numerical results presented in the chapter concern concrete beams reinforced with either traditional reinforcement or a combined reinforcement system to evaluate the differences in mechanical response of the two reinforcement systems.

Chapter 4 (Paper III) presents electrochemical measurements of initiation and propagation of corrosion along traditional reinforcement embedded in cracked concrete, plain concrete or SFRC beams. Corrosion along the reinforcement was measured us-

ing a recently developed instrumented reinforcement bar allowing for real-time measurements of the electrochemical potential as well as the corrosion rate along the reinforcement. Results from the electrochemical measurements are correlated with simulations of the damage along the traditional reinforcement to investigate the role of this debonding on initiation and propagation of corrosion in cracked concrete. The work presented in the chapter supplements the work presented in Chapter 3 concerning load-induced damage in reinforced concrete beams; thus a link between reinforcement-corrosion and load-induced damage along the concrete/reinforcement interface is presented.

Chapter 5 (Paper IV) considers the role of steel fibres on corrosion-induced cover cracking due to uniform corrosion of embedded, traditional reinforcement. A numerical model is applied for the determination of this corrosion-induced cracking of the concrete cover, and an extensive study of the parameters affecting the initiation as well as the propagation of this crack is carried out. The amount of corrosion products required to induce cover cracking is linked to time using Faraday's law by calculating the amount of corrosion products from a pre-defined (constant) corrosion current. In this chapter, special emphasis is put on analyses of the potential difference between corrosion-induced cover cracking in traditionally reinforced concrete compared to that in concrete containing combined reinforcement systems.

Chapter 6 contains two case studies carried out using a numerically based corrosion model. The case studies are carefully selected to evaluate the corrosion process in cracked and uncracked concrete reinforced with either traditional reinforcement or a combined reinforcement system using input-data presented in Chapters 2-4. The following case studies have been selected:

Numerical simulations of corrosion of reinforcement bars in uncracked concrete

The aim of this case study is to study the correlation between the electrical resistivity of concrete and the corrosion rate of reinforcement bars. The variations of the electrical resistivity caused by various amounts of conducting steel fibres (depassivated or corroding) and the impact of fluctuations in the ambient conditions, moisture content and temperature, are investigated and compared. The case study covers the corrosion propagation phase.

Numerical simulations of corrosion of reinforcement bars in cracked concrete

The aim of this case study is to study the impact of cracks and mechanically induced debonding along the concrete/steel interface on corrosion initiation and corrosion propagation. The numerical simulations are carried out for various combinations of crack width at the concrete surface and extents of debonding along the concrete/steel interface. Values for the debonding length at various crack width openings at the concrete surface as observed in plain concrete and SFRC (Chapter 3) are used as input for the model.

In the case studies, the corrosion rate is expressed in terms of the average corrosion current density. Basic information about reinforcement corrosion including descriptions of the assumptions and modeling approaches is provided in the chapter.

Finally, the conclusions to be drawn based on the presented work including the case studies are presented in Chapter 7. Additionally, the novel contributions to the field are highlighted and put into perspective and proposals for further research in line with the presented work are provided.

Chapter 2

Observations on the Electrical Resistivity of Steel Fibre Reinforced Concrete (Paper I)

Anders Ole Stubbe Solgaard

Department of Civil Engineering, Technical University of Denmark, Kgs. Lyngby, Denmark

COWI A/S Denmark, Kgs. Lyngby, Denmark

Mette Geiker

Department of Structural Engineering, Norwegian University of Science and Technology (NTNU), Trondheim, Norway

Carola Edvardsen

COWI A/S Denmark, Kgs. Lyngby, Denmark

André Küter

COWI A/S Denmark, Kgs. Lyngby, Denmark

Accepted for publication in the journal "Materials and Structures"
DOI: 10.1617/s11527-013-0064-y

Abstract

Steel fibre reinforced concrete (SFRC) is in many ways a well-known construction material, and its use has gradually increased over the last decades. The mechanical properties of SFRC are well described based on the theories of fracture mechanics. However, knowledge on other material properties, including the electrical resistivity, is sparse. Among others, the electrical resistivity of concrete has an effect on the corrosion process of possible embedded bar reinforcement and transfer of stray current.

The present paper provides experimental results concerning the influence of the fibre volume fraction and the moisture content of the SFRC on its electrical resistivity. The electrical resistivity was measured by alternating current (AC) at 126 Hz. Moreover, an analytical model for the prediction of the electrical resistivity of SFRC is presented. The analytical model is capable of predicting the observed correlation between the fibre volume fraction and the electrical resistivity of the composite (the SFRC) for conductive fibres and moisture saturated concrete. This indicates that the steel fibres were conducting when measuring the electrical resistivity by AC at 126 Hz. For partly saturated concrete the model underestimated the influence of the addition of fibres.

The results indicate that the addition of steel fibres reduce the electrical resistivity of concrete if the fibres are conductive. This represents a hypothetical case where all fibres are depassivated (corroding) which was created to obtain a conservative estimate on the influence of fibres on the electrical resistivity of concrete. It was observed that within typical ranges of variation the influence of the moisture content on the electrical resistivity was larger than the effect of addition of conductive steel fibres, but also that the relative impact on the electrical resistivity due to conductive steel fibres increased when the moisture content of the concrete was reduced.

Keywords

Steel Fibre Reinforced Concrete, Electrical Resistivity, Experimental and Analytical Analyses.

2.1 Introduction

Corrosion of steel reinforcement embedded in concrete is one of the most predominant threats to the durability and structural integrity of reinforced concrete structures. Annually a significant amount of money is spent for rehabilitation and repair of reinforced concrete structures viz. around $ 8.3 billion in the US [*Mokhtar et al., 2008*], $ 200 million in Canada [*Gu and Beaudoin, 1997*] and £ 550 million in the UK [*Corrosion-club, 2012*]. According to Rendell et al. [*Rendell et al., 2002*] 90% of the degradation problems associated to reinforced concrete structures are related to corrosion of embedded reinforcement. Moreover, maintenance and repair of reinforced concrete

structures within the civil infrastructure, eg bridges, often result in shorter or longer closure of the structure in question, causing delays for the road users.

Since corrosion of reinforced concrete structures has a significant impact on the general economy in society, the topic has been described in numerous text books and investigated in a vast amount of research projects in order to clarify and describe causes, consequences and possible precautions of reinforcement corrosion, eg [*Tuutti, 1982; Bertolini et al., 2004*].

Corrosion of embedded reinforcement is a multiphysical and complex process affected by numerous factors covering **environmental conditions,** eg chlorides, moisture, CO_2 and oxygen availability, and **concrete properties,** [*Tuutti, 1982*]. For un-cracked concrete it is generally accepted that the electrical resistivity of the concrete , ρ, plays a predominant role in the corrosion process of reinforcement, [*Tuutti, 1982*].

The electrical resistivity of plain concrete, and the factors influencing it, has been the focus of a variety of experimentally based research projects. Based on experimental observations it was concluded that the electrical resistivity of concrete is mainly affected by the moisture content eg [*Gjörv et al., 1977; Polder, 2001; Hötte, 2003*], the temperature eg [*Hope et al., 1985*], and the porosity of the concrete, which is controlled by, among other factors, the w/c ratio [*Gjörv et al., 1977*] and the maturity eg [*Monfore, 1968; Whittington et al., 1981*]. The impact of the electrical resistivity of plain concrete on the corrosion process of embedded reinforcement was numerically quantified in a number of papers eg [*Bazant, 1978; Osterminski et al., 2006; Michel et al., 2009*]. A literature review of research concerning the relationship between the electrical resistivity of concrete and the corrosion rate of embedded reinforcement is provided in [*Hornbostel et al., 2013*].

Over the past decades the use of steel fibre reinforced concrete (SFRC) as construction material within the civil infrastructure has increased. SFRC is favoured for its load-bearing capacity in the post-peak state due to the fibres transferring stresses across cracks. In contrast, plain concrete is considered as a brittle material that does not have any significant load-bearing capacity in the post-peak state. The mechanical properties of SFRC are well described eg by fracture mechanics, but certain material properties of SFRC still require experimental verification and suitable analytical models.

One of the key parameters to be experimentally investigated and analytically modelled is the electrical resistivity, which is relevant in relation to conventional reinforcement embedded in SFRC as seen in eg the Barcelona Metro [*Gettu et al., 2006*] and Faver- S.S. 612 tunnel lining in Italy [*Chiaia et al., 2008*]. Moreover, concrete can potentially transfer stray current to remote structures, such as steel pipelines or foundations and promote corrosion of these. Since the electrical resistivity of the concrete plays a predominant part in corrosion processes, it is relevant to quantify the effect of adding fibres to the concrete. The amount of literature concerning the electrical

resistivity of SFRC is sparse. However, a few experimental observations on the electrical resistivity of SFRC are reported in the literature, eg [*Lataste et al., 2008; Solgaard et al., 2009; Tsai et al., 2009*].

The present paper presents experimental observations of the effect of selected parameters on the electrical resistivity of SFRC. The experimental work was carried out applying alternating current (AC) at 126 Hz. The observations are compared with observations on plain concrete in order to isolate the differences in the electrical resistivity caused by the addition of steel fibres. The experimental observations are compared to analytical predictions taking into account the impact of the fibre volume fraction and the geometry of the fibres on the electrical resistivity. The analytical model was earlier presented in [*Solgaard et al., 2009*].

2.2 Research Significance

This paper contributes to the knowledge on the electrical resistivity of SFRC and plain concrete. It covers experimental results (AC) and analytical modelling of the influence of steel fibre volume fraction and the moisture content of concrete on the electrical resistivity of concrete.

Among others, the electrical resistivity of concrete has an effect on the corrosion process of possible embedded bar reinforcement and transfer of stray current.

The work presented here represents a conservative estimate of the impact of steel fibres on the electrical resistivity of the composite, ie all fibres transferring current.

2.3 Literature Study

2.3.1 Electrical Resistivity – Measurement Techniques

Different techniques for the determination of the electrical resistivity of concrete have been suggested in the literature, eg direct current (DC), [*Monfore, 1968*], and AC [*Hope et al., 1985; Barnett et al., 2010*]. It is generally accepted that the results are highly dependent on the measuring technique applied. Additionally, the application of DC for such measurements is not suitable due to:

- Polarization of electrodes, [*Hughes et al., 1985*]
- Spatial properties of the concrete matrix are changed over time, due to the migration of positive and negative ions

In order to overcome these obstacles, it has been suggested to measure the electrical resistivity of concrete by applying AC [*Hope et al., 1985*]. In this way the polarization of the electrodes is shifted as the current direction is switched with the frequency, and the spatial properties of the concrete matrix are not affected. This has lead to the development of the so-called Wenner Probe used for on-site measurements of the elec-

trical resistivity of concrete, which presumably is the pre-dominant equipment used for measurements of the electrical resistivity of concrete. The Wenner Probe applies a current at a predefined frequency, in some cases f = 128 Hz.

Such AC measurements allow for measurements of the impedance, Z, which for low frequency AC is similar to the DC resistance, R, of the material [*ACI, 2010*].

For DC the electrical resistance is given by Ohm's law:

$$R = \frac{V}{I} \tag{2.1}$$

where V is the potential and I is the current. The electrical resistivity in the applied set-up (see Section 2.4.2) is calculated from the resistance, cf. Eq. (2.1):

$$\rho = \frac{R}{L} \cdot A \tag{2.2}$$

where L is the distance over which the resistance, R, is measured and A is the cross section area of the test specimen. As mentioned above, the impedance, Z, corresponds to the resistance, R, at low excitation frequencies, f. Thus the resistivity can be calculated from Eq. (2.2) by substituting the resistance, R, by the impedance, Z.

2.3.2 Electrical Resistivity – Observations

The factors affecting the electrical resistivity of concrete and the connection to reinforcement corrosion has been investigated in a variety of research projects as mentioned in Section 2.1. Results from these studies have shown that the predominant factors affecting the electrical resistivity of concrete are moisture content and temperature. The influence of the **temperature** on the electrical resistivity of concrete has successively been modelled by the use of the so-called Arrhenius equation, eg [*Raupach, 1997*], given in Eq. (2.3):

$$\rho_x = \rho_y \cdot e^{b \cdot \left(\frac{1}{T_x} - \frac{1}{T_y}\right)} \tag{2.3}$$

where ρ_x and ρ_y are the electrical resistivity at temperatures T_x and T_y [K], respectively, and b is a constant accounting for the activation energy, E_a, and the ideal gas constant, R = 8.315 J/mol·K, $b = E_a/R$. The activation energy is in the range 12 – 37 KJ/mol [*Hope et al., 1985; Polder et al., 2000*] dependent on eg the moisture content and the w/c ratio.

The impact of the **moisture content** on the electrical resistivity of plain concrete is described by eg Hötte and Gjörv et al. [*Hötte, 2003; Gjörv et al., 1977*]. Moreover Weiss et al. have described the use of a saturation function accounting for less than saturated concrete when describing the electrical resistivity of concrete [*Weiss et al., 2012*] Experimental results published by Gjörv et al. [*Gjörv et al., 1977*] show that the

electrical resistivity of concrete increased three orders of magnitude when the degree of saturation was reduced from 100% to 40% (w/c ratio = 0.42). To the best of the authors' knowledge, similar experimental investigations concerning SFRC have not been reported.

Concerning SFRC, the influence of the fibre volume fraction on the electrical resistivity of the composite has been reported in eg [*Lataste et al., 2008; Tsai et al., 2009*] using AC at 128 Hz. According to the results reported in [*Lataste et al., 2008*] the electrical resistivity was reduced approx. 75 % by the addition of 2.0 vol.-% steel fibres. Further information about other material properties such as w/c ratio and moisture content is not available in the reference. Results presented in [*Tsai et al., 2009*] show that the addition of 1.0 vol.-% steel fibres (60 mm long, black steel) lead to a 50% decrease of the electrical resistivity of concrete with w/c = 0.32.

2.3.3 Electrical Resistivity – Analytical Predictions

Modelling of the influence of inclusions with low electrical resistivity, on the electrical resistivity of composites, has been proposed in a number of publications eg serial modelling and parallel modelling [*Reza et al., 2001*], Lichtenecker's logarithmic mixing rule [*McLachlan et al., 1990*] and the Maxwell-Wagner equation [*Bonanos and Lilley, 1981*] among others. However, the proposed models tend to either over- or underestimate the influence of the inclusions of the overall electrical resistivity of the composite. The main reason for such errors of the proposed models is potentially an incorrect formulation of the orientation of the fibres, since this is viable for the accuracy of the model predictions [*Hatta and Taya, 1985*].

A simple two-phase model, viz. matrix and inclusions, a so-called effective medium theory (EMT) model, for the modelling of the influence of low resistivity inclusions on the overall resistivity of composites has been used for predictions concerning the impact of the fibres on the electrical resistivity of the composite. The modelling approach was originally proposed by Takao et al. [*Takao et al., 1982*] and applied for the description of the thermal conductivity of fibre composites by Hatta and Taya, [*Hatta and Taya, 1985*]. The model was also used for the formulation of the correlation between the fibre volume fraction and the electrical resistivity of SFRC by Solgaard et al. [*Solgaard et al., 2009*]. The major advantage of this EMT-model lies in the formulation of the influence of the geometry and orientation of the fibres. For the EMT modelling approach it is assumed that the fibres are uniformly distributed. Moreover it is assumed that the composite can be considered as a 3D-Misoriented Short Fibre Composite (3D-MSFC) meaning that the fibres are randomly dispersed in three dimensions and that the fibres are considered as ellipsoidal in-homogeneities in an otherwise homogenous matrix.

The orientation of the fibres is accounted for by the use of the so-called S_{ii} tensor [*Hatta and Taya, 1985*], where indices i refer to the axis. Assuming the fibres as pro-

late spheroids with a complete random orientation and distribution, the *S*-tensors, S_{11} - S_{33} are given by Eq. (2.4) & (2.5), respectively ($S_{22} = S_{11}$).

$$S_{11} = \frac{ld^2}{2(l^2 - d^2)^{3/2}}\left[\frac{l}{d}\left(\frac{l^2}{d^2} - 1\right)^{1/2} - cosh^{-1}\left(\frac{l}{d}\right)\right] \tag{2.4}$$

$$S_{33} = 1 - S_{11} \tag{2.5}$$

$$R = 3(S_{11} + S_{33}) - \upsilon_f(2S_{11} + S_{33}) \tag{2.6}$$

It is seen from Eq. (2.4) & (2.5) that the *S*-tensors solely concern the shape (geometry) of the inclusions, in this case fibres considered as prolate spheroids. Further information about the *S*-tensors is provided in [*Hatta and Taya, 1985*].

The 3D-MSFC model for the electrical conductivity, $\sigma_{c,3D}$, of the composite is given by Eq. (2.7):

$$\sigma_{c,3D} = \sigma_m\left(1 - \frac{\upsilon_f(\sigma_m - \sigma_f)[(\sigma_f - \sigma_m)(2S_{33} + S_{11}) + 3\sigma_m]}{3(\sigma_f - \sigma_m)^2(1 - \upsilon_f)S_{11} + \sigma_m(\sigma_f - \sigma_m)R + 3\sigma_m^2}\right) \tag{2.7}$$

where indices *m, f* and c refer to *matrix, fibre* and *composite,* respectively and υ_f is the fibre volume fraction.

The analytical model presented above takes the geometry of the inclusions (fibres) into account, and it is seen from Eq. (2.4) & (2.5) that the geometry of the fibres can be a parameter within the modelling approach if required.

2.4 Experimental and Analytical Procedure

Three different series, viz. Series A-C, were used for the experimental observations of the impact of the fibre volume fraction and the moisture content on the electrical resistivity of the composite. The concrete composition of each series is described in the following along with a general description of the specimens used for the experimental observations. Moreover, the experimental procedure applied for the measurements of the electrical resistivity of the plain concrete/SFRC is described. A description of the test matrix per series is given in a separate section in the following. The so-called saturated specimens were permanently stored submerged after de-moulding except at time of testing. The authors are aware that the applied procedure does not necessarily imply that the specimens were fully saturated. Nonetheless, the term “saturated” will be used in the following to describe such specimens. Apart from the measurements concerning the electrical resistivity selected specimens with and without mixed-in chloride (Series B) were sectioned to quantify the possible effect on the microstructure by the addition of fibres and mixed-in chlorides.

The experimental observations were carried out at room temperature (~20º C).

2.4.1 Description of Parametric Study

2.4.1.1 Series A

The aim of the experimental observations covered by Series A was to investigate the influence of the fibre volume fraction on the electrical resistivity of SFRC and compare with the electrical resistivity of plain concrete. The fibre volume fractions investigated from Series A are similar to those seen in typical SFRC used in civil engineering, ie 0.5 – 1.5 vol.-%. The test matrix for Series A is shown in Table 2.1.

Table 2.1 *Test matrix for Series A.*

Concrete composition	Plain concrete	SFRC		
Fibre volume fraction [vol.-%]	0.0	0.5	1.0	1.5
	X	X	X	X

All the specimens were saturated at time of testing.

2.4.1.2 Series B

The initial aim of testing Series B was to quantify the electrical resistivity of SFRC with electrochemically passive as well as active fibres ie change the properties from electrically insulating to conducting.

The electrochemical state of the fibres was changed by mixing-in chlorides. However, as discussed below the experimental results of Series A revealed that passive fibres are electrically conductive when subjected to AC at 126 Hz. Consequently, Series B is used as supplement to Series A, providing data on the impact of conductive fibres in matrices of varying resistivity.

Electrochemically passive fibres embedded in concrete are, according to eg [*Torrents et al., 2000; Torrents et al., 2001; Mason et al., 2002*], electrically insulated, ie non-conducting, when subjected to direct current (DC) (comparable to low-frequency AC) whereas they act electrically conducting when subjected to (AC). Discussions on the frequency at which the fibres change from conducting to non-conducting has been presented in the literature by Woo et al. [*Woo et al., 2005*] suggesting that observations from AC measurements up to around 1 kHz are comparable to DC measurements, whereas others suggest that the transition-frequency is significantly lower (private communication with Prof. Rob Polder).

The specimens were cast with/without fibres (0, 0.5 and 1.0 vol-%) and with/without mixed-in $CaCl_2$ (0, 4 and 6 wt.-% Cl^-/wt.-% cem.), which was used as the source for chlorides. The test matrix for Series B is given in Table 2.2.

Table 2.2 *Test matrix for Series B.*

Concrete composition		Plain concrete	SFRC	
Fibre volume fraction [vol.-%]		0.0	0.5	1.0
Cl^- content [wt.-% Cl^-/wt.-% cem.]	0.0	X[1]	X	X[1]
	4.0	X	-	X[1]
	6.0	X	X	X[1]

The specimens were moisture saturated. One specimen per batch marked with [1] in Table 2.2 was sectioned for further analyses of the microstructure of the different concrete compositions, as previously explained.

2.4.1.3 Series C

The aim of the experiments concerning this series was to quantify the influence of degree of saturation on the electrical resistivity of plain concrete and SFRC. Three different moisture contents were investigated in Series C, viz. specimens conditioned to RH=45%, RH=75% and saturated specimens. The test matrix of Series C is shown in Table 2.3.

Table 2.3 *Test matrix for Series C.*

Concrete composition		Plain concrete	SFRC	
Fibre volume fraction [vol.-%]		0.0	0.5	1.0
Conditioning	RH = 45%	X	X	X
	RH = 75%	X	X	X
	Saturated	X	X	X

2.4.2 Experimental Work

2.4.2.1 Materials

The same type of specimens was used for all of the experimental investigations viz. cubes with side length 100 mm, which were cut from beam specimens, cf. Figure 2.1.

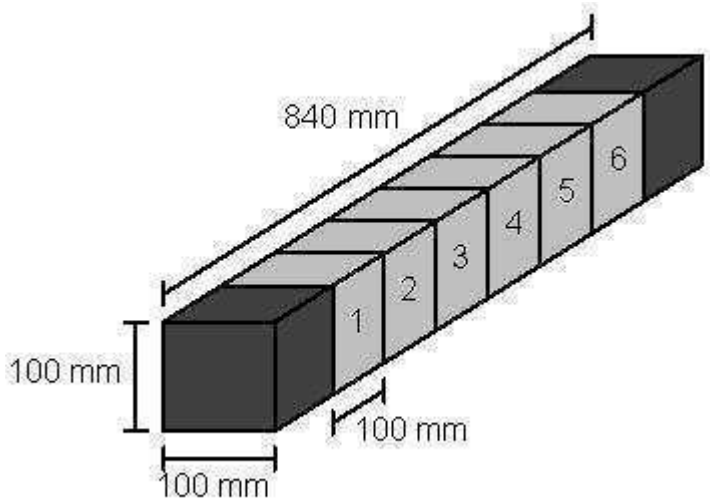

Figure 2.1 *Cutting of specimens from cast concrete beams.*

Cubes 1 - 6, cf. Figure 2.1 were used for the experimental investigations, whereas the end-pieces, ie the darker areas in Figure 2.1, were discarded as the mould ends affect the homogenous dispersion of the fibres.

The same type of steel fibres was used for all series, ie black steel fibres manufactured from cold drawn steel with hooked ends, d = 0.55 mm and l = 35 mm [*Bekaert, 2011*].

The aggregates used for all the series were excavated seabed materials, viz. naturally rounded, in accordance with [*DS 2426, 2004*] and tap water was used for the mixing-water. The materials and casting procedures for each series are given in separate sub-sections in the following.

2.4.2.2 Series A

The mixture design used for Series A is given in Table 2.4.

Table 2.4 *Concrete compositions for Series A (Assuming s.s.d. conditions of aggregates and 1.0 vol.-% air).*

Materials	Quantity [kg/m^3]			
	Plain concrete	SFRC		
	0.0 vol.-%	0.5 vol.-%	1.0 vol.-%	1.5 vol.-%
Cement	500	500	500	500
Water	240	240	240	240
Sand (0-4 mm)	1563	1550	1536	1523
Steel fibres	0	39	78	117

The w/c ratio was 0.48. Though maximum aggregate size was 4 mm, Series A is in the following referred to as concrete. Aalborg Portland White cement, CEM I 52.5 R (HS/EA/≤2) was used for the casting and additional information about the cement type is available in [*AAP, 2011a*].

A standard pan-mixer was used for mixing and sand, cement, and fibres (if added) were dry-mixed for three min. Subsequently water was added and mixing was continued for additional five min. Two beam specimens 100x100x840 mm per mix design were cast, and compacted by the use of a vibration table. After casting, the moulds were covered with plastic sheets to avoid evaporation from the fresh concrete surface, and left for curing at laboratory conditions, (~20ºC). The specimens were de-moulded after 24 h and stored in a water basin with lime rich water for further curing. After at least 28 days the specimens were cut into cubes with side length 100 mm, cf. Figure 2.1, and stored in lime rich water until time of testing.

2.4.2.3 Series B

The concrete compositions used for Series B are given in Table 2.5.

Table 2.5 *Concrete compositions for Series B (Assuming s.s.d. conditions of aggregates and 1.0 vol.-% air).*

Materials	Quantity [kg/m^3]							
	0.0 wt.-% Cl^-/wt.-% cem.			4.0 wt.-% Cl^-/wt.-% cem.		6.0 wt.-% Cl^-/wt.-% cem.		
	Plain concrete	SFRC		Plain concrete	SFRC	Plain concrete	SFRC	
	0.0 vol.-%	0.5 vol.-%	1.0 vol.-%	0.0 vol.-%	1.0 vol.-%	0.0 vol.-%	0.5 vol.-%	1.0 vol.-%
Cement	325	325	325	325	325	325	325	325
Water	163	163	163	163	163	163	163	163
Sand (0-4 mm)	814	814	814	814	814	814	814	814
Aggregates (4-8 mm)	1079	995	911	1079	911	1079	995	911
Steel fibres	0	39	78	0	78	0	39	78
Chlorides	0	0	0	20	20	31	31	31

The w/c ratio of Series B was 0.50, and the air content of the fresh concrete was assumed to be 1.0 vol.-%. The cement type used was Aalborg Portland Basis cement, CEM II/A-LL 52.5 N (IS/LA/≤2) [*AAP, 2011b*].

$CaCl_2$, which was used as the source of chlorides, was dissolved in ¼ of the mixing water and added at the very end of the mixing and mixed for additional 30 seconds to distribute the chlorides in the fresh concrete. This procedure was adapted to facilitate mixing by limiting early acceleration of the hydration process caused by the chloride ions. One beam specimen, as shown in Figure 2.1 was cast per chloride content and fibre volume fraction.

A standard pan mixer was used for mixing and cement, sand, aggregates and ¾ of the mixing water, viz. original amount of water minus water with mixed in chlorides, were mixed for two minutes. Subsequently fibres (if added) were mixed in the concrete for additional five min. The specimens were compacted by the use of a vibration table. Mixes containing chlorides needed more intense vibration, ie shorter vibration time and higher vibration frequency, than mixes without chlorides due to the accelerated setting caused by the addition of chlorides.

Finally the moulded specimens were covered with a plastic sheet to avoid evaporation from the fresh concrete surface and left for curing at laboratory conditions (~20ºC). 24 h after casting, the specimens were de-moulded and stored in a basin containing lime rich water for further curing. Specimens with mixed-in chlorides were stored in chloride and lime containing water to minimize exchange of chloride ions between specimens and water. Finally the specimens were cut in cubes, cf. Figure 2.1, after 28 days and stored saturated until time of testing.

2.4.2.4 Series C

The concrete compositions used for Series C are given in Table 2.6.

Table 2.6 *Concrete compositions for Series C (Assuming s.s.d. conditions of aggregates and 1.0 vol.-% air).*

Materials	Quantity [kg/m^3]		
	Plain concrete	SFRC	
	0.0 vol.-%	0.5 vol.-%	1.0 vol.-%
Cement	375	375	375
Water	163	163	163
Sand (0-4 mm)	761	755	750
Aggregates (4-8 mm)	56	55	55
Aggregates (8-16 mm)	1025	1018	1011
Steel fibres	0	39	78

The w/c ratio of the mixes given in Table 2.6 was 0.43. Aalborg Portland Basis cement, CEM II/A-LL 52.5 N (IS/LA/≤2), was used as cement [*AAP, 2011b*]. The amount of aggregates was reduced for SFRC compared to plain concrete to account for the addition of fibres, cf. Table 2.6. The same grading of the aggregates was maintained for the three different concrete compositions given in Table 2.6.

All concrete compositions given in Table 2.6 were mixed by the use of a standard pan mixer. Cement, water, sand, and aggregates were mixed for two min. Fibres (for SFRC mixes only) were added and the concrete was mixed for additionally two min. For plain concrete, where fibres were not added, the mix was also mixed two times two minutes. Four beam specimens, as shown in Figure 2.1, were cast per fibre volume fraction and the specimens were compacted by the use of a vibration table. The moulds were covered with a plastic sheet after casting to avoid evaporation from the fresh concrete surface. After storage for 24 h at laboratory conditions (~20ºC) the specimens were de-moulded. Subsequently to de-moulding, the specimens were stored in lime rich water for 28 days, at which age they were cut into cubes. The cubes were stored in lime rich water for another month. Four cubes per fibre volume fraction were conditioned to different levels of relative humidity (RH), viz. 45 and 75 % RH and additionally four specimens from each fibre volume fraction were stored in lime saturated water. Those four cubes subjected to the same RH, were selected from four different beam specimens to minimize the possible influence of the natural variation of the concrete material properties between the different beam specimens cast.

Cubes for RH = 45 % and RH = 75 % were conditioned using the rapid conditioning method described by [*Rilem, 1999*]: Initially the required mass loss was calculated based on sorption isotherms for the material. (The sorption isotherms were determined on smaller, crushed samples originating from companion cubes to those used for measurements of the electrical resistivity.) Subsequently the cubes were sealed on four sides to ensure 1-dimensional evaporation and oven-dried at 50 ^{o}C until the calculated mass loss was obtained. When the required mass-loss was reached, the cubes were sealed on all six sides and placed in the oven at 50 ^{o}C for at least 14 days to ob-

tain a more homogenous moisture distribution in the cubes. Finally, the cubes were taken out of the oven and stored in small sealed containers to minimize the exchange of moisture with the ambient air until the experimental investigations were initiated.

2.4.3 Methods

2.4.3.1 Electrical Resistivity Measurements

The impedance used for the determination of the electrical resistivity was measured in the frequency range 10 mHz – 20 MHz, by the use of a Solartron 1260 impedance/Gain-phase Analyser with ten measurements per decade. The specimens were subjected to a voltage drop between the electrodes and the corresponding current transfer was measured cf. Figure 2.2a. The amplitude of that voltage drop was 100 mV which is similar to the voltage drop applied by others for such measurements eg [*Gjörv et al., 1977*]. The electrical circuit is sketched in Figure 2.2a.

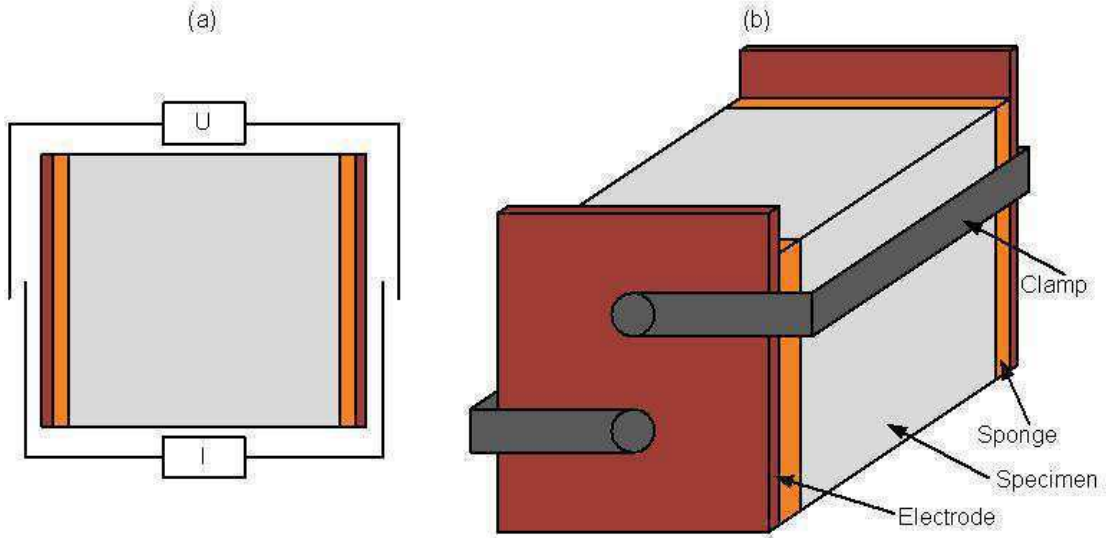

Figure 2.2 *(a) Sketch of electrical circuit for experimental set-up. (b) Sketch of experimental set-up.*

The experimental set-up is depicted in Figure 2.2b. Proper contact between the external electrodes and the specimen was ensured from wet sponges (approx. 2cm thick), soaked in tap water. The electrodes, manufactured from corroded black steel, were clamped to the specimen, cf. Figure 2.2b. The same pressure was applied via the insulated clamps, cf. Figure 2.2b, for all the experimental observations. The technique of using wet sponges to ensure electrical connection between the specimen and the sponges was used for Series A and B and for the saturated specimens of Series C. For the remaining specimens of Series C, proper electrical contact between the electrodes and the specimens was obtained by the use of hyper electrical conductive gel instead of wet sponges. This procedure was adapted to avoid capillary suction of water into the specimens. Initial analyses of results obtained from saturated specimens using these two different media for the electrical contact between the electrodes and the speci-

mens showed only marginal impact on the results from the choice of contact-medium. For all of the experimental investigations the specimen was placed on insulating rubber to avoid an electrical short circuit between the two electrodes. The aforementioned experimental procedure was carried out twice per specimen to ensure reproducibility of this procedure.

2.4.3.2 Sectioning and Inspection of Specimens

Four specimens from Series B were used for sectioning, cf. Table 2.2. The specimens were dried out in an oven for approximately 24 h and subsequently vacuum-saturated with fluorescent epoxy. The epoxy-impregnated specimens were left for hardening of the epoxy for additional 24 h, before the specimens were cut and polished. The specimens were cut parallel with the cut-surfaces cf. Figure 2.1 to analyse any possible changes between the top and the bottom of the specimen originating from the casting of the specimen. Finally the specimens were inspected by the use of UV light making the epoxy luminescent. This enables the possibility of quantifying the micro-structure such as the porosity and possible defects around aggregates and/or fibres.

2.4.3.3 Analytical Predictions

For all of the analytical predictions of the influence of the steel fibres on the electrical resistivity of SFRC, the electrical resistivity of the steel fibres has been set to, $\rho_f = 1.9 \cdot 10^{-9}$ Ωm (~0). Hence, for the analytical predictions it has been assumed that the fibres conduct current and as will be seen this approach presents the best fit of the experimental results.

Concerning the analytical predictions given within this paper, the electrical resistivity of the matrix, ρ_m, was obtained from the measurements on plain concrete assuming that the electrical resistivity of these specimens was representative for the electrical resistivity of the matrix of the SFRC specimens. Further descriptions of the analytical modelling approach, ie the theory concerning the 3D-MSFC model is given in [*Hatta and Taya, 1985*].

2.5 Experimental Results and Analytical Predictions

The experimental observations presented here were obtained using AC $f = 126$ Hz. Results obtained at other frequencies (lower as well as higher) showed the same trends as seen in Figures 2.3, 2.4 and 2.6. To avoid redundancy, these results are, however, not presented in this paper.

Results from the experimental observations are presented along with the analytical predictions by the use of the 3D-MSFC model Eq. (2.4) - (2.7), previously described.

The experimental results presented have been corrected to deduct the response relating to the sponges and electrodes. Thus data presented in the following corresponds to

the electrical resistivity of plain concrete or SFRC. Moreover, data forming the basis of the following section concern the average result per concrete composition along with this average result +/- 1 standard deviation. Results concerning the electrical resistivity are shown on a logarithmic scale as this presentation is suitable for such results where the span of the results may be up to several decades.

2.5.1 Series A

Results from Series A comprise the electrical resistivity of each specimen from the four concrete compositions given in Table 2.4. The results are presented in Figure 2.3.

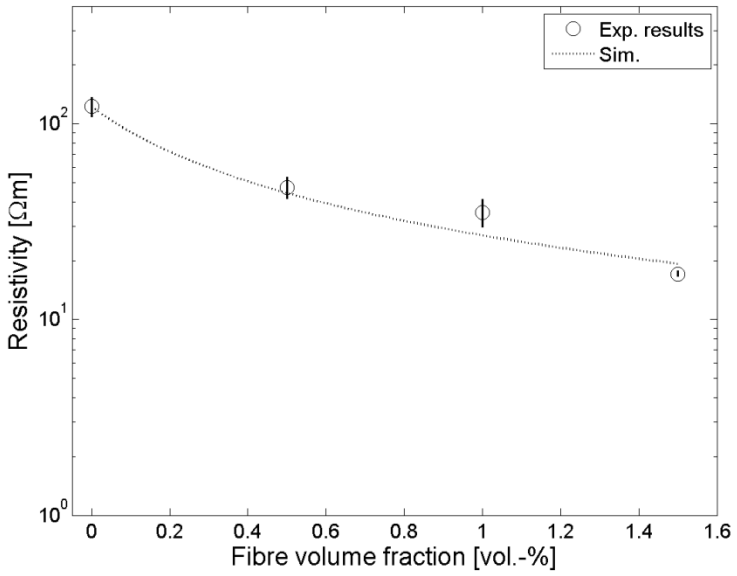

Figure 2.3 *Average electrical resistivity as a function of the fibre content as well as the average electrical resistivity +/- 1 st.dev for Series A along with analytical predictions.*

2.5.2 Series B

The results from Series B, which are shown in Figure 2.4, comprise the electrical resistivity per specimen for all concrete compositions given in Table 2.5.

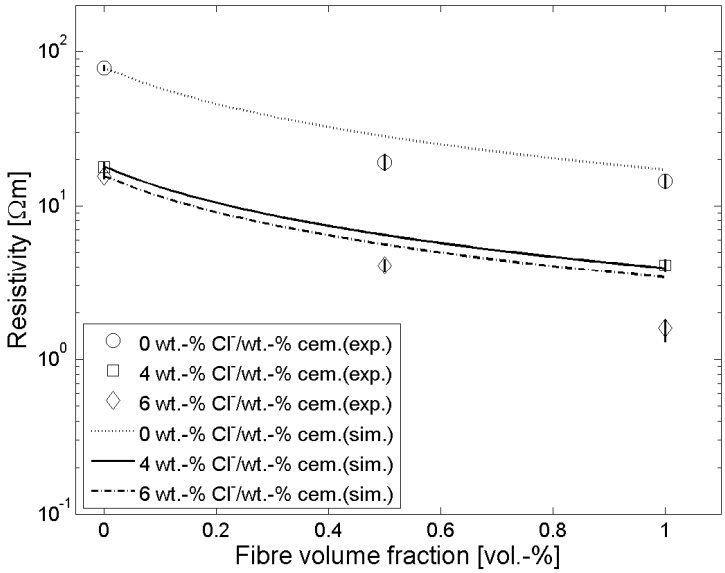

Figure 2.4 *Average electrical resistivity as a function of the fibre content as well as the average electrical resistivity +/- 1 st.dev for Series B along with analytical predictions.*

Additionally four specimens were sectioned to analyse the microstructure and identify possible changes which could be related to the addition of fibres and/or (mixed-in) chlorides. The sections of four specimens are illustrated in Figure 2.5.

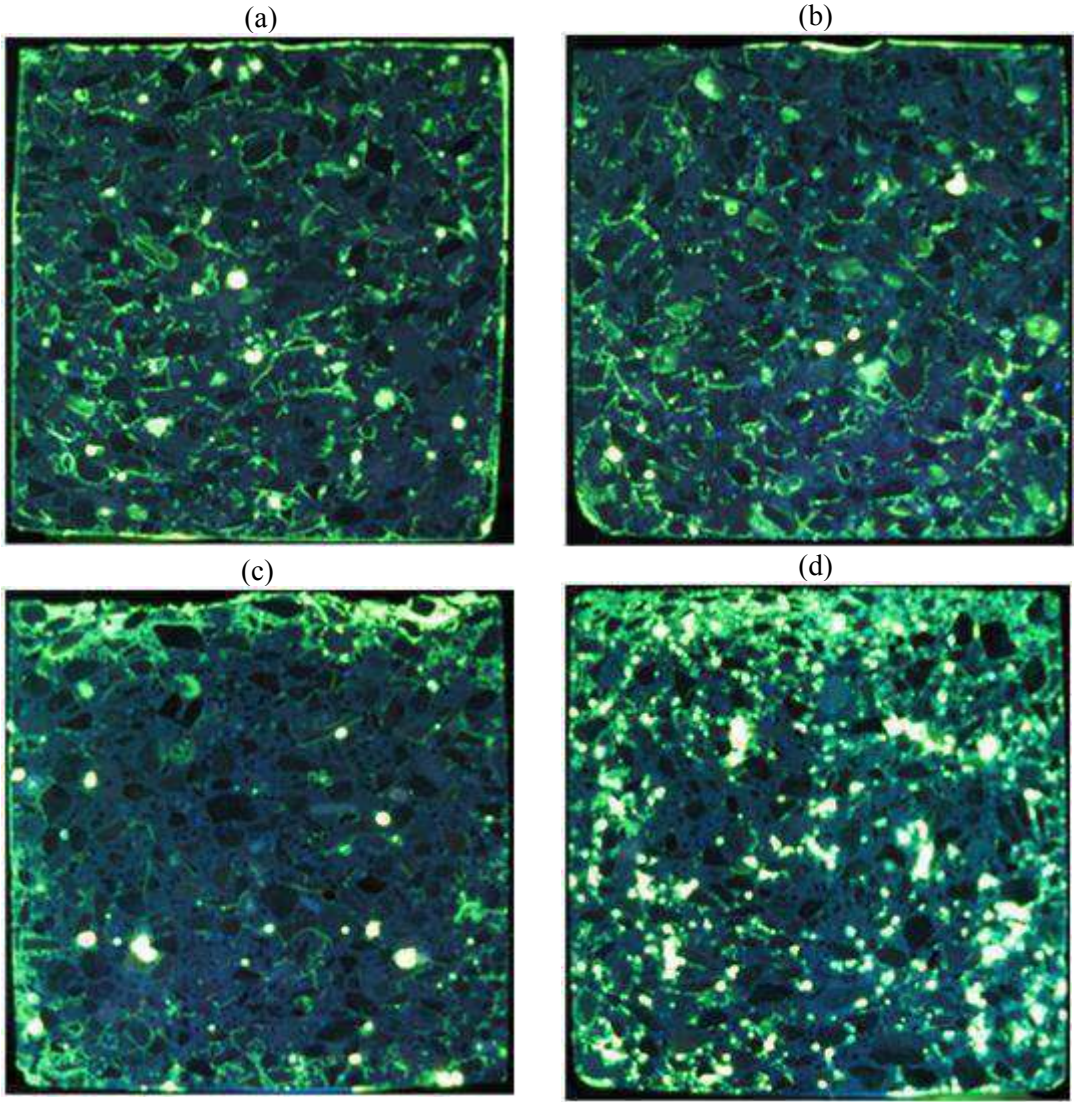

Figure 2.5 *(a): Section of PC with 0 wt.-% Cl⁻/wt.-% cem. (b): Section of 1.0 vol.-% SFRC with 0 wt.-% Cl⁻/wt.-% cem. (c): Section of 1.0 vol.-% SFRC with 4 wt.-% Cl⁻/wt.-% cem. (d) Section of 1.0 vol.-% SFRC with 6 wt.-% Cl⁻/wt.-% cem.*

The top of each picture given in Figure 2.5 correspond to the top of the specimen when the specimens were cast. The dimensions of the sections shown in Figure 2.5 are 100 x 100 mm.

2.5.3 Series C

Results from Series C are presented in Figure 2.6.

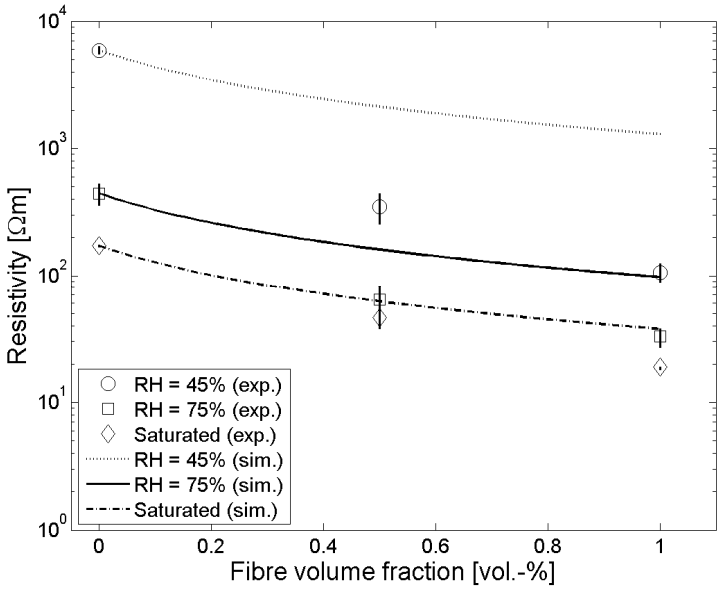

Figure 2.6 *Average electrical resistivity as a function of the fibre content as well as the average electrical resistivity +/- 1 st.dev for Series C along with analytical predictions.*

Results from the conditioning of the specimens are given in Table 2.7.

Table 2.7 *Average moisture content of specimens.*

Concrete composition	Plain concrete	SFRC	
Fibre volume fraction [vol.-%]	0.0	0.5	1.0
Conditioning	[wt.-%]	[wt.-%]	[wt.-%]
RH = 45 %	2.3	2.4	2.5
RH = 75 %	3.7	3.7	3.7
Saturated	5.0	4.8	5.0

2.6 Discussion

The discussions given in the following concern the quantification of the influence of the parameters varied in the experimental study, ie the fibre volume fraction and the moisture content of the concrete.

The influence on the electrical resistivity of concrete of the parameters varied is discussed based on their relative impact, eg the relative change in electrical resistivity between two concrete compositions where only one parameter, such as the fibre volume fraction, is changed. The results are compared to predictions of the influence of changes in the temperature using Arrhenius' equation, Eq. (2.3).

Initially the basis of the analytical model and its sensitivity is discussed.

2.6.1 Analytical Model

The sensitivity of the proposed model is discussed with regard to the ingoing parameters such as the resistivity of the steel fibres and the geometry of the fibres.

The influence of the fibres on the overall resistivity was predicted for various values for the electrical resistivity of the fibres and the same electrical resistivity of the matrix (ρ_m = 100 Ωm). The results are shown in Figure 2.7.

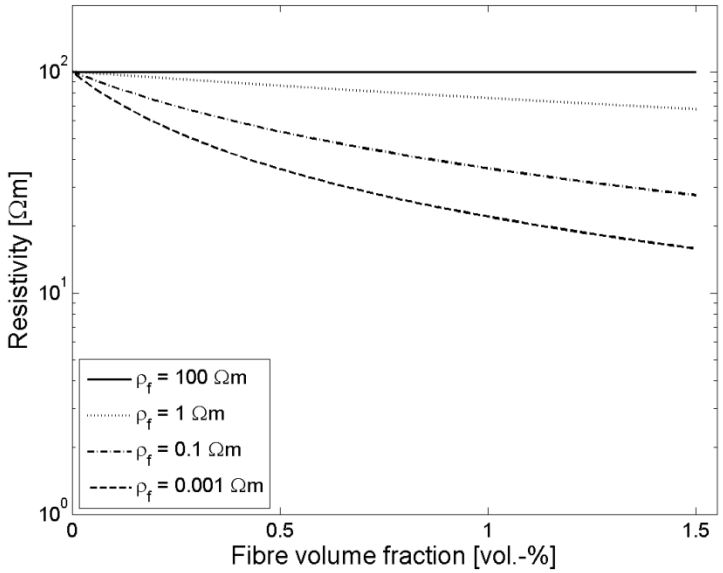

Figure 2.7 *Sensitivity analyses of the analytical 3D-MSFC model for varying values of ρ_f.*

According to the analytical predictions presented in Figure 2.7 the addition of fibres having a somewhat similar electrical resistivity as the matrix, only has a minor influence on the overall resistivity of the composite. However, even relatively small amounts of high conductive fibres change the electrical resistivity of the composite remarkably according to the analytical predictions. Additionally it is seen from Figure 2.7 that the analytical model is very sensitive to changes in the electrical resistivity of the inclusions when those have a value around 1‰ – 1% of the matrix resistivity. This is not relevant in this case, where the electrical resistivity of the fibres is negligible compared to that of concrete.

The influence of the fibre geometry was analysed for fibre lengths between 5.5 and 70 mm and constant diameter of the fibre (d = 0.55 mm). It is seen from Eq. (2.4) that the geometry tensor S_{11} is controlled by the ratio between the length of the fibre, l, and the diameter of the fibre, d, the so-called aspect ratio (AR). The values of the fibre length used for the sensitivity analyses presented in Figure 2.8 correspond to AR between 10 and 128 (AR = 65 for the fibres used for the experimental observations). For the predictions presented in Figure 2.8, ρ_m = 100 Ωm and $\rho_f = 1.9 \cdot 10^{-9}$ Ωm.

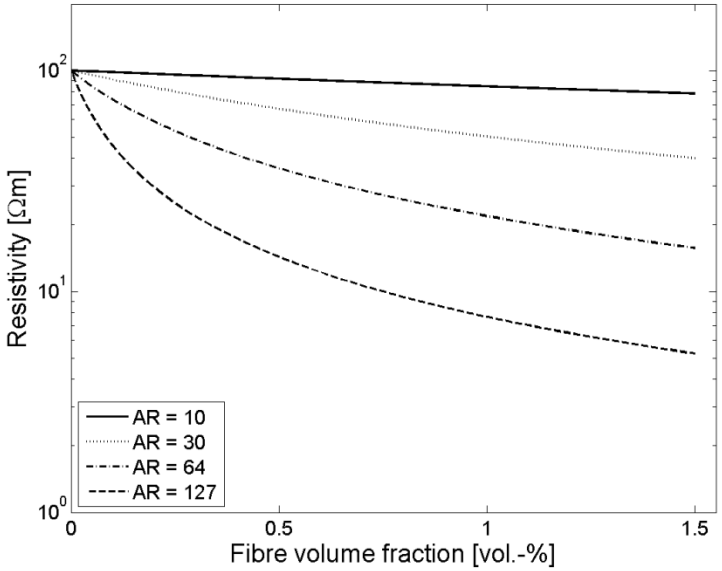

Figure 2.8 *Sensitivity analyses of the analytical 3D-MSFC model for varying fibre length.*

It is seen from Figure 2.8 that the influence of the AR of the fibres on the electrical resistivity is reduced with increasing values of the AR. Assuming that the diameter of the fibre is constant an increase in the AR corresponds to increasing the length of the fibre, and it is seen from Figure 2.8 that the increased length of the fibre results in a reduction of the electrical resistivity of the composite. This corresponds very well to the a-priori knowledge, that the risk of fibres touching each other and thereby forming a longer zero-resistance path through the composite is increased when the length of the fibres is increased.

2.6.2 Influence of the Fibre Volume Fraction

In general it is seen from the experimental observations comparing SFRC, either 0.5 vol.-% or 1.0 vol.-%, with plain concrete that the electrical resistivity was reduced by the addition of fibres. Comparing plain concrete and 0.5 vol.-% SFRC it is seen from Figures 2.3, 2.4 and 2.6 that the addition of 0.5 vol.-% of steel fibres had comparable relative impact on the electrical resistivity of saturated concrete for all three series varying in mix design, cf. Tables 2.4 – 2.6. A somewhat similar trend was observed by comparisons of results for plain concrete and 1.0 vol.-% SFRC. The influence of the addition of 1.0 vol.-% steel fibres on the electrical resistivity is in line with the observations by Tsai et al. [*Tsai et al., 2009*], cf. previous description of these results.

The analytical predictions of the electrical resistivity of saturated and un-contaminated specimens are also shown in Figures 2.3, 2.4 and 2.6. The predictions correspond to an upper-value of the electrical resistivity of the composite, when it is assumed that all of the fibres have zero resistance, ie electrically conductive. Comparisons between the experimental data and the results of the analytical model (assuming

zero electrical resistance of the fibres) show good correlation, eg Figure 2.3, indicating that the fibres are indeed conducting current at AC 126 Hz.

Comparing results for the electrical resistivity of plain concrete and 1.0 vol.-% SFRC with and without 4.0 wt.-% Cl^-/wt.-% cem. (Series B) a similar relative reduction of the electrical resistivity can be observed for the SFRC, cf. Figure 2.4. The addition of 6.0 wt.-% Cl^-/wt.-% cem. caused a relatively larger reduction of the electrical resistivity of 1.0 vol.-% SFRC, cf. Figure 2.4. The analytical model does not capture this un-expected reduction of the electrical resistivity.

Results concerning the influence of (mixed in) chlorides on the electrical resistivity of PC were presented by Gjörv et al. [*Gjörv et al., 1977*]; The addition of 4 wt.-% $CaCl_2$/wt.-% cem.% (corresponding to approx. 2.6 wt.-% Cl^-/wt.-% cem.), reduced the electrical resistivity of mortar (w/c = 0.50) by approx. 50%. The reduction of the electrical resistivity of PC caused by the addition of (mixed in) chlorides observed in this study, is in line with the observations presented in [*Gjörv et al., 1977*]. The impregnated and sectioned specimens of Series B presented in Figure 2.5, showed that the porosity appeared increased around the aggregates for all four sections shown, which indicated that bleeding, presumably due to vibration during casting, occurred. Comparing Figure 2.5a (plain concrete, 0 wt.-% Cl^-/wt.-% cem.) and Figure 2.5b (1.0 vol.-% SFRC, 0 wt.-% Cl^-/wt.-% cem.) it can be observed that the addition of 1.0 vol.-% steel fibres did not lead to major changes in the microstructure of the concrete matrix. From Figure 2.5c – d (specimens with cast-in chlorides) a higher luminescent, indicating increased porosity, is observed at the top surface and to some extent at the other surfaces. It is assumed that this phenomenon is caused by the need for increased vibration (frequency) of the specimens when chlorides were added. Note, that for SFRC specimens (Figures 2.5b and 2.5d) the fibres reflect the UV light, which could lead to an overestimation of the porosity. The reflecting fibres are recognized as circular luminescent inclusions in the figure. The increased inhomogeneity seen in Figure 2.5d is a possible explanation for the aforementioned un-expected reduction of the electrical resistivity by the addition of 6.0 wt.-% Cl^-/wt.-% cem. to 1.0 vol.-% SFRC.

2.6.3 Influence of the Moisture Content

The impact of the moisture content on the electrical resistivity of plain concrete and SFRC was investigated via Series C. As seen from Figure 2.6, the moisture content has a predominant effect on the electrical resistivity of the composite. According to experimental observations presented in [*Gjörv et al., 1977*] the electrical resistivity was increased a little less than three orders of magnitude when the degree of moisture saturation was reduced from 100% to 40 % saturation for plain concrete with w/c ratio = 0.42.

In order to describe the influence of the moisture content for plain concrete and SFRC (0.5 and 1.0 vol.-%) the electrical resistivity of these materials was plotted as a function of the relative humidity in Figure 2.9.

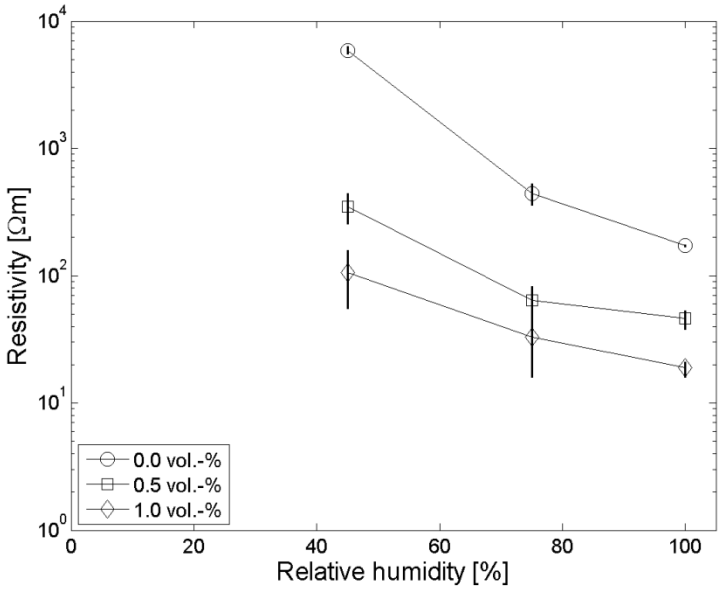

Figure 2.9 *Influence of the relative humidity of concrete on the electrical resistivity of PC and SFRC, Series C.*

Data presented in Figure 2.9 is reproduced from Figure 2.6 and Table 2.7.

Comparing the impact on the electrical resistivity of the three concrete compositions in Figure 2.9 it can be observed that the variation in the relative humidity, and thus the moisture content, has larger influence on plain concrete compared to SFRC. Note, that these results cannot automatically be related to other concrete compositions since the concrete properties, such as the age and the w/c ratio have a remarkable influence on the electrical resistivity.

The analytical predictions underestimate the influence of the steel fibres on the electrical resistivity of the composite for conditioned specimens, cf. Figure 2.6. Given that the specimens were cast from the same batch and conditioned to various moisture contents after at least 28 days of curing, this observed difference cannot be explained from natural variation in the microstructure of the concrete matrix. Moreover, the sectioned specimens shown in Figures 2.5a – 2.5b for plain concrete and 1.0 vol.-% SFRC, does not reveal that the addition of steel fibres changed the microstructure of the concrete matrix remarkably. A potential explanation is an inhomogeneous moisture distribution due to the outer surface being on the adsorption branch and the core being on the desorption branch of the sorption isotherms. The available data does not allow for any further assessment of this.

The observed influence of fibre addition and degree of saturation for Series C are summarized and presented in terms of ratios in Tables 2.8 and 2.9, respectively. The degree of moisture saturation is calculated from the values given in Table 2.7.

Table 2.8 *Change of the electrical resistivity due to the addition of fibres.*

	45	75	100
$\frac{\rho_{v=0\ vol.-\%}}{\rho_{v=0.5\ vol.-\%}}\left(\frac{\rho_{v=0.5\ vol.-\%}}{\rho_{v=0.0\ vol.-\%}}\right)$	12-25 (0.04-0.08)	4-12 (0.09-0.22)	3-5 (0.22-0.32)
$\frac{\rho_{v=0\ vol.-\%}}{\rho_{v=1.0\ vol.-\%}}\left(\frac{\rho_{v=1.0\ vol.-\%}}{\rho_{v=0.0\ vol.-\%}}\right)$	35-115 (0.01-0.03)	7-34 (0.03-0.14)	8-11 (0.09-0.12)

Table 2.9 *Change of the electrical resistivity due to changes in the degree of saturation.*

	Plain concrete	SFRC (0.5 vol.-%)	SFRC (1.0 vol.-%)
$\frac{\rho_{u=75\ \%}}{\rho_{u=100\ \%}}\left(\frac{\rho_{u=100\%}}{\rho_{u=75\%}}\right)$	2-3 (0.32-0.49)	0.9-2.1 (0.47-1.2)	0.8-3.1 (0.32-1.3)
$\frac{\rho_{u=50\ \%}}{\rho_{u=100\ \%}}\left(\frac{\rho_{u=100\ \%}}{\rho_{u=50\%}}\right)$	31-37 (~0.03)	5-12 (0.09-0.21)	3-10 (0.10-0.39)

A comparison of the values given in Tables 2.8 – 2.9 show that the addition of 1.0 vol.-% steel fibres to the saturated concrete corresponded to a reduction of the electrical resistivity comparable to that caused by an increase of the degree of saturation of plain concrete from approx. 75 % to 100 %.

2.6.4 Influence of Temperature – Analytical Quantifications

As previously described, the temperature has a significant influence on the electrical resistivity of cementitious composites. The influence of the temperature on the electrical resistivity has not been quantified experimentally in the presented work. However, as previously described its influence can be quantified by the use of Arrhenius' Equation, Eq. (2.3). The relative impact of the temperature on the electrical resistivity has been calculated by the use of Eq. (2.3) and illustrated in Figure 2.10. This influence was calculated for the upper and lower bound of the activation energy previously given. As seen from Figure 2.10, the point of departure for the calculations presented in Figure 2.10 is the electrical resistivity at 20 ^{o}C (the temperature at which experimental measurements were carried out), ie the relative electrical resistivity at that temperature equals 1.

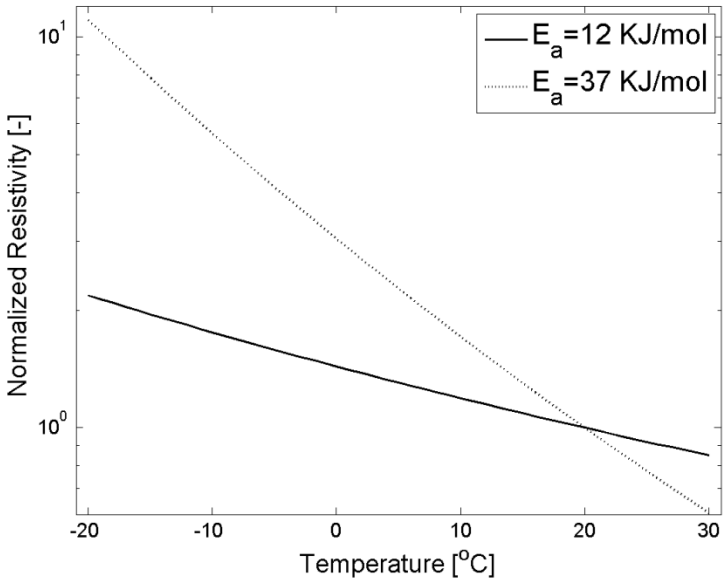

Figure 2.10 *Normalized resistivity vs. temperature calculated from Arrhenius equation assuming two different values of the activation energy.*

It is seen from a comparison of Table 2.8 and Figure 2.10 that the addition of 0.5 vol.-% steel fibres to the saturated concrete resulted in a decrease in the electrical resistivity which is comparable to an increase in the temperature from 20 °C to approx. 30 °C. Moreover, Figure 2.10 and Table 2.9 shows that the relative increase of the electrical resistivity caused by a reduction of the saturation from 100 % to approx. 75 % for all studied concrete compositions correspond to a decrease in the temperature from 20 °C to approx. 10 °C.

2.7 Conclusion

The aim of the paper was to quantify the impact of the fibre volume fraction and the moisture content on the electrical resistivity of steel fibre reinforced concrete (SFRC). The electrical resistivity was investigated experimentally and analytically. AC at 126 Hz was applied to SFRC (0, 0.5 and 1.0 vol.-%). The analytical model was based on the assumption of random 3D orientation of the fibres. The following observations were made:

- The results indicate that the fibres have been conducting during the AC measurements at 126 Hz. This approach provides a conservative estimate of the impact of steel fibres on electrical resistivity of SFRC, which are generally passive and hence electrically insulated at DC.
- The addition of steel fibres reduced the electrical resistivity, when applying AC at 126 Hz.

- The analytical model was capable of predicting the electrical resistivity of saturated SFRC with conductive fibres. However, the model underestimated the impact of fibres in non-saturated SFRC.
- Within the parameters and ranges investigated the moisture content had the largest influence on the electrical resistivity. The electrical resistivity differed orders of magnitude due to the variations in the degree of saturation, viz. specimens conditioned to RH = 45%, RH = 75% and capillary saturated specimens. The relative influence of the degree of saturation was less for SFRC than for plain concrete.
- The influence of adding 0.5 vol.-% fibres, which were conducting under AC, on the electrical resistivity of the saturated concrete was comparable to the calculated influence of a change in the temperature from 20 ^{o}C to approx. 30 ^{o}C.

Acknowledgements

The first author gratefully acknowledge the full financial support of the PhD project "Application of Fibre Reinforced Concrete in Civil Infrastructure" by the Danish Agency for Science, Technology and Innovation, COWI A/S, DTU, Bekaert NV, Grace and the Danish Road Directorate. Additionally, the helpfulness with the AC/IS equipment and the interpretation of the experimental data by Associate Professor Torben Jacobsen (DTU Kemi) is highly appreciated. Finally the help from students at the Department of Civil Engineering (DTU) with experimental observations is acknowledged.

Chapter 3

Numerical, Fracture Mechanical Modelling of Debonding in Reinforced Concrete Beams (Paper II)

Anders Ole Stubbe Solgaard

Department of Civil Engineering, Technical University of Denmark, Kgs. Lyngby, Denmark

COWI A/S Denmark, Kgs. Lyngby, Denmark

Alexander Michel

Department of Civil Engineering, Technical University of Denmark, Kgs. Lyngby, Denmark

Henrik Stang

Department of Civil Engineering, Technical University of Denmark, Kgs. Lyngby, Denmark

Submitted for the journal “Materials in Civil Engineering”

Abstract

The formation of cracks in the concrete cover of reinforced concrete is often related to mechanical loading. Although, the formation of cracks is inevitable due to the brittle nature of concrete, they are not accounted for in existing guidelines for service life design even though it is generally accepted that cracks in the concrete cover may promote the risk of reinforcement corrosion since the ingress rate of eg moisture and/or chlorides may increase.

To account for the influence of cracks and in the concrete cover in the service life design of a reinforced concrete structure it is of vital importance to determine the correlation between the risk of the initiation of reinforcement corrosion and the extent of cracking associated to the load applied. Experimental studies of load-induced crack formation have been presented in the literature. However, operational tools, eg numerical models, capable of correlating the applied load and the associated crack-formation in the concrete cover and debonding at the concrete/steel interface are not available at present.

The aim of this paper is to present a numerical model for the formation of tensile load-induced cracking in concrete. The model simulates the formation of a bending crack through the concrete cover as well as the formation of debonding at the concrete/steel interface. The numerical model is based on theories of fracture mechanics, viz. the fictitious crack model, and the numerical simulations are compared to experimental data. The experimental data cover observations of flexural loading of conventional reinforcement embedded in plain concrete as well as steel fibre reinforced concrete (0.5 and 1.0 vol.-%).

Comparisons of the numerical and experimental results show, that the proposed model is capable of simulating the formation of a bending crack and – at the same time – the slip and separation at the concrete/steel interface accurately. Based on those observations it may be concluded that the numerical model is based on correct physical assumptions.

Keywords

Numerical simulations, Fracture mechanics, Load-induced cracking, Service Life Design, Fibre Reinforced Concrete

3.1 Introduction

Reinforced concrete is the most widely used man-made construction material in the World for structures in the civil infrastructure. The serviceability of such structures is strongly related to the integrity, which is controlled by the durability. The deterioration of reinforced concrete structures is caused by a number of mechanisms such as freeze-thaw reactions, alkali-silica reactions and reinforcement corrosion, of which corrosion is the predominant deterioration mechanism [*Rendell et al., 2002*].

Corrosion of reinforcement occurs among others due to the ingress of de-passivating substances such as CO_2 and/or Cl^-. The ingress rate of those substances is strongly promoted by cracks in the concrete cover, which may be formed due to eg mechanical loading and/or shrinkage. Such cracks in the concrete cover act as pathways for the de-passivating substances [*Wang et al., 1997; Edvardsen, 1999; Aldea et al., 1999*]. The formation of cracks in concrete is effectively inevitable due to the quasi-brittle nature of concrete.

The identification of the predominant role of cracks in the concrete on the transport of de-passivating substances led to different formulations of the correlation between cracking and the risk of reinforcement corrosion. Such formulations are vitally important for the proper design of durable reinforced concrete structures.

One of those formulations is based on the hypothesis that the risk of reinforcement corrosion is correlated to the crack mouth opening displacement (CMOD) at the concrete surface eg [*Schießl and Raupach, 1997; Mohammed et al., 2001*]. The proposed models for that relationship show reasonable correlations for exposure times less than approx. three years. However, other experimental observations by eg Kennedy [*Kennedy, 1956*] and Francois and Arliguie [*Francois and Arliguie, 1998*] show no correlation at all between crack width and risk of reinforcement corrosion.

Bearing those observations in mind, it was proposed by Tammo [*Tammo and Thelandersson, 2009; Tammo et al., 2009*] that the risk of reinforcement corrosion is controlled by the crack opening displacement (COD) at the level of the reinforcement. The COD is not explicitly correlated with the CMOD eg due to the formation of concrete cones around the reinforcement, varying cover thickness, rebar-concrete bond etc. A similar approach for the formulation of the risk of reinforcement corrosion due to cracking of the concrete cover was suggested by Pease et al. [*Pease et al., 2006; Pease et al., 2011*] proposing that the cracking state along the concrete/steel interface is a more fundamental measure than the CMOD at the concrete surface to describe the susceptibility of reinforcement corrosion. Results presented in [*Pease et al., 2011*] were supported by observations presented in [*Win et al., 2004*] showing that cracking and debonding along the reinforcement resulted in a lateral ingress of chloride ions increasing the risk of reinforcement corrosion significantly.

Photogrammetric observations of the concrete/steel interface presented in [*Pease et al., 2006*] showed that significant cracking and debonding was induced at the concrete/steel interface for reinforced beams subjected to bending. Similar observations concerning reinforced concrete beams made from both plain concrete (PC) and Steel Fibre Reinforced Concrete (SFRC) were presented by Solgaard et al. [*Solgaard et al., 2013*].

A numerical model predicting the cracking state along the concrete/steel interface is thus required to allow for durability design of reinforced concrete structures and for obtaining better understanding of the parameters influencing the interfacial cracking state. Such a model should consider the formation of a bending crack through the concrete cover towards the reinforcement and characterization of the cracking state at the concrete/steel interface caused by applied flexural load. The cracking state at the concrete/steel interface consists of slip, the displacement discontinuity parallel to the rebar surface and separation, the displacement discontinuity perpendicular to the rebar surface.

Previous work concerning formation of cracks at the concrete/steel interface in conventional reinforced concrete beams subjected to mechanical loading has mainly focused on the slip behavior eg [*Tammo et al., 2009*] whereas the separation along the reinforcement has not been investigated to the same extent.

The present paper describes a numerical, finite element (FE) based model for the prediction of load-induced cracking of reinforced concrete specimens subjected to flexural load in a three point bending test (3 PBT). The numerical model describes the initiation and propagation of a main bending crack from the tensile surface of the concrete towards the reinforcement and the slip and separation at the concrete/steel interface. The presented numerical model is based on the fictitious crack model described by Hillerborg et al. [*Hillerborg et al., 1976*] taking the fracture mechanical properties of the concrete matrix into account. The numerical model is compared to experimental results presented in [*Solgaard et al., 2013*]. The procedure adapted for the experiments described in [*Solgaard et al., 2013*] covering state of the art techniques such as photogrammetric measurements is briefly presented in this paper.

3.2 Model Description

The numerical model simulated slip and separation at the concrete/steel interface associated with crack formation in the concrete cover for reinforced concrete beams loaded in three point bending assuming 2D plain strain and discrete crack formation. The location of the main bending crack at the centre of the reinforced concrete beams, was predefined. The modelling approach for the main bending crack and the slip and separation at the concrete/steel interface is illustrated in Figure 3.1.

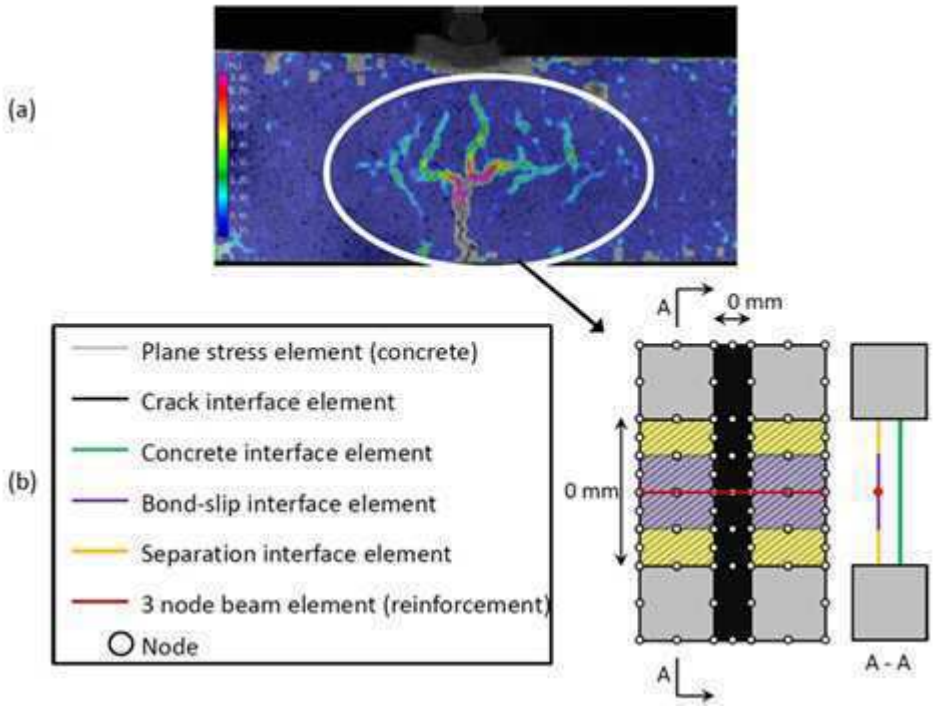

Figure 3.1 *a) Illustration from photogrammetric assessment of the load-induced cracking state in reinforced concrete specimens [Solgaard et al., 2013]. b) Concept of the serial-parallel model simulating cracking, slip and separation at concrete/steel interface. The illustration is not in scale. Inspired by [Olsen, 2010].*

A photogrammetric image of the reinforced concrete specimen is shown in Figure 3.1(a) whereas Figure 3.1(b) illustrates the details of the modelling approach at the centre of the specimen. A number of zero-thickness interface elements (in serial and parallel connection) were incorporated in the model, cf. Figure 3.1(b), to simulate the slip and separation at the concrete-reinforcement interface as well as cracking in the concrete domain. The upper and lower parts of the concrete body were connected through a concrete interface at the reinforcement level. In addition, the reinforcement, represented by beam elements, was connected to the lower and upper concrete body respectively through a serial connection of bond-slip and separation interfaces. The reinforcement and the remaining part of the concrete domain had linear elastic properties assigned. The various interface elements shown in Figure 3.1(b) are described in the following.

Formation and propagation of the main bending crack in the concrete domain was based on the fictitious crack model [*Hillerborg et al., 1976*]. The mechanical properties of the "crack interface elements" in the concrete domain cf. Figure 3.1(b) were defined using cohesive relationships and may be described as by Eq. (3.1).

$$\sigma = \begin{cases} \sigma_e(\varepsilon) = E_c\varepsilon & Pre-cracked\ state \\ \sigma_w(w) = g(w)f_t & Cracked\ state \end{cases} \tag{3.1}$$

where σ_e is the elastic stress, E_c is the Young's modulus of concrete, ε is the elastic strain, $\sigma_w(w)$ the normal bridging stress as a function of the crack width w, $g(w)$ is the dimensionless cohesive relationship and f_t is the concrete tensile strength. Multi-linear softening relations as presented by [*Olesen, 2001*] were used to describe the dimensionless cohesive relationship, $g(w)$:

$$g(w) = b_i - a_i w \quad \text{with } w_{i-1} < w < w_i \quad \text{and} \quad i = 1,\ldots n \tag{3.2}$$

where a_i describes the slopes of the cohesive branches, b_i the intercepts between the cohesive branches and w_i was defined as follows:

$$w_i = \frac{b_i - b_{i+1}}{a_i - a_{i+1}} \quad \text{with} \quad i = 1,\ldots,n-1 \quad \text{and} \quad w_n = w_{crit} = \frac{b_n}{a_n} \tag{3.3}$$

where w_{crit} is the critical crack width. For $w > w_{crit}$ the crack was considered stress-free.

The concrete interface connecting the upper and lower concrete body, cf. Figure 3.1(b), was described by the same mechanical properties as the main bending crack given above. This concrete interface was incorporated in the model to account for the formation of radial cracks around the reinforcement, which were not explicitly simulated by the model. These radial cracks allowed for the separation at the concrete/steel interface and consequently had to be accounted for in the model to simulate the cracking process.

The numerical model presented herein, is a 2D model, cf Figure 3.1, although the problem is 3D. In order to comply with this problem, the aforementioned concrete interface between the upper and lower parts of the concrete domain accounted for the properties in the remainder of the cross section where there was concrete only.

Separation at the concrete/steel interface was described by the use of a cohesive relationship linking the bridging stress and the crack width, see Eq. (3.4). For the separation interface elements the cohesive relationship was linear descending, n =1 in Eq. (3.5)-(3.6).

$$\sigma_{sep} = \begin{cases} \sigma_{e,sep}(\varepsilon_{sep}) = E_c\varepsilon_{sep} & Pre-cracked\ state \\ \sigma_{sep}(w_{sep}) = g(w_{sep})f_{t,sep} & Cracked\ state \end{cases} \tag{3.4}$$

where σ_{sep} is the stress in the interface, $\sigma_{sep}(w_{sep})$ is the bridging stress in the interface, and $f_{t,sep}$ is the strength of the separation interface. The dimensionless cohesive relationship for the separation interface is given from Eq.(3.5).

$$g(w_{sep}) = b_{sep,i} - a_{sep,i} w_{sep} \quad \text{with } w_{sep,i-1} < w_{sep} < w_{sep,i} \quad \text{and} \quad i = 1,\ldots n \tag{3.5}$$

$a_{sep,i}$ describes the slopes of the cohesive branche of the cohesive relationship, $b_{sep,i}$ is the interception between the cohesive branches and $w_{sep,i}$ was given from Eq. (3.6):

$$w_{sep,i} = \frac{b_{sep,i} - b_{sep,i+1}}{a_{sep,i} - a_{sep,i+1}} \quad \text{with} \quad i = 1, \ldots, n-1 \quad \text{and} \quad w_{sep,n} = w_{sep,crit} = \frac{b_{sep,n}}{a_{sep,n}} \tag{3.6}$$

$w_{sep,crit}$ is the critical separation. For separation greater than the critical separation the crack was considered stress-free.

Finally, the bond-slip interface, which accounted for sliding at the concrete/steel interface, cf. Figure 3.1(b), was described by a cubic-relationship between the shear stress and slip, proposed by Dörr [*Dörr, 1980*]. The relationship attained a constant value, cf. Eq. (3.7) for a given value of slip, the so-called constant slip value, Δt^0:

$$t_t = \begin{cases} f_{t,slip}\left(1.4\left(\frac{\Delta t}{\Delta t^0}\right)^3 - 4.5\left(\frac{\Delta t}{\Delta t^0}\right)^2 + 5\left(\frac{\Delta t}{\Delta t^0}\right)\right) & for \quad 0 \le \Delta t < \Delta t^0 \\ 1.9 f_{t,slip} & \Delta t \ge \Delta t^0 \end{cases} \tag{3.7}$$

where Δt is the slip, t_t is the shear stress (bond), and $f_{t,slip}$ is the strength of the slip interface.

Typical mechanical properties of the different interface elements, cf. Figure 3.1(b), are illustrated in Figure 3.2.

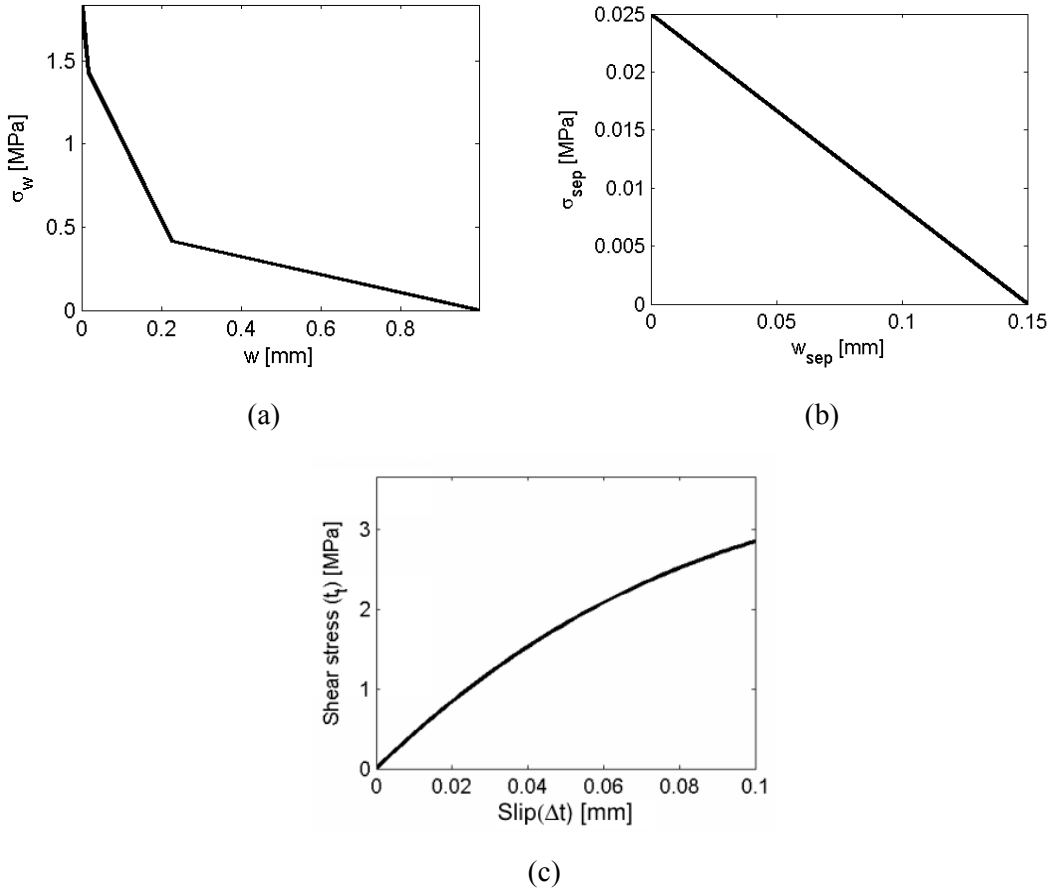

Figure 3.2 *(a) normal stress-separation law for cracking in concrete domain, (b) normal stress-separation law for separation between concrete and reinforcement and (c) shear stress-slip relation between concrete and reinforcement.*

The relationships of the various interface elements given in Figure 3.2(a)-(c) are not representative for all simulations described in the following sections. However, the illustrations serve as visual representations of Eqs. (3.1)-(3.7).

The three latter interfaces, viz. the concrete interface between the upper and lower part of the concrete domain, the bond-slip relationship and the separation interface were modelled along the entire concrete/steel interface, while the crack interface was only located at the centre of the reinforced concrete specimen, cf. Figure 3.1.

The numerical model, viz. the serial-parallel model shown in Figure 3.1(b), was constructed, so that physical meaningful values can be assigned to the various interfaces to simulate cracking, slip and separation.

It is seen from Figure 3.1(b) and the descriptions given above, that the formation of slip and separation at the concrete/steel interface were modelled as two independent processes. The authors are aware that these processes are linked and may be described by mixed-mode fracture behaviour, see eg Carol et al. [*Carol et al., 1997*], Lourenco and Rots [*Lourenco and Rots, 1997*] and Nielsen et al. [*Nielsen et al., 2010*]. Howev-

er, there still lacks a proper formulation of this mixed-mode behaviour which can be implemented in FEM simulations.

A description of the values assigned to the input parameters of the numerical model is given in a separate section.

3.2.1 Details on Numerical Model

Numerical simulations described in the present paper were carried out by the use of the commercially available FEM software package TNO DIANA. Details on the numerical model such as the meshing, element types etc. are described in the following. Note that due to symmetry considerations only half of the reinforced concrete beam was modelled to reduce computational time. As previously mentioned, the results of the numerical simulations were compared to experimental results concerning initiation of the bending crack and formation of slip and separation along the reinforcement reported in [*Solgaard et al., 2013*]. The experimental observations were determined from flexural loading (3 PBT) of 150 x 150 x 650 mm (h x w x l) reinforced concrete specimens. Additional information is provided in Section 3.2.4.

The numerical model consisted of 1184 quadrangular elements and 2353 nodes. The interface accounting for the simulations of the main bending crack (black interface in Figure 3.1) was divided into two lines, viz. one below and one above the reinforcement, each consisting of 60 elements. The number of elements in the interface accounting for the bond-slip behaviour (purple interface in Figure 3.1) was 98, which was the same number of elements used for the interface accounting for the separation at the concrete/steel interface (yellow interface in Figure 3.1). Note: The maximum number of line divisions of an interface, and thereby maximum number of elements, was 98.

A convergence analysis of the number of elements for each of the three interfaces was carried out using input data corresponding to SFRC (1.0 vol.-%) at one load level (50 KN). Convergence analysis was also carried out for other load levels, however not presented here, showed similar results. The convergence analysis shown in Figure 3.3 for the main bending crack interface refers to the interface below the reinforcement.

Figure 3.3. presents the convergence analysis for all three interfaces. The results in Figure 3.3. concern the normalized CMOD for the bending crack interface, the normalized slip 10 mm from the main bending crack and the normalized separation 10 mm from the main bending crack.

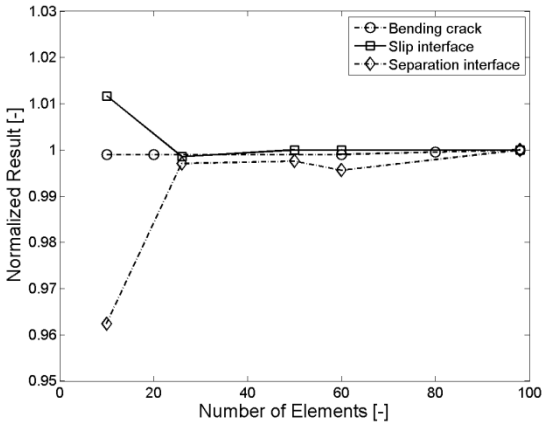

Figure 3.3 *Normalized results from convergence analyses as function of the number of elements in main bending crack (normalized CMOD), slip interface (normalized slip 10 mm from main bending crack) and separation interface (normalized separation 10 mm from main bending crack).*

It is seen from the results presented in Figure 3.3 that the number of elements in the main bending crack interface has a minor influence on the results of the numerical simulations. The relative change is approx. 1‰ when reducing the number of elements from 98 to 60. From Figure 3.3 it is seen that the slip does not change significantly when the number of elements in that interface was increased from 50 to 98. Finally it is seen from Figure 3.3 that the separation is changed less than 5 ‰ increasing the number of elements from 60 to 98. Based on these three observations it is concluded that the number of elements of each of the interface used within the numerical simulations, was sufficient.

3.2.2 Limitations for Numerical Simulations

The proposed numerical model is based on the fictitious crack model. Thus, the numerical model is based on the assumption of discrete crack formation due to the applied load. As multiple cracking may occur, especially when considering SFRC, the results concerning the formation of the main bending crack predicted by the numerical model may be overestimated.

The results concerning the slip-length and separation-length were based on an interpretation of deformations of elements in the slip and separation interface, respectively. These interpretations were based on relative displacements between two nodes within an element at the interface for each load step. The one part of that element is connected to the reinforcement whereas the other part of that element is connected to the surrounding concrete. This is explained from Eq. (3.8)-(3.9) for slip and separation respectively:

$$\Delta u_x = \left|u_x^i - u_x^j\right| - \Delta u_{x,e} \quad (3.5)$$

$$\Delta u_y = \left|u_y^i - u_y^j\right| - \Delta u_{y,e} \quad (3.6)$$

where indices i and j refer to the node in the top and bottom of the element, respectively, and indices x and y relate to the coordinate system. The x-axis of this coordinate system is aligned with the direction of the reinforcement. $\Delta u_{x,e}$ and $\Delta u_{y,e}$ are the elastic deformations in the two directions, ie parallel and perpendicular to the reinforcement, respectively. These elastic deformations are controlled by the elastic stiffness of the elements. A high value for the elastic stiffness was assigned to these elements in the numerical model and consequently the elastic deformations were negligible (less than 1 μm). Consequently the elastic part of Eqs. (3.8)-(3.9) may be assumed to vanish. The separation and slip along the reinforcement was simulated assuming threshold values of Δu_x = 10 μm and Δu_y = 5μm for the separation and slip, respectively. These values correspond to the resolution of the experimental results obtained by the use of photogrammetric equipment.

A non-physical fitting parameter was applied to the simulations concerning the separation at the concrete/steel interface. This non-physical fitting parameter does not influence the slip and the opening of the main bending crack, but was incorporated in the model to account for the phenomenon that the formation of the slip and the separation at the concrete/steel interface are linked processes (mixed mode fracture), whereas the numerical model simulated those as independent processes.

3.2.3 Parameters

The numerical model described in the present paper was tested comparing the results the numerical simulations with experimental observations concerning 3 PBT of reinforced concrete beams cast from PC, 0.5 vol.-% SFRC and 1.0 vol.-% SFRC, originally presented in [*Solgaard et al., 2013*]. Two types of input parameters were used for the numerical model; input parameters determined from separate, experimental observations and fitted parameters. The input parameters, and their origin, are further described in the following.

The fracture mechanical properties of the main bending crack interface were determined from standard 3PBT of concrete beams in accordance with [*Rilem, 2002; DS/EN 14651-A1, 2007*]. The fracture mechanical properties incl. the cohesive relationships for the three concrete compositions were determined from these experiments using inverse analysis adapting the procedure described by Skoček and Stang [*Skoček and Stang, 2010*]. The cohesive relationship for the concrete compositions investigated are shown in Figure 3.4 and the fracture mechanical properties are given in Table 3.1

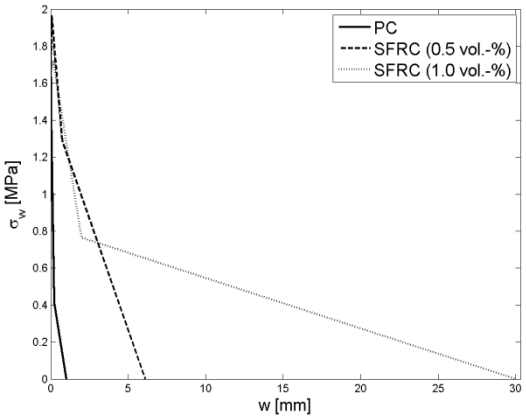

Figure 3.4 *Cohesive relationships for PC and SFRC (0.5 and 1.0 vol.-%). From [Solgaard et al., 2013].*

Table 3.1 *Fracture mechanical properties of "bending crack"-interface elements. Data from [Solgaard et al., 2013].*

Concrete composition	PC	SFRC	
Fibre fraction [vol.-%]	0.0	0.5	1.0
f_t [MPa]	1.8	1.7	1.7
w_{crit} [mm]	1.0	6.1	30
G_f [J/m^2]	400	4700	13000

Values for the slip and separation interfaces, ie $f_{t,slip}$, $f_{t,sep}$, and Δt^0 are difficult to measure experimentally, and the values of these input parameters were fitted. Experimentally obtained data from [*Solgaard et al., 2013*] concerning the slip-load relationship and the separation-load were used for fitting the values of these input parameters.

As an example results from fitting of the slip interface, $f_{t,slip}$ and experimentally obtained results of the slip 10 mm from the main bending crack at the level of the reinforcement are shown in Figure 3.5 for 1.0 vol.-% SFRC.

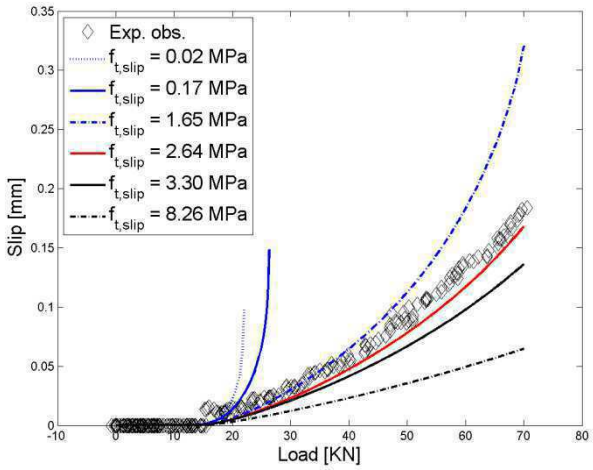

Figure 3.5 *Slip 10 mm from main bending crack, Numerical simulations for different values of $f_{t,slip}$ along with experimental results from 1.0 vol.-% SFRC reported in [Solgaard et al., 2013].*

It is seen from Figure 3.5 that the slip was initiated for the same load level regardless of the value assigned to the tensile strength of the slip interface, $f_{t,slip}$, and it is also clear from Figure 3.5, that the propagation of the slip was sensitive to changes in the value assigned to $f_{t,slip}$. Fitting of the tensile strength of the separation interface, $f_{t,sep}$, was carried out in a similar way.

As previously described, the slip at the concrete/steel interface was modelled by Dörr's model, cf. Eq. (3.7). It is seen from Eq. (3.7) that the shear stress-slip relationship attains a constant level for a given slip, Δt^0. The value of Δt^0 to be assigned for the numerical simulations was fitted assigning different values to Δt^0 and modelling the corresponding slip at the concrete/steel interface. As an example, results from fitting of Δt^0 for 1.0 vol.-% SFRC are presented in Figure 3.6 along with experimental data from [*Solgaard et al., 2013*].

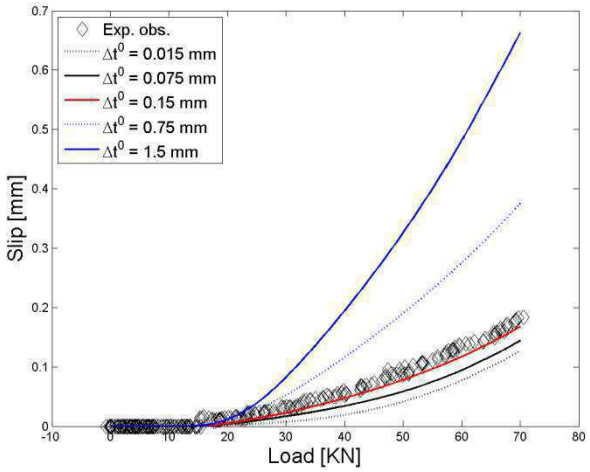

Figure 3.6 *Slip 10 mm from main bending crack, Numerical simulations for different values of Δt^0 along with experimental results for 1.0 vol.-% SFRC reported in [Solgaard et al., 2013].*

It is seen from Figure 3.6 that slip is initiated for the same load level for the various values assigned to Δt^0 and that a too high value assigned to Δt^0 result in an overestimation of the slip.

Values assigned to $f_{t,slip}$, $f_{t,sep}$, and Δt^0 in the numerical simulations presented in the following are given in Table 3.2.

Table 3.2 *Mechanical properties of slip and separation interfaces.*

Concrete composition	PC	SFRC	
Fibre fraction [vol.-%]	0.0	0.5	1.0
$f_{t,slip}$ [MPa]	2.57	1.10	2.31
$f_{t,sep}$ [MPa]	0.03	0.03	0.03
Δt^0 [mm]	0.15	0.15	0.15

Further information about the properties of the concrete, casting procedure, experimental procedure, etc. used for these experimental studies are available in the following section.

3.2.4 Experimental Procedure

The experimental procedure allowed for the assessment of load-induced cracking of reinforced concrete beams subjected to 3 PBT, ie:

- Measurements of the crack initiation and propagation at the concrete tensile surface.
- Measurements of the slip and separation at the concrete/steel interface.

The experimental observations were carried out for PC, 0.5 vol.-% and 1.0 vol.-% SFRC to quantify the possible beneficial effect on the crack- and debonding formation from the addition of steel fibres.

3.2.4.1 Materials and Specimens

The experimental program comprised specimens cast from PC and SFRC (0.5 and 1.0 vol.-%). The mix designs for the three different mix compositions are shown in Table 3.3.

Table 3.3 *Mix composition for the three mix designs (assumed s.s.d. conditions of the aggregates).*

Constituent	Density	PC		SFRC 0.5 vol.-%		SFRC 1.0 vol.-%	
	[kg/m^3]	[kg/m^3]	[m^3/m^3]	[kg/m^3]	[m^3/m^3]	[kg/m^3]	[m^3/m^3]
Cement	3100	375	0.121	375	0.121	375	0.121
Water	1000	156	0.156	156	0.156	156	0.156
Sand	2540	760	0.299	755	0.297	750	0.295
Sand	2625	56	0.021	56	0.021	56	0.021
Gravel	2615	1025	0.392	1018	0.389	1011	0.387
Stones	-	-	0.010	-	0.010	-	0.010
Air	7850	-	-	39	0.005	78	0.010

The cement type used for all mix compositions was Aalborg Portland RAPID cement, CEM I 52,5 N (MS/LA/≤ 2). Further information about the properties of RAPID cement is available in [*AAP, 2011*]. Aggregates were excavated sea bed materials natural rounded corresponding to Class E for sand (0-4 mm), class A for gravel (4-8 mm) and Class A for stones (8-16 mm) according to national standards [*DS 2426, 2004*]. Prior to mixing, the actual water content of the aggregates was determined by the use of the weigh-dry-weigh method to adjust the amount of mixing water and to maintain the target w/c ratio.

The w/c ratio for the mix compositions given in Table 3.3 was 0.43. The fibres used for the SFRC mixes were DRAMIX 65/35, viz. length 35 mm and diameter 0.55 mm (aspect ratio 65) manufactured by Bekaert NV. The fibres were hooked ended and manufactured from cold drawn black steel. More details about the fibres are available in [*Bekaert, 2011*]. A standard pan mixer (capacity 300 l) was used for mixing of concrete.

The specimens were cast with two rebars (Ø12), viz. one conventional rebar and one special rebar. The arrangement of the rebars is seen from Figure 3.7.

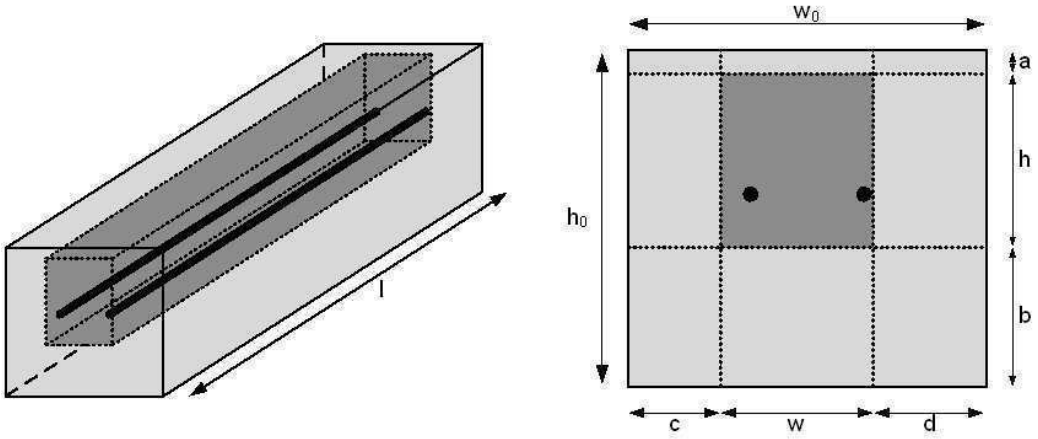

Figure 3.7 *Specimen for photogrammetric observations of load induced cracking. Left: Original specimen (light grey) and final specimen after cutting (dark grey). Right: Cross section of original specimen (light grey) and final specimen (dark grey) along with measures. The illustrations are not in scale. From [Solgaard et al., 2013].*

The special rebar was a hollowed conventional rebar (the diameter of the hollowing was 6 mm). The special rebar had mechanical properties similar to those of the instrumented rebar developed by Pease et al. [*Pease et al., 2011*], and was used since the observations presented in this paper form the basis of another experimental program concerning the risk of corrosion along the reinforcement in cracked concrete described in a separate study [*Michel et al., 2013a*], where the instrumented rebar was used. It has been shown by Pease et al. [*Pease et al., 2011*] that the slightly different mechanical properties of the special rebar compared to those of conventional reinforcement did not have a significant influence on the crack and debonding formation. This special rebar is not discussed any further in this paper.

The specimens were cast in 290 x 310 x 650 mm moulds and vibrated by the use of a vibrating table. In order to avoid wall effect of fibre orientation, viz. 2D orientation of the fibres caused by the mould sides, the specimens were cast in oversize, and cut to the size of the test specimens prior to mechanical testing.

After casting, the specimens were covered with plastic sheets to avoid moisture evaporation from the fresh concrete surface and left for curing for 24 h at laboratory conditions (20 ± 2 ºC) before demoulding. After demoulding the specimens were stored in lime rich water (minimum 28 days) until cutting and testing. Cutting of the specimens is presented in Figure 3.7, illustrating the specimen before and after cutting. The final dimensions of the specimens were 150 x 140 x 650 mm (h x w x l). The dotted lines in Figure 3.7 illustrate the cutting lines, and the dimensions given in the illustration are reproduced in Table 3.4.

Table 3.4 *Dimensions of specimens before and after cutting.*

h_0 [mm]	w_0 [mm]	a [mm]	b [mm]	c [mm]	d [mm]	h [mm]	w [mm]	l [mm]
290	315	40	100	80	95	150	140	650

The right cutting line shown in the right illustration of Figure 3.7 is approx. 2 – 4 mm from the rebar. Thus the rebar was covered by a minute concrete cover on the side. This was done in order to avoid damaging the concrete/steel interface during the cutting process.

3.2.4.2 Photogrammetric Measurements

The load-induced cracking at the concrete/steel interface (slip and separation) and the initiation and formation of bending cracks in the concrete cover, were measured by the use of photogrammetric equipment monitoring the surface of the specimen. The photogrammetric measurements were carried out on the surface of the specimen with the rebar closest to the vertical surface, viz. the right vertical side of the specimen in Figure 3.7. The photogrammetric equipment consisted of two CCD cameras positioned at the same level as the specimen. The set-up of the photogrammetric equipment is illustrated in Figure 3.8.

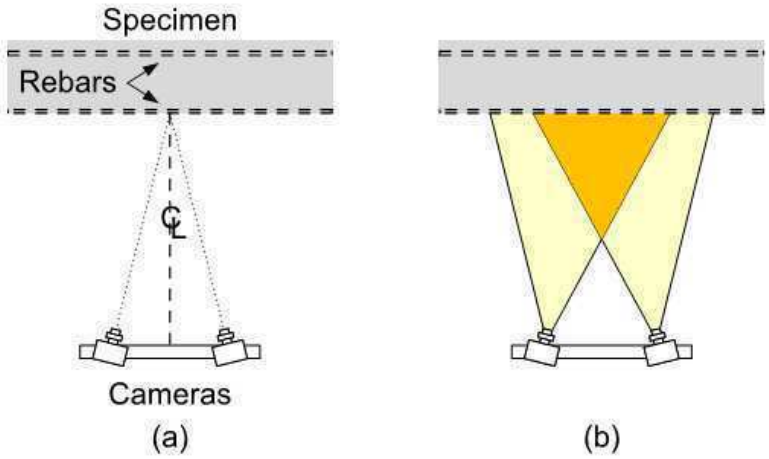

Figure 3.8 *Top-view of set-up of photogrammetric equipment. (a) Alignment of cameras and specimen and (b) monitored surface at concrete specimen. The illustration is not in scale [Solgaard et al., 2013].*

The area of the concrete surface of each camera is indicated with yellow in Figure 3.8b whereas the part of the concrete surface monitored by both cameras is indicated with orange in Figure 3.8b.

Prior to the mechanical testing, the monitored surface of the concrete specimen was painted (white) and subsequently a random pattern (black) was applied, as shown in Figure 3.9.

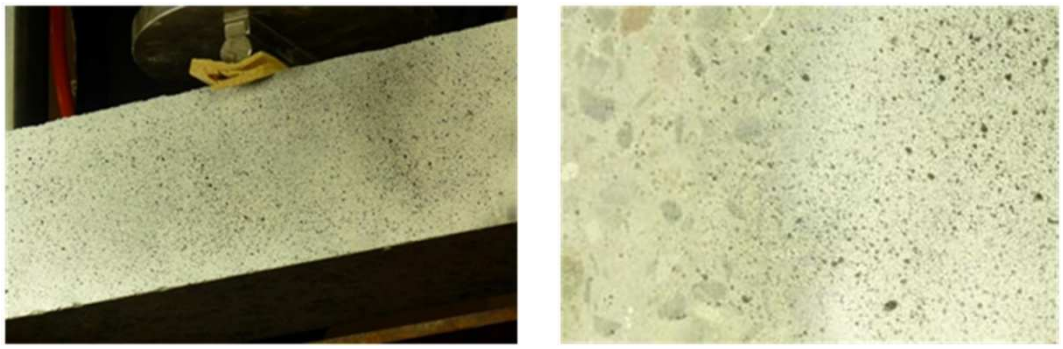

Figure 3.9 *Left: Concrete beam mounted in rig. Right: Surface of specimen showing original surface (left) and surface with applied random pattern (right) [Solgaard et al., 2013].*

The pattern applied to the monitored surface of the specimen was used for the post-processing of the photogrammetric observations; the deformations were calculated from a comparison of the random black pattern at the concrete surface during loading and the same pattern before loading, viz. the so-called reference picture. The frequency of data acquisition was 0.5 Hz.

The area of the specimen monitored by both cameras, was approx. 350 x 150 mm (length x height) and was positioned around the center of the specimen. The resolution of the CCD cameras used for the photogrammetric observations was 2 Megapixel.

Data from the photogrammetric observations were analysed by the use of the commercially available software ARAMIS. The analysis allowed for deformation and strain measurements to be undertaken in any point of the measurement-area after the experiments were carried out and the deformation and strain fields in the same area were visualized. Furthermore, the technique allowed for identification of cracks as zones with localized strain. Further details on the photogrammetric equipment, ie software and the procedure for the subsequent analyses, are given in eg [*GOM, 2009; Pereira et al., 2011*]. Additional information about the experimental procedures and results obtained is provided in [*Solgaard et al., 2013*].

3.3 Results

Results of the numerical model for load-induced cracking in the concrete cover and slip and separation in the concrete/steel interface presented above were compared to experimental observations. The observations cover:

- CMOD at the concrete tensile surface vs. applied load
- Separation at concrete/steel interface vs. applied load
- Slip at concrete/steel interface vs. applied load
- Extent of slip and separation vs. applied load
- Extent of slip and separation vs. CMOD at the concrete tensile surface

for all specimens cast from the concrete mix compositions presented in Table 3.3. The numerically obtained results are presented along with experimental results [*Solgaard et al., 2013*], except for simulations concerning the extent of slip and separation, since no experimental results were obtained for those observations.

The numerical simulations and comparisons with the experimental results presented in the following correspond to the formation of the main bending crack up to CMOD of 0.5 mm and a rebar stress of 192 MPa (PC), 131 MPa (SFRC 0.5 vol.-%) and 186 MPa (SFRC 1.0 vol.-%). Hence the rebar was in the elastic state.

The experimental and numerical results concerning the CMOD vs. applied load for specimens from PC, 0.5 vol.-% SFRC and 1.0 vol.-% SFRC are presented in Figure 3.10.

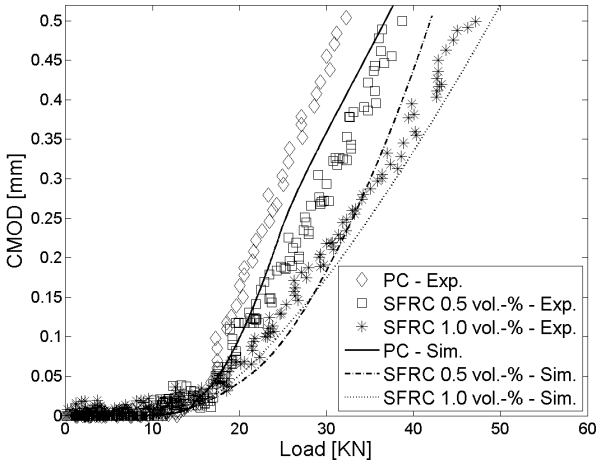

Figure 3.10 *Numerical simulations and experimental results of the CMOD-load relationship for PC, 0.5 vol.-% SFRC and 1.0 vol.-% SFRC at a point 10 mm from the main bending crack.*

Numerical and experimental observations concerning the separation at the concrete/steel interface are illustrated in Figure 3.11. The observations show the separation between concrete and reinforcement 10 mm from the main bending crack.

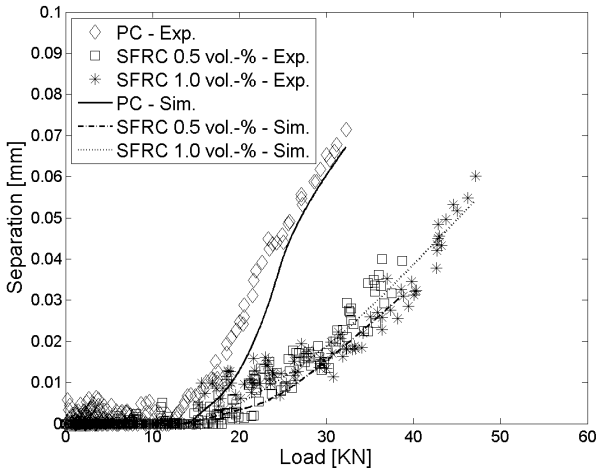

Figure 3.11 *Numerical simulations and experimental results of the separation-load relationship for PC, 0.5 vol.-% SFRC and 1.0 vol.-% SFRC 10 mm from the main bending crack.*

The slip at the concrete/steel interface as a function of the applied load (3 PBT) is presented in Figure 3.12. The presented simulations and experimental observations show the slip between concrete and reinforcement located 10 mm away from the main bending crack.

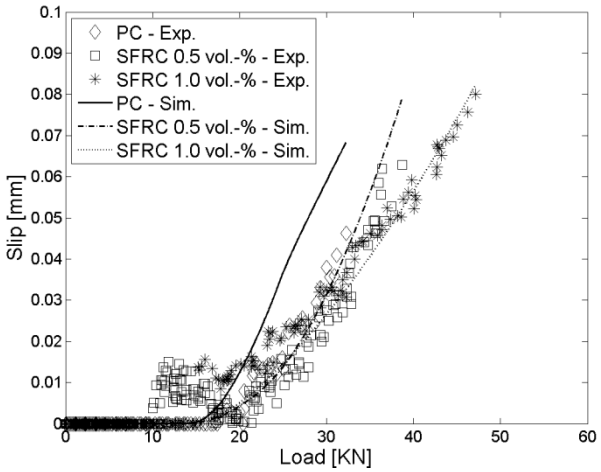

Figure 3.12 *Numerical simulations and experimental results of the slip-load relationship for PC, 0.5 vol.-% SFRC and 1.0 vol.-% SFRC 10 mm from the main bending crack.*

The extent of the separation along the concrete/steel interface is shown in Figure 3.13 for PC, 0.5 vol.-% SFRC and 1.0 vol.-% SFRC, respectively.

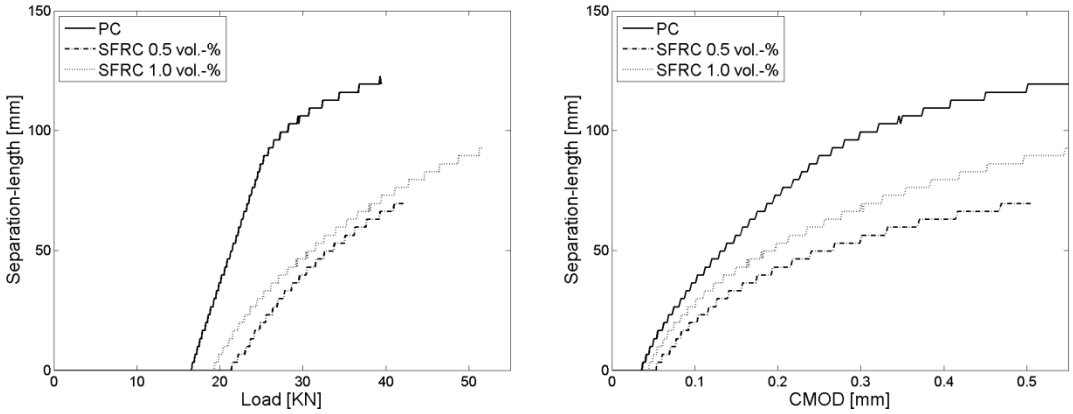

Figure 3.13 *Numerical simulations of the length of separation along the reinforcement for PC, 0.5 vol.-% SFRC and 1.0 vol.-% SFRC. (a) Length of separation as function of load, (b) Length of separation as function of CMOD.*

The extent of slip along the concrete/steel interface was simulated for all three concrete compositions.

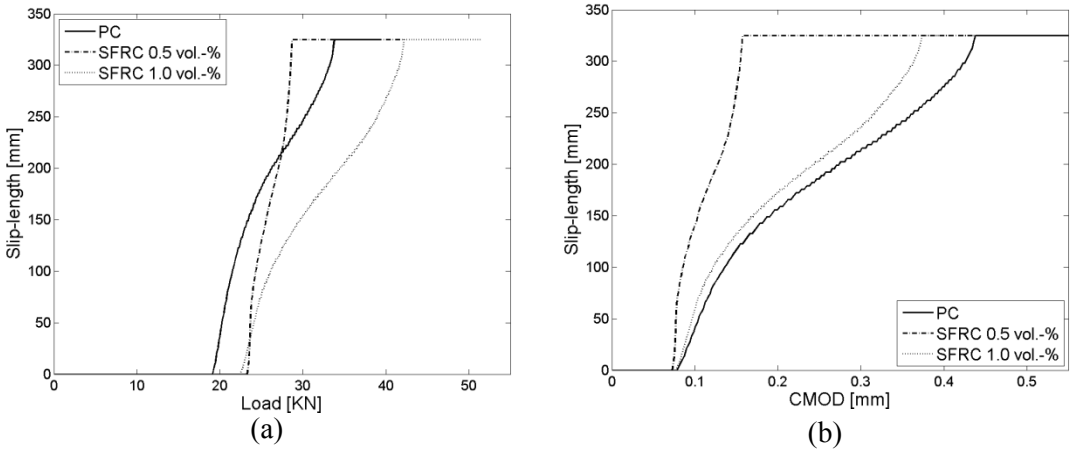

Figure 3.14 *Numerical simulations of the length of slip along the reinforcement for PC, 0.5 vol.-% SFRC and 1.0 vol.-% SFRC. (a) Length of slip as function of load, (b) Length of slip as function of CMOD.*

Note that the numerical simulations were carried out for half of the beam, ie the length is 325 mm. Thus the flat plateau which is eventually reached in Figure 3.14 corresponds to full slip along the concrete/steel interface.

3.4 Discussion

The discussions presented in the following concern the correlation between experimental observations and numerical simulations for CMOD, slip and separation. Additionally, the approach for the simulations, ie the numerical model presented above, is discussed. The sensitivity of the numerical model is not discussed any further. Please see Section 3.2.1 for convergence analyses of the mesh, and Section 3.2.3 presenting the sensitivity of the fitted input parameters.

3.4.1 Fracture Mechanical Properties

The fracture mechanical properties of the interfaces shown in Figure 3.1 are given in Tables 3.1 – 3.2. The properties given in Table 3.1, ie the tensile strength of the concrete domain, the fracture energy and the critical crack width were obtained from inverse analysis of experimental results and it is clear that the addition of fibres did not have a significant impact on the tensile strength of concrete, whereas the ductility, described from the fracture energy and the critical crack width was significantly increased by the addition of fibres. The observations concerning the crack width and fracture energy were in line with observations presented in eg [*Löfgren et al., 2005; Kazemi et al., 2007*].

The properties of the slip and separation interfaces are given in Table 3.2. Those properties were estimated by the numerical model to fit the experimental data. The values used for the tensile strength of the slip interface of the different concrete compositions were in the same order of magnitude (1.1 MPa – 2.57 MPa). However, there was no clear correlation between the fibre content and the fitted tensile strength of the slip-interface.

The strength of the separation interface was constant for all three concrete compositions investigated, viz. $f_{t,sep}$ = 0.03 MPa. The strength of the separation-interface was very low compared to the slip-interface and the tensile strength of the interface for the main bending crack. This separation interface described the chemical bond between the concrete and steel and such values have to the best of the authors' knowledge not been described in the literature. Furthermore, numerical simulations on the impact of $f_{t,sep}$ showed no considerable influence on the formation of the horizontal crack along the reinforcement. Hence, the separation was controlled by the formation of internal cracks caused by local stress transfer from the reinforcement to the concrete via the ribs as described in eg [*Goto, 1971*]. In the presented model this was accounted for by the interface connecting the upper and lower parts of the concrete body, cf. previous descriptions Section 3.2.1.

3.4.2 CMOD

The correlation between the initiation and propagation of the main bending crack and the applied load, was well reproduced by the numerical model, cf. Figure 3.10. In general, the model underestimated the CMOD for a given load level. Comparing the experimental results for the three concrete compositions, it is seen that the crack was initiated for approx the same load level, viz. approx 15-18 KN. The numerical model was capable of fitting the crack initiation and the crack width increase as a function of the applied load for all the concrete compositions. Further, the reduction in CMOD for the SFRC specimens compared to the PC specimen at the same load seen from the experimental observations was captured by the numerical model.

It is underlined that any differences between the numerical simulations and the experimental results may be caused by in-accuracies in the fracture mechanical properties of the concrete given in Table 3.1 and Figure 3.6. Those values were determined independently, from experimental observations, as previously described, and were not subject to fitting within the present numerical model.

3.4.3 Separation

The formation of separation at the concrete/steel interface 10 mm from the main bending crack is seen from Figure 3.11. The relationship between the applied load and the slip observed from the numerical simulations was reproduced accurately by the numerical model for all three concrete compositions. However, higher deviations between the numerical simulations and the experimental results were observed for the separation-load relationship for 0.5 vol.-% SFRC.

Comparing the experimental results for the CMOD-load and the separation-load relationships for each concrete composition, it is seen that separation at the concrete/steel interface did not take place before the main bending crack was initiated. It is also seen from the same figure, that the numerical model simulated this phenomenon very well, although this relation had not been set as a prerequisite in the numerical model. This indicates that the numerical model reproduced the load-induced debonding formation physically correct. Moreover, the experimental and the numerical results indicated that the separation at the concrete/steel interface is controlled by the deformation of the specimen caused by the applied load. This is concluded from the observation that the initiation of the separation at the concrete/steel interface was only marginally affected by the addition of fibres.

3.4.4 Slip

The slip formation at the concrete/steel interface 10 mm from the main bending crack is shown in Figure 3.12. It is clear that the numerical simulations captured the experimental observations very well, though the relationship was slightly overestimated for PC, cf. Figure 3.12. The scatter in the experimental observations for 0.5 vol.-% SFRC is most likely due to the limited resolution of the experimental optical/digital technique. Moreover, it is seen by comparisons of the experimental results concerning the slip at the concrete/steel interface and the CMOD-load relationships, that slip did not take place at the concrete/steel interface until the main bending crack was initiated. The numerical model was capable of simulating the on-set of slip at the concrete/steel interface as well as the slip-propagation due to increased load applied.

3.4.5 Extent of Separation and Slip

It is seen from Figure 3.13a that the separation was not initiated for the same load level applied to the three concrete compositions, and that the separation propagates at approximately the same rate along the reinforcement in 0.5 vol.-% SFRC and 1.0 vol.-% SFRC whereas the separation rate, ie the growth of separation as function of the applied load, along the reinforcement was higher for PC. It can be assumed, based on those observations that separation at the concrete/steel interface did not initiate before the main bending crack reached the reinforcement, which was in agreement with the experimental results concerning the separation 10 mm from the main bending crack. From the results presented in Figure 3.13a it may be concluded that the addition of fibres lead to a decrease in the separation rate along the reinforement. From Figure 3.13b it is seen that the addition of fibers results in a reduced separation for a given CMOD, and that the growth of the separation-length, is less steep for SFRC than for PC. However, it is noted, that contrary to expectation, the curve corresponding to 0.5 vol.-% SFRC is lower than the curve corresponding to 1.0 vol.-%.

The analyses concerning the length of slip along the concrete/steel interface as a function of the load revealed that the slip was initiated for the same load level for SFRC (0.5 vol.-% and 1.0 vol.-%) whereas the load level required to form slip in PC was slightly lower, see Figure 3.14b. Once the slip at the concrete/steel was initiated the propagation of the slip, as function of the load, along the reinforcement was lower for SFRC compared to PC. That may indicate that the addition of fibres prevented the slip formation at the interface. With regard to the slip-length along the concrete/steel interface as a function of the CMOD, see Figure 3.14b, it is seen that slip was initiated for the same CMOD for all three concrete compositions. However, the development of the slip-length for 0.5 vol.-% SFRC is much steeper than the curves for 1.0 vol.-% SFRC and PC. Considering previously presented observations showing correlation between experimental observations and numerical simulations it may be concluded that the numerical model is physically-correct based. Therefore, the observations

presented in Figure 3.14b, showing no clear trend in the slip-length – CMOD relationship for concrete with/without steel fibres shall not per se be assigned to problems with the numerical model. Thus, based on these observations it appears that there is no unambigous correlation between the slip-length and the CMOD.

It should be stressed that the numerical simulations conerning the extent of slip and separation were not compared to experimental data. Conseqeuntly the results presented in Figures 3.13 – 3.14 should be interpreted with caution since they are not supported by experimental observations.

The numerical simulations and the experimental results presented and discussed above revealed that the separation and slip along the concrete/steel interface were not two independent phenomena as proposed by the numerical model, cf. Figure 3.1. The fracture process is a mixed-mode process, ie the two processes are linked as previously discussed. A non-physical fitting parameter was implemented in the model to account for this problem. The same value was assigned to this non-physical fitting parameter for all of the numerical simulations presented. This indicates that this parameter accounted for a problem related to the basis of the model since its value was constant regardless of the concrete properties.

3.5 Conclusions

A numerical model for the formation of load-induced cracking and debondinf at the concrete/steel interface of reinforced concrete subjected to 3 PBT was established. The numerical model simulated the formation of a main bending crack through the concrete cover and debonding along the reinforcement (separation and slip) and was based on non-linear fracture mechanics (fictitious crack model and general cohesive fracture mechanics). Based on the numerical simulations and the comparisons of those with experimental data it can be concluded:

- Sensitivity analyses of the numerical model revealed that the initiation of slip at the concrete/steel interface was weakly dependant on the tensile strength of the slip interface, $f_{t,slip}$. However, once slip was initiated the propagation of the slip was dependent on the tensile strength of this interface.
- The bond-slip behavior utilized for the numerical model was adequate for the formulation of the relationship. The relationship was cubic and attaines a constant level of bond for a given slip, Δt^0. The numerical model was sensitive to changes in the value assigned to Δt^0.
- The correlation between the results from the numerical model and the experimental results was very good for all three mechanisms analysed (cover-cracking as well as slip and separation at the concrete/steel interface).

- Input parameters for the main bending crack, which were obtained from independent testing appeares to represent the fracture mechanical behavior of that interface well.
- For a given load level or CMOD, the length of slip along the reinforcement was reduced for SFRC (0.5 vol.-% and 1.0 vol.-%) compared to PC. There appeared to be no clear correlation between the length of separation and the amount of steel fibres.

Acknowledgements

The first author gratefully acknowledge the full financial support of the Ph.D. study "Application of Fibre Reinforced in Civil Infrastructure" by the Danish Agency for Science, Technology and Innovation, COWI A/S, DTU, Bekaert NV, Grace, and the Danish Road Directorate. Financial supports of the Ph.D. study "Nanotechnology for Civil Engineering Structures: Resistance to Reinforcement Corrosion in Concrete Structures" by Femern Bælt A/S, Sund & Bælt Holding A/S and The Danish Agency for Science, Technology and Innovation as well as COIN (COncrete INnovation centre, www.coinweb.no) and its partners are also acknowledged as well as financial contributions from the Danish Expert Centre for Infrastructure.

Chapter 4

Experimental investigations of the relation between damage at the concrete-steel interface and initiation of reinforcement corrosion in plain and fibre reinforced concrete
(Paper III)

Alexander Michel

Department of Civil Engineering, Technical University of Denmark, Kgs. Lyngby, Denmark
Department of Structural Engineering, Norwegian University of Science and Technology (NTNU), Trondheim, Norway

Anders Ole Stubbe Solgaard

Department of Civil Engineering, Technical University of Denmark, Kgs. Lyngby, Denmark
COWI A/S Denmark, Kgs. Lyngby, Denmark

Bradley Justin Pease

Department of Civil Engineering, Technical University of Denmark, Kgs. Lyngby, Denmark

Mette Rica Geiker

Department of Civil Engineering, Technical University of Denmark, Kgs. Lyngby, Denmark
Department of Structural Engineering, Norwegian University of Science and Technology (NTNU), Trondheim, Norway

Henrik Stang

Department of Civil Engineering, Technical University of Denmark, Kgs. Lyngby, Denmark

John Forbes Olesen

Department of Civil Engineering, Technical University of Denmark, Kgs. Lyngby, Denmark

Submitted for the journal “Corrosion Science”

Abstract

Cracks in covering concrete are known to hasten initiation of steel corrosion in reinforced concrete structures. To minimize the impact of cracks on the deterioration of reinforced concrete structures, current approaches in (inter)national design codes often limit the concrete surface crack width. Recent investigations however, indicate that the concrete-reinforcement interfacial condition is a more fundamental criterion related to reinforcement corrosion. This work investigates a new potential design concept to describe the impact of cracks on reinforcement corrosion, namely estimation and limitation of interfacial damage. Comparisons of experimental and numerical results indicate a strong correlation between corrosion initiation and interfacial condition.

Keywords

Steel Reinforced Concrete, Atmospheric Corrosion

4.1 Introduction

Concrete reinforced with steel bars is nowadays the most used manmade construction material in the world. Embedding steel in concrete has several advantages and helps to overcome shortcomings of both materials. Concrete has a high compressive strength, but a low tensile strength and is therefore reinforced for structural purposes, while the steel is protected by the concrete from potentially harmful environmental exposure. Usually, the reinforcement in uncracked concrete is protected due to the high alkalinity (pH around 13) [*Bertolini et al., 2004*] and the concrete cover as a physical barrier itself against the ingress of corrosion initiating substances, such as water, chloride ions, carbon dioxide and oxygen. In the case of uncracked and uncontaminated concrete, the quality and thickness of the concrete cover are the most influential factors for reinforcement corrosion. In practice however, cracks can be found in nearly all reinforced concrete structures originating from hygral or thermal shrinkage and/or mechanical loading.

Within the past decades, numerous investigations on the impact cracks have on the ingress of corrosion initiating substances and reinforcement corrosion have generally concluded that cracks facilitate rapid ingress [*Jacobsen et al., 1996; Aldea et al., 1999a; Edvardsen, 1999; Gowripalan, 2000; Rodriguez and Hooton, 2003; Win et al., 2004; Lindquist et al., 2006; Pease et al., 2009*] and subsequently reduce the time to corrosion initiation. Both laboratory studies [*Gautefall and Vennesland, 1983; Berke et al., 1993; Arya and Ofori-Darko, 1996; Schießl and Raupach, 1997; Francois and Arliguie, 1999; Mohammed et al., 2001*] and in-situ observations [*Rehm and Moll, 1964; Schießl, 1976; Katawaki, 1977; Fidjestol and Nilson, 1980; O'Neil, 1980*] have noted an expedited corrosion initiation in cracked concrete compared to

pristine concrete. Commonly used approaches, see eg [*Rehm and Moll, 1964; Schießl, 1976; Katawaki, 1977; O'Neil, 1980; Gautefall and Vennesland, 1983; Berke et al., 1993; Schießl and Raupach, 1997; Francois and Arliguie, 1999; Mohammed et al., 2001*], attempt to relate corrosion initiation and propagation to the concrete surface crack width. Thus, controlling concrete surface crack widths has become the norm to attempt to minimize the impact of cracks on corrosion-induced deterioration in structural design codes and recommendations [*NZS, 1995; ACI, 2001; DAfStb, 2003; Eurocode, 2004; AIJ, 2006; AASHTO, 2007; DIN 1045-1, 2008*]. Various probabilistic, empirical, and quasi-analytical cracking models are utilized in these structural design codes to predict crack widths based upon numerous geometric and stress (or strain) parameters. However, predicted and observed crack widths can vary significantly [*Schießl and Wölfel, 1986*]. Further, a number of studies (both from laboratory and in-situ observations) indicate that the concrete surface crack width alone cannot accurately assess the impact of cracks on reinforcement corrosion as other factors, such as concrete cover thickness [*Schießl, 1976; Schießl and Raupach, 1997*], concrete composition (in particular water-to-cement ratio [*Makita et al., 1980; Berke et al., 1993; Schießl and Raupach, 1997; Miyazato and Hiraishi, 2005; Otieno et al., 2010*] and addition of supplementary cementitious materials [*Gautefall and Vennesland, 1983; Marcotte and Hansson, 2003; Scott and Alexander, 2007*], stress level in the reinforcement [*Yoon et al., 2000*], and crack orientation [*Poursaee and Hansson, 2008*] alter the influence of the crack width on reinforcement corrosion.

One possible explanation for the lacking relationship between concrete surface crack width and reinforcement corrosion behaviour is that the surface crack width alone does not reliably describe the condition of the concrete-reinforcement interface [*Tammo et al., 2009; Pease, 2010*]. The condition of the concrete-reinforcement interface appears to be a more fundamental criterion than the concrete surface crack width influencing the corrosion protection ordinarily provided by concrete. Several references report accelerated corrosion initiation and relatively excessive cross-sectional reductions (compared to reinforcement with good cohesion with concrete) take place at sites of various interfacial defects, including entrapped or cast-in voids [*Mohammed et al., 2002; Nygaard, 2003; Buenfeld et al., 2004; Nygaard and Geiker, 2005*], casting joints [*Nagataki et al., 1997*], spalled concrete [*O'Neil, 1980*], and interfacial slip and separation caused by mechanical loading [*Pease et al., 2011*]. Results of experimental studies indicate that such interfacial defects at the concrete-reinforcement interface reduce the critical chloride threshold for corrosion initiation, see eg [*Buenfeld et al., 2004; Nygaard and Geiker, 2005*]. This, coupled with the increased ingress of corrosion-initiating substances associated with concrete cracks described above, clearly illustrates the potential deleterious impact of concrete cracks on reinforced concrete structures.

The main focus of this study was to test the hypothesis that controlling the concrete-reinforcement interfacial condition can be used as a single indicator for the impact of

cracks on the risk of corrosion initiation along the reinforcement. The relation between interfacial damage and risk of corrosion initiation along the reinforcement was investigated for plain (PC) and steel fibre reinforced concrete (SFRC) beams subjected to flexural loading. A numerical model, developed and calibrated using specimens with similar geometries and identical materials, provided estimates on the extent of interfacial damage for the applied loads and measured surface crack widths. The impact of concrete cover thickness, concrete composition, stress level in the reinforcement and crack orientation on the mechanical response of the beam, ie cracking and interfacial damage was directly accounted for in the numerical model. Location- and time-dependent corrosion measurements along the reinforcement were performed using recently developed "instrumented rebars", which have a largely similar mechanical behaviour as conventional reinforcement [*Pease et al., 2011*]. For each beam, the open circuit corrosion potential (OCP) was measured at 17 locations and the macrocell current at 8 locations along the instrumented rebar. Comparisons of the cracking behaviour in [*Pease et al., 2011*] indicated the formation of interfacial damage due to flexural loading, ie slip and separation between the concrete and steel, is very similar for the conventional and instrumented rebar. Therefore, the instrumented rebar is a useful tool to investigate a potential link between mechanically-induced concrete-reinforcement interfacial damage and the corrosion response of the reinforcement. However, it should be mentioned that a practical application of instrumented rebars may be difficult due to the intensive monitoring equipment required for continuous OCP and macrocell current measurements. Nevertheless, previous results [*Pease, 2010; Pease et al., 2011*] and results of the present study indicate that instrumented rebars are suitable for laboratory investigations to study the effect of load-induced damage on reinforcement corrosion and to strengthen the hypothesis that load-induced interfacial damage can be used as an indicator for the risk of reinforcement corrosion.

4.2 Experimental Investigations

To investigate the impact of cracks and the associated interfacial damage between concrete and reinforcement on the initiation of corrosion, reinforced concrete specimens were prepared, cracked, and tested in a corrosive environment. Experimental studies included mechanical and electrochemical testing as well as destructive visual investigation of plain (PC) and steel fibre reinforced (SFRC) specimens. During mechanical testing, photogrammetric investigations were performed to monitor load-induced cracking, slip, and separation between concrete and reinforcement. In addition, fracture mechanical properties of the different concrete compositions were determined using inverse analysis of experimental results obtained from three point bending tests (3PBT) as described in [*Skoček and Stang, 2010*]. The 3PBTs were conducted in accordance with [*RILEM, 2002; DS/EN 14651-A1, 2007*]. Electrochemical testing included time- and location-dependent OCP and macrocell current measurements with so-called instrumented rebars, which were embedded in each of the tested

specimens along with a conventional rebar. The test matrix for the various experimental investigations is given in Table 4.1, including information on the naming convention and numbers of tested specimens. For each concrete composition, three specimens (MSF) were tested to determine fracture mechanical properties by inverse analysis of 3PBT results. Results of individual specimens of one concrete composition were then averaged. Four specimens (MSA) were tested for each concrete composition, ie two different concrete cover thicknesses (20 and 60 mm), to investigate load-induced cracking and associated interfacial damage by means of photogrammetry and subsequent digital image correlation. However, for simplicity, only results of specimens with a concrete cover thickness of 60 mm are presented in this study. Finally, one specimen (ESE) was tested for each concrete composition to study the influence of cracking and interfacial damage on the initiation of reinforcement corrosion using instrumented rebars, which allow for continuous OCP and macrocell current measurements. After termination of electrochemical testing, the electrochemical test specimens (ESE) were used for destructive visual investigations.

Table 4.1 *Test matrix for experimental investigations.*

	Concrete composition		
	PC	SFRC	
	Fibre content [vol.%]		
Experimental investigation	0.0	0.5	1.0
Fracture mechanical properties	MSF 1-3	MSF 4-6	MSF 6-8
Photogrammetric investigations	MSA 1-4	MSA 5-8	MSA 9-12
Electrochemical testing	ESE 1	ESE 2	ESE 3

4.2.1 Materials and Specimen Preparation

Beams of plain (PC) and steel fibre reinforced concrete (SFRC) with a water-to-cement ratio of 0.43 were cast. Aalborg Rapid® Portland cement (type 52.5N cement [*DS/EN 197-1, 2001*]) was used and the mix designs for the different concrete compositions are given in Table 4.2. DRAMIX 65/35 fibres (hooked ended and made from cold drawn black steel) were used for the SFRC mixes with a length of 35 mm and diameter of 0.55 mm. As reinforcement, two rebars with 12 mm diameter, ie one conventional rebar and one instrumented rebar (described in Section 4.2.2), were embedded in each of the 290×310×650 mm^3 (height × width × length) prisms. The steel fibre reinforced beams were cast in oversize to avoid fibre orientation caused by the sides of the moulds. After casting, the beams were stored for 24 hours in laboratory conditions under a plastic sheet (ie 20 ± 2 °C) and then demolded. Upon demoulding, the beams were stored in lime rich water for additional 28 days at 20 ± 2 °C until testing. Prior to cracking and testing, the SFRC beams were cut using a water-cooled concrete saw. Unreinforced MSF beams, ie specimens used for the determination of fracture mechanical properties, were cut to 150×150×650 mm^3 in accordance with the size recommended in [*Rilem, 2002*]. Specimens used for photogrammetric investigations (MSA) were cut to 150×120×650 mm^3, where part of the concrete covering the

reinforcement was removed to allow for monitoring of load-induced cracking and interfacial damage. However, a minute concrete cover remained (approximately 3 - 5 mm) to, among others, avoid damaging the concrete-reinforcement interface during the cutting process. Finally, a stochastic black and white speckle pattern was applied to the remaining concrete cover, which was used later for photogrammetric investigations. The final dimensions of the ESE beams, ie specimens used for electrochemical testing, were 190×150×650 mm^3 with 60 mm concrete cover thickness. A sketch of the cutting procedure for the different specimens is shown in Figure 4.1, where the dark grey area represents the final specimen geometry. Detailed information on initial and final specimen dimensions can be found in Table 4.3.

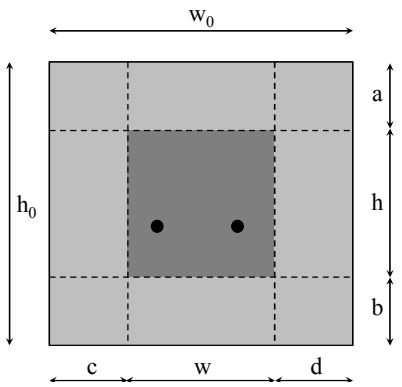

Figure 4.1 *Cutting of MSF, MSA, and ESE specimens. Please note: sketch is not to scale.*

Table 4.2 *Mix designs of investigated concrete compositions.*

Constituent	PC [kg/m^3]	SFRC 0.5 vol.% [kg/m^3]	SFRC 1.0 vol.% [kg/m^3]
Cement	375	375	375
Water	156	156	156
Sand (0 - 4 mm)	760	755	750
Gravel (4 - 8 mm)	56	56	56
Stones (8 - 16 mm)	1025	1018	1011
Fibres	-	39	78

Table 4.3 *Initial, final, and cutting dimensions for tested specimens.*

	Specimen		
Parameter [mm]	MSF	MSA	ESE
a	40	40	0
b	100	100	100
c	80	80	80
d	80	110	80
h	150	150	150
h_0	290	290	290
w	150	140	150
w_0	310	310	310

4.2.2 Instrumented Rebar

A sketch of the design of the instrumented rebar is illustrated in Figure 4.2. The applicability of the instrumented rebar to monitor time- and location-dependent OCP in concrete, while having a similar mechanical behaviour as a conventional rebar, was tested and presented in [*Pease, 2010; Pease et al., 2011*].

The instrumented rebar consisted of three individual sections of standard 12 mm diameter deformed rebar cut to lengths, which were connected via screw threads. The mid-section of the instrumented rebar was hollowed providing a 6 mm diameter void along the centre. Hollowing of the instrumented rebar resulted in a 6.25 % reduction in bending stiffness (ie, EI), a 25 % reduction in cross-sectional area, and an axial stiffness (ie, EA) equivalent to a standard rebar with a 10.39 mm nominal diameter. Seventeen holes, with 4.5 mm diameter, were drilled through the outer surface with a 10 mm spacing. In each hole, a 4 mm diameter steel pin was placed. A lead wire was soldered to each of the steel pins and afterwards encased in glue-coated heat-shrink tube to ensure electrical disconnection between the individual steel pins and the rebar. Finally, the hollowed section was filled with epoxy to protect the wires, electrical connections, and steel pins. The two solid rebar sections were connected to the hollowed mid-section using threaded connections. In contrast, to the configuration presented in [*Pease, 2010; Pease et al., 2011*] the sensors were installed flush in this study as results in [*Pease, 2010; Pease et al., 2011*] indicated that protruding sensors reduce the load-induced separation between reinforcement and concrete to some extent.

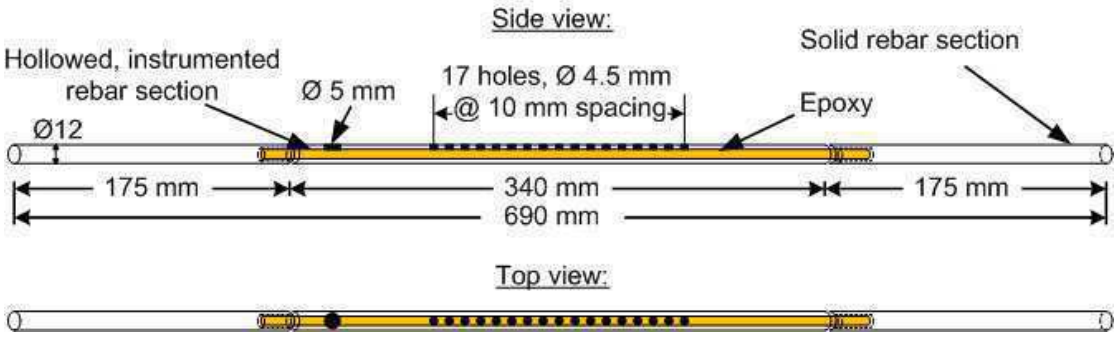

Figure 4.2 *Design of instrumented rebar for time- and location-dependent OCP measurements (Note: ribs are not shown in sketch), after [Pease et al., 2011].*

4.2.3 Photogrammetric Investigations

To monitor load-induced cracking and the associated interfacial damage of the MSA specimens (see Tab.4.1), photogrammetric equipment was used. The set-up of the photogrammetric equipment is illustrated in Figure 4.3 consisting of two charged-coupled device (CCD) cameras placed on a rig parallel to the specimen. The two CCD cameras were positioned at a mutual distance from the specimen and the angle between the cameras was constant. An area of approximately 350×150 mm^2 (width × height) was thereby monitored by both cameras, which was positioned around the centre of the specimen. Images with the CCD cameras were recorded every two seconds until testing was terminated. Captured images were subsequently processed with a commercially available software package [*GOM, 2009*], which utilized the stochastic speckle pattern to identify unique regions, called facets, on the specimen surface at each measurement time. The software tracks the movements of the facets and utilizes standard digital image correlation (DIC) techniques to compute, among others, deformations and strain fields (see Figure 4.4) at the specimen surface. DIC also allows for identification of cracks as zones with localized strain. Additional information on the hardware used and the DIC technique is available in [*Pease et al., 2006; Pereira et al., 2011*].

All specimens were tested in a load-controlled set-up. Experimental results covered applied load as well as strain and deformation fields at the specimen surface. Interfacial damage, ie slip and separation between reinforcement and concrete were determined from DIC results measuring the relative displacement between points adjacent to the reinforcement. In addition, slip and separation between concrete and reinforcement were determined for various distances from the centre of the primary bending crack.

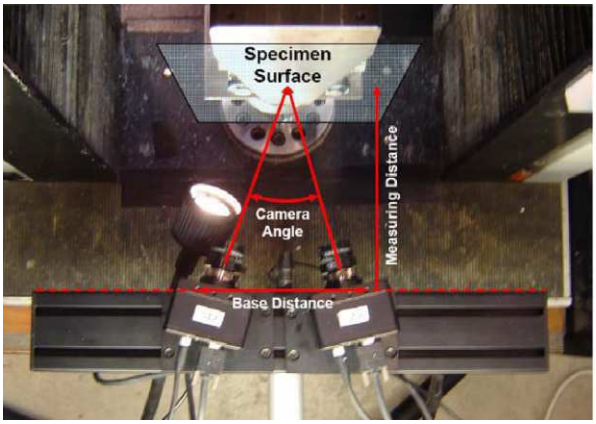

Figure 4.3 *Set-up of photogrammetric equipment, from [Pease et al., 2011].*

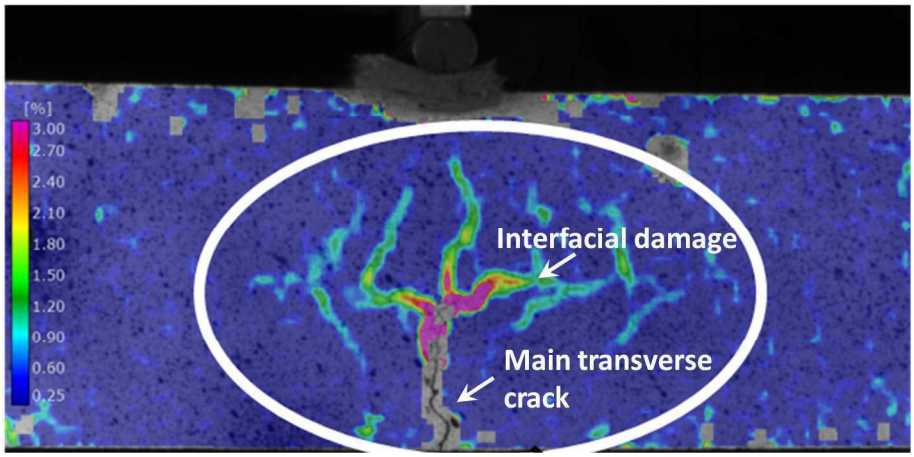

Figure 4.4 *Results of DIC measurements, indicating main transverse crack and associated damage due to mechanical loading. Please note: colour scale indicates strain calculated by DIC.*

4.2.4 Electrochemical Testing

4.2.4.1 Loading and Environmental Exposure

Figure 4.5 illustrates the customized steel cracking frames, which were used to hold open cracks and interfacial damage. As the steel cracking frames were not designed to induce cracks (because of insufficient stiffness of steel channel and threaded rods), a standard loading machine was used to pre-crack the beams. During pre-cracking, load was applied to estimated cracking loads predicted by the numerical cracking model described in Section 4.3. The pre-cracked beams were then loaded in the customized steel cracking frames to preset load levels given in Table 4.4 and the crack mouth opening displacement (CMOD) at the tensile surface and applied load were measured. Load was measured and recorded using customized ring load cells, which were tested and calibrated before using a standard loading machine. Load was applied by tightening the bolts until the defined target load was reached. After application of the load, the sides of each beam were sealed using silicone caulk to prevent leaking of the test

solution throughout the exposure. Afterwards, a plastic ponding dike was placed on the tension surface, ie over the main bending crack, and the area outside the ponding dike sealed with silicone caulk. The reservoir was filled with a 3% sodium chloride (NaCl) solution by weight and refilled as necessary during testing.

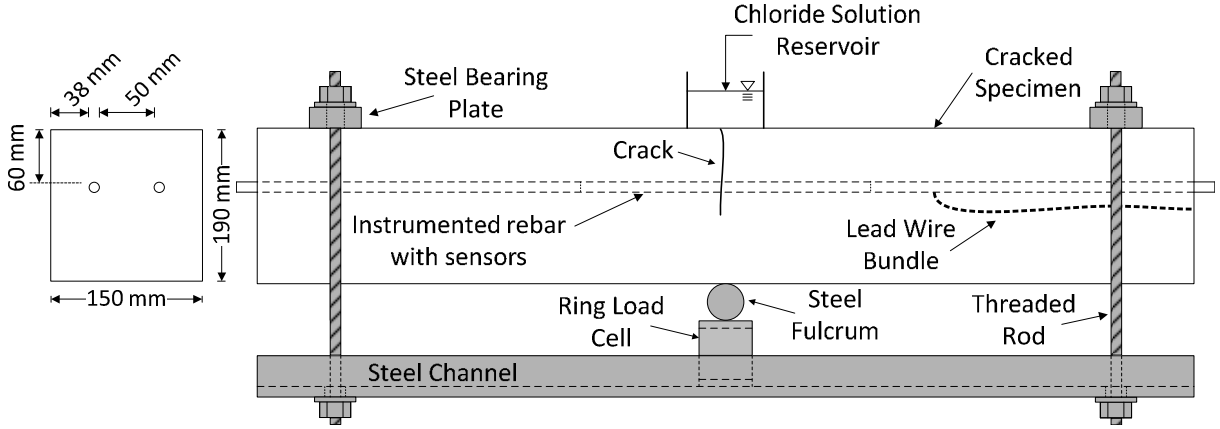

Figure 4.5 *Steel cracking frames for loading of beams with specimen illustrating the instrumented rebar and ponding reservoir, after [Pease et al., 2011].*

Table 4.4 *Applied loads, measured CMODs, and estimated extent of slip and separation for all materials tested.*

Specimen	Load[1] [kN]	CMOD[2] [mm]	Extent of slip[3,4] [mm]	Extent of separation[3,4] [mm]
PC	31.2	0.069	± 325	~ ± 40
SFRC 0.5 vol.%	45.7	0.139	± 325	~ ± 70
SFRC 1.0 vol.%	35.6	0.068	± 325	~ ± 35

[1] *measured with customized ring load cells*
[2] *measured average CMOD at concrete tensile face*
[3] *estimated by finite element model (see Section 4.3)*
[4] *distance from main bending crack*

4.2.4.2 OCP and Macrocell Current Measurements

Open circuit corrosion potentials (OCP) of all sensors along the instrumented rebar were measured against a standard calomel electrode (SCE), which was placed in the ponding reservoir. The reference electrodes were maintained on a weekly basis. Maintenance included refilling with saturated potassium chloride solution, potassium chloride crystals, and calibration against a silver/silver chloride reference electrode in a pH buffered solution. Due to the frequent maintenance and constant temperature of the exposure solution, the readings of the reference electrode were regarded stable.

In addition to the potential measurements, macrocell current measurements were taken for half of the sensors along the instrumented rebar. The electrical connection between the counter electrode and working electrode (individual sensors along the instrumented rebar) may be established over a resistor, and the macrocell current is

measured as the proportional potential over the resistor, or as done in the present study, over a zero-impedance-ammeter, ie without introducing resistance to the system. A ruthenium/iridium mixed metal oxide activated titanium mesh (MMO) was used as a counter electrode, which was also placed in the ponding reservoir. The measured current flow between the individual sensors and MMO was transferred to a voltage output before connection to the corresponding data logger terminals. The transformation was performed by two electrically separated ammeters, which were driven by two rechargeable 9 V block batteries. The batteries were automatically recharged to keep the supply voltage at a constant level. In this way, the ammeters were operated with a stable supply voltage that was insulated from any perturbation sources. The ammeters provided an exact linear relation between voltage output and current input with a transformation factor of 1 V/mA. The ammeters were nulled, based on the applied supply voltage and zero current before the electrical connection between working and counter electrode was established. When the individual sensors were connected to the MMO, a mixed corrosion potential was obtained and the current flow through the ammeters was enabled without introducing resistance. While for the passive state of sensors current flows of approximately zero μA were measured, considerably higher current flows were measured for active sensors, see eg Fig. 5.11 (b). Since the exposure area of the individual sensors of the instrumented rebar was well defined (0.126 cm^2), the measured current flows allowed for an estimate of the corrosion current density. The increase in current flow with initiation of active corrosion was sharp and well defined, so that the onset of corrosion could be clearly identified. However, it should be emphasised that only the macrocell current between the dissimilar was measured and consequently the micro- and macrocell corrosion activity on the preferential corroding metal surface is not reflected. Nevertheless, the technique is frequently used in the area of reinforcement corrosion due to its simplicity and clear indication of corrosion initiation by a sharp increase in macrocell current with depassivation, see eg [*Andrade et al., 1992; Andrade et al., 2008; Holmes et al., 2011*]. Furthermore, it can be assumed that the measured macrocell current flows contributed the major part of the corrosion activity of the individual sensors in the present experimental set up as the anodic area was considerably smaller than the cathodic area (approximately 3 cm^2), see eg [*Andrade et al., 1992; Andrade et al., 2008*].

OCP and current flow measurements were taken automatically every 2 h by a LabVIEW controlled system using cluster measurements to minimize the number of data logging channels [*Küter, 2009*]. For each measurement time, a switch card hosting up to eight electrodes (sensors) was connected to a SCE and the OCP recorded until the system automatically switched to the next card and established a new connection. After connecting to each of the individual cards, a delay period of 2 min was set in the program at which the OCP was measured and recorded for each sensor along the instrumented rebar.

In addition, to the electrochemical OCP and macrocell current measurements, destructive visual investigations were conducted after terminating the electrochemical testing. The concrete covering the instrumented and standard rebar was removed cutting 25 mm deep notches above and below the rebars and crack opening the beam using chisel and hammer. Visual inspections included the extent and amount of corrosion as well as penetration of chloride ions (spraying silver nitrate on the concrete as an indicator) in the concrete and along the instrumented and standard rebar.

4.3 Modelling of Load-induced Cracking and Interfacial Damage

4.3.1 Model Description

To estimate the extent of load-induced interfacial damage along the reinforcement for the tested flexural beams, a finite element method (FEM) model was used. The model was based on a two dimensional, plain strain formulation that allows for simulation of cracking and interfacial damage, ie slip and separation between reinforcement and concrete, in reinforced concrete subjected to flexural loading. The basic concept of the modelling approach is given in Figure 4.6. To simulate the different damage phenomena in concrete and along the reinforcement associated with flexural loading (ie cracking, slip, and separation) a number of zero thickness interface domains are incorporated in the model. The various interface domains are established in serial and parallel connection to represent a realistic mechanical response of the beam during loading and the subsequent formation of associated damage. In the FEM model, slip denotes the local displacement between the reinforcement and the surrounding concrete parallel to the reinforcement, while separation corresponds to the deformation between the reinforcement and the surrounding concrete perpendicular to the reinforcement.

Formation and propagation of load-induced damage in the crack, concrete, and separation interface (see Figure 4.6) was modelled by a fictitious cracking approach [*Hillerborg et al., 1976*] where the tension softening behaviour is based on a cohesive discrete cracking model with multi-linear softening relations, which may be given as follows:

$$\sigma = \begin{cases} \sigma_e(\varepsilon) = E_{conc}\varepsilon & Pre-cracked\ state \\ \sigma_w(w) = g(w) f_{t,conc} & Cracked\ state \end{cases} \tag{4.1}$$

where σ_e is the elastic stress, E_{conc} the Young's modulus of concrete, ε the elastic strain, σ_w the normal bridging stress as a function of the crack width w, g the dimensionless cohesive relationship and $f_{t,conc}$ the concrete tensile strength. Formulation of

the multi-linear softening relations used to describe the dimensionless cohesive relationship, *g*, was adopted from [*Skoček and Stang, 2010*] and may be given as follows:

$$g(w) = b_i - a_i w \quad for \quad w_{i-1} < w < w_i \quad and \quad i = 1, \dots, n \tag{4.2}$$

where a_i describes the slopes of the cohesive branches, b_i the intercepts between the cohesive branches and w_i may be defined as follows:

$$w_i = \frac{b_i - b_{i+1}}{a_i - a_{i+1}} \quad for \quad i = 1, \dots, n-1 \quad and \quad w_n = w_{crit} = \frac{b_n}{a_n} \tag{4.3}$$

where w_{crit} is the critical crack width. Further, it is assumed that no stresses are transferred across the crack once $w > w_{crit}$. For the crack and concrete interface, *n* was set to 3, while $n = 1$ (ie linear tension softening behaviour) was chosen for the separation interface.

To describe the slip between concrete and reinforcement a modified cubic-relationship between the shear stress and slip, proposed in [*Dörr, 1980*], was used, which may be given as follows:

$$t_t = \begin{cases} f_{t,slip}\left(1.4\left(\frac{\Delta u_t}{\Delta {u_t}^0}\right)^3 - 4.5\left(\frac{\Delta u_t}{\Delta {u_t}^0}\right)^2 + 5\left(\frac{\Delta u_t}{\Delta {u_t}^0}\right)\right) for & 0 \le \Delta u_t < \Delta {u_t}^0 \\ 1.9 f_{t,slip} & \Delta u_t \ge \Delta {u_t}^0 \end{cases} \tag{4.4}$$

where t_t is the shear stress, $f_{t,slip}$ the strength of the slip interface, u_t the slip, and u_t^0 the value at which the curve reaches a plateau. For the different concrete compositions, the strength of the slip interface, $f_{t,slip}$, and u_t^0 were modified during the FEM simulations to fit the experimental observations.

Although, mainly physical meaningful parameters are used in the FEM model to describe the different damage phenomena in the concrete domain and along the concrete-reinforcement interface due to flexural loading, it should be noted that the formation of slip and separation at the concrete-reinforcement interface was modelled as independent processes. The authors are aware that the combination of these damage processes may be described by mixed-mode fracture behaviour. However, despite many efforts, see eg [*Carol et al., 1997*; *Lourenco and Rots, 1997*; *Nielsen et al., 2010*], there still appears to be a lack of proper mixed-mode behaviour formulations, which can be implemented in models for FEM simulations.

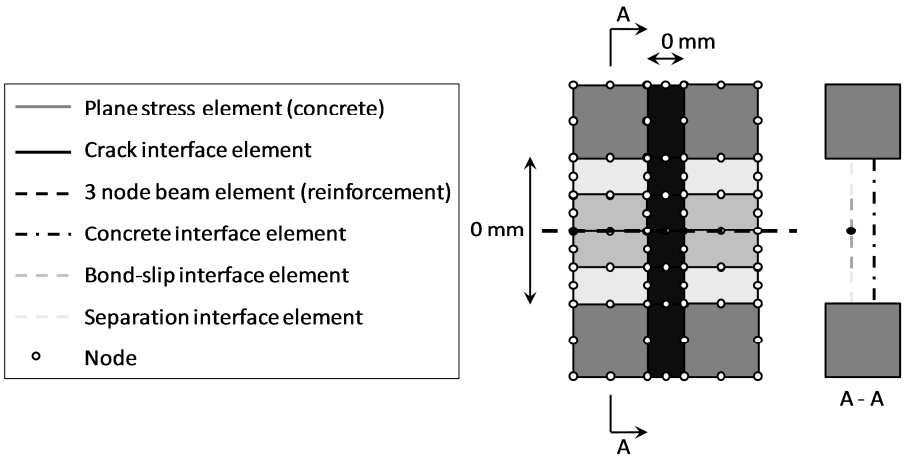

Figure 4.6 *Concept of the serial-parallel model simulating cracking and interfacial damage. Please note: illustration is not to scale.*

4.3.2 Numerical Model, Input Parameters, and Mesh Analysis

For the solution of the problem the commercial FEM software package TNO DIANA was used. The model consisted of 1184 quadrangular elements with 2353 nodes representing half of the beam due to symmetry of loading and boundary conditions of the three point bending test (see Figure 4.5). Nonlinear solution of the system of equations was obtained using a standard Newton-Raphson method with a displacement controlled convergence criterion.

To investigate the impact of varying mesh sizes on the solution of the problem, a range of interface discretisations were studied. Number of elements along the crack, separation, and slip interface were varied between 10 and 100 elements. Results of the mesh analysis are given in Figure 4.7. For all interfaces, no considerable effect on the solution of the problem (less than 1 % difference between the different mesh sizes) was found once more than 20 elements were used to discretize the interfaces. Based upon the results presented in Figure 4.7, the crack, slip, and separation interfaces were discretized with 60 elements each.

An overview of the required input parameters for the developed FEM model to simulate load-induced damage in PC and SFRC beams is given in Table 4.5. Input parameters cover elastic and fracture mechanical properties of steel and concrete as well as cracking, slip, and separation interface. The reduced cross section of the instrumented rebar (hollowed part) is directly accounted for in the FEM model. To fit the experimental results (see Section 4.4.1.2), the tensile strength of the slip interface, $f_{t,slip}$, and the value, u_t^0, (see Eq. (4.4)) were varied during the numerical simulations.

Table 4.5 *FEM model input parameters to simulate load-induced damage.*

Parameter	Symbol	Value	Unit
Young's modulus concrete	E_{conc}	28000	[MPa]
Poisson ratio concrete	μ_{conc}	0.2	[-]
Tensile strength concrete	$f_{t,conc}$	see Table 4.6	[MPa]
Young's modulus steel	E_{steel}	210000	[MPa]
Poisson ratio steel	μ_{steel}	0.3	[-]
Yield strength steel	$f_{y,steel}$	550	[MPa]
Tensile strength slip interface	$f_{t,slip}$	fitted	[MPa]
Constant slip value	dt^0	fitted	[mm]
Tensile strength separation interface	$f_{t,sep}$	0.03	[MPa]

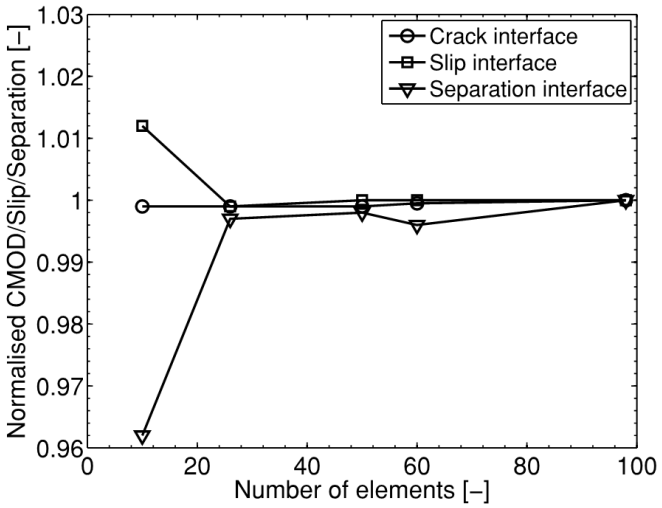

Figure 4.7 *Normalised results of mesh analysis.*

4.4 Results

Experimental and numerical results for plain and steel fibre reinforced concrete are presented in the following. Results of mechanical testing include fracture mechanical properties, photogrammetric investigations on load-induced cracking, slip and separation at the concrete-reinforcement interface, and comparisons between experimental (ie photogrammetric investigations) and numerical results for the various concrete compositions. All experimental and numerical results are presented for crack mouth opening displacement (CMOD) at the concrete tensile surface, separation, and slip at the concrete-reinforcement interface against applied load. Electrochemical results cover information on time- and location-dependent open circuit corrosion potential (OCP) and macrocell current measurements for the various concrete compositions. Finally, visual observations of the extent of corrosion along the instrumented and standard rebar and chloride ion ingress are given.

4.4.1 Mechanical Testing

4.4.1.1 Fracture Mechanical Properties

As mentioned previously, inverse analysis of experimental results of 3PBTs was used to determine fracture mechanical properties of the different concrete compositions tested in this study (see Table 4.2). Selected experimental results and results of the corresponding inverse analysis are given in Figure 4.8.

A very good agreement between experimental and numerical results, obtained by inverse analysis of load-CMOD curves, is found for all specimens tested. Furthermore, the impact of fibres on the mechanical response is clearly observed, ie an increasing ductile material behaviour with increasing fibre content. Fracture energy, G_f, and tensile strength, $f_{t,conc}$, of the various concrete compositions determined by means of inverse analysis are given in Table 4.6. The multi-linear cohesive relations used in the FEM model to describe the tension softening behaviour (see Eq. (4.2)) of the different concrete compositions are presented in Figure 4.9.

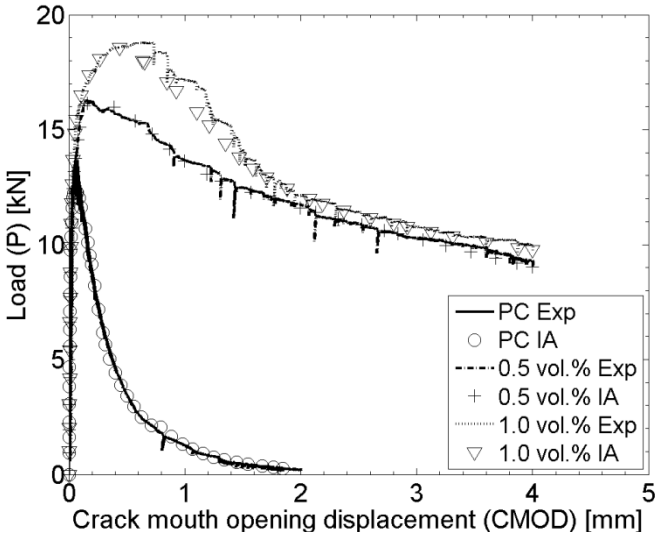

Figure 4.8 *Selected experimental (Exp) and inverse analysis (IA) load-CMOD curves for concrete compositions tested in this study.*

Table 4.6 *Fracture energy (G_f) and tensile strength ($f_{t,conc}$) determined from inverse analysis of 3PBTs.*

Concrete Composition	$f_{t,conc}$		G_f	
	Mean [MPa]	St. Dev. [MPa]	Mean [J/m^2]	St. Dev. [J/m^2]
PC	1.8	0.1	569	55
SFRC 0.5 vol.%	1.7	0.1	4700	700
SFRC 1.0 vol.%	1.7	0.6	9000	2800

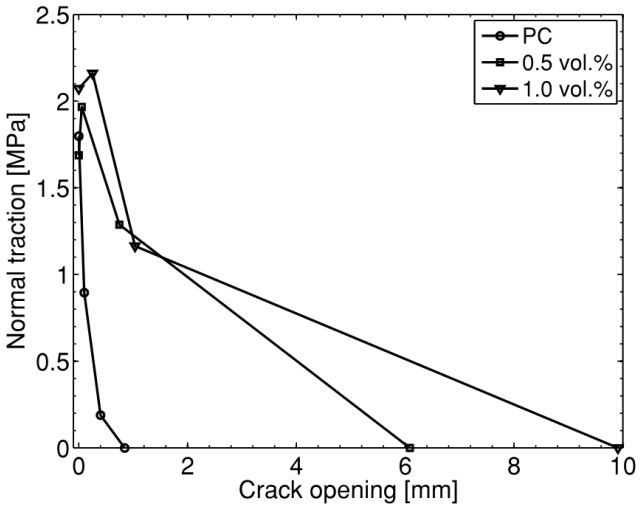

Figure 4.9 *Cohesive relations (mean of three test specimens for each concrete composition) for PC and SFRC (0.5 vol.% and 1.0 vol.%) to describe tension softening behaviour (see Eq. (4.1)).*

4.4.1.2 Experimental and Numerical Results of Load-induced Damage

Experimental and numerical results illustrating load-induced damage, ie cracking, slip and separation between concrete and reinforcement, are given in Figure 4.10 as a function of the applied load. For simplicity, comparisons between experimental and numerical results are only given for one specimen, ie MSA 11 (1.0 vol.% SFRC) with 60 mm concrete cover thickness. However, similar results were obtained for all concrete compositions tested in this study, ie PC and SFRC specimens with 20/60 mm concrete cover thickness, respectively. It should be noted that although multiple cracking occurred in most specimens during mechanical loading, results are presented for the primary bending crack, which was defined as the first crack being formed. For all specimens the primary bending crack was located at or near the centre of the specimen.

Figure 4.10 (a) illustrates experimental and numerical results of the crack mouth opening displacement (CMOD) at the concrete tensile surface against the applied load. It is seen from the presented results that the numerical model can accurately capture both, crack initiation and increase in crack width. It should be further noticed that the fracture mechanical properties describing the tension softening behaviour of the material (see Eq. (4.2)) were determined independently from 3PBTs, ie no fitting of fracture mechanical parameters was performed to reproduce the experimental data. A comparison between numerical and experimental results concerning slip and separation between concrete and reinforcement (at 10 mm distance from the main bending crack) is given in Figure 4.10 (b). It is seen from the presented results that the developed FEM model can properly reproduce both damage phenomena. The numerical model is further capable of simulating the initiation as well as propagation of slip and separation at the concrete-reinforcement interface due to increasing load. The ob-

served scatter in the experimental data is most likely attributed to the limited resolution of the photogrammetric equipment used in this study.

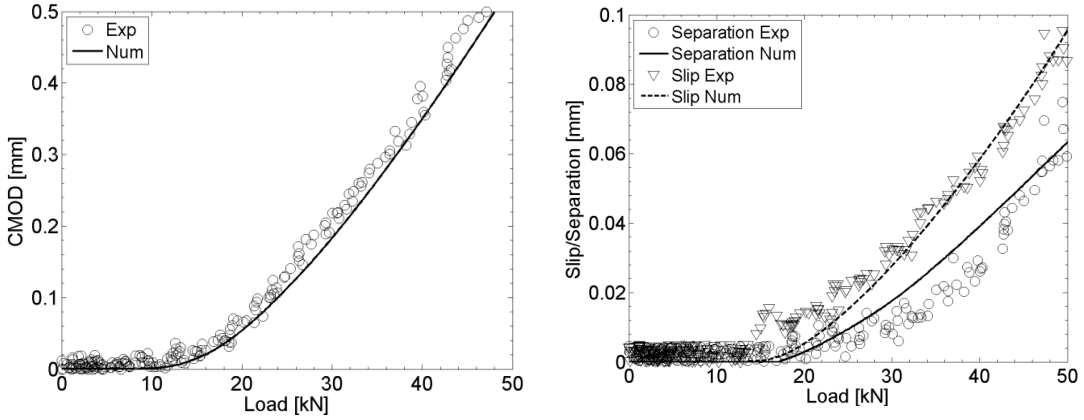

(a) *(b)*

Figure 4.10 *Experimental and numerical results illustrating (a) CMOD and (b) slip and separation between concrete and reinforcement (at 10 mm distance from main bending crack) as a function of load for MSA 11 (1.0 vol.% SFRC).*

4.4.2 Electrochemical Testing

4.4.2.1 Plain Reinforced Concrete

Typical OCP and macrocell current density measurements for plain reinforced concrete are given in Figure 4.11 for 24 days of exposure. Results are presented for selected sensors of the instrumented rebar and indentified by their distance from the main bending crack. It can be seen from the results that OCPs are decreasing for sensors located closer to the crack throughout the exposure time, which indicates a change in the favoured thermodynamical corrosion state from passive to active. The change in thermodynamical state of sensors located in the vicinity of the crack was confirmed by corresponding macrocell current density measurements. In contrast to sensors located closer to the main bending crack, the OCP for the sensor located at a distance of 70 mm from the crack initially decreases slightly to a potential of approximately -0.7 V_{SCE} and then gradually increases to approximately -0.2 V_{SCE} (see Fig. 4.11 (a)). The behaviour of the sensor might be explained by an initial lack of oxygen (due to previous storage under water) as well as variations in the moisture content and concrete resistivity. Also, considerable smaller current densities were observed for sensors located furthest from the crack (see Fig. 4.11 (b)), which facilitate the assumption of the passive state of the sensor.

Contour plots illustrating results of all sensor locations along the instrumented rebar for plain reinforced concrete are shown in Figure 4.12. Results are given as a function of the exposure time (in days) and location from the crack (in mm) as well as OCP (in

V_{SCE}) and macrocell current density (in μA/cm^2), which are indicated by a colour scale.

Initially, corrosion potentials around -0.2 to 0 V_{SCE} were measured for all sensors along the instrumented rebar. As mentioned earlier, considerable lower OCPs were measured for sensors located in a distance between 40 to 80 mm from the crack, which may be attributed to a lack of oxygen. Similar OCPs of passive reinforcement in an oxygen deprived environment can be found in the literature, see eg [*Arup, 1983*]. As time progressed, a considerable decrease in OCP was seen for all sensors located between -40 and 30 mm from the crack indicating initiation of corrosion. No decrease in OCP was measured during the exposure time for sensors located between -80 to -40 mm from the crack. Concurrent macrocell current density measurements for sensors located 10 to 80 mm from the crack correlate well with the decrease in OCP. Macrocell current densities up to approximately 10 μA/cm^2 were measured for actively corroding sensors. For sensors located in the region between 30 and 80 mm considerable smaller current densities were measured, which confirms the assumption that the initial low potential was not attributed to active corrosion.

In addition to the electrochemical measurements, simulated results of the slip and separation between the reinforcement and concrete are illustrated in Figure 4.12 (c). As can be seen from the figure, 7 to approximately 12 μm slip are estimated along the reinforcement between -80 and 80 mm from the crack. Separation between the reinforcement and concrete is estimated to extend approximately from -40 to 40 mm from the crack. Comparing electrochemical and mechanical results, a very good correlation between the simulated extent of separation and measured extent of active corrosion can be found (see Fig. 4.12).

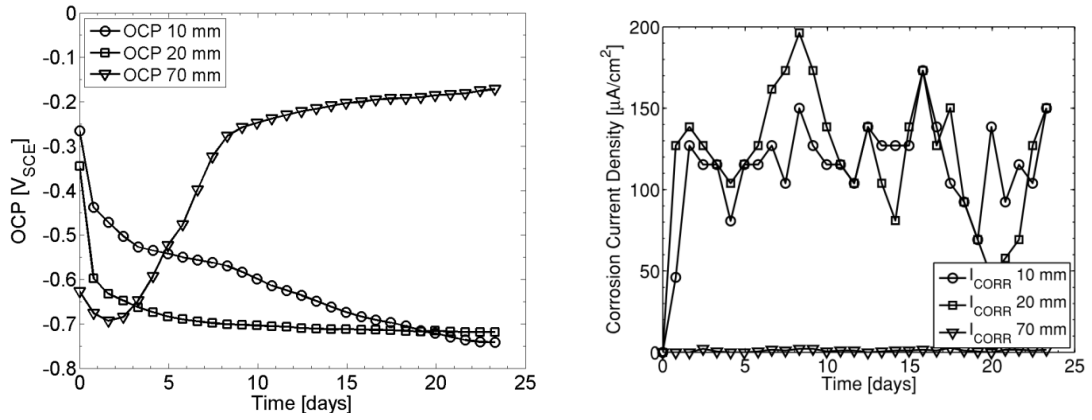

(a) *(b)*

Figure 4.11 *(a) Corrosion potential (OCP) and (b) corrosion current density (I_{CORR}) measurements of selected sensors along the instrumented rebar for ESE 1 (PC). Sensors are identified by their distance to the main bending crack.*

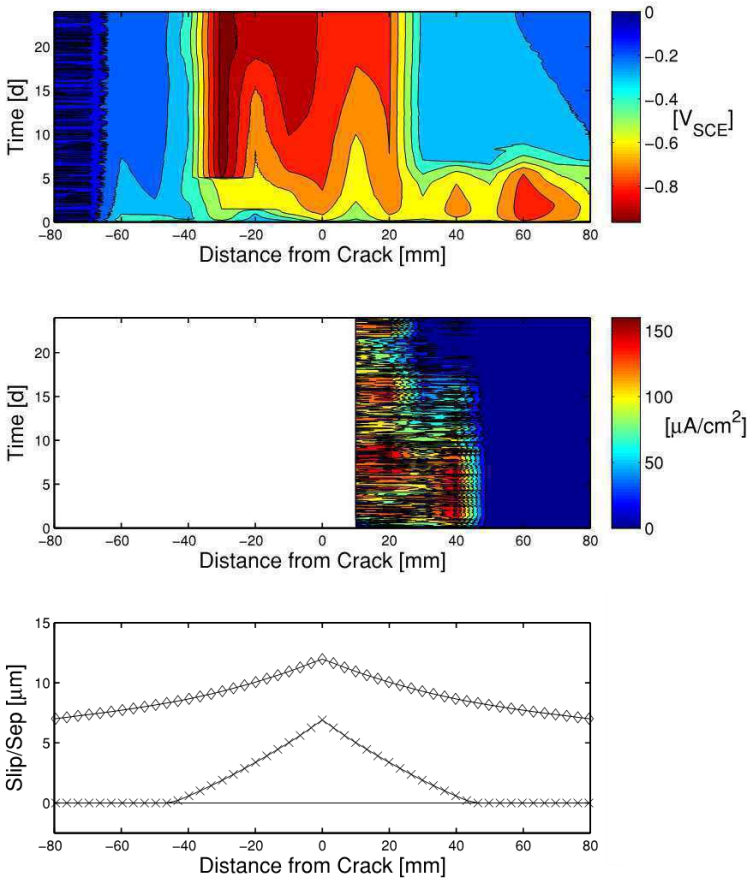

Figure 4.12 *(a) location- and time-dependent OCP and (b) corrosion current density (only for half of the sensors) measurements for ESE 1 (PC). (c) simulated extent of slip (diamond symbols) and separation (cross symbols) between concrete and reinforcement.*

4.4.2.2 Steel Fibre Reinforced Concrete

Selected OCP and macrocell current density measurements for specimens ESE 2 and 3 are given in Figures 4.13 and 4.14, respectively. Results are presented for sensors located 10, 40, and 70 mm from the main bending crack for ESE 2 (0.5 vol.% SFRC). In contrast to the OCP measurements for ESE 1, considerable potential drops were observed for sensors located 10 and 40 mm from the crack. For the sensor located closest to the crack (10 mm), a first drop in OCP was seen after approximately 1.5 days of exposure, which was accompanied by an increase in macrocell current density. The OCP drop was however, smaller than usually described in literature (approximately -0.2 V_{SCE}) indicating a change in state of corrosion, see eg [*Küter, 2009*]. After approximately 3 days of exposure, the sensor located 40 mm from the crack showed a drop in OCP and at the same time an increase in macrocell current density was recorded. A gradual decease in OCP can be seen for the sensor located furthest from the crack (70 mm) and a sudden increase in macrocell current density after approximately 3.5 days of exposure indicating active corrosion.

Figure 4.14 shows OCP and current density measurements for sensors located 10, 20, and 70 mm from the main bending crack for the ESE 3 specimen (1.0 vol.% SFRC). Similar to the results presented for plain reinforced concrete (ESE 1), a rather gradual decrease than a sudden drop in OCP can be observed for the sensors located closest to the crack. However, concurrent macrocell current density measurements showed a considerable increase for these sensors indicating active corrosion. Throughout the complete exposure no decrease in OCP or increase in current density was measured for the sensor located 70 mm from the crack, which indicates a passive state of the sensor.

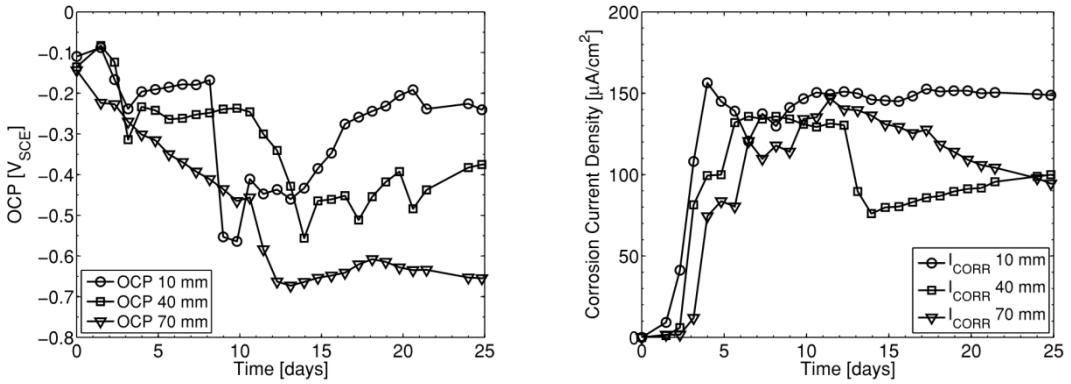

(a) *(b)*

Figure 4.13 *(a) Corrosion potential (OCP) and (b) corrosion current density (I_{CORR}) measurements of selected sensors along the instrumented rebar for ESE 2 (0.5 vol.% SFRC). Sensors are identified by their distance to the main transverse crack.*

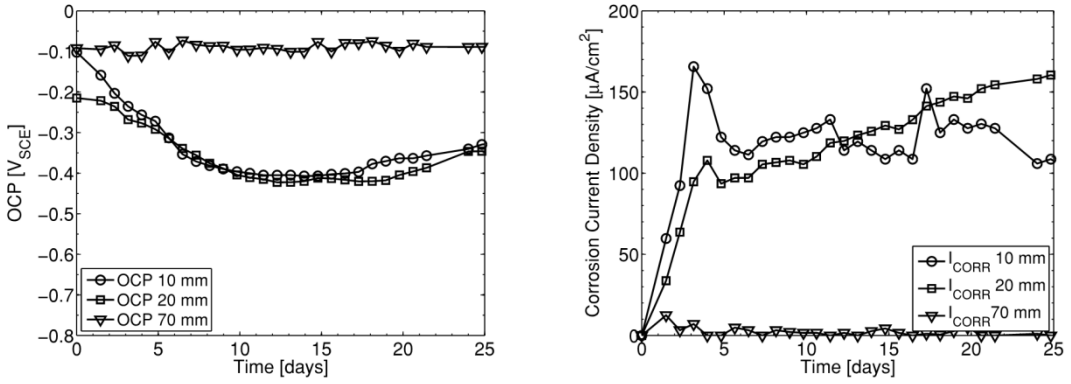

(a) *(b)*

Figure 4.14 *(a) Corrosion potential (OCP) and (b) corrosion current density (I_{CORR}) measurements of selected sensors along the instrumented rebar for ESE 3 (1.0 vol.% SFRC). Sensors are identified by their distance to the main transverse crack.*

Contour plots showing results for all sensors along the instrumented rebar are given in Figures 4.15 and 4.16 for specimens ESE 2 and 3 (ie 0.5 vol.% and 1.0 vol.% SFRC), respectively. Results presented include OCP measurements in a region between -80 mm to 80 mm and macrocell current density measurements between 10 mm to 80 mm

from the main bending crack. Initially, values between approximately -0.2 to 0 V_{SCE} were measured for the sensors along the instrumented rebar for ESE 2 (see Fig. 4.15). With progressing exposure time all sensors located between -70 mm and 70 mm from the bending crack showed a considerable decrease in OCP, which was accompanied with an increase in macrocell current density indicating active corrosion in that region. Furthermore, it can be seen that with increasing distance from the crack, initiation of corrosion was delayed as indicated by the macrocell current density measurements in Figure 4.15 (b). For the various sensors along the instrumented rebar, corrosion current densities up to approximately 150 $\mu A/cm^2$ were recorded during the exposure time. Comparisons between the extent of simulated interfacial damage, in particular the separation between concrete and reinforcement, correlate very well with the extent of measured active corrosion. Both, electrochemically measured active corrosion and simulated separation are seen in a region between -70 mm to 70 mm from the main transverse crack (see Fig.4. 15).

Similar initial OCPs, as for ESE 1 and ESE 2 (ie PC and 0.5 vol.% SFRC), were measured for ESE 3 (ie 1.0 vol.% SFRC) with values ranging from -0.2 to 0 V_{SCE}. With increasing exposure time, decreasing OCPs were observed for sensors located -30 mm to 30 mm from the main bending crack indicating initiation of corrosion (see Fig. 4.16 (a)). Concurrent macrocell current density measurements taken for sensors in this region also showed an increased macrocell current density confirming the assumption of active corrosion. For actively corroding sensors along the instrumented rebar, macrocell current densities up to approximately 150 $\mu A/cm^2$ were recorded during the exposure time. Sensors located outside this region (in the region between -80 mm to -30 mm and 30 mm to 80 mm), showed neither an increase in macrocell current density nor a decrease in OCP throughout the exposure period indicating no change in corrosion state, ie the sensors remained in the passive state. Comparisons of the electrochemical measurements (OCP and macrocell current density) and mechanical results showed again a good correlation between the simulated extent of separation (-35 mm to 35 mm from crack) and measured risk of corrosion (-30 mm to 30 mm).

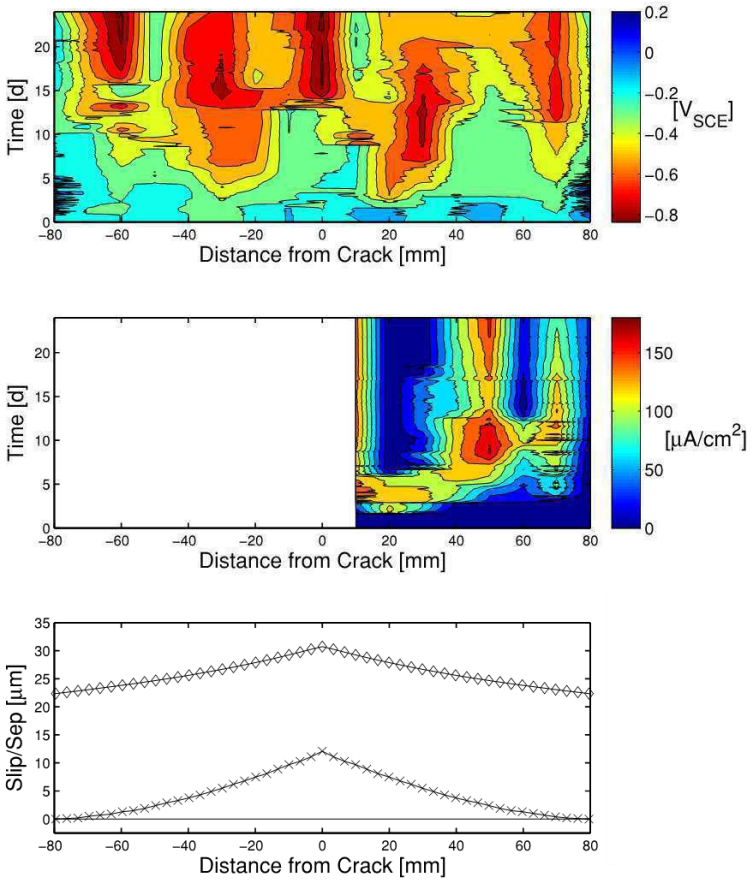

Figure 4.15 *(a) location- and time-dependent OCP and (b) corrosion current density (only for half of the sensors) measurements for ESE 2 (0.5 vol.% SFRC). (c) simulated extent of slip (diamond symbols) and separation (cross symbols) between concrete and reinforcement.*

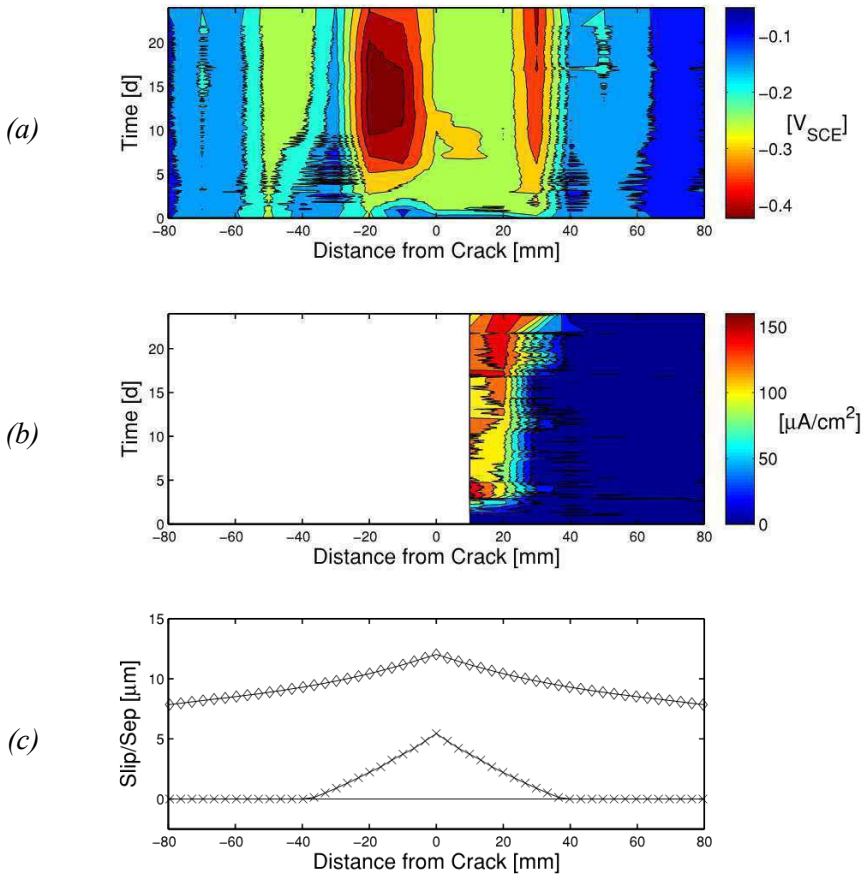

Figure 4.16 *(a) location- and time-dependent OCP and (b) corrosion current density (only for half of the sensors) measurements for ESE 3 (1.0 vol.% SFRC). (c) simulated extent of slip (diamond symbols) and separation (cross symbols) between concrete and reinforcement.*

4.4.3 Visual Observations

Exemplary results of destructive visual observations are presented in Figures 4.17 and 4.18, respectively. Figure 4.17 illustrates the extent of chloride ingress (indicated by the broken line), the crack path (indicated by the solid line) and signs of rust stains (indicated by circled areas) observed in ESE 2 (0.5 vol.% SFRC). Silver nitrate was used to highlight the chloride ingress at the concrete surface.

The extent of chloride ingress is clearly visible along the main bending crack path and in the vicinity of the reinforcement in Figure 4.17. The ingress extended around 85 mm from the crack in both directions along the reinforcement. No considerable ingress in the bulk material was observed indicating the interfacial damage along the reinforcement, in particular the separation between reinforcement and concrete, acted as a rapid pathway for the chloride ingress as proposed by eg [*Pease, 2010*]. Similar observations, ie extent of chloride ingress along the reinforcement and crack path, were made for the conventional reinforcement. Measured extents of chloride ingress for ESE 1 and ESE 3 (ie PC and 1.0 vol.% SFRC) were substantially less as the crack

mouth opening displacement at the concrete tensile surface and extent of separation between concrete and reinforcement was considerably lower (see Table 4.4). In all specimens rust stains were found throughout the area of chloride ingress indicating active corrosion of the reinforcement (instrumented as well as conventional reinforcement). No visual signs of active corrosion were seen outside the area where chloride ions were indicated by silver nitrate.

In addition to the chloride ingress, the extent of corrosion for all instrumented and conventional rebars was investigated with a stereomicroscope. A typical image obtained for a sensor of an instrumented rebar (10 mm distance from crack) previously embedded in ESE 3 (1.0 vol.% SFRC) is given in Figure 4.18. The location of the sensor is highlighted by a broken line in the figure. Clear signs of corrosion can be seen at the surface of the sensor as well as the surface of the rebar confirming the open circuit corrosion potentials and macrocell current density measurements. Similar results were obtained for all sensors indicating active corrosion throughout the electrochemical measurements. Furthermore, similar extents of corrosion were seen along the conventional and instrumented rebar for all materials tested, ie PC, 0.5 and 1.0 vol.% SFRC, as indicated by the electrochemical measurements.

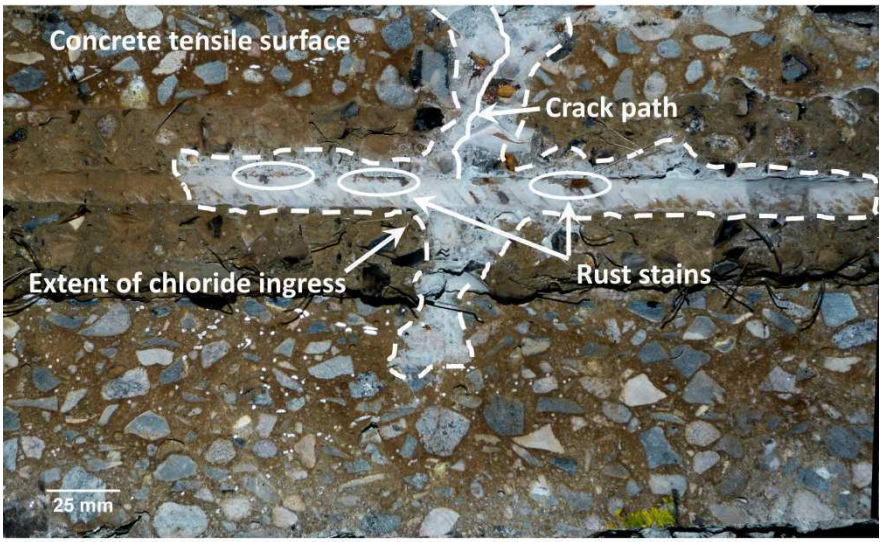

Figure 4.17 *Extent of chloride ingress (broken line), crack path (solid line) and rust stains (circled areas) in ESE 2 (0.5 vol.% SFRC) specimen after termination of experiment.*

Figure 4.18 *Sensor (indicated by broken line) of instrumented rebar located next to main bending crack with signs of corrosion at the sensor and the instrumented rebar for ESE 3 (1.0 vol.% SFRC) beam.*

4.5 Discussion of Results

4.5.1 Fracture Mechanical Properties and Load-induced Damage

Fracture mechanical properties of the cracking interface in the FEM model (see Fig. 4.6) describing the initiation and propagation of a load-induced bending crack were determined by inverse analysis of independent experimental investigations (see Section 4.4.1.1). Results of the inverse analysis, ie tensile strength and fracture energy, were presented in Table 4.6 for the different concrete compositions tested in this study. From the results it can be seen that the addition of fibres has no considerable influence on the tensile strength of the concrete. However, with increasing amounts of fibres, the ductility of the concrete, described by the fracture energy, is considerably increased. Similar observations were made by eg [*Löfgren et al., 2005; Kazemi et al., 2007*].

For all load-induced damage phenomena, ie cracking, slip, and separation, very good agreements between experimental and numerical results were found for the different concrete compositions tested in this study (see Fig. 4.10). Formation of the main bending crack was observed for loads between 15 and 18 kN for the different concrete composition, which was in good agreement with results of the numerical simulations. Initiation of separation between concrete and reinforcement was observed for higher loads for all concrete compositions. The numerical model was also able to simulate this phenomenon indicating the load-induced damage is reproduced in a physically correct manner. Furthermore, the influence of additional fibres on various damage phenomena, eg decreased CMOD, slip, and separation with increasing fibre content, was accurately reproduced by the developed FEM model.

To fit the experimental data, two parameters were varied in the FEM model, ie the tensile strength of the slip interface, $f_{t,slip}$, and u_t^0. Values used for the tensile strength of the slip interface for the different concrete compositions were in the same order of magnitude (1.1 MPa to 2.6 MPa). However, no correlation between the fibre content and the fitted tensile strength of the slip interface was observed. The strength of the separation interface, $f_{t,sep}$, was set to 0.03 MPa for all investigated concrete compositions, which was considerably lower than the tensile strength of the slip and crack interface (see Fig. 4.6), respectively. The separation interface accounts for the chemical adhesion between concrete and steel for which, to the authors' knowledge, mechanical properties have not been described in the literature. Furthermore, results of a parametric study on the impact of $f_{t,sep}$ showed no considerable impact on the investigated damage phenomena (cracking, slip, and separation). Numerical results indicated that the separation is controlled by the mechanical properties of the concrete interface connecting the upper and lower part of the concrete domain (see Fig. 4.6), which accounts for the formation of internal cracks caused by local stress transfer from the reinforcement to the concrete via the ribs.

4.5.2 Open Circuit Corrosion Potential and Macrocell Current Density Measurements

Comparisons of contour plots presented in Section 4.4.2, showed similar open circuit corrosion potentials (OCPs) for all concrete compositions tested at the beginning of exposure. Initially, OCPs of approximately -0.2 to 0 V_{SCE} were measured indicating a passive corrosion state of the reinforcement. Similar OCP values for passive reinforcement are reported in the literature, see eg [*Küter, 2009; Pease et al., 2011*]. With progressing time, an either gradual decrease or sudden drop in OCP was seen for certain sensors along the instrumented rebar indicating active corrosion was thermodynamically favoured. For the ESE 1 and ESE 3 specimens (ie PC and 1.0 vol.% SFRC) a gradual decrease in potential was observed immediately after ponding, while for ESE 2 (ie 0.5 vol.% SFRC) a sudden drop in OCP was seen. OCPs for ESE 1 and ESE 2 decreased to values of approximately -0.8 V_{SCE} and -0.4 V_{SCE} for ESE 3, which is in good agreement with values that have been reported in the literature for active corrosion, see eg [*Schießl, 1976; Elsener et al., 2003*]. Signs of active corrosion were observed for OCP drops ranging from approximately 0.1 to 0.4 V_{SCE} for the different concrete compositions. Active corrosion was confirmed by concurrent macrocell current density measurements.

However, time to corrosion initiation and extent of corrosion varied for the tested PC and SFRC beams. Macrocell current density measurements obtained for ESE 2 and ESE 3 (ie SFRC specimens) showed a delay in active corrosion compared to ESE 1. Signs of active corrosion were recorded after approximately 1 day of exposure for ESE 3 and 1.5 days of exposure for ESE 2, respectively. Similar macrocell current densities (up to approximately 10 $\mu A/cm^2$) were measured for all concrete composi-

tions, which is in good agreement with values that have been reported in literature for comparable anode-to-cathode rations, see eg [*Andrade et al., 1992; Andrade et al. 2008*]. No considerable influence of the fibre content on the macrocell current density was observed in this study, which was confirmed by visual observations indicating similar depths of corrosion for the conventional and instrumented rebars embedded in the test specimens.

4.5.3 Correlation between Interfacial Damage, Crack Width, and Risk of Corrosion

The presented results facilitate the hypothesis that the concrete-reinforcement interfacial condition can be used as a reliable indicator to quantify the impact of load-induced cracks on the risk of corrosion initiation along the reinforcement. Very good agreements between the simulated interfacial damage, in particular the separation between reinforcement and concrete, and extent of active corrosion along the instrumented rebar (indicated by the electrochemical measurements) were obtained for all concrete compositions tested. For ESE 1 (ie PC), active corrosion was measured for sensors located at a distance of -40 mm to 35 mm from the main bending crack compared to around -40 mm to 40 mm simulated by the FEM model (see Fig. 4.12). Extents of separation were simulated and active corrosion measured in a region between -70 mm to 70 mm and -30 mm to 30 mm from the main transverse crack for ESE 2 and ESE 3 (ie 0.5 vol.% SFRC and 1.0 vol.% SFRC), respectively (see Fig. 4.15 and 4.16).

Similar to the interfacial damage, a good correlation between the crack width at the concrete surface and extent of corrosion along the reinforcement was found for the specimens tested in this study. For a crack width of approximately 0.07 mm at the concrete surface (see Tab. 4.4), similar extents of corrosion were found for ESE 1 (around 40 mm) and ESE 3 (around 35 mm), respectively. However, for larger crack widths at the concrete surface, the correlation between crack width and extent of corrosion may not hold true, especially with regards to the use of SFRC as experimental and numerical results of the mechanical testing indicate that the addition of steel fibres alters the extent of interfacial damage compared to PC.

4.5.4 Visual observations

Electrochemical measurements (OCP and macrocell current density) and numerical simulations of separation between reinforcement and concrete are in good agreement with visual observations (chloride ingress and extent of corrosion along the instrumented and conventional reinforcement) for all concrete compositions tested.

The highest lateral chloride ingress along the reinforcement was observed for ESE 2 (around 80 mm in both directions from the main bending crack) with a measured surface crack width of 0.139 mm. Less lateral ingress of chloride ions was observed for

ESE 1 (around 45 mm in both directions) and ESE 3 (around 40 mm in both directions) with measured surface crack widths of 0.068 mm and 0.069 mm, respectively. Visual signs of corrosion for the conventional and instrumented rebar were obtained for all specimens in the region where chloride ions were indicated by the application of silver nitrate. Within the same region, electrochemical measurements, ie OCP and macrocell current density measurements, of sensors along the embedded instrumented rebars indicated active corrosion for all tested concrete compositions. Furthermore, similar extents of separation between the reinforcement and concrete were simulated by means of a finite element model for all materials. Slightly higher extents of chloride ingress measured by visual observations may be attributed to additional transport phenomena, such as convection and/or diffusion of chloride ions, throughout the time of exposure.

4.6 Conclusions

In this study plain concrete (PC) and steel fibre reinforced concrete (SFRC) flexural beams were cracked and exposed to a 3 % sodium chloride solution. Instrumented rebars, embedded in the beams, provided location- and time-dependent open circuit corrosion potential (OCP) and macrocell current density measurements. From the presented electrochemical measurements (OCP and macrocell current density measurements), mechanical simulations (predictions of the extent of slip and separation between concrete and reinforcement) and destructive visual observations (extent of chloride ingress and corrosion along the conventional and instrumented reinforcement) it may be concluded that:

- The presented FEM model can simulate various damage phenomena (cracking, slip, and separation) associated with three point bending tests, which was demonstrated comparing experimental results obtained from photogrammetric investigations and numerical results for three different concrete compositions. Input parameters describing the fracture mechanical behaviour of the crack, slip, and separation interface were either obtained from independent tests or varied to fit experimental data, where fitted parameters appear to be in the correct order of magnitude.
- The concrete-reinforcement interfacial condition can be used as a reliable indicator to quantify the impact of load-induced cracks on the risk of corrosion initiation along the reinforcement. In particular, the simulated extent of separation along the reinforcement is in very good agreement with all experimental observations, ie mechanical, electrochemical, and visual. Future investigations may also focus on other factors such as surface roughness and treatment of reinforcement, mechanical and chemical bonding etc., which may affect the concrete-reinforcement-interfacial condition.

- Since the applied FEM model directly accounts for the impact of various parameters (eg concrete cover thickness, concrete composition, stress level in the reinforcement and crack orientation) on the mechanical response of the beam (extent and magnitude of slip and separation between reinforcement and concrete), the predicted interfacial damage may be used as a parameter to quantify the risk of corrosion initiation in subsequent service life analyses.

Acknowledgements

The first author gratefully acknowledges the financial support of Femern Bælt A/S, Sund & Bælt Holding A/S and The Danish Agency for Science, Technology and Innovation as well as COIN (COncrete INnovation centre, www.coinweb.no) and its partners for facilitating the research behind this paper. Financial supports of the Ph.D. study “Application of Fibre Reinforced Concrete in Civil Infrastructure” by the Danish Agency for Science, Technology and Innovation, COWI A/S, DTU, Bekaert NV, Grace, and the Danish Road Directorate are also acknowledged as well as financial contributions from the Danish Expert Centre for Infrastructure.

Chapter 5

Concrete Cover Cracking due to Uniform Reinforcement Corrosion

(Paper IV)

Anders Ole Stubbe Solgaard

Department of Civil Engineering, Technical University of Denmark, Kgs. Lyngby, Denmark
COWI A/S Denmark, Kgs. Lyngby, Denmark

Alexander Michel

Department of Civil Engineering, Technical University of Denmark, Kgs. Lyngby, Denmark
Department of Structural Engineering, Norwegian University of Science and Technology (NTNU), Trondheim, Norway

Mette Rica Geiker

Department of Civil Engineering, Technical University of Denmark, Kgs. Lyngby, Denmark
Department of Structural Engineering, Norwegian University of Science and Technology (NTNU), Trondheim, Norway

Henrik Stang

Department of Civil Engineering, Technical University of Denmark, Kgs. Lyngby, Denmark

Accepted for publication in the journal "Materials and Structures"
DOI: 10.1617/s11527-013-0016-6

Abstract

Service Life Design (SLD) is an important tool for civil engineers to ensure that the structural integrity and functionality of the structure is not compromised within a given time frame, ie the service life. In SLD of reinforced concrete structures, reinforcement corrosion is of major concern and reinforcement de-passivation is a frequently used limit state. The present paper investigates an alternative limit state: corrosion-induced cover cracking. Results from numerical simulations of concrete cover cracking due to reinforcement corrosion are presented. The potential additional service life is calculated using literature data on corrosion rate and Faraday's law. The parameters varied comprise reinforcement diameter, concrete cover thickness and concrete material properties, viz. concrete tensile strength and ductility (plain concrete and fibre reinforced concrete). Results obtained from the numerical simulations reveal that, depending on the serviceability limit state applied, the service life of a reinforced concrete structure can be increased significantly by allowing minor damage of the cover.

Keywords

Service Life Design, Cracking of Concrete Cover, Numerical Simulations, Fibre Reinforced Concrete

5.1 Introduction

Over the last decades service life design (SLD) has become an important tool within civil engineering for design of durable reinforced concrete structures. The concept of service life design is used to assure that, within a given time frame during which the structure is routinely maintained, ie the service life, little or no repair is required to maintain the purpose and integrity of the structure. A typically used requirement for reinforced concrete structures at risk of reinforcement corrosion, is that no corrosion of embedded reinforcement takes place within the service life of the structure [*DuraCrete, 2000; fib, 2006*]. To fulfil such a requirement, existing guidelines for SLD eg [*DuraCrete, 2000; fib, 2006*] establish that the end of service life has been reached when the passive layer of embedded reinforcement has been broken down. In other words de-passivation of the reinforcing steel is typically used as a serviceability limit state. In eg [*fib, 2006*] other limit states associated with reinforcement corrosion are also considered, however, associated models for analyses are not described as opposed to models associated with the de-passivation limit state. One of the concepts founding the basis of SLD for reinforced concrete structures is Tuutti's model of reinforcement corrosion [*Tuutti, 1982*], establishing that reinforcement corrosion is divided into two phases, viz. the initiation phase and the propagation phase. The propagation phase was further characterized in terms of various types of cracking damage in [*fib, 2006*], including 'formation of cracks' and 'spalling of the concrete cover'.

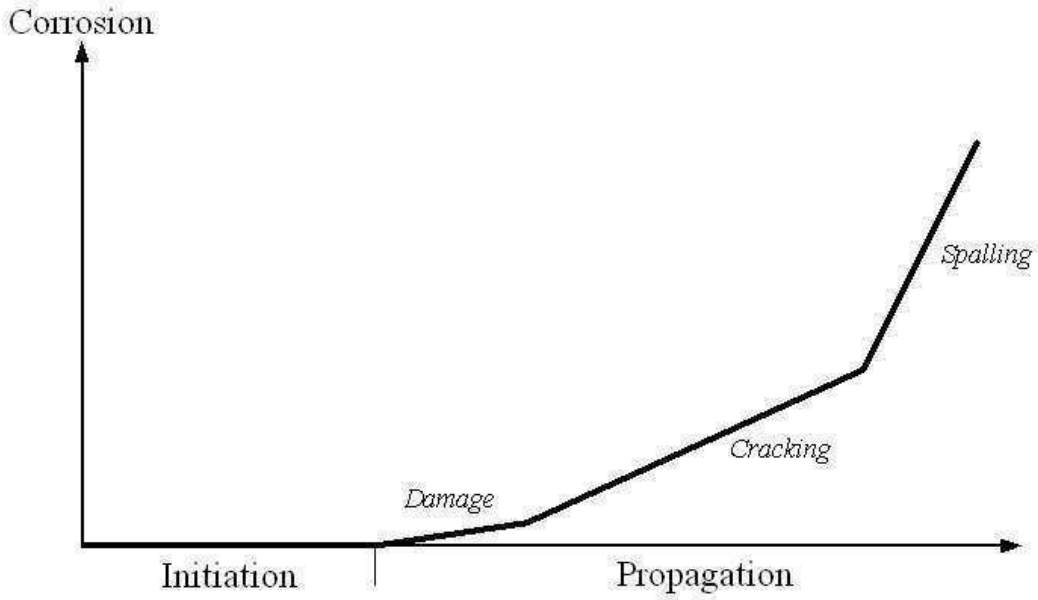

Figure 5.1 *Model for corrosion initiation and propagation and the terminology used in the current study for characterizing the propagation phase. After Tuutti, [Tuutti, 1982] and fib Model Code for Service Life Design [fib, 2006].*

During the initiation phase substances like Cl^- and CO_2 may ingress through the concrete cover leading to de-passivation of the reinforcing steel (at the end of initiation phase). During the propagation phase the actual corrosion of the reinforcement takes place. The formation of solid corrosion products will lead to a build-up of pressure in the concrete/steel interface as the corrosion products take up more volume than the steel consumed.

The italicized labels in Figure 5.1 characterize the structural consequences in the concrete surrounding the reinforcement due to reinforcement corrosion; "*Damage"* refers to the formation and propagation of cracks inside the concrete cover, *"Cracking"* refers to the formation and opening of cracks reaching the concrete cover surface, and "*Spalling"* refers to the phenomenon of cover concrete being pushed off due to the corrosion process and the expansive nature of the corrosion products. The above definitions are used in this study; the definitions used in the literature vary. The crack initiation at the concrete/steel interface and the formation of damage prior to cracking reaching the concrete surface has been experimentally observed by Michel et al. [*Michel et al., 2011*].

The transition from the damage phase to the cracking phase, cf. Figure 5.1, is defined as the time when the crack, which propagates through the concrete cover from the reinforcement towards the concrete cover surface, reaches the cover surface. However, since the exact time is difficult to determine when inspecting existing structures as well as in numerical simulations of concrete cover cracking, in the present paper a value of the crack width at the concrete surface, W, of $W = 50$ μm is used to define the end of the damage phase, viz. $W_{lim,c} = 50$ μm. A crack of approx. $W = 50$ μm is the

smallest crack possible to observe with the naked eye, a so-called hairline crack, and the value is also used in existing guidelines for SLD, eg [*DuraCrete, 2000*] as the definition of crack initiation.

Another characteristic state of the corroding reinforced concrete structure can be defined as the time for which W attains a certain value. This state could be defined as the end of the cracking phase (not necessarily corresponding to the start of the concrete spalling phase). Both the end of the damage phase and the end of the cracking phase could be used as limit states. The end of the cracking phase has previously been suggested as a durability limit state eg by Andrade et al. [*Andrade et al., 1993*] and the corresponding crack width limit should be dependent on exposure conditions, concrete type etc.

A vast amount of literature concerning concrete cover cracking caused by reinforcement corrosion already exists, covering, among others, experimental observations [*Rasheeduzzafar et al., 1992; Andrade et al., 1993; Alonso et al., 1998*], analytical models [*Bazant, 1979; Liu and Weyers, 1998; Chernin et al., 2010*] and FEM-based models for cracking [*Suda et al., 1993; Isgor and Razaqpur, 2006; Chernin et al., 2010*]. Several modelling approaches have been proposed based on experimental results, eg a model for the prediction of time of the initiation of corrosion-induced cracking by Liu & Weyers [*Liu and Weyers, 1998*], and models for the prediction of crack width as a function of the volume of corrosion products [*Molina et al., 1993; Vu et al., 2005*]. Previous models described in the literature introduce a so-called *porous zone* or *corrosion accommodating region* around the reinforcement capable of accommodating corrosion products [*Liu and Weyers, 1998; Vu et al., 2005*]. Thus, according to this assumption, not all the corrosion products formed during the corrosion process contribute to the build-up of pressure in the concrete/steel interface. The properties of this corrosion accommodating region viz. thickness, porosity, etc. are of importance for the relationship between formation and propagation of cracks and the associated number of corrosion products. Consequently, since the properties of this corrosion accommodating region are unknown, it is possible to vary them in order to fit a proposed model to experimental data. Though numerous models concerning cracking of concrete cover due to reinforcement corrosion already exists, the models have not been operationalized for SLD

The objective of the present paper is to present a fracture mechanics based numerical model for the simulation of damage and cracking of cover concrete in reinforced concrete structures due to uniform reinforcement corrosion. Moreover, it is the objective of the paper to illustrate the applicability of such analyses for SLD of reinforced concrete structures making the use of limit states related to the corrosion propagation phase. Finally, the ability of such models to address Design issues such as the possible use of Fibre Reinforced Concrete (FRC) to increase durability is demonstrated.

The numerical model is a fracture mechanics based finite element (FE) model, with fracture mechanical properties based on the so-called effective cohesive relationship of concrete. The damage and cracking phases of the concrete cover are analysed by the use of the model for different combinations of concrete cover thickness, reinforcement diameter. The influence of the extent of the corrosion is the analysis itself. As previously explained, the end of the damage phase is defined as the time for which $W = W_{lim,d} = 50$ μm, whereas the end of the cracking phase is defined as the time for which $W = W_{lim,c} = 0.2$ mm, which is in line with the durability limit states suggested in [*Andrade et al., 1993*]. The limit state for the damage phase has been set to $W_{lim,d} = 50$ μm. This value is considered as an operational zero-value for such numerical simulations, as the exact transition from the un-cracked state to the cracked state is difficult to determine more accurately (convergence of the model).The model does not consider spalling of cover concrete since this phase is beyond the durability limit state of concrete, which is the main focus area of the present paper. The limit states proposed cannot be seen as stand-alone limit states, since the extent of corrosion required to form such cracks may reduce the mechanical properties, ie load-bearing capacity of the structure, significantly. Therefore a proper assessment of the load-bearing capacity of corroded, reinforced concrete structures has to be carried out in conjunction with these limit states.

Results from the numerical mechanical modelling in terms of the relation between damage and/or cracking of concrete cover and extent of uniform reinforcement corrosion causing formation of solid products at the steel-concrete interface can be related to time, by the use of Faraday's law. Hence, results presented in this paper can, as will be shown, be directly linked to SLD making the use of limit states associated with reinforcement corrosion operational. It is emphasized, that this is only applicable for uniform reinforcement corrosion and for the formation of solid corrosion products which is not the case for chloride-induced corrosion.

5.2 Model Description

The numerical model for the simulation of damage and cracking in concrete cover related to uniform corrosion of reinforcement embedded in homogenous defect-free concrete is presented in the following. The model simulates the expansion of corrosion products and the associated damage and cracking in the concrete cover for a semi-infinite concrete body assuming 2D plane strain and discrete crack formation.

Cracking of concrete covers due to reinforcement corrosion might be divided into two distinct phases, viz. the damage phase and the cracking phase, as illustrated in Figures 5.2 – 5.3, showing in Figure 5.2 the relationship between concrete surface crack width, W, and the change in un-constrained rebar radius, ΔR, (due to corrosion). In Figure 5.3 the change in ΔR is associated to different cracking configurations with

$\Delta R_{crit,c}$ denoting the radius change associated with the transition from the damage state to the cracking state.

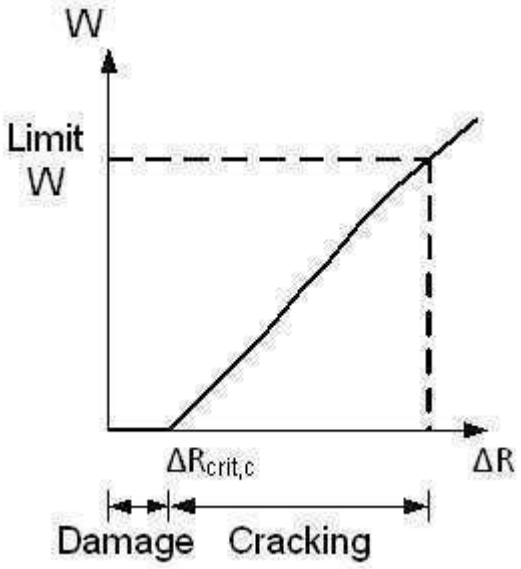

Figure 5.2 *Schematic of damage and cracking of concrete cover during the propagation phase. Inspired by [Vu et al., 2005].*

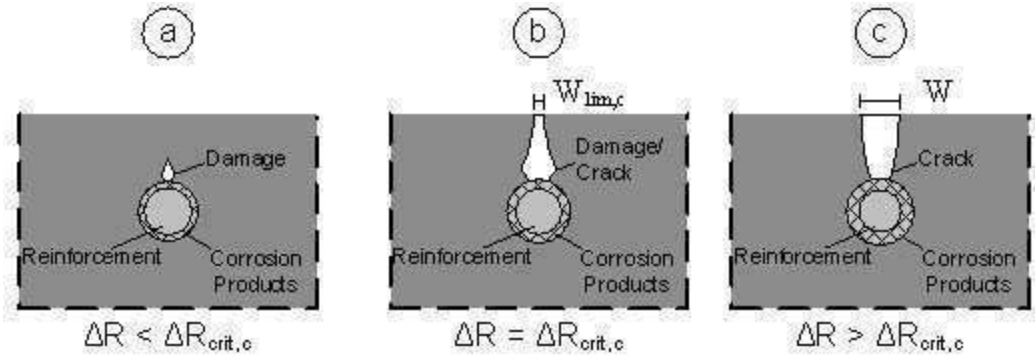

Figure 5.3 *Damage and cracking in a semi-infinite concrete body. a) $\Delta R < \Delta R_{crit,c}$ $W = 0$, b) Limit of damage phase, $\Delta R = \Delta R_{crit,c}$ $W = W_{lim,c}$ and c) Cracking $\Delta R > \Delta R_{crit,c}$ $W > W_{lim,c}$. The illustrations are not in scale.*

The damage is initiated at the concrete/steel interface. However, the damage has not reached the cover concrete surface, for $\Delta R < \Delta R_{crit,c}$, as illustrated in Figure 5.3a. The thickness of corrosion products increases as the corrosion process continues and eventually $\Delta R = \Delta R_{crit,c}$, as illustrated in Figure 5.3b. For $\Delta R = \Delta R_{crit,c}$ the end of the damage phase has been reached, ie the damage has reached the concrete surface. Once the damage has reached the concrete surface, the cracking phase has been initiated, and the crack continues to open for $\Delta R > \Delta R_{crit,c}$, cf. Figure 5.3c. Secondary radial cracks may be formed during the corrosion process. However, such cracks are not taken into consideration in the present model.

Furthermore the model described in the following does not account for a corrosion accommodating region around the reinforcement. Hence, all corrosion products

formed contribute to the build-up of pressure at the concrete/steel interface. Recent investigations [*Michel et al., 2011; Pease et al., 2012*] show that movement of corrosion products into the surrounding concrete can be significant, especially in the early stages of the corrosion process, while corrosion products tend to concentrate on or close to the rebar at later stages. Thus it is expected that the model presented furnishes a conservative estimate of the relationship between damage/cracking and the associated amount of corrosion products. Further details and descriptions of the model are given in the following.

5.2.1 Modelling Corrosion of Reinforcement

Reinforcement embedded in sound, "un-contaminated" concrete is thermodynamically passive due to the high alkalinity of concrete (~pH 13) [*Bertolini et al., 2004*]. However substances like Cl^- and CO_2 may ingress through the concrete cover leading to de-passivation of the reinforcement. Various types of corrosion products can be formed, dependent on primarily the oxygen and chloride availability. It is in this paper assumed that solid products are formed homogeneously around the reinforcement. Since the solid phase corrosion products take up more volume than the consumed steel, a pressure is built up on the concrete/steel interface due to the confinement by the surrounding concrete. The volume and linear expansion coefficients of some of the most common corrosion products potentially forming on embedded reinforcement are given in Table 5.1.

Table 5.1 *Expansion coefficients of selected common corrosion products. From [Caré et al., 2008].*

Identification	Chemical composition	η_{vol} [-]	η_{lin} [-]
Magnetite	1/3 Fe_3O_4	2.08	0.69
Hematite	½ Fe_2O_3	2.12	0.71
Goethite	α-FeOOH	2.91	0.97
Lepidocrocite	$Fe_2O_3 \cdot H_2O$	6.40	2.13

It is assumed that the corrosion products are homogeneous and isotropic and that the primary corrosion product is hydrated hematite ($Fe_2O_3 \cdot H_2O$). Within the present model, this expansion is modelled by the use of a fictitious thermal load, an approach also utilized by eg Molina et al. [*Molina et al., 1993*]. Modelling of the transformation from steel to corrosion products and the associated expansion of corrosion products is outlined in Figure 5.4.

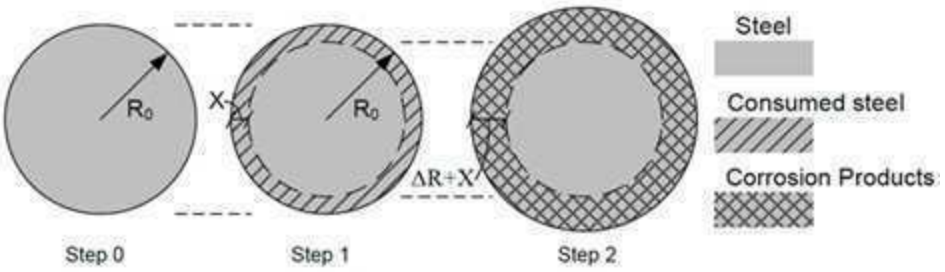

Figure 5.4 *Schematic illustration of modelling the expansion of corrosion products.*

Step 0) Reinforcement with initial radius, R_0, is modelled.

Step 1) A prescribed corrosion depth, X, is applied to the model, cf. Figure 5.4. The virgin steel bar is transformed into a two-phase domain, viz. steel and corrosion products with different material properties: The inner domain consists of steel, with Young's modulus and Poisson's ratio of steel, E_{st} and γ_{st} respectively, whereas the outer domain consists of corrosion products with the properties of the corrosion product investigated, E_{cor} and γ_{cor} respectively. Further a fictitious thermal expansion coefficient is assigned to the outer domain.

Step 2) A fictitious thermal load, T_{cor}, adjusted to the fictitious expansion coefficient and together corresponding to the linear expansion coefficient of the corrosion products, is applied to the outer domain. The thermal load leads to an increase in volume of the outer domain, viz. the corrosion products, cf. Figure 5.4.

The free expansion of the corrosion products shown in Figure 5.4 is hindered due to the confinement of the surrounding concrete. The pressure sustained by the confining concrete is illustrated in Figure 5.5.

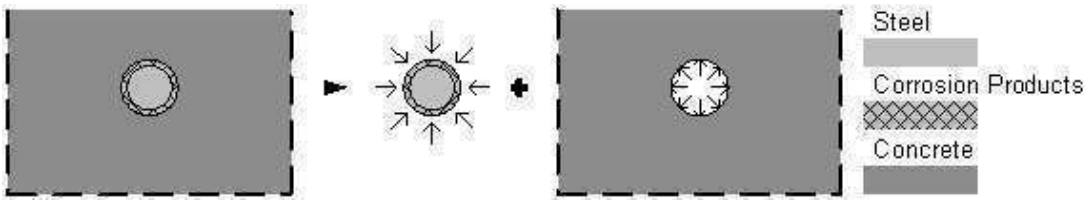

Figure 5.5 *Illustration of internal pressure due to the expansion of corrosion products. Inspired by Liu & Weyers [Liu and Weyers, 1998].*

The fictitious thermal, linear load applied to the outer domain appears from Eq. (5.1):

$$T_{cor} \cdot \alpha_{cor} = \eta_{lin} \tag{5.1}$$

where α_{cor} is the fictitious thermal expansion coefficient of the corrosion products.

The volume of the unconstrained corrosion products formed appears in Eq. (5.2):

$$V_{cor} = (1 + \eta_{vol}) \cdot V_s \tag{5.2}$$

where V_{cor} is the volume of corrosion products and V_S is the volume of steel consumed. The approximation used in Eq. (5.3) can be used for the connection between the unconstrained increase of the radius of the reinforcement, ΔR, and the corrosion depth, X:

$$\Delta R = \eta_{lin} \cdot X \tag{5.3}$$

Thus the thickness of the corrosion products is given by $X+X\cdot\eta_{lin}$ as shown in Figure 5.4.

5.2.2 Fracture Mechanical Model

The mechanical model for the damage and cracking of concrete cover is based on non-linear fracture mechanical theory and models damage and cracking in a 2D semi-infinite concrete body, assuming plane strain. The expansion of corrosion products described above results in damage and crack formation in the concrete cover, cf. Figure 5.3, and a debonding of the concrete/steel interface. The model is illustrated in Figure 5.6.

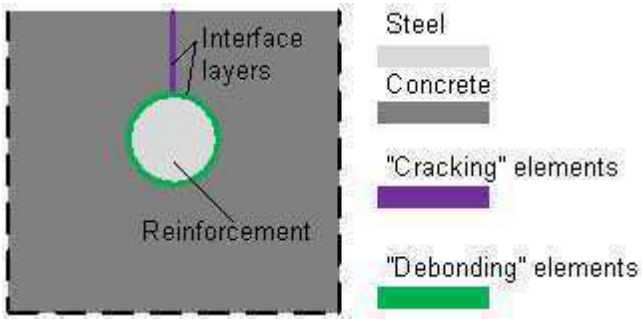

Figure 5.6 *Schematic of fracture mechanical model for simulation of damage and cracking.*

Zero-thickness interface elements are placed vertically through the concrete cover above the centre line of the reinforcement and on the circumference of the reinforcement, cf. Figure 5.6. The interface elements through the concrete cover model Mode I fracture, whereas the interface elements on the circumference of the reinforcement account for the debonding in the concrete/steel interface, which is governed by sliding and separation. Debonding is modelled by the use of Mode I elements with a reduced strength for the separation whereas the sliding is modelled by applying constant shear stiffness after cracking. The remaining part of the concrete body has been modelled assuming linear elastic properties.

The mechanical properties of the interface elements are described from Eq. (5.4):

$$\sigma = \begin{cases} \sigma_e(\varepsilon) = E_c \cdot \varepsilon & Pre-cracked\ state \\ \sigma_w(w) = -a_1 \cdot w \cdot f_t & Cracked\ state \end{cases} \tag{5.4}$$

where σ_e is the elastic stress, ε is the elastic strain, $\sigma_w(w)$ is the bridging stress as a function of the crack opening w, a_1 is the slope of the softening branch and f_t refers to either $f_{t,D}$ or $f_{t,C}$ for the debonding and cracking elements respectively. The principles of the cohesive law governing the mechanical properties of cracked concrete, cf. Eq. (5.4) are described in Figure 5.7.

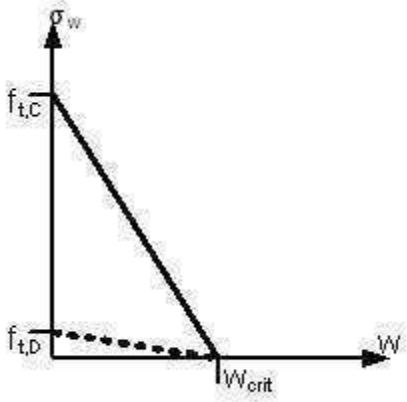

Figure 5.7 *Schematic of mono-linear softening curve of concrete.*

The cohesive laws for the cracking elements, and the debonding elements, are sketched in Figure 5.7 where w_{crit} refers to the critical crack opening of the concrete, for which no stress is transferred across the crack. As seen from Eq. (5.4) the mechanical response of the cracked concrete elements is simplified by the use of a decreasing linear function. For the modelling approach described later in this paper, it is assumed that the strength of the debonding elements, $f_{t,D}$, is 1/10 of the strength of the cracking elements, $f_{t,C}$. The value of $f_{t,D}$ is based on the assumption that the adhesion between the reinforcement and the confining concrete is significantly reduced due to the corrosion process. The fracture energy, G_f, is the energy dissipated per unit area in Mode I in the crack represented by Eq. (5.5):

$$G_f = \int_0^{w_{crit}} \sigma(w)dw \tag{5.5}$$

As the fracture energy given from Eq. (5.5) is not a sufficient measure for the toughness of concrete, [*Hillerborg et al., 1976*], the toughness of concrete is often described in terms of the characteristic length, l_{ch}, [*Rosselló et al., 2005*]. The characteristic length was introduced by Hillerborg [*Hillerborg et al., 1976*], and is defined by Eq. (5.6):

$$l_{ch} = \frac{E_c \cdot G_f}{f_t^2} \tag{5.6}$$

The FE-based cracking model was established and solved by the use of the commercial software DIANA. The problem was solved for plane strain. Damage and cracking were investigated by monitoring the horizontal displacement of nodes in the vertical interface, cf. Figure 5.6. The vertical interface consists of 100 elements, regardless of concrete cover thickness. The semi-infinite concrete body as well as the reinforcement domain has been modelled from quadrangular elements, utilizing a total of 2150-2772 nodes and 978-1280 elements depending on the geometry analysed, viz. concrete cover thickness, C, and reinforcement diameter, D.

The number of elements in the interface has proven sufficient. Selected results from an analysis of mesh convergence for FRC2, cf. Table 5.3, C = 60 mm and D = 20 mm are depicted in Figure 5.8.

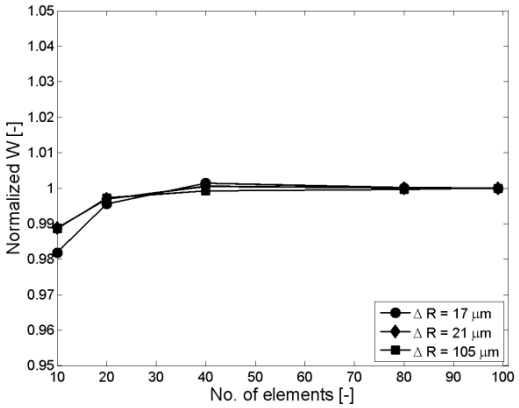

Figure 5.8 *Normalized results from analyses of mesh convergence.*

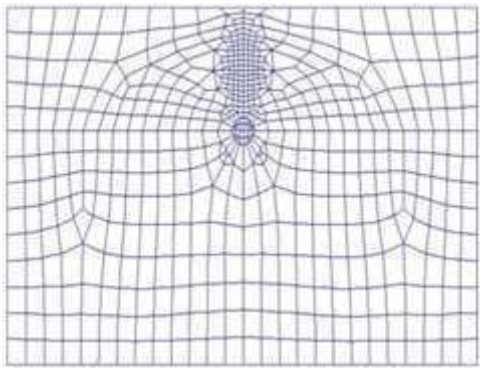

Figure 5.9 *Mesh for numerical simulations.*

The convergence analysis was carried out for 10, 20, 40, 80 and 100 elements in the interface. Results given in Figure 5.8 have been normalized with respect to the results for 100 elements. It is seen that maximum deviation is approx. 2% when increasing the number of elements in the vertical interface from 10 elements to 100 elements and changing the number of elements in the interface from 40 to 100 only affects the results with less than 2‰. Hence it is concluded, that the number of elements in the vertical interface is sufficient and it is actually possible to reduce the number of elements to optimize computational time without compromising the accuracy of the simulations significantly.

The mesh used for the numerical simulations is shown in Figure 5.9. It is seen that the mesh is significantly denser at the vertical interface in order to increase the accuracy of the numerical simulations. The measures of the semi-infinite concrete body are 100 mm on each side of the reinforcement, except from cover side, which has revealed to be sufficient.

5.2.3 Limitations for Numerical Simulations

The numerical model presented above has been used for the assessment of damage and cracking connected with uniform reinforcement corrosion in a semi-infinite concrete body. The authors are aware that uniform corrosion of embedded reinforcement is not to be expected in chloride exposed concrete structures. The term uniform refers to corrosion where the anodic and cathodic reactions take place close to each other and alternate as seen for example in carbonated concrete. The numerical model is time-independent, ie the model does not account for time-dependent properties of the concrete matrix eg creep. Additionally, the model is built on the assumption that the corrosion products do not precipitate into either the concrete matrix or the crack. Hence all corrosion products formed contribute to the build-up of pressure at the concrete/steel interface which reduces the time-to-cracking compared to the case where corrosion products can penetrate into the concrete matrix and/or the crack. Further it is assumed that the corrosion products are of hydrated hematite corresponding to a linear expansion coefficient of 2.1 when the steel is corroding.

Due to constraints in the FE-modelling, the minimum corrosion depth modelled is 2.5 μm.

The mechanical model is only capable of simulating damage and cracking in a pre-defined path, cf. Figure 5.6. However, the location of the pre-defined crack path, viz. vertically above the reinforcement through the concrete cover, is in accordance with experimental observations, eg [*Molina et al., 1993; Cabrera, 1996*]. Since the present framework for SLD of reinforced concrete structures is based on the formation of cracks in the concrete cover, secondary cracks which are formed subsequently to the crack through the concrete cover and not propagating to the concrete cover surface are not considered in the model.

Overall it is assumed that the numerical model presents a conservative estimate of the connection between extent of uniform corrosion of reinforcement and crack initiation, propagation and crack opening displacement at concrete surface. With this combined effect of the simplifications, of which some are on the safe side and some may be on the unsafe side, it is still possible to simulate the crack formation cf. Section 5.2.4 and this is the basis of the work provided in this paper.

5.2.4 Verification of Numerical Model

The numerical model presented above was verified against experimental data obtained by Vu et al. [*Vu et al., 2005*]. The experimental observations were carried out in an accelerated corrosion set-up applying a constant current, leading to a constant current density to the steel reinforcement, i_{cor} = 100 μA/cm^2. The applied current density is related to the amount of steel consumed by the use of Faraday's law, assuming no other causes for corrosion, uniform corrosion and 100% current efficiency:

$$X(t) = \frac{M_{Fe} \cdot i_{cor} \cdot \Delta t}{\rho_s \cdot n \cdot F} \tag{5.7}$$

where M_{Fe} is the molar mass of iron, i_{cor} is the corrosion current density, Δt is time, ρ_s is the density of steel, n is the valence of the corrosion product and F is Faraday's constant. As i_{cor} is the corrosion current normalized with the surface area it will be seen from Eq. (5.7) that assuming constant corrosion current, ie identical conditions for various reinforcement diameters, requires different time scales to form the same corrosion depth, X. Further information about the experimental investigations is given in [*Vu et al., 2005*].

Experimental results in terms of concrete surface crack width as a function of time as well as the corresponding numerical simulation are shown in Figure 5.10.

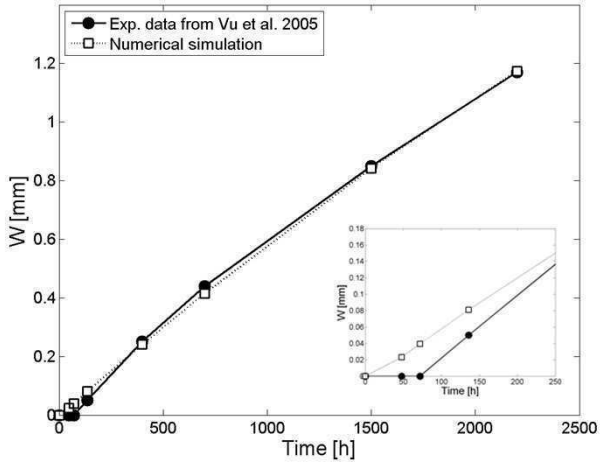

Figure 5.10 *Verification of numerical model with data from [Vu et al., 2005] showing concrete surface crack against time in accelarated tests and the corresponding numerical simulation.*

The verification of the numerical model shown in Figure 5.10 is carried out for E_c = 42.25 MPa, f_t = 3.94 MPa, D = 16 mm and η_{vol} = 2.94 obtained from [*Vu et al., 2005*]. Young's modulus of corrosion products has been set to E_{cor} = 2.1 GPa, which is in accordance with experimental observations obtained by Ouglova [*Ouglova et al., 2006*].

It is seen from Figure 5.10 that the numerical model is capable of simulating the experimental data well for crack widths larger than 0.2 mm. However, the time to cracking is underestimated when using the model compared to the experimental data, ie the numerical model presents a conservative approach to corrosion-induced cracking. This is caused by the limitations of the numerical model, ie all solid corrosion products formed contribute to the build-up of pressure at the concrete/steel interface as discussed previously.

The debonding at the concrete/steel interface is modelled with the assumption that the strength of the "debonding" elements, $f_{t,D}$, is one tenth of the cracking strength $f_{t,C}$. Sensitivity analyses of the numerical model not presented here have established that

the influence of $f_{t,D}$ on the damage and cracking is negligible. Thus, the results presented in this paper are not dependent on $f_{t,D}$.

5.3 Parameter Study

A parametric study is described in the following, studying the influence of various factors, covering geometrical as well as material aspects. Four key parameters have been varied:

- Reinforcement diameter
- Concrete cover thickness
- Tensile strength of concrete
- Fracture energy of concrete

Simulations are carried out for various extents of corrosion, ie corrosion depths, X.

The geometrical parameters, viz. reinforcement diameter and concrete cover thickness, and the material parameters, viz. tensile strength and fracture energy of concrete, are described in separate subsections in the following.

5.3.1 Geometrical Parameters

The range of concrete cover thicknesses and reinforcement diameters used for the numerical simulations are given in Table 5.2.

Table 5.2 *Range of geometrical parameters.*

Parameter	Identification	Min. value	Max. value	Unit
Concrete Cover Thickness	C	10	80	mm
Reinforcement Diameter	D	5	20	mm
Corrosion Depth	X	2.5	50	µm

The ranges of concrete cover thicknesses and reinforcement diameters given in Table 5.2 are within limits used for reinforced concrete structures in the civil infrastructure, depending on exposure conditions and structural purpose. The limits of corrosion depths given in Table 5.2 are negligible compared to the initial diameter of the reinforcement and thus it is assumed not sufficient to compromise the load-bearing capacity of a reinforced structure.

5.3.2 Concrete Material Properties

Two parameters, viz. tensile strength and fracture energy of concrete have been varied in order to quantify the influence of material properties on the damage and cracking of concrete covers due to uniform reinforcement corrosion. The fracture mechanical properties of the model, cf. Figure 5.6 are given in Table 5.3.

Table 5.3 *Concrete material properties investigated in numerical simulations.*

Identification	Concrete properties				Concrete/steel interface properties			
	$f_{t,C}$ [MPa]	w_{crit} [mm]	G_f [J/m^2]	l_{ch} [mm]	$f_{t,D}$ [MPa]	w_{crit} [mm]	G_f [J/m^2]	l_{ch} [mm]
PC1	2	0.2	200	1500	0.2	0.2	20	15000
PC2	4	0.2	400	780	0.4	0.2	40	7800
PC3	6	0.2	600	520	0.6	0.2	60	5200
FRC1	2	7.5	7500	58000	0.2	7.5	750	$58 \cdot 10^4$
FRC2	4	7.5	15000	29000	0.4	7.5	1500	$29 \cdot 10^4$
FRC3	6	7.5	22500	19000	0.6	7.5	2250	$19 \cdot 10^4$

The six combinations of concrete material properties given in Table 5.3 are divided into plain concrete (PC1-PC3) and fibre reinforced concrete (FRC1-FRC3). The cohesive relationship of plain concrete does not vary significantly and the critical crack width opening, w_{crit}, of plain concrete is within the range 0.1-0.4 mm dependent on eg *w/c* ratio and aggregate size [*Pease et al., 2007*]. However, the addition of even relatively small numbers of steel fibres changes the mechanical properties significantly [*Kazemi et al., 2007; Löfgren et al., 2008*]. Values given in Table 5.3 for the mechanical properties of FRC correspond to the addition of app. 0.5-1.0 vol-% of steel fibres and are comparable in terms of critical crack width, w_{crit}, with experimental data [*Löfgren et al., 2005*]. Thus, though data given in Table 5.3 is not obtained from specific experimental investigations, the parameters reflect typical properties of PC and FRC respectively.

5.3.3 Constants

Properties of the elastic domains, ie the virgin reinforcement steel, the corrosion products and the confining concrete without the interface layers are constant for all numerical simulations. The properties are given in Table 5.4.

Table 5.4 *Constants for elastic domains.*

Constant	Identification	Value	Unit
Young's modulus of steel	E_s	210	GPa
Young's modulus of concrete	E_c	31	GPa
Young's modulus of corrosion products	E_{cor}	2.1	GPa
Poisson's ratio of steel	γ_s	0.3	-
Poisson's ratio of concrete	γ_c	0.2	-
Poisson's ratio of corrosion products	γ_{cor}	0.2	-
Linear expansion coefficient of corrosion products	η_{lin}	2.1	-

Values for the properties of steel and concrete are typical values for those materials. The mechanical properties of corrosion products depend on the type of corrosion product, the conditions under which they are formed, eg availability of oxygen, confinement etc. Due to the obvious difficulties in measuring properties of confined corrosion products, the amount of available literature is sparse. The difficulties in assessing the properties of such corrosion products are further described in eg [*Chitty et al., 2005; Demoulin et al., 2010*] describing the development and the time-dependency of the formation of corrosion products in embedded steel. The mechani-

cal properties of corrosion products, viz. Poisson's ratio and Young's modulus, given in Table 5.4 are obtained by Ouglova [*Ouglova et al., 2006*], and Pease et al. [*Pease et al., 2012a*] have shown that these values are representative for solid corrosion products formed on embedded reinforcement and further that their influence on the deformations in the corroding reinforcement/concrete interface is relatively weak. The linear expansion of corrosion products corresponds to that of hydrated hematite, $Fe_2O_3 \cdot H_2O$, [*Caré et al., 2008*].

5.4 Results and Discussion

The numerical studies of reinforcement corrosion and associated damage and cracking of concrete cover are described in the following. Results are presented in terms of W, concrete surface crack width, and corresponding ΔR, viz. the increase in the radius of the embedded reinforcement caused by the expansion of the corrosion products, see Eq. (5.3). The section is divided into separate subsections treating damage and cracking of concrete cover respectively. The two limit states already described, viz. the end of the damage phase and crack width limit in the cracking phase, corresponding to $W = W_{lim,c}$ and $W = W_{lim,d}$ respectively are illustrated in Figure 5.11, showing W as a function of ΔR for $C = 60$ mm, $D = 5$ mm and concrete quality PC2.

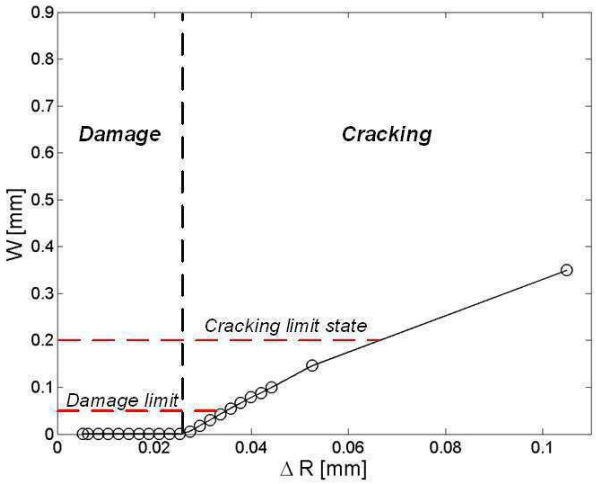

Figure 5.11 *Calculated crack width at surface, W, for C = 60 mm and D = 5 mm and PC2, as function of increase in radius of reinforcement ΔR. The limit stages for damage and cracking are illustrated in the figure.*

It is shown in Figure 5.11 that a non-negligible ΔR_{crit}, is required before the damage phase is exceeded, which is also illustrated in Figure 5.3. Subsequently, in the cracking phase, W at the concrete surface is almost a linear function of the increase in corrosion products. Similar results have been obtained for other values and combinations of C, D and concrete quality. This linear trend in the ΔR-W relationship during the cracking phase has been experimentally observed by eg Vu et al., [*Vu et al., 2005*] and described by Andrade et al., [*Andrade et al., 1993*].

5.4.1 Formation of Damage and Cracking in Concrete Cover

The damage and cracking of the concrete cover have been simulated for all geometries and combinations of concrete material properties given in Table 5.3. Damage and cracking in the concrete cover for C = 60 mm, D = 5 mm, and concrete quality PC2 for various values of the increase of the reinforcement radius are shown in Figures 5.12 – 13.

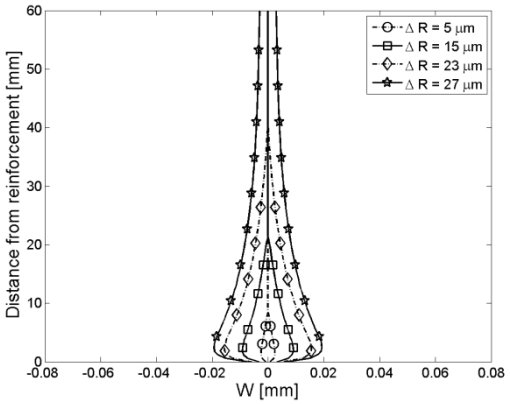

Figure 5.12 *Damage in cover, for D = 5 mm, C = 60 mm and PC2.*

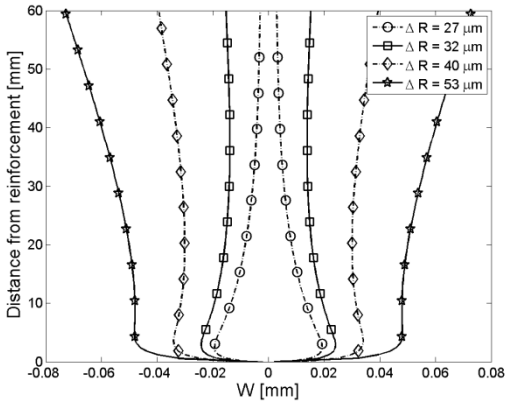

Figure 5.13 *Cracking in cover, for D = 5 mm, C = 60 mm and PC2.*

Similar plots have been obtained for other combinations of D, C and concrete quality.

Initially a closed crack, ie damage, is formed within the concrete cover, cf. Figure 5.12. Damage is formed for small values - but not negligible - of ΔR, cf. Figure 5.11 – 5.12. The damage front is propagated, as the expansion of the corrosion products increases and eventually the damage front reaches the concrete surface, cf. Figure 5.12, and the cracking phase has been reached. Once the cracking phase is reached, the crack opening at the concrete surface is increased rapidly as a function of ΔR, cf. Figure 5.13. The formation of a closed crack, which propagates from the surface of the reinforcement towards the concrete cover surface, has been experimentally observed by the application of x-ray equipment on corroding reinforcement embedded in concrete, eg Michel et al. [*Michel et al., 2011*].

5.4.2 The Damage Limit State

Damage and the associated ΔR have been investigated for various combinations of f_t, C, D and w_{crit}. The ranges of the parameter variation are given in Tables 5.2 and 5.3. The increase in the reinforcement radius required to reach the damage limit state, viz. ΔR_{crit}, depends on the concrete material properties and the geometry of the reinforced concrete body, ie reinforcement diameter and concrete cover thickness. In general, the simulations reveal that the limit of the damage phase, ie $W = W_{lim,c}$, has been reached for ΔR_{crit} = 13 - 46 μm for PC and ΔR_{crit} = 13 – 57 μm for FRC for 10 mm ≤ C ≤ 60

mm and 5 mm ≤ D ≤ 20 mm. The influence of the various parameters is seen from Figures 5.14 – 5.21.

5.4.2.1 The Influence of Concrete Tensile Strength

The critical increase in reinforcement radius, ΔR_{crit}, as a function of the tensile strength, f_t, is shown in Figures 5.14 – 5.15 for plain concrete (PC1-PC3) for D = 5 mm and D = 20 mm respectively.

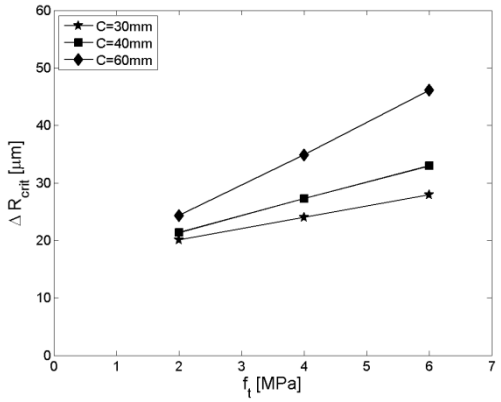

Figure 5.14 *ΔR_{crit} vs f_t for D = 5 mm, PC1-PC3.*

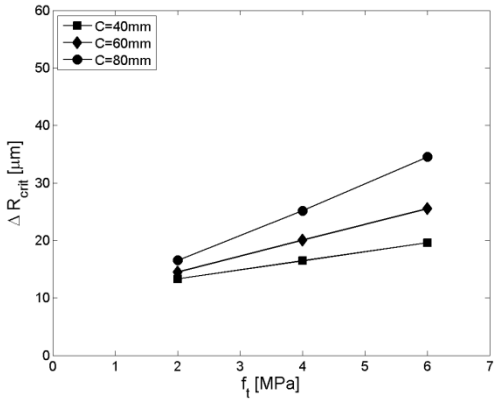

Figure 5.15 *ΔR_{crit} vs f_t for D = 20 mm, PC1-PC3.*

The same relationship, but for fibre reinforced concrete (FRC1-FRC3), is given in Figures 5.16 – 5.17 for D = 5 mm and D = 20 mm respectively.

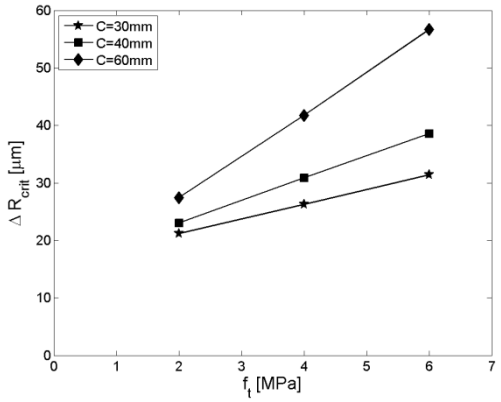

Figure 5.16 *ΔR_{crit} vs f_t for D = 5 mm, FRC1-FRC3.*

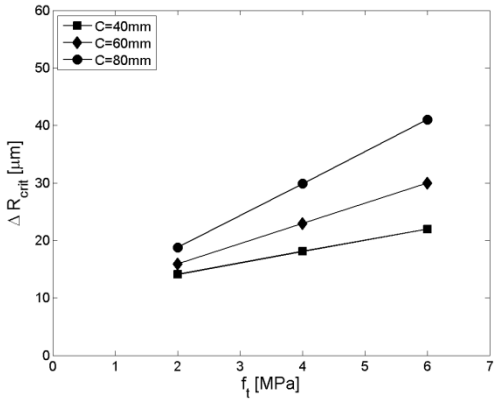

Figure 5.17 *ΔR_{crit} vs f_t for D = 20 mm, FRC1-FRC3.*

From Figures 5.14 – 5.17 it will be seen that there is a linear correlation between ΔR_{crit}, and f_t for C = 30 - 60 mm when D = 5 mm and C = 40 – 80 mm when D = 20 mm. For smaller covers the simulations do not reveal the same relationship. However, this is probably due to the limitations of the numerical model since the minimum corrosion depth in the numerical model is 2.5 μm, corresponding to $\Delta R \approx 5$ μm which is presumably greater than the critical increase of the reinforcement radius caused by the

corrosion process ΔR_{crit} for these smaller covers. Results for such small covers are not presented.

The linear correlation in the f_t - ΔR_{crit} relationship is valid for PC as well as FRC, cf. Figures 5.14 – 5.17. However, comparing the figures concerning PC (Figures 5.14 – 5.15) with the figures concerning FRC (Figures 5.16 – 5.17) it will be seen that the regression line for FRC lies higher compared to that of PC. This indicates that the propagation of the damage front is restrained when the fracture energy of the concrete matrix is increased.

5.4.2.2 The Influence of Fracture Energy

The influence of the fracture energy of the concrete matrix on the relationship between ΔR_{crit} and damage is seen from Figures 5.18 – 5.19 for D = 5 mm and D = 20 mm respectively for different concrete cover thicknesses.

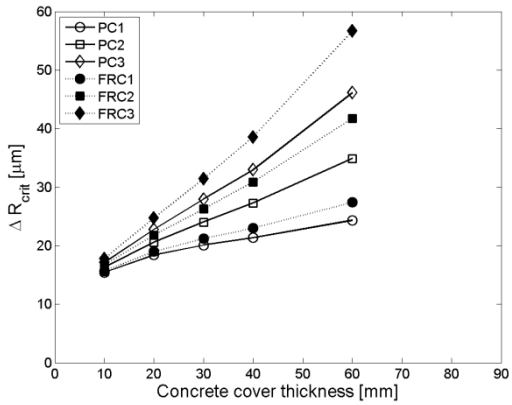

Figure 5.18 ΔR_{crit} *vs C for various* f_t *and* w_{crit}*, D = 5 mm.*

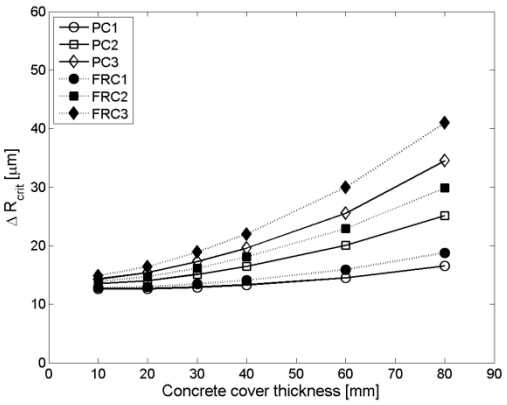

Figure 5.19 ΔR_{crit} *vs C for various* f_t *and* w_{crit}*, D = 20mm.*

As can be seen from Figures 5.18 – 5.19 the influence of increasing the fracture energy of the concrete matrix becomes more pronounced when the tensile strength is increased. As an example, the increase in ΔR_{crit} for C = 60 mm and f_t = 2 MPa is 17 % and 9 % for D = 5 mm and D = 20 mm respectively, whereas the increase for the same cover and diameters but with an increased tensile strength, f_t = 6 MPa, is 23 % and 17 % respectively. The increase in ΔR_{crit} between PC and FRC is an increasing function of the concrete cover thickness, cf. Figures 5.18 – 5.19. Hence, the geometrical influence of the concrete cover thickness is important. For small covers, the increase in ΔR_{crit} by shifting from PC to FRC is negligible, whereas the gain is quite significant for larger concrete cover thicknesses. The explanation of this phenomenon is as follows; for the smallest cover thicknesses, the cohesive stress associated with the end of the damage phase is almost constant (and equal to the tensile strength) due to the small crack openings for both PC and FRC. The result is little difference in resistance and ΔR_{crit} between the PC and FRC cases. For the largest concrete covers the cohesive stress at the end of the damage state is far from constant along the crack due to the larger crack openings while the stress is closer to constant in the FRC case because of

the more flat softening curve - thus giving rise to a significant difference in resistance and ΔR_{crit}.

5.4.2.3 The Influence of Reinforcement Diameter

The critical increase of the reinforcement radius required to reach the damage limit state varies with the diameter of the reinforcement. The critical increase of the radius of the embedded reinforcement at the damage limit state as a function of the reinforcement diameter is shown for various thicknesses of concrete cover for PC2 and FRC2 in Figures 5.20 – 5.21 respectively.

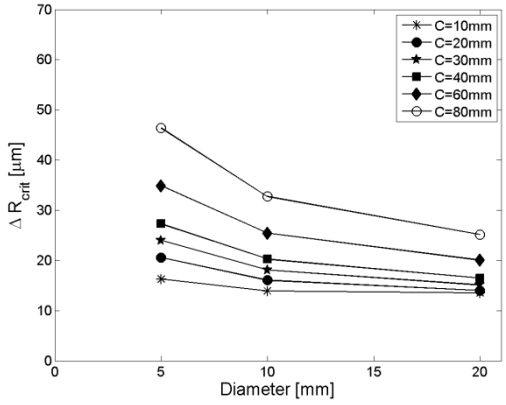

Figure 5.20 ΔR_{crit} *vs vs D for various C, PC2.*

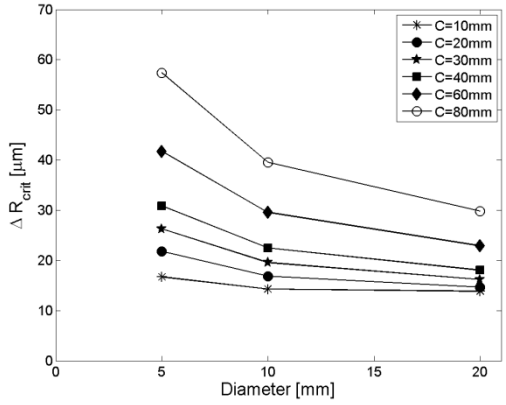

Figure 5.21 ΔR_{crit} vs D for various C, FRC2.

The influence of the reinforcement diameter on the critical increase of the reinforcement radius to reach the end of the damage phase is very limited for small covers, viz. almost the same corrosion depth initiates the crack at the concrete surface, cf. Figures 5.20 – 5.21. However, increasing the concrete cover thickness results in a more pronounced dependence between ΔR_{crit} and the reinforcement diameter. For all covers, the relationship between ΔR_{crit} and reinforcement diameter descends asymptotically, indicating that beyond a certain value of reinforcement diameter there is little variation in the ΔR_{crit} vs. D relationship.

5.4.3 The Cracking Limit State

Cracking of the concrete cover is investigated for the same parameters as the damage phase, viz. cover thickness, reinforcement diameter and concrete material properties, cf. Tables 5.2 and 5.3. The cracking limit state is illustrated in Figure 5.11. The cracking phase and the associated crack formation in the concrete cover are illustrated in Figure 5.13 whereas Figures 5.22 – 5.25 depict the opening at the concrete cover surface. Figure 5.13 illustrates the crack formation in the concrete cover when the damage front has reached the concrete cover surface. It will be seen that once the damage limit is reached, the crack mainly opens at the concrete surface when the radius of the reinforcement is increased.

The increase in reinforcement radius required to reach $W = W_{lim,c}$ as a function of concrete cover thickness and reinforcement diameter is shown in Figures 5.22 – 5.23 and Figures 5.24 – 5.25 respectively. Results from the numerical simulations reveal that the cracking limit state is reached for ΔR = 38 – 74 μm for PC and ΔR = 42 – 105 μm for FRC for 10 mm ≤ C ≤ 60 mm and 5 mm ≤ D ≤ 20 mm.

5.4.3.1 The Influence of Fracture Energy

The influence of the fracture energy, G_f, to reach the cracking limit state, is analyzed in the following and illustrated as a function of the concrete cover thickness for all concrete qualities investigated and D = 5 mm and D = 20 mm in Figures 5.22 – 5.23.

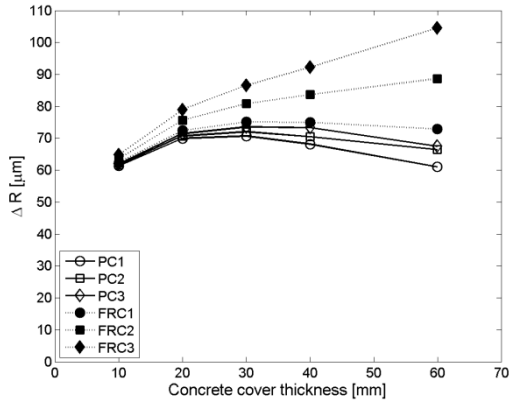

Figure 5.22 *ΔR (for $W = W_{lim,c}$) vs C, D = 5 mm.*

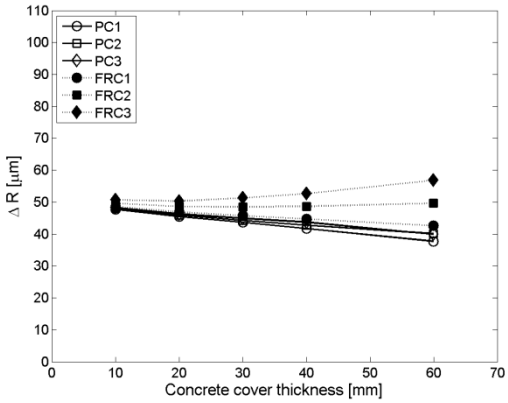

Figure 5.23 *ΔR (for $W = W_{lim,c}$) vs C, D = 20 mm.*

For PC the required ΔR to exceed the cracking limit state shows only a negligible variation as a function of the cover thickness for constant reinforcement diameter, cf. the hollow symbols in Figures 5.22 – 5.23. Comparing PC and FRC with the same tensile strength it is seen that the addition of fibres results in a substantial increase in ΔR for D = 5 mm, cf. Figure 5.22. Moreover, this effect gets more pronounced for increasing tensile strength of the concrete matrix. For D = 20 mm, the increase in ΔR is not as clear as for D = 5 mm, when comparing PC and FRC, cf. Figure 5.23.

5.4.3.2 The Influence of Reinforcement Diameter and Cover Thickness

The influence of geometry, viz. reinforcement diameter and concrete cover thickness are shown in Figures 5.24 – 5.25. The figures illustrate the relationship between ΔR for $W = W_{lim,c}$ and the diameter of reinforcement for C = 10 – 80 mm, for PC2 and FRC2, respectively.

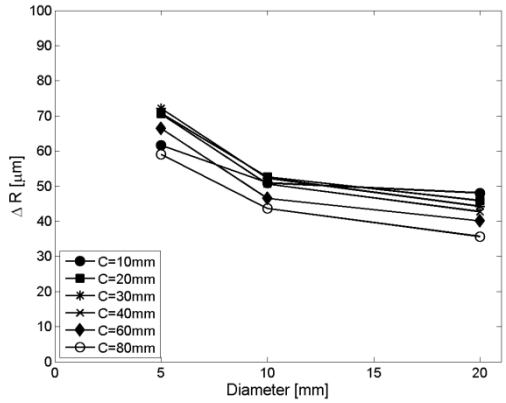

Figure 5.24 *ΔR (for $W = W_{lim,c}$) vs D for various C, PC2.*

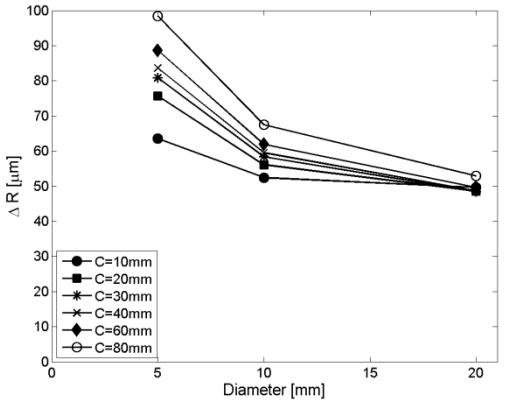

Figure 5.25 *ΔR (for $W = W_{lim,c}$) vs D for various C, FRC2.*

For all cover thicknesses, regardless of concrete fracture energy the relationship descends asymptotically. However, it will also be seen for PC, ie Figure 5.24, that ΔR for D = 5 mm increases up to C = 30 mm, after which ΔR is a decreasing function of the concrete cover thickness. The same tendency is seen for D = 10 mm. The same phenomenon is not seen for FRC, since a larger cover always results in an increased ΔR, cf. Figure 5.25.

The increased cover thickness, which was seen as beneficial with regard to the damage limit, cf. previous section and Figures 5.20 – 5.21, is a drawback with regard to the cracking limit state, cf. Figures 5.24 – 5.25. For PC, the possibility of redistributing stresses is overshadowed by the geometrical aspect of the increased cover thickness, ie an increased rotation of the cover concrete around the rotation point (the center of the reinforcement), because the crack opening due to rotation is proportional to the concrete cover thickness. For FRC, the beneficial effect of an increased concrete cover thickness is not cancelled out by the increased rotation connected with the increasing concrete cover thickness due to the favorable stress distribution over the length of the crack even for large crack openings.

Comparing the required ΔR for $W = W_{lim,c}$ (W = 0.2 mm) for the same tensile strength, but different fracture energy, viz. w_{crit} = 0.2 mm and w_{crit} = 7.5 mm cf. Figures 5.24 – 5.25 respectively it will be seen that ΔR is increased significantly when the fracture energy is increased and that this effect, as discussed before, is larger for larger concrete covers.

Assuming that service life of reinforced concrete structures can be defined as being exceeded when a given W is reached, cf. considerations given above, service life can be increased significantly by increasing the fracture energy of the concrete matrix, assuming the same exposure conditions, transport properties of the concrete matrix, etc. for PC and FRC.

5.4.4 General Discussion

Results obtained for the simulation of damage and cracking in concrete covers due to uniform reinforcement corrosion, presented in the previous sections are discussed in the following, and comparisons with data from the literature are given, in the relevant passages.

Results from the numerical simulations have been presented in terms of W and corresponding ΔR. The reason for this is twofold: 1) The pressure built up at the concrete/steel interface is directly connected to the expansion of the corrosion products. Relative changes in volume of the most common corrosion non-chloride containing products formed on embedded steel varies significantly, within a range of 2-6.3 cf. Herholdt et al. [*Herholdt et al., 1985*] and Table 5.1. Thus the corrosion depth is not a direct measure for the increase of the radius of the reinforcement and the corresponding build-up of pressure and therefore it is the authors' opinion that it is a misleading to present crack formation with the associated corrosion depth. 2) The simulations are carried out for only one type of corrosion products. In this case there is a unique relationship between X and ΔR. However, since most results in the literature concerning cracking in concrete covers are presented in terms of W and the assumed corresponding corrosion depth, comparisons of simulated data and experimental data from the literature will be based upon the corrosion depth (X).

Experimental results reported in the literature concerning the cracking phase are given in terms of assumed corrosion depth, X_{crit}, and related W at concrete surface, eg X_{crit} = 15-18 μm for $W \approx 50$ μm [*Andrade et al., 1993*], X_{crit} = 10-65 μm for $W \approx 50$ μm [*Vu et al., 2005*] and X_{crit} = 15-30 μm for $W \approx 50$ μm [*Alonso et al., 1998*] for varying tensile strength of concrete, f_t, concrete cover thickness, C, and reinforcement diameter, D. Values of X_{crit} given above have not been measured but are calculated based on Faraday's law, Eq. (5.7), assuming 100% current efficiency, which may be incorrect and thus used as an explanation for the scatter of the results. However, the results given in the literature corresponds well with results from the numerical simulations presented here.

The model has been compared with accelerated experimental results presented in [*Vu et al., 2005*], cf. Figure 5.10. The numerical model reproduces the experimental results very accurately. Though there is a limit in the prediction of the end of the damage phase, viz. W = 50 μm, it is the authors' opinion that there is a good correlation between numerical and experimental results. The difference in the prediction of the end of the damage phase may be reduced if a corrosion accommodating region [*Michel et al., 2011*] around the reinforcement is taken into account. However, more knowledge gained from experimental observations about the properties of this corrosion accommodating region is required before it can be implemented in the model, cf. explanation given later in this section.

The formation of damage and the associated cross section reduction are in themselves not sufficient to affect the overall integrity of the structure as the corrosion depth is within the range of a few microns to create damage. Hence, in the light of that it may be possible to extend the service life by including the damage phase in the service life. Note that this only refers to uniform reinforcement corrosion and not other types of corrosion like eg pitting corrosion, which might have fatal consequences to the overall integrity and functionality of a reinforced concrete structure, even for relatively limited corrosion attacks.

The existence of the corrosion accommodating region is recognized by the authors. However, since the properties of this corrosion accommodating region, eg porosity and thickness have not been thoroughly described on the basis of experimental observations, it was omitted for the numerical simulations. Furthermore, it is assumed that the corrosion products do not precipitate into the crack formed.

Finally, it is noted that the model does not take the formation of secondary cracks into account. Thus the expansive nature of the corrosion products contributes only to the formation of the crack vertically through the concrete cover which may result in an underestimation of the corrosion products required to open up the crack to a predefined W.

Taking those three limitations of the model into account, the numerical model presents a conservative estimate of the duration of the damage phase and the $\Delta R - W$ relationship for the cracking phase. Thus the results presented here forms a conservative approach.

5.4.5 Interpretation of Data in an SLD Perspective

The results in terms of the increase of the reinforcement radius required to reach the damage or cracking limit state are related to time in order to set them into a service life perspective. According to eg Bertolini et al. [*Bertolini et al., 2004*], corrosion rates can be divided into six categories. The corrosion rate is governed by, among other things, the oxygen availability, concrete resistivity and extent of carbonation. The categories are given in Table 5.5.

Table 5.5 *Categorization of corrosion current densities. Modified from [Bertolini et al., 2004].*

Corrosion rate category	Corrosion current density [mA/m^2]
Negligible	< 0.2
Low	0.2 - 0.4
Moderate	0.4 - 0.9
Intermediate	0.9 - 4.3
High	4.3 - 8.5
Very high	> 8.5

Assuming uniform corrosion and constant current rate, the $X(t)$ can be calculated based on Faraday's law, cf. Eq. (5.7).

As previously mentioned, the damage phase is reached for $\Delta R = 13 - 46$ μm and $\Delta R = 13 - 57$ μm for PC and FRC, respectively (10 mm ≤ C ≤ 60 mm and 5 mm ≤ D ≤ 20 mm). Results for the time required to form this thickness of corrosion products are given in Table 5.6, along with corresponding C and D.

Table 5.6 *Time to reach damage limit, based on Faraday's law.*

				Required time [Years]				
	ΔR limits [μm]	C [mm]	D [mm]	Low $i_{cor} = 0.2$ [mA/m^2]	Moderate $i_{cor} = 0.4$ [mA/m^2]	Intermediate $i_{cor} = 0.9$ [mA/m^2]	High $i_{cor} = 4.3$ [mA/m^2]	Very high $i_{cor} = 8.5$ [mA/m^2]
PC	13	10	20	6.5	2.6	1.3	0.3	0.1
	46	60	5	23	9.2	4.6	0.9	0.5
FRC	13	10	20	6.5	2.6	1.3	0.3	0.1
	57	60	5	29	11	5.7	1.1	0.6

From Table 5.6 it appears that it is possible to increase the service life of a reinforced concrete structure by at least a year in most situations by accepting the damage phase as part of the service life. For low corrosion rates, the gain in service life, on the assumptions previously given is significant: up to 29 years, cf. Table 5.6.

The time required to reach the cracking limit state, is calculated in the same way as above, assuming uniform corrosion, constant corrosion rate and no movement of corrosion products into the crack or the bulk concrete. The required increase of the radius of the embedded reinforcement to reach the cracking limit state is, as already explained, $\Delta R = 38 - 74$ μm for PC and for FRC $\Delta R = 42 - 105$ μm for 10 mm ≤ C ≤ 60 mm and 5 mm ≤ D ≤ 20 mm. Results are given in Table 5.7.

Table 5.7 *Time to reach cracking limit state, based on Faraday's law.*

				Required time [Years]				
	ΔR limits [μm]	C [mm]	D [mm]	Low $i_{cor} = 0.2$ [mA/m^2]	Moderate $i_{cor} = 0.4$ [mA/m^2]	Intermediate $i_{cor} = 0.9$ [mA/m^2]	High $i_{cor} = 4.3$ [mA/m^2]	Very high $i_{cor} = 8.5$ [mA/m^2]
PC	38	60	20	19	7.6	3.8	0.8	0.4
	74	30	5	37	15	7.4	1.5	0.7
FRC	42	60	20	21	8.4	4.2	0.8	0.4
	105	60	5	53	21	11	2.1	1.1

The results given in Table 5.7 indicate that the service life of a reinforced concrete structure can, under certain conditions, be increased significantly allowing cracks up to $W = 0.2$ mm in the cover concrete, assuming that the cracks do not influence the corrosion rate. Furthermore, it is worth noticing that the gain in time is significant comparing FRC with PC, viz. approximately 50%, comparing maximum values of ΔR of PC and FRC respectively in Table 5.7.

5.5 Conclusions

Cracking of concrete cover due to uniform reinforcement corrosion has been investigated by the use of an FE model based on the fictitious crack model. Simulations have been carried out for various combinations of concrete cover thickness, reinforcement diameter, and concrete material properties to identify governing parameters for damage and subsequent cracking of the concrete cover. Based on the investigation, it is concluded:

- Results from the numerical model compare well with experimental observations from the literature. However, the time to cracking is underestimated by the numerical model.
- The tensile strength of the concrete is the most important parameter with regard to the damage limit state.
- Increasing the concrete cover thickness always increases the ΔR associated with reaching the damage limit state.
- Increasing the concrete cover thickness only increases the ΔR associated with the cracking limit state, if the fracture energy is high – with a low fracture energy increasing the cover thickness can lead to a reduced ΔR due to geometrical effects associated with the crack opening profile.
- Increasing the fracture energy has little effect on the ΔR associated with the damage limit state due to the small crack openings associated with this state.
- Increasing the fracture energy extends the ΔR associated with the cracking limit state.

The paper presents simplified analyses of the results from the mechanical model and sets them into SLD perspectives. Based on these calculations, significant service life may be gained by allowing the formation of small cracks in the concrete cover. Estimates given in the paper show up to 37 years of additional service life if cracks up to $W = 0.2$ mm are allowed in the concrete cover for PC. This gain in service life can be increased by an additional 50% if the cover consists of FRC compared to PC.

5.6 Future Work

Based on the results, discussions and conclusions presented it is suggested to couple the numerical mechanical model with a model for the formation of corrosion cells on embedded reinforcement as shown by eg Michel et al., [*Michel et al., 2010a*]. Establishing a link between fracture mechanical models and electrochemical models would be the next step towards operational SLD models including the propagation phase. However, before the model could be used within such an SLD framework it should be verified with more experimental data.

A link between the changed transport properties of the concrete due to the formation of cracks and the corrosion rate of embedded reinforcement should be established in future work, in order to establish a more realistic link between reinforcement corrosion and the width of corrosion-induced cracks.

Given that the corrosion accommodating region around the reinforcement plays a significant role in the time to cracking it is of importance to clarify experimentally the properties of the corrosion accommodating region. Hence, it is suggested that experimental observations concerning, among other things, the influence of w/c ratio, concrete composition, reinforcement diameter and corrosion rate on the properties of the corrosion accommodating region should be carried out. The experimental observations should be carried out as non-destructive measurements, eg x-ray measurements and accompanying inverse analysis of results as done by Michel et al. [*Michel et al., 2011*].

Moreover, the mechanical properties of corrosion products under confinement should be analyzed experimentally to verify the value used for the present work.

Finally, models for the impact of cross sectional reduction on the structural performance should be developed to cover chloride-induced corrosion where inhomogeneous corrosion and formation of different types of corrosion products is likely to occur.

Acknowledgements

The first author gratefully acknowledges the full financial support of the PhD project “Application of Fibre Reinforced Concrete in Civil Infrastructure” by the Danish Agency for Science, Technology and Innovation, COWI A/S, DTU, Bekaert NV, Grace and the Danish Road Directorate. The second author acknowledges the financial support from Femern Bælt A/S, Sund & Bælt Holding A/S, and the Danish Agency for Science, Technology and Innovation.

Chapter 6

Case Studies

This chapter contains two case studies on corrosion of embedded reinforcement bars. The case studies concern numerical simulations of corrosion of reinforcement embedded in either plain concrete (PC) or SFRC, uncracked and cracked, using results presented in Chapters 2-4. The aim of this chapter is to set the results presented in Chapters 2-4 into perspective showing the relevance of these results with regard to reinforcement corrosion.

The numerical simulations are carried out using finite element (FE) based, electrochemical models recently developed at the Department of Civil Engineering at the Technical University of Denmark, [*Michel, 2013*]. This chapter contains background information about the numerical modelling approaches used for the case studies whereas detailed descriptions of the models are available in [*Michel, 2013*].

The case studies cover the following scenarios:

- Case Study 1: Corrosion propagation in uncracked concrete
- Case Study 2: Corrosion initiation and corrosion propagation in cracked concrete

In both case studies, the corrosion rate during the propagation phase is calculated and presented in terms of the average corrosion current density, $i_{cor,av}$. According to Bertolini et al. [*Bertolini et al., 2004*] the corrosion rate can be categorized into six categories, as shown in Table 6.1:

Table 6.1 *Categorization of corrosion rate and corresponding corrosion depth. After [Bertolini et al., 2004].*

Corrosion category	Corrosion depth [μm/year]	Average corrosion current density [μA/cm^2]
Negligible	< 2	< 1.7
Low	2 - 5	1.7 - 4.3
Moderate	5 - 10	4.3 - 8.5
Intermediate	10 - 50	8.5 – 43
High	50 - 100	43 – 86
Very high	> 100	> 86

The corrosion depths presented in Table 6.1 are calculated from the average corrosion current densities by the use of Faraday's law (Eq. 5.7), assuming 100% current efficiency in the corrosion process (10 μA/cm^2 = 11.7 μm/year). In both case studies the categorization presented in Table 6.1 will be used for discussing the results, ie evaluating the intensity of the calculated average corrosion current densities.

6.1 Case Study 1 – Uncracked Concrete

6.1.1 Aim and Scope

The aim of this case study is – through numerical simulation – to quantify the influence of depassivated or corroding, electrically conducting steel fibers (hereafter referred to as conductive steel fibers) on the corrosion rate of reinforcement embedded in un-cracked concrete. The study is a worst case scenario where all fibers present are considered conducting. In the study the presence of conducting steel fibers is expressed solely through their influence on (average) electrical resistivity as described by the results presented in Chapter 2 concerning the electrical resistivity of PC and SFRC at various degrees of humidity. The study first determines the average corrosion current density as a function of the electrical resistivity and the anode to cathode area-ratio. Secondly, the results are interpreted in terms of the effect of presence of conductive fibers at varies degrees of humidity and this effect is compared with the effect of temperature in order to put the results into perspective. Finally the results are summarized and discussed.

The numerical simulations are limited to non-transient conditions, assuming no exchange of heat and moisture with the surroundings and a constant anode to cathode ratio. The impact of the anode to cathode ratio is evaluated running the numerical model repetitively with various input values-

Though data used for the electrical resistivity of different concrete types under different humidity conditions has been obtained from AC measurements it is assumed to be representative for the DC electrical resistivity.

6.1.2 Model Description

The corrosion current density (corrosion rate) of the embedded steel is determined from Ohm's law, Eq. (6.1). For the numerical simulations it is assumed that the resistivity of the electrolyte is pre-defined.

$$i_{cor} = \rho^{-1} \frac{\partial E}{\partial n} \tag{6.1}$$

In Eq. (6.1) i_{cor} is the corrosion current density, ρ is the electrical resistivity of the electrolyte (concrete), n is the direction normal to the surface of the embedded reinforcement, and E is the potential. The resistivity of the electrolyte (concrete) is considered constant throughout the concrete domain. It is assumed that there is electrical charge conservation in the electrolyte and that the conductivity of the electrolyte is isotropic, ie the potential distribution is governed by Laplace's equation, Eq. (6.2).

$$\nabla^2 E = 0 \tag{6.2}$$

The current density, anodic or cathodic, can be described by the Butler-Volmer equation given in Eq. (6.3):

$$i = i_0 \cdot exp(\Psi) \tag{6.3}$$

where

$$\Psi = \ln(10) \cdot \left(\frac{E - E_0}{b}\right) \tag{6.4}$$

In Eqs. (6.3) – (6.4) the anodic or cathodic current density is denoted i, i_0 is the anodic or the cathodic exchange current density, E_0 is the equilibrium potential (anodic or cathodic) and b is the tafel constant, which is defined as

$$b = \ln(10) \cdot \left(\frac{R \cdot T}{z \cdot \alpha \cdot F}\right) \tag{6.5}$$

where R is the gas constant, T is the temperature, z is the valence, α is the so-called symmetry factor and F is Faradays constant.

To account for polarisation resistance due to the lack of oxygen, which affects the cathodic process, the Butler-Volmer equation, Eq. (6.3), is rewritten according to eg [*Böhni, 2005*] for the cathodic current density:

$$i = i_0 \cdot exp\left(\frac{1 - \Psi}{1 + i_0/i_{lim} \cdot \Psi}\right) \tag{6.6}$$

where Ψ is defined in Eq. (6.4) and i_{lim} is the limiting corrosion current density.

In this case study, the anodic current density, ie the corrosion current density, is calculated from Eq. (6.3) whereas the cathodic current density is calculated from Eq. (6.6) accounting for the polarisation resistance.

The kinetics of the corrosion process are affected by the temperature, cf. eg [*Bardal, 2004*]. To take this phenomenon into consideration the anodic and cathodic current densities as calculated from Eqs. (6.3) and (6.6), respectively, are re-evaluated using the proposal given in [*Tanaka and Tamamushi, 1964*], see Eq. (6.7). The anodic and cathodic current densities at the reference temperature are denoted $i_{0,ref}$ in Eq. (6.7):

$$i_{0,T} = i_{0,ref} \cdot exp\left[\left(\frac{\alpha \cdot z \cdot F \cdot E_0}{R}\right) \cdot \left(\frac{1}{T_{ref}} - \frac{1}{T}\right)\right] \tag{6.7}$$

where, $i_{0,T}$ is the exchange current density at temperature T and $i_{0,ref}$ is the exchange current density (anodic or cathodic) at the reference-temperature T_{ref}. The corrosion

current density-distribution is averaged along the length of the anodic site to determine the average corrosion current density, $i_{cor,av}$.

6.1.3 Model Geometry

The 2D model shown in Figure 6.1 was used for the numerical simulations.

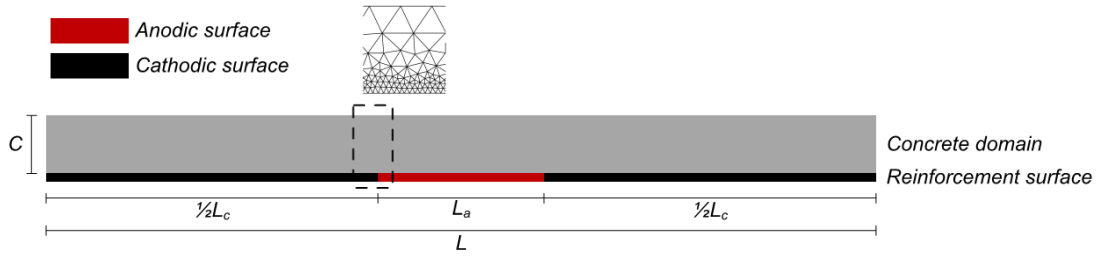

Figure 6.1 *Illustration of the model-geometry applied for Case Study 1 (the figure is not in scale). A zoom of the mesh applied for the framed area is shown.*

In Figure 6.1 L_a and L_c denote the length of the anode and the cathode, respectively ($L = L_a + L_c$).

The traditional reinforcement bar is modelled as a surface, ie a discretization of the lower horizontal side of the concrete domain with electrochemical boundary conditions as for steel. The current densities, ie the cathodic and the anodic (corrosion), of the reinforcement are calculated from Eqs. (6.3) – (6.7). Triangular elements are applied for the mesh of the FE simulations, and as seen from Figure 6.1 the mesh-density is largest at the reinforcement surface to refine the numerical calculations. The maximum element size used for the mesh is 25 mm, and 50 elements are applied to the anodic surface, for all sizes of the anodic site investigated in this study. In total, the model consists of approx. 800 triangular elements and solving for approx. 12000 degress of freedom. The dimensions of the model-geometry presented in Figure 6.1 are presented in Table 6.2.

Table 6.2 *Dimensions of model for numerical simulations of Case Study 1.*

Model parameter	Symbol	Unit	Value
Length	L	m	2
Concrete cover thickness	C	mm	60
Anode to cathode ratio	A/C	-	0.1 – 1.0

6.1.4 Input

Input for the model covers variations of the electrical resistivity of the concrete. Moreover, the temperature and the anode to cathode ratio are varied for the numerical simulations. The range of each of the parameters varied in this case study is given in Table 6.3 along with constant values describing the electrochemical boundary conditions of the reinforcement, etc.

Table 6.3 *Modeling parameters for Case Study 1.*

Model parameter	Symbol	Unit	Value	Reference
Electrical resistivity	ρ	Ωm	10 - 7000	-
Temperature	T	K	273 - 313	-
Faradays constant	F	C/mol	96485	[*Bardal, 2004*]
Valence	z	-	2	[*Bardal, 2004*]
Cathodic equilibrium potential	$E_{0,c}$	V_{SCE}	0.16	[*Ožbolt et al., 2011*]
Anodic equilibrium potential	$E_{0,a}$	V_{SCE}	-0.78	[*Ožbolt et al., 2011*]
Cathodic exchange current density	$i_{0,c}$	A/m^2	$6.25 \cdot 10^{-6}$	[*Ožbolt et al., 2011*]
Anodic exchange current density	$i_{0,a}$	A/m^2	$1.88 \cdot 10^{-4}$	[*Ožbolt et al., 2011*]
Gas constant	R	J/mol·K	8.314	-
Anodic Tafel constant	b_a	V/decade	0.06	[*Ožbolt et al., 2011*]
Cathodic Tafel constant	b_c	V/decade	0.16	[*Ožbolt et al., 2011*]
Limiting current density	i_{lim}	A/m^2	1	[1)]
Reference temperature	T_{ref}	K	293	-

[1)] This value of the limiting current density was chosen assuming that sufficient oxygen for the corrosion process will be available

The range of the electrical resistivity used for the numerical simulations is based on values observed from AC measurements of the electrical resistivity of PC and SFRC reported in Chapter 2. The observed values of the electrical resistivity of PC and SFRC corresponds to T = 20°C, which is set as the reference temperature in the numerical simulations. The impact of changes in the temperature on the corrosion rate is calculated applying Eq. (6.7) as described in Section 6.1.2.

6.1.5 Results

The results of the parameter study are presented in Figure 6.2 providing a surface plot of the relationship between $i_{cor,av}$ and the parameters varied, ie the electrical resistivity, and the anode to cathode ratio at T = 20°C.

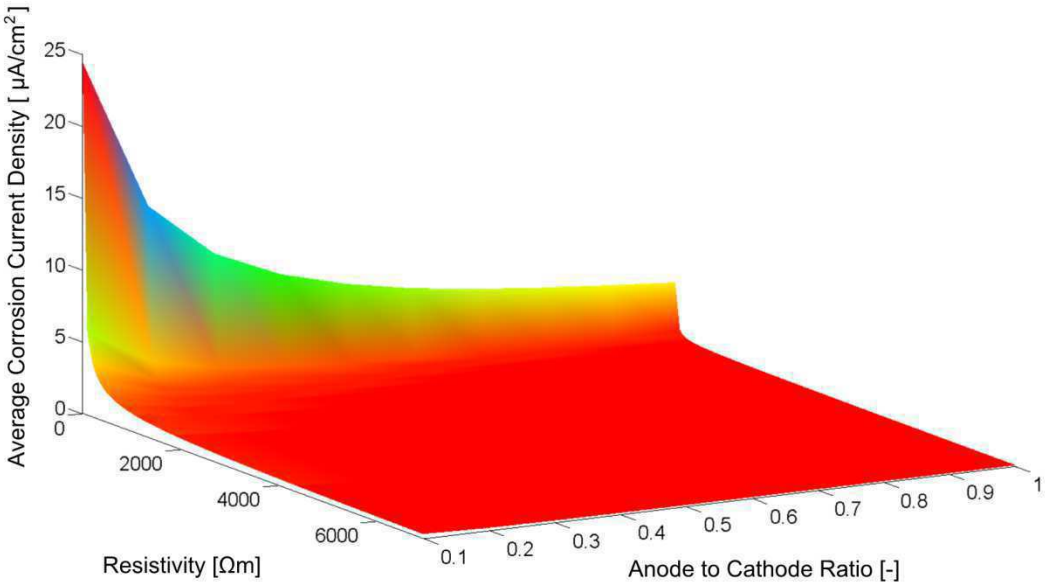

Figure 6.2 *Surface plot of the average corrosion current density as function of electrical resistivity and anode to cathode ratio at T = 20°C.*

It will be seen from the results presented in Figure 6.2 and the corrosion-categorization provided in Table 6.1 that the corrosion rate can be considered *negligible* for an electrical resistivity greater than approx. 1000 Ωm regardless of the anode to cathode ratio at T = 20°C. For lower values of the electrical resistivity, ie below approx. 1000 Ωm, the corrosion rate cannot be considered *negligible*, see Table 6.1, and the average corrosion current density is largely affected by the electrical resistivity. For values of the electrical resistivity moving towards zero it will be seen from Figure 6.2 that the average corrosion current density is highly affected by changes in the electrical resistivity.

Moreover, it will be seen from Figure 6.2 that the corrosion current density is also controlled by the anode to cathode ratio. The results presented in Figure 6.2 are in accordance with expectations, viz. a reduced anode to cathode ratio results in an increased corrosion current density, for a pre-defined value of the electrical resistivity. The impact of the anode to cathode ratio is not assessed any further in the following, since its role on the corrosion current density can be separated from the role of the electrical resistivity, which is the focus area of the case study.

6.1.6 Interpretation of Results

Data presented in Chapter 2 concerning the electrical resistivity of PC and SFRC (0.5 vol.-% and 1.0 vol.-%) for selected moisture conditions (RH = 45%, RH = 75% and saturated) at T = 20°C is applied to interprete the impact of conductive steel fibres and the moisture content of the concrete on the corrosion rate of embedded reinforcement. Data adapted from Chapter 2, viz. the average of the measured electrical resistivity and the standard deviation is given in Table 6.4 (data corresponds to Series C in Chapter 2).

Table 6.4 *Experimentally obtained values of the electrical resistivity of concrete (PC and SFRC), see Chapter 2.*

Material	Unit	RH = 45 %		RH = 75 %		Saturated	
		Avg.	St. dev	Avg.	St. dev	Avg.	St. dev
PC	[Ωm]	5894	397	445	86	172	3
SFRC (0.5 vol.-%)	[Ωm]	349	95	64	18	46	8
SFRC (1.0 vol.-%)	[Ωm]	106	52	33	17	21	3

It will be seen from a comparison of Figure 6.2, Table 6.1 and Table 6.4 that the average corrosion current densities (and the corrosion rate) corresponding to the measured values of the electrical resistivity are non-*negligible* (apart from the average corrosion current density corresponding to the measured value of the electrical resistivity of PC at RH = 45%).

The categorization of the corrosion-rate (Table 6.1) is presented in selected figures in the following, for easy identification of the corrosion categories.

6.1.6.1 Impact of Moisture

The impact of changes in the moisture content of the concrete on the average corrosion current density of embedded reinforcement is illustrated in Figure 6.3. Results presented in Figure 6.3 are calculated from the average electrical resistivity ± the standard deviation. The input for the numerical simulations presented in the figure, ie the electrical resistivity correspond to the electrical resistivity of PC at T = 20°C.

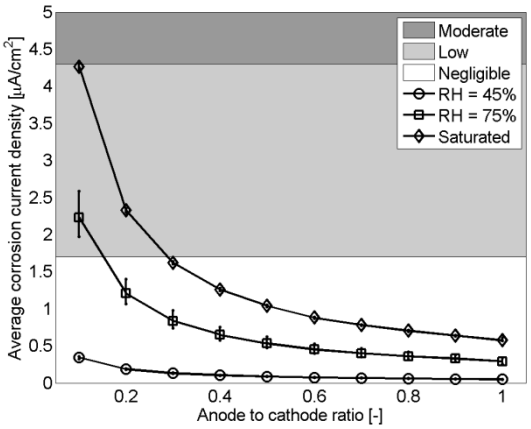

Figure 6.3 *Average corrosion current density, $i_{cor,av}$, as a function of the anode to cathode ratio (input data corresponds to average measured data ± the standard deviation for PC at T = 20°C at various moisture conditions).*

It appears from Figure 6.3 that the average corrosion current density is changed by a factor of approx. 6, comparing the average corrosion current density for RH = 45% and RH = 75%, regardless of the anode to cathode ratio. According to Table 2.7, these relative humidities correspond to a moisture content of 2.3 wt,-% and 3.7 wt.-%, respectively.

Comparing the average corrosion current densities corresponding to the electrical resistivity of PC at RH = 75% and saturated, it appears from Figure 6.3 that the average corrosion current density is changed by a factor of approx. 2 for all anode to cathode ratios studied. The moisture content of these two conditions correspond to 3.7 wt.-% and 5.0 wt.-% for RH = 45%, cf. Table 2.7.

The absolute difference in moisture content from RH = 45% to RH = 75% and RH = 75% to saturated is approx. the same, viz. 1.3 wt.-%, cf. Table 2.7. As would be expected, the impact on the electrical resistivity (and thereby the average corrosion current density) is changed remarkably as the relationship between the moisture content and the electrical resistivity of concrete is non-linear and the largest influence is seen for relatively dry concrete [*Hötte, 2003*].

For all anode to cathode ratios and conditionings simulated, the calculated corrosion rate is categorized as either *low*/*negligible*.

6.1.6.2 Impact of Conductive Steel Fibres

The average corrosion current density for the average electrical resistivities presented in Table 6.4 are presented in Figure 6.4. For each conditioning, the average corrosion current density is calculated based on the average value of the electrical resistivity measured for each material, ie PC or SFRC (0.5 vol.-% and 1.0 vol.-%). Additionally, for each conditioning the range of the average corrosion current density per material is presented. This range of the average corrosion current density is calculated from the average electrical resistivity ± the standard deviation for each material and represented with errors bars. The same axes have been used for all figures to ease comparision of graphs in different figures.

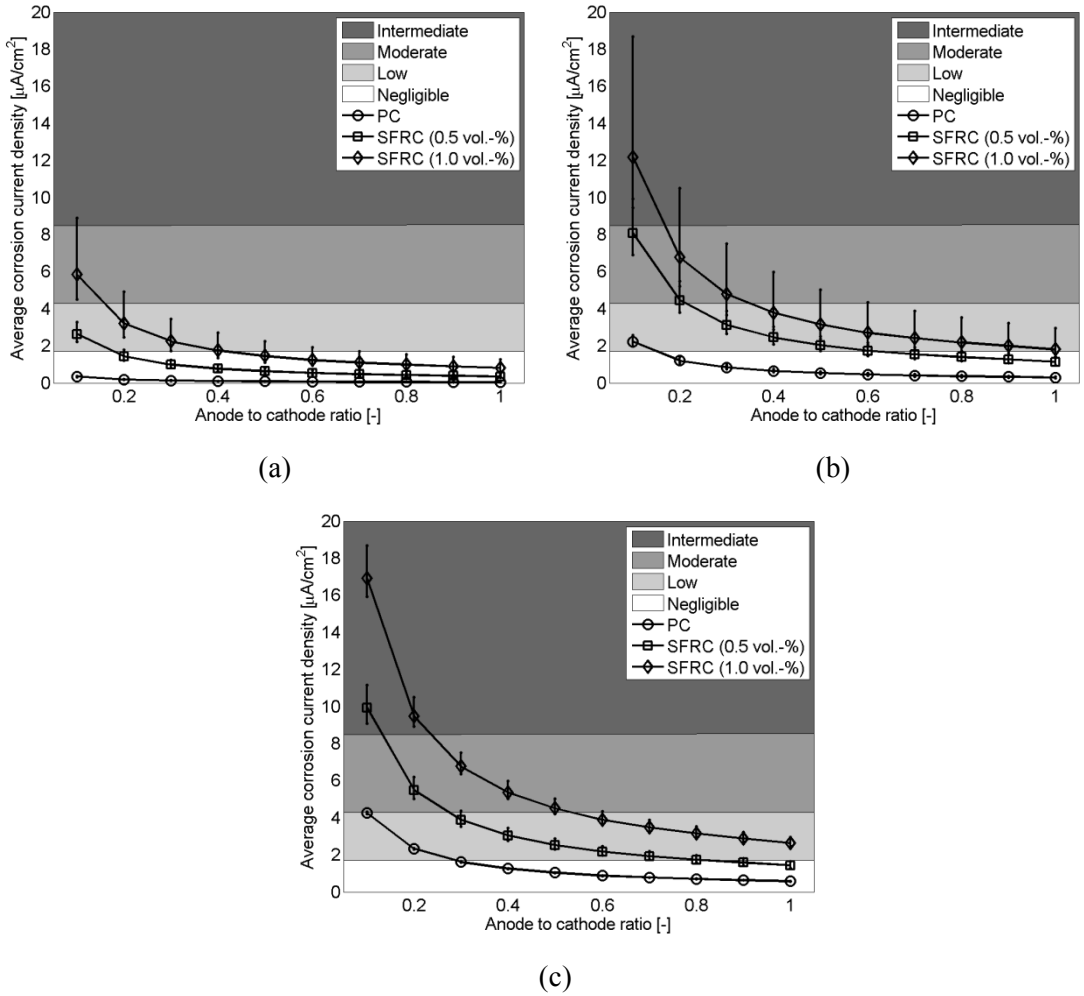

Figure 6.4 *Average corrosion current density, $i_{cor,av}$, as a function of the anode to cathode ratio. Input data corresponds to average measured data ± the standard deviation for PC, SFRC (0.5 vol.-% and 1.0 vol.-%), at T = 20°C and various conditionings. (a): RH = 45%. (b): RH = 75%. (c): saturated conditions.*

The results presented in Figure 6.4 are normalized with the average corrosion current density for PC in Table 6.5, to illustrate the relative impact on the average corrosion current density of the fibres at the conditionings investigated.

Table 6.5 *Normalized average corrosion current density (for all anode to cathode ratios) for all materials and conditionings investigated.*

	Unit	PC	SFRC (0.5 vol.-%)	SFRC (1.0 vol.-%)
RH = 45%	[-]	1	~7	~17
RH = 75%	[-]	1	~4	~6
Saturated	[-]	1	~2	~4

The results presented in Table 6.5 indicate that the impact of conductive steel fibres on the average corrosion current density due to their change of the electrical resistivity is reduced when the moisture content is increased.

For a low moisture content (concrete conditioned to RH = 45%, Figure 6.4a) the relative impact of conductive steel fibres is large. However, the average corrosion current density is still relatively small and for SFRC (1.0 vol.-%) the corrosion rate category is *low*/*moderate* (compared to the corrosion rate of PC which can be categorized as *negligible*). It will be seen from Figure 6.4b that the average corrosion current density at RH = 75%, in PC corresponds to a *negligible*/*low* corrosion rate. The average corrosion current density for SFRC, 0.5 vol.-% as well as 1.0 vol.-%, is higher, and can be categorized as *low*/*intermediate*, depending on the fibre volume content and the anode to cathode ratio. Finally, for saturated concrete the corrosion rate is categorized as *low* in PC and *low*/*intermediate* for SFRC (0.5 vol.-% and 1.0 vol.-%).

6.1.6.3 Impact of Temperature

The impact of the temperature on the average corrosion current density is illustrated in Figure 6.5. The figure presents the average corrosion current density, $i_{cor,av}$, as a function of the anode to cathode ratio ($\rho \approx 450$ Ωm).

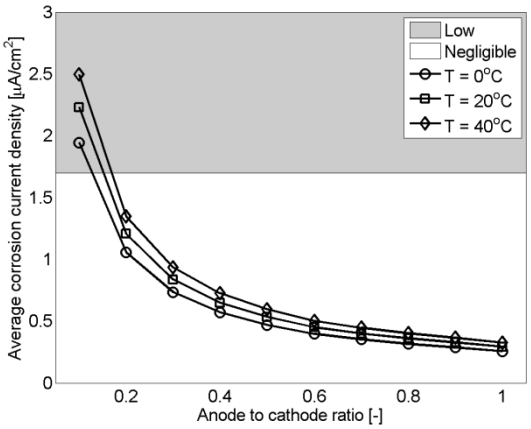

Figure 6.5 *Average corrosion current density, $i_{cor,av}$, as a function of the anode to cathode ratio for $\rho \approx 450$ Ωm.*

It will be seen from Figure 6.5 that the lower the temperature, the lower the average corrosion current density, $i_{cor,av}$, which is in accordance with the apriori knowledge that increased temperatures increase the corrosion rate as described in eg [*Bertolini et al., 2004*]. Similar observations have been observed for other values of the electrical

resistivity investigated as part of this case study, though not reported here. The maximum relative increase in the average corrosion current density within the range of the parameters investigated herein, cf. Table 6.3, is less than 50% when increasing the temperature from T = 0°C to T = 40°C. Thus, compared to the other parameters affecting the electrical resistivity, as discussed above, the impact of the temperature on the corrosion rate is minor.

6.1.7 Summary

Based on the results presented in Section 6.1.6 it is summarized:

- For values of the electrical resistivity above approx. 1000 Ωm the corrosion rate can be categorized as *negligible*.
- For values of the electrical resistivity below 1000 Ωm the average corrosion current density is non-*negligible*. This range of the electrical resistivity corresponds to the values measured for PC and SFRC (0.5 vol.-% and 1.0 vol.-% by the use of AC at 126 Hz.), see Chapter 2.
- Considering the measured values of the electrical resistivity of PC, the corresponding corrosion rate can be categorized as *negligible*/*low*, depending on the conditioning of the concrete.
- For SFRC (0.5 vol.-%) the corrosion rate can be categorized as *low*/*intermediate* depending on the conditioning of the concrete, whereas the corrosion rate of SFRC (1.0 vol.-%) is categorized as *low*/*intermediate*. Hence conductive steel fibres (corresponding to depassivated or corroding steel fibres) potentially increase the corrosion rate from *low* to *intermediate* in saturated conditions.
- The largest relative difference in the average corrosion current between PC and SFRC is observed for concrete with a low moisture content. The corrosion rate for low moisture contents, ie conditioned to RH = 45% is categorized as *low*/*moderate*.
- An increase in the temperature results in an increasing average corrosion current density. However, compared to the influence of moisture and/or conductive steel fibres, the impact of the temperature is considered subordinate.

It is stressed that the scenario where all steel fibres conduct current relates to a scenario where all fibres are depassivated. As previously presented (Chapter 1), this scenario is somewhat hypothetical. In practical applications utilizing combined reinforcement systems this would correspond to a scenario where the traditional reinforcement presumeably has suffered from corrosion for some time, since the fibres are more corrosion resistant than traditional reinforcement, see descriptions of corrosion-resistance of traditional reinforcement bars and steel fibres in Chapter 1.

6.2 Case Study 2 – Cracked Concrete

6.2.1 Aim and Scope

The aim of this case study is to quantify the impact of steel fibres on corrosion initiation and propagation of reinforcement embedded in cracked concrete. The scope of this case study covers the influence of cracks and mechanically induced debonding along the concrete/steel interface on chloride-induced corrosion of reinforcement embedded in concrete (PC or SFRC). A parametric study on the influence of the crack width at the concrete surface and the length of debonding along the concrete/steel interface on initiation and propagation of reinforcement corrosion is carried. The results of the numerical simulations are compared to the experimental observations presented in Chapter 4.

The numerical simulations are transient in order to simulate corrosion initiation and propagation. However, it is assumed that the material properties of the concrete, eg the electrical resistivity, are constant throughout the simulated time. Thus it is assumed that the steel fibres remain passive (non-conducting), ie the chloride concentration is below the chloride threshold level of the steel fibres.

6.2.2 Model Description

The numericl model presented in Chapter 3 is used for determination of the load-induced cracking and debonding of PC and SFRC and the corrosion process is modelled using the same approach as for Case Study, see Section 6.1.2.

The modelling approach including assumptions, boundary conditions and equations used for simulating the transport of chlorides through the concrete cover towards the reinforcement are presented in the following. Initially the boundary conditions concerning chloride-induced corrosion assigned to the reinforcement bar are described.

The corrosion process, is modelled using the approach used in Case Study 1. In this case study, the reinforcement bar is initially, ie at time $t = 0$, electrochemically passive having cathodic boundary conditions throughout the length of the reinforcement bar. Reinforcement corrosion is initiated when the chloride level in an element at the level of the reinforcement bar, C, reaches the chloride threshold level, c_{crit}. The boundary conditions at the surface of the reinforcement, are described as follows:

Cathodic boundary conditions: $C < c_{crit}$ and $i = i_c$,

Anodic boundary conditions: $C \geq c_{crit}$ and $i = i_a$,

where i_c and i_a are the cathodic and anodic polarisation curves, respectively. The chloride threshold of embedded reinforcement is controlled by the properties at the concrete/steel interface, eg cracks and voids, moisture content of the concrete, cement/binder type, etc. An overview of the influencing factors is provided eg by Angst

et al. [*Angst et al., 2009*], showing that the chloride threshold may attain values in the range 0.04 – 8.3 wt.-% Cl/wt.-% cem. Experimental observations presented by Buenfeld et al. [*Buenfeld et al., 2004*] show that the chloride threshold is largely affected by voids and/or defects, eg separation at the concrete/steel interface. Thus, for the numerical simulations presented in the following, various values of the chloride threshold are assigned to the surface of the reinforcement accounting for voids at the concrete/steel interface:

$$c_{crit} = c_{crit}(x) \tag{6.8}$$

where

$$c_{crit}(x) = \begin{cases} c_{crit,deb} \text{ for } 0 < x \leq l_{sep} \\ c_{crit,bon} \text{ for } x > l_{sep} \end{cases}$$

and $c_{crit,deb}$ is the chloride threshold assigned to the debonded surface of the reinforcement, $c_{crit,emb}$ is the chloride threshold of the bonded surface of the reinforcement, x is the horizontal coordinate along the reinforcement, see Figure 6.6, and l_{sep} is the length of the separated/debonded area.

For the numerical simulations, the chloride threshold at the debonded surface of the reinforcement is constant, $c_{crit,deb}$ = 0.1 wt.-% Cl/wt.-% cem., whereas the chloride threshold for the bonded surface of the reinforcement is varied linearly from 0.1 wt.-% Cl/wt.-% cem. at $x = l_{sep}$ to 1.0 wt.-% Cl/wt.-% cem. at the end of the reinforcement. The linear variation of the chloride threshold along the bonded surface of the reinforcement is applied to account for the impact of possible micro-defects at the concrete/steel interface closest to the debonded area. The chloride threshold assigned along the reinforcement surface is illustrated in Figure 6.8 for half the length of the domain shown in Figure 6.6 (right side of the domain).

Reinforcement corrosion is induced by Cl^- through the concrete cover. The surface chloride concentration, ie the chloride load from the environment, is considered constant throughout the time of simulation, and the transport of chlorides through the concrete cover is determined by solving Fick's 2nd law:

$$\frac{\partial C}{\partial t} = D(x,y)\frac{\partial^2 C}{\partial y^2} \tag{6.9}$$

where y is the vertical distance from the surface, C is the chloride concentration, t is the time and $D(x,y)$ is the chloride transport coefficient (diffusion coefficient).

To account for the differences in chloride transport properties of cracked and uncracked concrete the concrete volume is divided into three domains, viz. the bulk domain (uncracked concrete), the cracked domain (cracked concrete), and the

debonded domain (cracked concrete along the reinforcement surface). Fick's 2nd law is used for simulations of chloride ingress in the uncracked domain as well as the cracked domains of the concrete and each domains has different values of the chloride transport coefficient assigned.

The amount of literature on chloride transport properties of concrete is large and covers uncracked concrete eg [*Tang, 1996; Song et al., 2008*] and cracked concrete eg [*Rodriguez and Hooton, 2003; Pease, 2010*] and literature cited therein. However, for cracked concrete there appears to be limited information concerning the correlation between the crack width and the chloride transport properties. Additionally, such a correlation is influenced by, among other factors, the moisture content of the concrete, the binder composition and the morphology of the cracks, among other factors, which further complicates the formulation of such a correlation. In this case study, a simplified approach is used to account for the correlation between the chloride transport properties and the crack width as described in the following. The approach used for assigning different values to the chloride transport coefficients of the uncracked as well as the cracked and debonded domains is inspired by the work of Pease, see eg [*Pease, 2010; Pease et al., 2011*].

The chloride transport coefficient in the bulk domain, D_{bulk}, is constant assuming homogenous, defect-free conditions. In the cracked domain, (blue domain in Figure 6.6), the chloride transport coefficient is assumed linearly decreasing from the concrete surface to the level of the reinforcement. The value of the chloride transport coefficient at the concrete surface is denoted $D_{crack,surf}$, whereas the chloride transport coefficient for this crack at the level of the reinforcement (origo of the coordinate system shown in Figure 6.6) is denoted $D_{crack,reinf}$. The chloride transport coefficient of the debonded domain (red domain in Figure 6.6) varies linearly from the value $D_{crack,reinf}$ at the origo of the coordinate system shown in Figure 6.6 to the value D_{bulk} at the end of the debonded length. The approach for the description of the chloride transport coefficient in the debonded domain accounts for changed transport properties along the debonded length as a result of the change in separation at the concrete/steel interface. Finally it is noted that the same value of the electrical resistivity of all three domains is used in the numerical model.

The geometry of the three domains of the concrete volume is described in the following along with the geometry of the model. The model is used repetitively to cover the parametric study.

6.2.3 Model Geometry

The 2D domain used for the numerical simulations is illustrated in Figure 6.6.

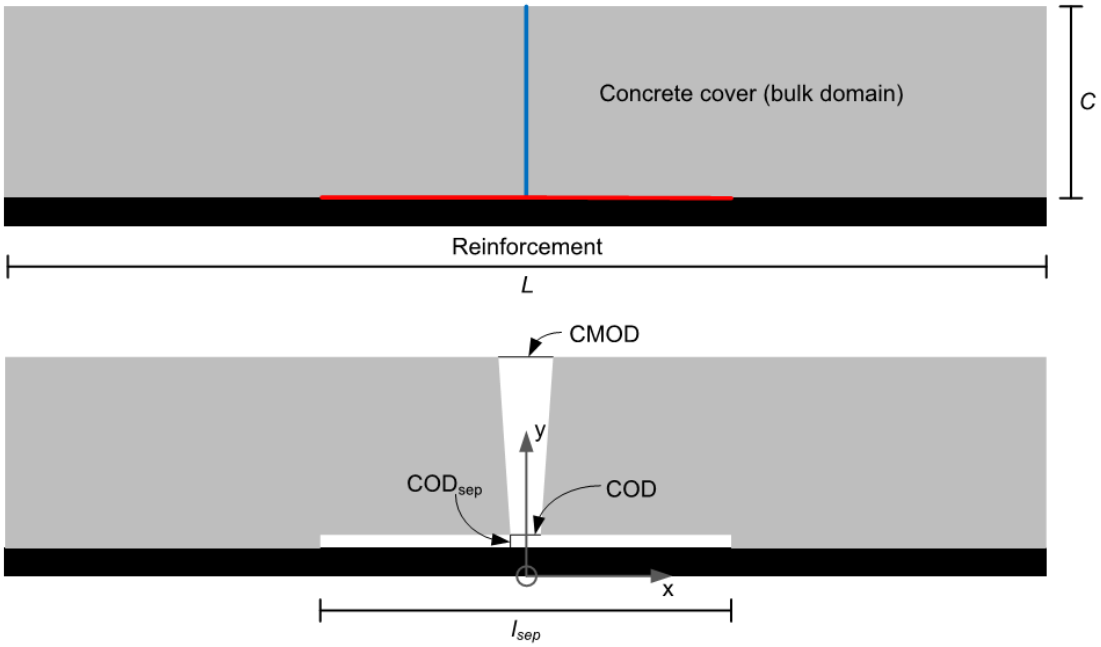

Figure 6.6 *Top: Illustration of the model-geometry applied for the numerical simulations of Case Study 2. Bottom: Illustration of the cracked domain and the debonded domain. The figures are not in scale.*

The blue and red lines in the top figure of Figure 6.6 illustrate the cracked domain and the debonded domain, respectively, the grey area is the bulk domain and the black area is the reinforcement domain. The concrete cover thickness (C) and length (L) of the model shown in Figure 6.6 are given in Table 6.6.

Table 6.6 *Dimensions of model for numerical simulations of Case Study 2.*

Model parameter	Symbol	Unit	Value
Length	L	m	0.65
Concrete cover thickness	C	mm	60

The geometry of the 2D domain correspond to the concrete cover-part of the model used for simulations of load-induced cracking and debonding presented in Chapter 3 and the specimens used for electrochemical experiments presented in Chapter 4.

The reinforcement is modelled as a discretization of the lower horizontal side of the concrete domain with electrochemical boundary conditions as for steel, ie the same approach as used for Case Study 1, see Section 6.1.3. The current densities (anodic and cathodic) of the reinforcement are calculated from Eqs. (6.3) – (6.7).

A simplified description of the geometry of the cracked domain is applied for the numerical simulations, viz. a wedge-shaped crack, cf. the bottom figure of Figure 6.6. The maximum crack width is at the concrete surface, CMOD, whereas the minimum crack width is at the level of the reinforcement, COD. The crack width is assumed lin-

early decreasing from the surface to the level of the reinforcement. The debonded domain is modelled assuming constant separation, COD_{sep}, throughout the debonded length of the reinforcement, l_{sep}, see Figure 6.6.

Due to symmetry around the vertical centre line of the model shown in Figure 6.6, only half of the domain is used for the numerical simulations, in order to reduce the computational time. Results presented in the following therefore relates to one half of the domain. The mesh used for the cracked domain, and parts of the bulk domain and debonded domain is illustrated in Figure 6.7.

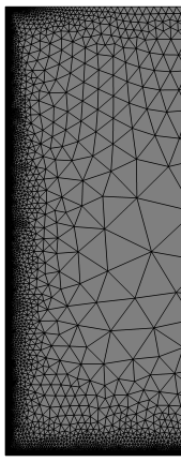

Figure 6.7 *Zoom of mesh applied for numerical simulations.*

As seen from Figure 6.7, the mesh density is highest in the cracked and debonded domains. Triangular elements are used for the model. The maximum element size is 7 mm, and the model is simulated with approx. 15000 elements and solved for approx 16000 degrees of freedom. Input data for the model is described in the following section.

6.2.4 Input

Values assigned to the constants of the equations in the numerical simulations, Eqs. (6.1) – (6.9) are provided in Table 6.7.

Table 6.7 *Input parameters for electrochemical evaluations of Case Study 2.*

Model parameter	Symbol	Unit	Value	Reference
Electrical resistivity	ρ	Ωm	100	-
Chloride transport coefficient at concrete surface	$D_{crack,surf}$	m^2/s	$5 \cdot 10^{-7}$	[*Wang and Ueda, 2011*] [1)]
Chloride transport coefficient at reinforcement	$D_{crack,reinf}$	m^2/s	$1 \cdot 10^{-8}$	[*Wang and Ueda, 2011*] [1)]
Chloride transport coefficient of bulk concrete	D_{bulk}	m^2/s	$1 \cdot 10^{-11}$	- [2)]
Surface, chloride concentration	Cl_S^-	wt.-% Cl/wt.-% cem.	3	-
Chloride threshold, debonded surface	$c_{crit,deb}$	wt.-% Cl/wt.-% cem.	0.1	-
Chloride threshold, bonded surface	$c_{crit,bon}$	wt.-% Cl/wt.-% cem.	0.1 – 1.0	-
Temperature	T	K	293	-
Faradays constant	F	C/mol	96485	[*Bardal, 2004*]
Valence	z	-	2	[*Bardal, 2004*]
Cathodic equilibrium potential	$E_{0,c}$	V_{SCE}	0.16	[*Ožbolt et al., 2011*]
Anodic equilibrium potential	$E_{0,a}$	V_{SCE}	-0.78	[*Ožbolt et al., 2011*]
Cathodic exchange current density	$i_{0,c}$	A/m^2	$6.25 \cdot 10^{-6}$	[*Ožbolt et al., 2011*]
Anodic exchange current density	$i_{0,a}$	A/m^2	$1.88 \cdot 10^{-4}$	[*Ožbolt et al., 2011*]
Gas constant	R	J/mol·K	8.314	-
Anodic Tafel constant	b_a	V/decade	0.06	[*Ožbolt et al., 2011*]
Cathodic Tafel constant	b_c	V/decade	0.16	[*Ožbolt et al., 2011*]
Limiting current density	i_{lim}	A/m^2	1	[3)]

[1)] The value applied for the numerical simulations of this case study is based on the range of the values given in the reference. However, the exact value used here is not provided in the reference.

[2)] This value corresponds to typical concrete properties

[3)] This value of the limiting current density is chosen assuming that sufficient oxygen for the corrosion process will be available

Input concerning the crack geometry as well as the length of separation along the reinforcement is adapted from the numerical simulations presented in Chapter 3. Corresponding values for COD, COD_{sep} and l_{sep} are determined for the same value of CMOD for PC and SFRC (0.5 vol.-%) and are presented in Table 6.8.

Table 6.8 *Input parameters for crack formation in PC and SFRC (0.5 vol.-%).*

CMOD [mm]	COD [mm]		COD_{sep} [mm]		l_{sep} [mm]	
	PC	SFRC	PC	SFRC	PC	SFRC
0.1	0.04	0.04	0.05	0.06	93	40
0.2	0.11	0.09	0.09	0.10	179	86
0.3	0.17	0.14	0.14	0.15	206	113
0.4	0.24	0.20	0.19	0.20	232	126
0.5	0.31	0.24	0.25	0.25	245	139

6.2.5 Results

The results of the simulations presented in the following cover initiation and propagation of corrosion through a 90 days time span. Results presented in the following only concern one half of the domain as ingress of chloride etc. is considered symmetric around the vertical centre line of the domain illustrated in Figure 6.6, as already presented.

The numerical model simulates ingress of chloride and the corresponding changes in the electrochemical potential of the reinforcement, the chloride concentration throughout the concrete volume, and the corrosion current density along the rein-

forcement. As an example a surface plot of the chloride concentration in the concrete volume for PC, (CMOD = 0.1 mm) after 30 days of exposure is shown in Figure 6.8.

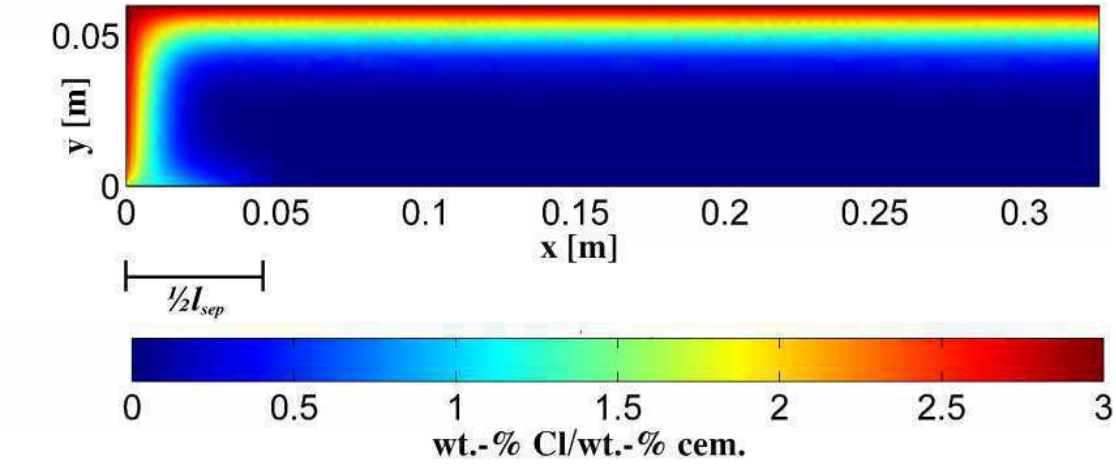

Figure 6.8 *Surface plot of chloride concentration after 30 days, for PC (CMOD = 0.1 mm).*

It will be seen that the chloride concentration is highest at the exposed surface (top horizontal surface) as well as in the cracked domain and the chloride ingress in the debonded domain is, for this particular simulation, limited.

The chloride concentration along the reinforcement for selected durations of exposure is shown in Figure 6.9, whereas the corresponding potential distribution along the reinforcement is presented in Figure 6.10. Both figures show results corresponding to PC (CMOD = 0.1mm).

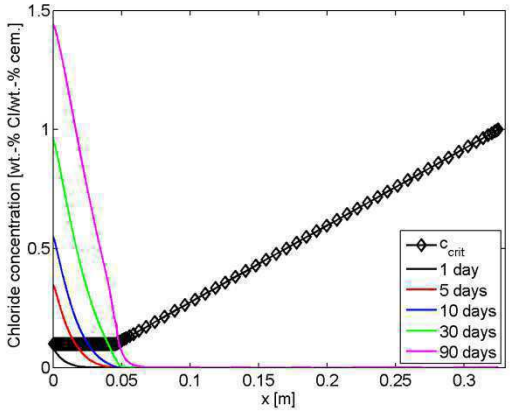

Figure 6. 9 *Chloride concentration along reinforcement for various time of exposure.*

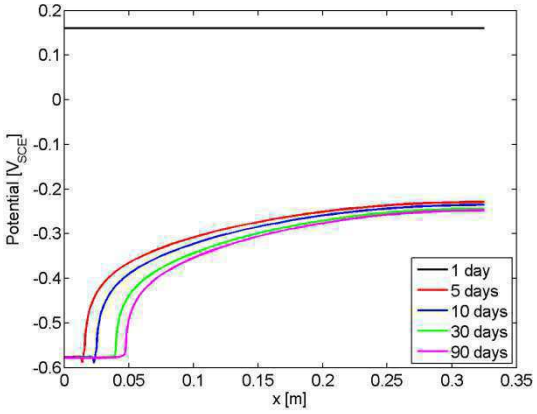

Figure 6.10 *Potential distribution along reinforcement for various time of exposure.*

Comparing the results presented in Figures 6.9 and 6.10 it is seen that until the chloride threshold at the level of the reinforcement is reached, the reinforcement is electrochemically passive (cf. the results after 1 day of exposure showing values of the potential in the cathodic range). Continued ingress of chlorides results in the formatino of an anode and an increased anodic site of the reinforcement over time, ie the po-

tential drops (Figure 6.10). In the following, corrosion initiation and corrosion propagation are discussed separately.

6.2.5.1 Corrosion Initiation

The results of the numerical simulations concerning the time-to-corrosion-initiation in PC and SFRC are shown in Figure 6.11

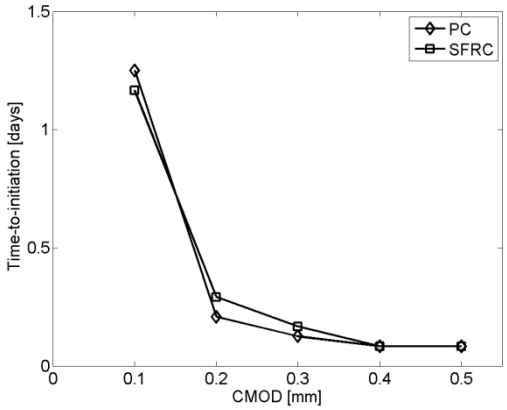

Figure 6.11 *Time-to-corrosion-initiation as a function of CMOD.*

It appears from Figure 6.11 that the time-to-corrosion-initiation is similar in PC and SFRC for the same CMOD when using the boundary conditions as described previously in this section.

The results presented in Figure 6.11 correspond well to the experimental results presented in Chapter 4, showing that corrosion was initiated after approx. 1-1.5 days in concrete beams (PC or SFRC) similar to those modelled for CMOD ~ 0.1 mm.

6.2.5.2 Corrosion Propagation

The average corrosion current density $i_{cor,av}$ as well as the length of the anodic area as a function of exposure time are presented and discussed in the following. It is noted that the maximum simulated chloride concentration at the level of the reinforcement is in the range 1.5 – 2.3 wt.-% Cl/wt.-% cem. depending on the surface crack width. According to Dauberschmidt the chloride threshold of embedded steel fibres is approx. 4 – 6 wt.-% Cl/wt.-% cem. [*Dauberschmidt, 2006*], and it is therefore concluded that the steel fibres are electrochemically passive. Thus they do not change the electrical resitivity of the concrete, cf. descriptions given in Section 6.1, and the assumption of neglecting their impact on the electrical resistivity is valied.

6.2.5.2.1 Corrosion Current Density

The average corrosion current density as a function of the simulated time for various geometries of the cracked domain and the debonded domain given in Table 6.8 is presented in Figures 6.12 and 6.13 for PC and SFRC respectively. The same scaling of the axes is applied to the two figures allowing for easy comparison.

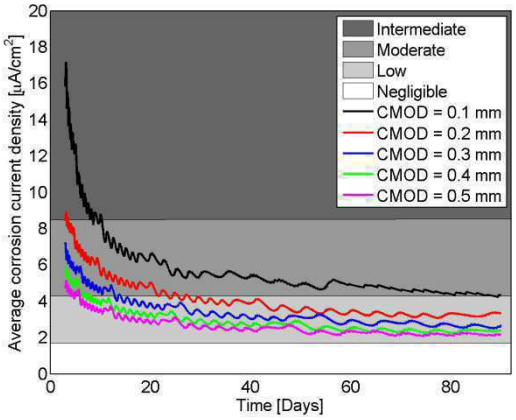

Figure 6.12 *Average corrosion current density, as a function of the exposure time, PC.*

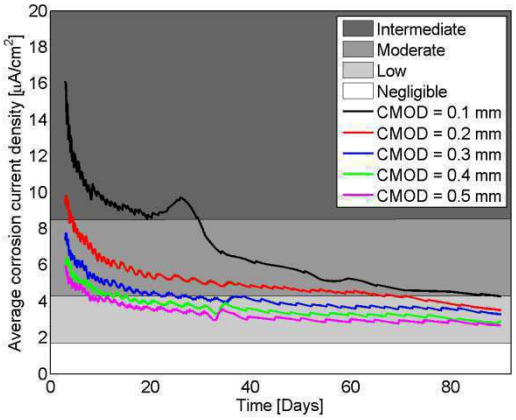

Figure 6.13 *Average corrosion current density, as a function of the exposure time, SFRC.*

The average corrosion current density decreases asymptotically over time in PC as well as in SFRC cf. Figures 6.12 and 6.13. This is due to the increase in the length of the anodic site, which will be discussed separately in the following section. Comparing Figures 6.12 and 6.13 it is seen that for the same CMOD of the two materials, the average corrosion current density is in the same range. The values of the average corrosion current density are comparable to values reported in the literature, eg [*Andrade et al., 1992; Andrade et al., 2008*]. The results of the numerical simulations cannot be compared directly with the results of the experimental observations presented in Chapter 4 since the experimental observations are reported in terms of the macrocell current density. However, according to information provided in Section 4.2.4.2 the cathode is approx. 20 times larger than the anode for the experimental observations. Thus the corrosion current density is approx. 20 times less than the macrocell current densities reported in Section 4.4. Comparing the experimental observations and the numerical simulations of the average corrosion current density it is observed that they are within the same order of magnitude. The simulated values of the average corrosion current densities decrease from *intermediate* to *low*/*negligible* over time.

6.2.5.2.2 Length of Anodic Site

The length of the anodic site as a function of time for various geometries of the crack domain and the debonding domain (see Table 6.8) is presented in Figures 6.14 – 6.15 for PC and SFRC, respectively.

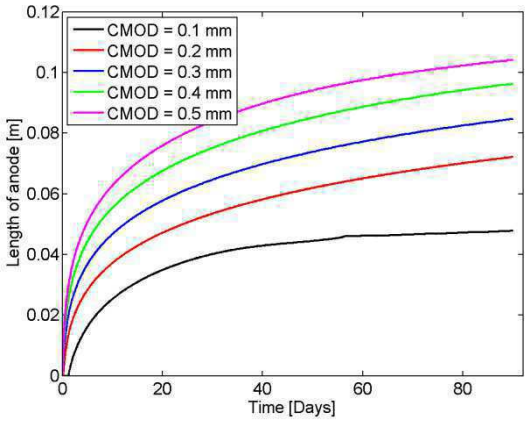

Figure 6.14 *Length of anode as a function of the exposure time, PC.*

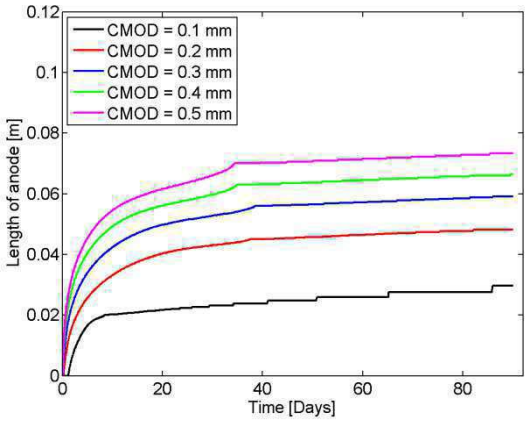

Figure 6.15 *Length of anode as a function of the exposure time, SFRC.*

It is seen from Figures 6.14 and 6.15 that the simulated propagation of the anodic site over time is smaller in SFRC compared to PC. From Figure 6.14 it appears that the length of the anode for CMOD = 0.1 mm after 24 days of exposure is approx. 35-40 mm. Comparing this result with the experimental results concerning corrosion along the reinforcement embedded in PC, Figure 4.12, it is seen that the value obtained from the numerical simulations is comparable with the experimental result indicating an approx. length of the anodic site after 24 days of exposure around 25-40 mm. Hence it the numerical modelling approach, with the given boundary conditions, provides results which are comparable with the experimental observations presented in Chapter 4. From Figure 6.15 is seen that the length of the anodic site along the reinforcement is approx. 20 mm after 24 days of exposure for CMOD = 0.1 mm. The experimental results concerning corrosion along the reinforcement in SFRC (0.5 vol.-%) are presented in Figure 4.15 and the extent of chloride-ingress along the reinforcement is presented in Figure 4.17. The figures illustrate that the length of the anodic site (Figure 4.15) and the extent of chloride ingress along the reinforcement (Figure 4.17) are approx. 80 mm from the transverse crack. Thus the results presented in Figure 6.15 concerning the length of the anodic site do not correlate well with the experimental observations. A potential explanation of this difference between the experimental observation and the numerical result is that the ingress rate of chlorides along the reinforcement in the numerical model is too low (increased ingress rate will result in a faster ingress along the reinforcement surface). Another explanation could be, that the chloride threshold assigned to the reinforcement surface in the model is too high (a lower chloride threshold will increase the length anodic site in the model).

The slower growth of the anodic site in SFRC compared to PC is due to the boundary conditions applied in the numerical model; The linear decrease of the chloride transport coefficient over the length of the separated part of the reinforcement, cf. description in Section 6.2.2, results in a dependency between the chloride transport coefficient and the length of separation. Hence the results of the numerical simulations are highly dependent on the values assigned to $D_{crack,\ reinf}$ and D_{bulk}.

To illustrate this sensitivity of the numerical model, a small sensitivity study is carried out. Within this sensitivity study, the chloride transport properties of the cracked domain and the debonded domain are varied, see corresponding values in Table 6.9. Values assigned to other parameters are the same as presented in Table 6.7. The geometry of the cracked domain and the debonded domain corresponds to that for PC, CMOD = 0.5 mm, see Table 6.8.

Table 6.9 *Input parameters for chloride transport coefficients for sensitivity study.*

Sensitivity study	$D_{crack,\ surf}$ [m^2/s]	$D_{crack,\ reinf}$ [m^2/s]	D_{bulk} [m^2/s]
Reference	$5 \cdot 10^{-7}$	$1 \cdot 10^{-8}$	$1 \cdot 10^{-11}$
1	$5 \cdot 10^{-7}$	$1 \cdot 10^{-7}$	$1 \cdot 10^{-11}$
2	$5 \cdot 10^{-7}$	$1 \cdot 10^{-9}$	$1 \cdot 10^{-11}$

The chloride transport properties in the debonded domain for the three sensitivity studies, ie the values presented in Table 6.9, are illustrated in Figure 6.16. Note, 'Reference' corresponds to the base case, viz. the same values are assigned to the chloride transport properties of the debonded domain as given in Table 6.7. The transport of chlorides in the cracked domain is not discussed in this sensitivity study.

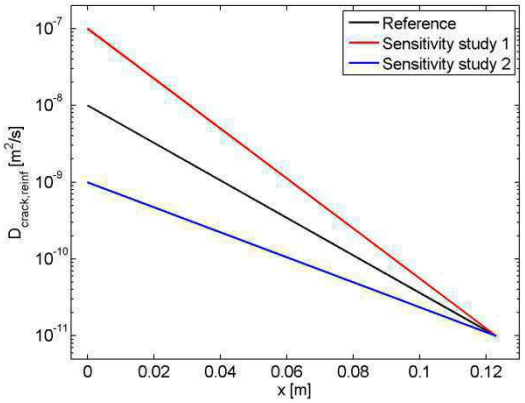

Figure 6.16 *Chloride transport properties in the debonded domain used for sensitivity studies.*

For these three sensitivity studies the average corrosion current density and the length of the anodic site, both as functions of the exposure time, are presented in Figure 6.17 and Figure 6.18, respectively. Additionally, the length of the debonded domain along the reinforcement is illustrated in Figure 6.18.

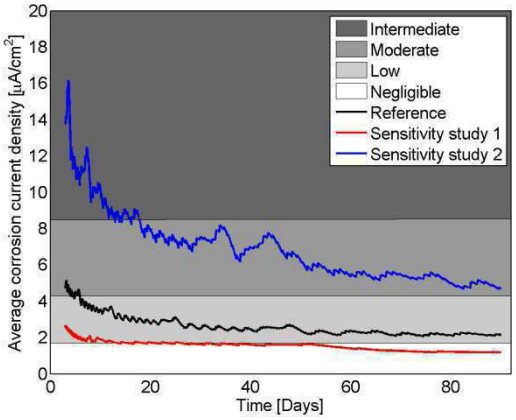

Figure 6.17 *Average corrosion current density, as a function of the exposure time, for the three sensitivity studies.*

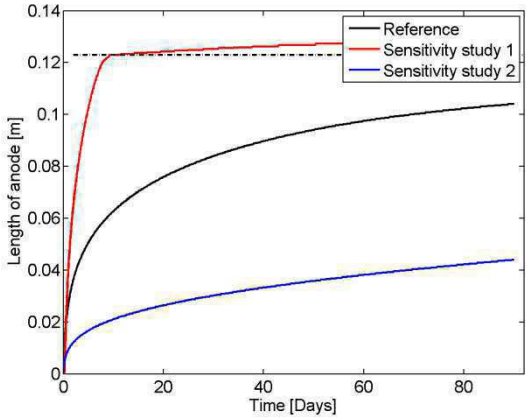

Figure 6.17 *Length of anode as a function of the exposure time, for the three sensitivity studies.*

It appears from Figure 6.17 that the average corrosion current density for the reference study and sensitivity study 1 is in the same range within the time of exposure, whereas the average corrosion current density for sensitivity study 2 is somewhat higher. Comparing with the results presented in Figure 6.18 it is concluded that the increased average corrosion current density of sensitivity study 2 compared to the others is caused by the smaller anodic site of this sensitivity study.

From Figure 6.18 it appears that the length of the anodic site as a function of the exposure time is heavily dependent on the chloride transport properties in the debonded domain, as would be expected. It is seen that increasing the value of $D_{crack,\ reinf}$ with an order of magnitude compared to the reference study, ie sensitivity study 1, implies that the full debonded length of the reinforcement acts anodically within approx. 10 days. Decreasing the value of $D_{crack,\ reinf}$ one order of magnitude compared to the base study implies that the length of the anodic site at the end of the simulation time is reduced to approx. 1/3.

6.2.6 Summary

Based on the results of the numerical simulations as presented in Section 6.2.5, the following may be concluded:

- The time-to-initiation-of corrosion is the same in PC and SFRC, when the crack width at the concrete surface is the same. For CMOD = 0.1 mm, the numerical simulations correspond well with experimentally obtained data presented in Chapter 4.
- The simulated values of the average corrosion current density are in the same range, for the same value of CMOD, for PC and SFRC. For the same crack width as used for the experimental observations (CMOD = 0.1 mm) the simu-

lated average corrosion current densities are within the same order of magnitude as the experimental observations.

- The simulated length of the anodic site at the reinforcement bar is slightly smaller in SFRC compared to PC. The results of the numerical simulations concerning the length of the anodic site correlate well with experimental observations presented in Chapter 4 for PC wheras the simulated results do not correlate that well with the experimental observations for SFRC.
- Though the steel fibres have an impact on the mechanically induced crack formation and length of debonding at the concrete/steel interface as presented in Chapter 3 and [*Solgaard et al., 2013*] it cannot be concluded from the numerical simulations presented above, that combined reinforcement systems are less susceptible to initiatiation of corrosion. Moreover, the length of the anodic site and the corrosion current densities are in the same range for the same crack width at the concrete surface for the two materials. Thus the numerical simulations do not show that combined reinforcement systems are superior to traditional reinforcement with regard to corrosion resistance in cracked concrete for the same crack width at the concrete surface.
- The length of the anodic site is controlled by the ingress rate of chlorides in the debonded domain as discussed from a minor sensitivity study presented above. Further research on these transport properties, eg quantification of the correlation between the ingress rate and the crack width and quantification of the correlation between the transport rate and the moisture condition of the concrete, is required. Such information will refine the predictions of the numerial model.

Chapter 7

Conclusions and Recommendations for Future Work

The aim of the work presented in this Ph.D. thesis was to quantify the impact of steel fibres on corrosion of reinforcement bars embedded in concrete. Focus of the work was set on the influence of steel fibres on propagation of reinforcement corrosion in uncracked concrete and the impact of steel fibres on initiation and propagation of cracks in concrete reinforced with combined reinforcement systems. Corrosion of the steel fibres was not considered (apart from the effect of depassivated/corroding steel fibres on corrosion of the reinforcement bars).

The study included experimental, analytical and/or numerical analysis of the impact of electrically conducting (depassivated/corroding) steel fibres on the electrical resistivity of concrete as well as crack development in concrete with combined reinforcement systems, corrosion of reinforcement bars in cracked PC and SFRC and corrosion-induced cover-cracking. The results of the aforementioned studies were used as input for two case studies covering corrosion in uncracked and cracked concrete, respectively.

The conclusions from the experimental and numerical studies, which are presented in Chapters 2 – 5, are summarized in Section 7.1, along with a summary of the conclusions from the case studies presented in Chapter 6. The scientific achievements, limitations and recommendations for future work are given in Section 7.2.

7.1 Experimental and Numerical Work

The impact of steel fibres on the electrical resistivity of concrete was investigated in relation to corrosion propagation of reinforcement bars in uncracked concrete since the electrical resistivity is known to affect the corrosion rate of reinforcement, eg [*Tuutti, 1982*].

Electrochemically passive steel fibres do not transfer current, ie they do not affect the electrical resistivity of concrete [*Torrents et al., 2000; Torrents et al., 2001; Mason et al., 2002*], apart from possible changes in the microstructure of concrete which are considered subordinate. Electrochemically active (de-passivated/corroding) steel fibres, hereafter referred to as conductive steel fibres, can, however, transfer current and thereby change the electrical resistivity of concrete. Experimental studies on the impact of various amounts of conductive steel fibres on the electrical resistivity of concrete were carried out, and the results were presented in Chapter 2. The experimental studies were carried out applying AC at 126 Hz (electrochemically passive and

active steel fibres conduct current under these conditions). The impact of conductive steel fibres on the electrical resistivity of various compositions of concrete was compared to the impact of other parameters known to affect the electrical resistivity of concrete, viz. the moisture content and the temperature. An analytical model for the prediction of the correlation between the content of conductive steel fibres and the electrical resistivity of concrete was presented in Chapter 2.

The addition of conductive steel fibres reduced the electrical resistivity of all the concrete compositions investigated. Variations in the moisture content from approx. 2.3 wt.-% to 5.0 wt.-%, which in this work corresponded to RH = 45% and capillary saturated concrete, respectively, changed the electrical resistivity orders of magnitude for PC and SFRC (0.5 vol.-% and 1.0 vol.-%). The relative influence of conductive steel fibres on the electrical resistivity decreased with increasing moisture content; for concrete conditioned to RH = 45%, the addition of 1.0 vol.-% conductive steel fibres reduced the electrical resistivity more than two orders of magnitude, whereas the reduction of the electrical resistivity of capillary saturated concrete due to the addition of 1.0 vol.-% conductive steel fibres was less than one order of magnitude. Finally, the experimentally obtained observations were compared to the calculated impact of changes in the temperature on the electrical resistivity. It was shown that the influence of the addition of 0.5 vol.-% conductive steel fibres on the electrical resistivity was comparable to a change in the temperature from 20°C, at which the experimental studies were carried out, to approx. 30°C. The analytical model for predictions of the impact of conductive steel fibres was capable of predicting the correlation between the content of conductive steel fibres and the electrical resistivity for capillary saturated concrete. However, the predictions of the model underestimated the actual measured impact of conductive steel fibres for non-saturated concrete.

The correlation between the electrical resistivity of concrete and the corrosion rate, in terms of the average corrosion current density, of embedded reinforcement was assessed in a non-transient, numerically based case study, Chapter 6. The simulated corrosion rate was categorized using the approach presented in eg [*Bertolini et al., 2004*]. Data from the studies described above was used to interpret the corrosion rate of traditional reinforcement embedded in PC or SFRC (0.5 vol.-% and 1.0 vol.-%). From the numerical simulations it was observed that the largest relative impact of conductive steel fibres on the corrosion rate of embedded reinforcement bars was seen for a low moisture content of the concrete, in this case approx. 2.3 wt.-%. For this moisture content the corresponding corrosion rate was in the ranges *low* to *moderate*, depending on the anode to cathode ratio of the corrosion cell and the content of conductive steel fibres. For increasing moisture content of the concrete the relative impact of the steel fibres on the corrosion rate was reduced, but the corrosion rate was increased. For capillary saturated concrete the numerical simulations showed that 1.0 vol.-% conductive steel fibres increased the average corrosion current density with a factor of approx. 4 compared to PC. In the case of a small anode to cathode ratio (0.1), the corro-

sion category was changed from *negligible* to *intermediate*. Based on this observation, it cannot be excluded that under extreme conditions (a small anode to cathode ratio, saturated concrete and harsh chloride exposure resulting in corrosion of all the steel fibres in a cross section), the corrosion process will be accelerated by the presence of steel fibres. However, this scenario might be somewhat hypothetical.

The impact of steel fibres on initiation and propagation of cracks in concrete containing combined reinforcement systems was investigated experimentally and numerically. Those observations were linked to corrosion of reinforcement bars in cracked concrete (PC or SFRC) through experimental observations and numerical simulations. Such studies provide a holistic view on the pros and cons on the impact of steel fibres when considering combined reinforcement systems.

A numerical, fracture mechanically based model was developed for the simulation of such load-induded cracking and debonding along the concrete/steel interface, presented and discussed in Chapter 3. The model simulated the formation of a main bending crack from the tensile surface of a concrete element towards the level of the reinforcement as well as the slip and separation at the concrete/steel bar interface. The numerical model was verified with experimental observations obtained from three point bending tests of reinforced concrete containing either traditional reinforcement or combined reinforcement systems. The development (initiation and propagation) of load-induced bending cracking of the concrete cover and debonding at the concrete/steel bar interface was studied experimentally by the use of state-of-the-art photogrammetric equipment [*Solgaard et al., 2013*]. The experimental studies showed that the main bending crack at the tensile surface was induced at the same load level for regardless of the reinforcement system, ie a combined reinforcement system or traditional reinforcement. However, the development of the crack width at the tensile surface due to increased applied load was retarded in combined reinforced concrete beams compared to traditionally reinforced concrete beams. A similar trend was observed for the development of the width of the main bending crack at the level of the reinforcement, clearly indicating the crack-width-limiting-effect of the steel fibres. The numerical model was capable of reproducing the correlation between the applied load and the development of the main bending crack accurately. Furthermore the experimental studies showed, that the magnitude of the debonding, ie slip and separation, at the concrete/steel bar interface was reduced for the combined reinforcement system compared to traditional reinforcement. Again, the numerical model was capable of simulating those experimental observations. Finally it was shown by the use of the numerical model that there appears to be no clear impact of steel fibres on the correlation between the crack width at the concrete surface and the length of the separation along the reinforcement. Based on the observations presented in Chapter 3 it is concluded that the addition of steel fibres may be an effective solution for limiting the propagation of load-induced cracking of the concrete cover whereas the impact of

steel fibres on the length of debonding at the concrete/steel-bar interface still is not fully understood.

The influence of steel fibres on load-induced concrete cover-cracking and debonding at the concrete/steel-bar interface of reinforced concrete beams (combined reinforcement system or traditional reinforcement), was linked to corrosion of the traditional reinforcement, Chapter 4, through electrochemical experiments. Companion concrete beams were subjected to a corrosive environment (ponded with a NaCl solution, 3% by weight) and simultaneously electrochemical observations were conducted to assess the initiation and propagation of corrosion along the reinforcement bar. These concrete beams were pre-cracked to the same crack width (~0.1 mm) at the tensile surface and the aforementioned, electrochemical experiments were carried out while the crack was kept open using a customized frame. From these studies it was observed that corrosion was initiated almost immediately, ie approx. 1-2 days, after start of exposure for traditionally reinforced concrete beams as well as combined reinforced concrete beams. The experiments were terminated after 24 days and the concrete beams were split-open. Chloride ingress and corrosion was observed in all concrete beams at the separated part but not at the bonded part of the reinforcement bar. Based on this observation it was concluded that the extent of separation at the concrete/steel bar interface was a reliable indicator for the risk of corrosion initiation and propagation along the reinforcement, which is in line with results presented in [*Pease et al., 2011*].

A numerically-based case study concerning transient simulations of initiation and propagation of reinforcement-corrosion embedded in cracked concrete (PC or SFRC) was presented, Chapter 6. The numerical simulations covered chloride-induced corrosion by simulating chloride ingress through a transverse crack in the concrete cover and chloride transport along the reinforcement resulting in initiation and propagation of reinforcement corrosion. The geometrical boundary conditions as well as the exposure boundary conditions (temperature and surface chloride concentration) used for the model were similar to those of the experimental observations described in Chapter 4 and above thus allowing for comparison between the numerical simulations and the experimental observations. From the numerical simulations, corrosion initiation of the reinforcement bar was observed within 1-2 days, which was comparable to the observations from the experimental studies for a surface crack width of approx. 0.1 mm. Concerning the corrosion propagation phase it was observed from the numerical simulations that the average corrosion current density and the length of the anodic site along the reinforcement bar were in the same range for traditionally reinforced concrete beams and concrete beams containing a combined reinforcement system. The results concerning the average corrosion current density in PC and SFRC, for a surface crack width of approx. 0.1 mm were in the same range as observed in the experimental studies presented above. The length of the anodic site in PC was also comparable to the experimental observations whereas the numerical results for the combined reinforcement system did not correlate well with the experimental observations. Based

on the results of this case study, with the boundary conditions applied, it was concluded that the time-to-corrosion-initiation in cracked concrete is not delayed for combined reinforced concrete beams compared to traditionally reinforced concrete beams if the crack width at the concrete surface is the same. Thus, for the same surface crack width, the numerical simulations showed that combined reinforcement systems are not superior to traditional reinforcement with regard to corrosion-initiation. In relation to the corrosion-propagation phase it was concluded that the length of the anodic site and the average corrosion current density were similar for both types of reinforcement. Hence, based on the numerical simulations, no significant impact, neither positive nor negative, from steel fibres on corrosion of reinforcement bars can be observed. From a practical (engineering) point of view, where design of reinforced concrete structures for a pre-defined maximum crack width has to be considered, the positive impact of steel fibres on reducing crack widths is recognized. This crack-width limiting effect of the steel fibres may allow for structural design with combined reinforcement systesm considering the crack-width-limiting-effect of the steel fibres. However, based on the studies presented herein there is no clear indleunce (positive or negative) of the fibres on corrosion of the embedded reinforcement. It is emphasized that these conclusions are based on a limited case study, which is verified with short-term experimental observations and that the results of the numerical simulations are sensitive to changes in the input parameters eg the chloride transport properties in cracked concrete. Hence conclusions cannot per se be extrapolated to cover corrosion of combined reinforcement systems in cracked concrete in general.

The ultimate consequence of reinforcement corrosion is corrosion-induced concrete cover cracking which was analysed by the use of a numerical, fracture mechanically based FE model. A parametric study of the numerical model was presented in Chapter 5, with focus on the impact of the concrete toughness (mechanically representing the steel fibres) on corrosion-induced damage and cracking of the concrete cover. The numerical studies showed, that the increased toughness of the concrete, caused by the addition of fibres, did not change the conditions (thickness of corrosion products) required for initiation of the crack. However, the following propagation phase – and in particular the opening phase - of the crack was influenced by the increased toughness of concrete; the thickness of corrosion products to form a pre-defined crack width at the concrete surface was increased by increasing the toughness of the concrete. The thickness of corrosion products required to form a crack with a pre-defined crack width at the concrete surface was correlated to time through simplified electrochemical calculations. This analysis showed that, dependent on the concrete cover thickness and the diameter of the reinforcement bar, the time required to form a crack with a pre-defined crack width at the surface (0.2 mm), was increased with several years for combined reinforcement systems compared to traditionally reinforced concrete. These studies become relevant if reinforced concrete structures are designed for a durability limit state related to corrosion-induced cracking. However, at present the prevailing

limit state for durability design of concrete structures is corrosion initiation. Thus the presented work related to corrosion-induced cover cracking will only become relevant for durability-design if corrosion of the reinforcement is considered as an acceptable limit state. It is, however, noted that reinforcement corrosion in a concrete structure may occur and cause cracking of the concrete cover, although the service life is not exceeded. In this particular case the steel fibres will have a positive effect on the remaining service life of the structure, as they can prolong the crack propagation phase and thereby delay the negative impact of the crack on the reinforcement, eg increased ingress rate of hazardous substances.

7.2 Scientific Achievements, Limitations and Future Work

The work presented in this PhD thesis concerning combined reinforcement systems provided the following scientific achievements:

1) Experimental and numerical descriptions of a (conservative) correlation between the steel fibre volume fraction and the electrical resistivity of concrete and its link to corrosion propagation of reinforcement,
2) Establishment of a modelling framework coupling load-induced crack formation with initiation and propagation of corrosion for concrete beams reinforced with combined reinforcement systems and its experimental verification under accelerated, or even extreme, conditions,
3) Quantification of the impact of steel fibres on reducing corrosion-induced cover cracking caused by uniform reinforcement corrosion through an experimentally verified fracture-mechanically based modelling approach.

For the scientific achievements described above, special focus was placed on highlighting the impact of the steel fibres for such reinforcement systems. This is one of the few studies revealing and describing the mechanisms related to the durability of combined reinforcement systems and see them as a whole by linking the fracture mechanical properties and the material properties with the risk of corrosion initiation and corrosion propagation. Hence the presented studies provide important information required for the understanding of the differences between traditional reinforced concrete and combined reinforced concrete. Such information facilitates the possibility of a quantitative evaluation of the mechanisms, with regard to corrosion-related service life, which the steel fibres have a positive impact on and on which they have a potential negative impact.

However, limitations are attached to the scientific achievements of the work presented herein. With regard to 1) the presented electrical resistivity of concrete (PC or SFRC) was linked to the corrosion rate of embedded reinforcement bars using a non-transient model. However, the results of such modelling can only be seen as a snapshot of the corrosion rate, as other factors affecting the corrosion process, eg the ambient condi-

tions (temperature, humidity and possibly the oxygen supply) as well as the geometrical boundary conditions (anode to cathode ratio), may vary over time, resulting in changes in the corrosion rate. Considering 2) the framework for coupling load-induced damage and corrosion of the reinforcement bars has been established. However, further experimental studies on the concrete cracking and debonding at the concrete/steel bar interface and (long-term) electrochemical observations of corrosion initiation and propagation are required for further utilization of this framework. Additionally, further experimental studies on the transport rate in cracks and debonded areas are needed for PC and SFRC before the numerical model can be used in practice. Finally, concerning 3) further experimental verifications of the numerical model are required. Additionally, it shall be investigated whether the numerical model presents overly conservative predictions, eg due to the missing corrosion accommodating region (CAR) in the model.

Bearing these limitations and the aforementioned conclusions of the work in mind a list of ideas for future work is presented in the following. With regard to corrosion in uncracked concrete it is suggested to further study the electrical resistivity of SFRC. This includes establishment of an experimental procedure for the investigation of the possible impact of electrochemically passive steel fibres, eg changed microstructure, on the electrical resistivity of SFRC to verify whether or not such changes can be neglected (as suggested herein). The link between the electrical resistivity and the corrosion rate of reinforcement bars could potentially be strengthened using a transient model including exchange of heat and moisture and possibly chloride ingress. Moreover it is recommended to experimentally investigate the corrosion rate of combined reinforcement systems.

Concerning corrosion in cracked concrete it is suggested to investigate initiation and propagation of cracks and debonding, experimentally as well as numerically for other geometries, eg specimen size and concrete cover thickness and concrete having other material properties eg due to different fibre geometries/contents. Preferably such fracture mechanical studies should be coupled to reinforcement corrosion (initiation and propagation) eg using the methods presented herein, Chapter 4.

The chloride transport properties in cracked concrete have a major impact on the time-to-initiation of corrosion as well as the subsequent corrosion-propagation phase, as already presented in Chapter 6. Experimental observations on chloride transport in cracked concrete, PC as well as SFRC, considering various exposure conditions (wet/dry and/or fully submerged) and various concrete properties (binder composition, w/c ratio, etc.) are therefore recommended. In particular, knowledge on the transport properties in the debonded area along the reinforcement is lacking. Potentially, such investigations can be carried out using x-ray attenuation methods as presented in eg [*Pease et al., 2009; Pease et al., 2012b*].

Finally, with regard to corrosion-induced cracking in concrete it is suggested to refine the numerical model presented in Chapter 5. The numerical model presented is capable of simulating cover-cracking caused by corrosion products uniformly distributed at the circumference of the reinforcement. However, non-uniform reinforcement corrosion, should be covered by the model as well, as it reasonable to assume that the location of the reinforcement products largely affects the damage and crack formation. Moreover it is suggested to implement a CAR around the reinforcement bar in which the corrosion products can precipitate into. The properties of this CAR, which is further described by eg Michel et al. [*Michel et al., 2011*], could potentially be studied experimentally by the use of x-ray attenuation measurements and/or digital image correlation. Finally the link between thickness of corrosion products and cracking of the concrete cover should be investigated further numerically, using a transient corrosion model accounting for eg exchange of heat and moisture with the surroundings as well as movements of the corrosion products into the CAR and the crack.

Bibliography

[Abrycki and Zajdzinski, 2012] Abrycki, M. and Zajdzinski, A. (2012), *Effect of fibres on corrosion of steel reinforcement*, Master of Science Thesis, Department of Civil and Environmental Engineering, Chalmers University of Technology, Göteborg, Sweden.

[ACI, 2001] ACI Committee 224 (2001), *ACI 224R-01: Control of cracking in concrete structures*, American Concrete Institute, Farmington Hills, MI, USA.

[ACI, 2010] ACI Committee 544 (2010), *ACI 544.5R-10: Report on the Physical Properties and Durability of Fiber-Reinforced Concrete*, American Concrete Institute, Farmington Hills, MI, USA.

[AIJ, 2006] AIJ (2006),'Recommendations for Practice of Crack Control in Reinforced Concrete Buildings (Design and Construction)', (In Japanese).

[Aldea et al., 1999] Aldea, A.-M., Shah, S.P. and Karr, A. (1999), Effect of Cracking on Water and Chloride Permeability of Concrete, *Journal of Materials in Civil Engineering* **11** (3), 181-187.

[Aldea et al., 1999a] Aldea, C.-M., Shah, S. and Karr, A. (1999a), Permeability of cracked concrete, *Materials and Structures* **32** (219), 370-376.

[Alonso et al., 1998] Alonso, C., Andrade, C., Rodriguez, J. and Diez, J.M. (1998), Factors controlling cracking of concrete affected by reinforcement corrosion, *Materials and Structures* **31** (7), 435-441.

[Andrade et al., 1992] Andrade, C., Maribona, I.R., Feliu, S., Gonzalez, J.A. and Feliu Jr., S. (1992), The effect of macrocells between active and passive areas of steel reinforcements, *Corrosion Science* **33** (2), 237-242.

[Andrade et al., 1993] Andrade, C., Alonso, C. and Molina, F.J. (1993), Cover cracking as a function of bar corrosion: Part 1-Experimental test, *Materials and Structures* **26** (8), 453-464.

[Andrade et al., 2008] Andrade, C., Garcés, P. and Martínez, I. (2008), Galvanic currents and corrosion rates of reinforcements measured in cells simulating different pitting areas caused by chloride attack in sodium hydroxide, *Corrosion Science* **50** (10), 2959-2964.

[Angst et al., 2009] Angst, U., Elsener, B., Larsen, C.K. and Vennesland, Ø. (2009), Critical chloride content in reinforced concrete – A review, *Cement and Concrete Research* **39**, 1122-1138.

[Arup, 1983] Arup, H. (1983), *The mechanisms of protection of steel by concrete*, In Crane A.P. (ed.) Corrosion of reinforcement in concrete construction, Chichester, England:Horwood.

[Arya and Ofori-Darko, 1996] Arya, A. and Ofori-Darko, F. (1996), Influence of cracks frequency on reinforcement corrosion in concrete, *Cement and Concrete Research* **26** (3), 345-353.

[AAP, 2011] http://www.aalborgportland.dk/default.aspx?m=2&i=93, *retrieved 18th of October 2011.*

[AAP, 2011a] http://www.aalborgportland.dk/default.aspx?m=2&i=95, *retrieved 10th of October 2011.*

[AAP, 2011b] http://www.aalborgportland.dk/default.aspx?m=2&i=92, *retrieved 10th of October 2011.*

[AASHTO, 2007] AASHTO (2007), *Load Resistance Factor Design Bridge Design Specifications*, SI Units, 4th Edition.

[Bardal, 2004] Bardal, E. (2004), *Corrosion and Protection*, Springer-Verlag, London, UK.

[Barnett et al., 2010] Barnett, S.J., Lataste, J.F., Parry, T. Millard, S.G. and Soutsos M.N. (2010), Assessment of fibre orientation in ultra high performance fibre reinforced concrete and its effect on flexural strength, *Materials and Structures* **43**, 1009-1023.

[Bazant, 1978] *Bazant, Z.P.* (1978), *Physical model for corrosion of steel in concrete*, CBI Forskning 5.

[Bazant, 1979] Bazant, Z.P. (1979), Physical model for steel corrosion in concrete sea structures - Application, *Journal of the Structural Division* **105** (6), 1155-1166.

[Bekaert, 2011] http://www.bekaert.com/~/media/Files/Download%20Files/Construction/Concrete%20reinforcement/Dramix%20General/Datasheet%20Dramix%20RC-6535-BN.ashx, *retrieved 30th of September 2011.*

[Bentur et al 1998] Bentur, A., Berke, N., and Diamond, S. (1998), *Steel Corrosion in Concrete: Fundamentals and civil engineering practice (Modern Concrete Technology)*, Spon Press, London.

[Berke et al., 1993] Berke, N., Dallaire, M., Hicks, M. and Hoopes, R. (1993), Corrosion of steel in cracked concrete, *Corrosion Engineering* **49** (11), 934-943.

[Bertolini et al., 2004] Bertolini, L., Elsener, B., Pedeferri, P. and Polder, R. (2004), *Corrosion of steel in concrete, Prevention, Diagnosis, Repair*, Wiley-VCH Verlag GmbH & Co. KGaA, Weinheim.

[Bonanos and Lilley, 1981] Bonanos, N. and Lilley, E. (1981), Conductivity Relaxations in Single Crystals of Sodium Chloride Containing Suzuki Phase Precipitates, *Journal of Physics and Chemistry of Solids* **42**, 943-952.

[Böhni, 2005] Böhni, H. (2005), *Corrosion in reinforced concrete Structures*, Woodhead Publishing Ltd.

[Buenfeld et al., 2004] Buenfeld, N., Glass, G., Reddy, B., and Viles, F. (2004), *Process for the Protection of Reinforcement in Reinforced Concrete,* United States Patent 6685822.

[Cabrera, 1996] Cabrera, J.G. (1996), Deterioration of Concrete due to Reinforcement Steel Corrosion, *Cement and Concrete Composites* **18** (1), 47-59.

[Caré et al., 2008] Caré, S., Nguyen, Q.T., L'Hostis, V. and Berthaud, Y. (2008), Mechanical properties of the rust layer induced by impressed current method in reinforced mortar, *Cement and Concrete Research* **38** (8-9), 1079-1091.

[Carol et al, 1997] Carol, I., Prat, P.C. and López, C.M. (1997), Normal/shear cracking model: Application to discrete crack analysis, *Journal of Engineering Mechanics* **123** (8), 765-773.

[Chiaia et al., 2008] Chiaia, B. Fantilli, A.P. and Vallini, P. (2008), Combining Fiber-reinforced concrete with traditional reinforcement in tunnel linings, *Engineering Structures* **31**, 1600-1606.

[Chitty et al., 2005] Chitty, W.J. Dillmann, P. L'Hostis, V and Lombard, C. (2005), Long-term corrosion resistance of metallic reinforcements in concrete – a study of corrosion mechanisms based on archaeological artefacts, *Corrosion Science* **47**, 1555-1581.

[Chernin et al., 2010] Chernin, L., Val, D.V. and Volokh, K.Y. (2010), Analytical modelling of concrete cover cracking caused by corrosion of reinforcement, *Materials and Structures* **43** (4), 543-556.

[CNR-DT 204, 2006] National Research Council of Italy (2006), *Guidelines for design, construction and production control of fiber reinforced concrete structures*.

[CSR, 1992] Concrete Society Report (1992), *Non-structural cracksin concrete*, Technical report No. 22, 3rd edition, Concrete Society, London, England.

[Corrosion-club, 2012] http://corrosion-club.com/concretecosts.htm, *retrieved 12th of January 2012.*

[COWI, 2013] http://www.cowi-gulf.com/menu/news/news/Pages/WorkbeginsonAbuDhabi%E2%80%99snewundergroundtunnelsystem.aspx, *retrieved 13th of May2013.*

[DAfStb, 2003] German Committee on Reinforced Concrete (DAfStb) (2003), 'Guideline waterproof concrete constructions.

[Dauberschmidt, 2002] Dauberschmidt, C. (2002), Corrosion Mechanisms of Steel Fibres in Chloride Containing Concrete, *Proceedings of the 4th International PhD Symposium in Civil Engineering.*

[Dauberschmidt, 2006] Dauberschmidt, C. (2006), *Untersuchungen zu den Korrosionsmechanismen von Stahlfasern in chloridhaltigem Beton*. Dissertation, RWTH Aachen, 03 Fakultät für Bauingenieurwesen, Germany.

[Davies et al., 2006] Davies, H., Woods, E. and Shuttleworth, P. (2006),'Focusing on Fibres: CTRL Experience, *British Tunneling Society*, 29-32.

[DBV, 2001] Deutscher Beton- und Bautechnik Verein (2001), *DBV-Merkblatt Stahl-faserbeton*.

[Demoulin et al., 2010] Demoulin, A. Trigance, C. Neff, D, Foy, E. Dillmann, P. and L'Hostis, V. (2010), The evolution of the corrosion of iron in hydraulic binders analysed from 46- and 260-year-old buildings, *Corrosion Science* **52**, 3168-3179.

[DIN 1045-1, 2008] DIN 1045-1 (2008),'Reinforced concrete and prestressed concrete structures, Part 1: Design and construction.

[Dörr, 1980] Dörr, K. (1980), *Ein Beitrag zur Berechnung con Stahlbetonscheiber unter besonderer Berücksichtung des Verbundverhaltens*, Ph.D. Thesis, University of Darmstadt, Darmstadt, Germany.

[DS/EN 197-1, 2001] DS/EN 197-1, (2001),'Cement – Part 1: composition, specification and conformity criteria for common cements'.

[DS 2426, 2004] DS 2426, (2004),'Concrete materials – rules for application EN 206-1 in Denmark'.

[DS/EN 14651-A1, 2007] DS/EN 14651-A1, (2007),'Test method for metallic fibre concrete – Measuring the flexural tensile strength (limit or proportionality (LOP), residual)',Technical Report, Danish Standard Association.

[DuraCrete, 2000] DuraCrete (2000), *Probabilistic performance based durability design of concrete structures*, The European Union-Brite EuRam III.

[Elsener et al., 2003] Elsener, B., Andrade, C., Gulikers, J., Polder, R. and Raupach, M. (2003), Half-cell potential measurements – potential mapping on reinforced concrete structures, *Materials and Structures* **36** (261), 461-471.

[Edvardsen, 1999] Edvardsen, C. (1999), Water Permeability and Autogenous Healing of Cracks in Concrete, *ACI Materials Journal* **96** (4), 448-454.

[Eurocode, 2004] Eurocode 2 (2004),'Design of concrete structures, Part 1, General rules and rules for buildings', BS EN 1992-1-1.

[*fib*, 2006] *fib* (2006), *fib Bulletin 34, Model code for service life design*, Tech. Rep. fib Bulletin 34, International Federation for Structural Concrete (*fib*).

[*fib*, 2012] *fib* (2006), *fib Bulletin 65, Model Code 2010*, Tech. Rep. fib Bulletin 65, International Federation for Structural Concrete (*fib*).

[Fidjestol and Nilson, 1980] *Fidjestol, P. and Nilson, N.* (1980), *Field test of reinforcement corrosion in concrete*, ACI Special Publication **65**, 205-217.

[Francois and Arliguie, 1998] Francois, R. And Arliguie, G. (1998), Influence of service cracking on reinforcement steel corrosion, *Journal of Materials in Civil Engineering* **10** (1), 14-20.

[Francois and Arliguie, 1999] Francois, R. And Arliguie, G. (1999), Effect of microcracking and cracking on the development of corrosion in reinforced concrete members, *Magazine of Concrete Research* **51** (2), 143-150.

[Gautefall and Vennesland, 1983] Gautefall, O. and Vennesland, O. (1983), Effects of cracks on the corrosion of embedded steel in silica-concrete compared to ordinary concrete, *Nordic Concrete Research* **2**, 17-28.

[Gettu et al., 2006] Gettu, R., Barragán, B., Garcia, T., Ortiz, J. and Justa, R. (2006), Fiber Concrete Tunnel Lining - Construction of a subway line in Barcelona, *Concrete International*, 63-69.

[Gjörv et al., 1977] Gjörv, O.E., Vennesland, Ø. And El-Busaidy, A.H.S. (1977), Electrical resistivity of concrete in the oceans, *Proceedings of the 9th Annual Offshore Technology Conference.*

[GOM, 2009] *GOM* Optical Measuring Techniques (2009), *Aramis User Manual – Software, Aramis v6.1 and higher*, GOM mbh.

[Goto, 1971] Goto, Y. (1971), Cracks Formed in Concrete Around Deformed Tension Bars, *Journal of ACI* **68**, 244-251.

[Gowripalan et al., 2000] Gowripalan, N., Sirivivatnanon, V. and Lim, C. (2000), Chloride diffusivity of concrete cracked in flexure, *Cement and Concrete research* **30** (5), 725-730.

[Granju and Balouch, 2005] Granju, J.-L. and Balouch, S.L. (2005), Corrosion of steel fibre reinforced concrete from the cracks, *Cement and Concrete Research* **35**, 572-577.

[Graybeal, 2006] Graybeal, B.A. (2006), *Material Property Characterization of Ultra-High Performance Concrete*, Technical report No. FHWA-HRT-06-103, Federal Highway Administration, Georgetown Pike, Virgian, USA.

[Gu and Beaudoin, 1997] Gu, G.P. and Beaudoin, J.J. (1997), Research on Cost-Effective Solutions for Corrosion Prevention and Repair in Concrete Structures, *Construction Canada* **39** (6), 36-39.

[Hansen, 1999] Hansen, E.J.D.P. (1999), *Holdbarhed af fiberarmeret beton*, (Danish Language) Technical report Series R No. 63, Department of Civil Engineering at the Technical University of Denmark, Kgs. Lyngby, Denmark.

[Hatta and Taya, 1985] Hatta, H. and Taya, M. (1985), Effective Thermal Conductivity of a Misoriented Short Fiber Composite, *Journal of Applied Physics* **58** (7), 2478-2486.

[Herholdt et al., 1985] Herholdt, A., Justesen, C.F.P., and Nepper-Christensen, P. (1985),. *Beton Bogen*, Aalborg Portland A/S, Aalborg.

[Hillerborg et al., 1976] Hillerborg, A., Modéer, M. and Petersson, P.-E. (1976), Analysis of crack formation and crack growth in concrete by means of fracture mechanics and finite elements, *Cement and Concrete Research* **6** (6), 773-782.

[Hillerborg, 1980] Hillerborg, A. (1980) Analysis of fracture by means of the fictitious crack model - particularly for fibre reinforced concrete, *The International Journal of Cement Composites* **2**, 177-184.

[Holmes et al., 2011] Holmes, S.P., Wilcox, G.D., Robins, P.J., Glass, G.K. and Roberts A.C. (2011), Responsive behaviour of galvanic anodes in concrete and the basis for its utilisation, *Corrosion Science* **53** (10), 3450-3454.

[Hope et al., 1985] Hope, B.B., Ip, A.K. and Manning D.G. (1985), Corrosion and electrical impedance in concrete, *Cement and Concrete Research* **15** (3), 525-534.

[Hornbostel et al., 2013] Hornbostel, K, Larsen, C.K. and Geiker, M.R. (2013), Relationship between concrete resistivity and corrosion rate – a literature review, *Cement and Concrete Composites* (In press), http://dx.doi.org/10.1016/j.cemconcomp.2013.03.019.

[Hötte, 2003] Hötte, C. (2003), *Bestimmung des Feuchtezustandes von Mauerwerk mit Hilfe von Multiring-Elektroden - Untersuchungen zum Ankoppelungsmörtel und an Probewänden,* Diplomarbeit, Institut für Bauforschung, Technische Hochschule Aachen, Germany.

[Hughes et al., 1985] Hughes, B.P., Soleit, A.K.O. and Brierley, R.W. (1985), New technique for determining the electrical resistivity of concrete, *Magazine of Concrete Research* **37** (133), 243-248.

[Isgor and Razaqpur, 2006] Isgor, B.O. and Razaqpur, G.A. (2006), Modelling steel corrosion in concrete structures, *Materials and Structures* **39** (3), 291-302.

[Jacobsen et al., 1996] Jacobsen, S., Marchand, J. and Boisvert, L. (1996), Effect of Cracking and Healing on Chloride Transport in OPC Concrete, *Cement and Concrete Research* **26** (6), 869-881.

[Janotka et al., 1989] Janotka, I., Krajči, L., Komloš, K. and Frtalova, D. (1989), Surface corrosion of steel fibre reinforced concrete, *The International Journal of Cement Composites and Lightweight Concrete* **11** (4), 221-228.

[Johnston, 1974] Johnston, C.D. (1974) Steel fibre reinforced mortar and concrete – A review of mechanical properties *Fiber reinforced concrete ACI – SP44*.

[Kasper et al., 2008] Kasper, T., Edvardsen, C., Wittneben, G. and Neumann, D. (2008), Lining design for the district heating line in Copenhagen with steel fibre reinforced concrete segments, *Tunneling and Underground Space Technology* **23** (5), 574-587.

[Katawaki, 1977] Katawaki, K. (1977), Corroion of steel in the concrete exposed to seawater spray zone, *Symposium Proceedings on cracking of concrete structures.*

[Kazemi et al., 2007] Kazemi, M.T., Fazileh, F. and Ebrahiminiezhad, M.A. (2007), Cohesive Crack Model and Fracture Energy of Steel-Fiber-Reinforced-Concrete Notched Cylindrical Specimens, *Journals of Materials in Civil Engineering* **19** (10), 884-890.

[Kennedy, 1956] Kennedy, T.B. (1956), Tensile Crack Exposure Tests of Stressed Reinforced Concrete Beams, *ACI Journal* **56** (6), 1049-1063.

[Kooiman, 1999] Kooiman, A.G. (1999), *Modelling Steel Fibre reinforced Concrete for Structural Design*, PhD thesis, Technical University of Delft, The Netherlands.

[Kosa, 1988] Kosa, K. (1988), *Corrosion of Fiber Reinforced Concrete*, Ph.D. thesis, University of Michigan, Ann Arbor, USA.

[Kosa and Naaman, 1990] Kosa, K. & Naaman, A.E. (1990), Corrosion of steel fiber reinforced concrete, *ACI Materials Journal* **87** (1), 27-37.

[Küter, 2009] Küter, A. (2009), *Management of reinforcement corrosion: a thermodynamical approach*, Ph.D. Thesis, Department of Civil Engineering, Technical University of Denmark, Kgs. Lyngby, Denmark.

[Lataste et al., 2008] Lataste, J.F., Behloul, M. and Breysse, D. (2008), Characterisation of fibres distribution in a steel fibre reinforced concrete with electrical resistivity measurements, *NDT&E International* **41**, 638-647.

[Lindquist et al., 2006] Lindquist, W.D., Darwin, D., Browning, J. and Miller, G.G. (2006), Effect of cracking on chloride content in concrete bridge decks, *ACI Materials Journal* **103** (6), 467-473.

[Liu and Weyers, 1998] Liu, Y. and Weyers, R.E. (1998), Modeling the Time-to-Corrosion Cracking in Chloride Contaminated Reinforced Concrete Structures, *ACI Materials Journal* **95** (6), 675-680.

[Lourenco and Rots, 1997] Lourenco, P.B. and Rots, J.G. (1997), Multisurface interface model for analysis of masonry structures, *Journal of Engineering Mechanics* **123** (7), 660-668.

[Löfgren et al., 2005] Löfgren, I., Olesen, J.F. and Flansbjer, M. (2005), *Application of WST-method for fracture testing of fibre-reinforced concrete*, NT Technical Report, Norway.

[Löfgren et al., 2008] Löfgren, I., Stang, H. and Olesen, J.F. (2008), The WST method, a fracture mechanics test method for FRC, *Materials and Structures* **41** (1), 197-211.

[Maidl, 1995] Maidl, B.R. and Dietrich, J. (1995), *Steel Fibre Reinforced Concrete*, Ernst & Sohn, Berlin.

[Makita et al, 1980] *Makita, M., Mori, Y. and Katawaki, K.* (1980), *Marine corrosion behavior of reinforced concrete exposed at Tokyo bay*, ACI Special Publication **65**, 271-290.

[Mangat and Gurusamy, 1987a] Mangat, P.S and Gurusamy, K. (1987a), Chloride diffusion in steel fibre reinforced marine concrete, *Cement and Concrete Research* **17**, 385-396.

[Mangat and Gurusamy, 1987b] Mangat, P.S and Gurusamy, K. (1987b), Chloride diffusion in steel fibre reinforced concrete containing PFA, *Cement and Concrete Research* **17**, 640-650.

[Marcotte and Hansson, 2003] Marcotte, T. and Hansson, C. (2003), The influence of silica fume on the corrosion resistance of steel in high performance concrete exposed to simulated sea water, *Journal of Materials Science* **28**, 4765-4776.

[Mason et al., 2002] Mason, T.O, Campo, M.A., Hixson, A.D. and Woo, L.Y. (2002), Impedance spectroscopy of fibre-reinforced cement composites, *Cement and Concrete Research* **24**, 457-465.

[McLachlan et al., 1990] McLachlan, D.S., Blaszkiewicz, M. and Newnham, R.E. (1990), Electrical Resistivity of Composites, *Journal of the American Ceramic Society* **73** (8), 2187-2203.

[Metha and Monteiro, 2006] Metha, P.K. and Monteiro, P.J.M. (2006), *Concrete – Microstructure, Properties and Materials*, McGraw-Hill, New York.

[Michel et al., 2009] Michel, A., Solgaard, A.O.S., Geiker, M.R., Stang, H., and Olesen, J.F (2009), Influence of resistivity on the corrosion of reinforcement in concrete, *Proceedings of 3rd Int. PhD Workshop on Modelling the Durability of reinforced Concrete.*

[Michel et al., 2010a] Michel, A., Solgaard, A.O.S., Geiker, M.R., Stang, H. and Olesen, J.F. (2010), Modelling Formation of Cracks in Concrete Cover due to Reinforcement Corrosion, *Proceedings of FraMCoS-7 – 7th International Conference on Fracture Mechanics of Concrete and Concrete Structures*.

[Michel et al., 2011] Michel, A., Pease, B.J., Geiker, M.R., Stang, H. and Olesen, J.F. (2011), Monitoring reinforcement corrosion and corrosion-induced cracking using non-destructive x-ray attenuation measurements, *Cement and Concrete Research* **41** (11), 1085-1094.

[Michel, 2013] Michel, A. (2013), *Reinforcement Corrosion: Numerical Simulation and Service Life Prediction*, Ph.D. Thesis, Department of Civil Engineering,Technical University of Denmark, Kgs. Lyngby, Denmark.

[Michel et al., 2013a] Michel, A., Solgaard, A.O.S., Pease, B.J., Geiker, M., Stang, H. and Olesen, J.F. (2013a), Experimental investigations on the relation between damage at the concrete-steel interface and initiation of reinforcement corrosion in plain and fibre reinforced concrete, *Submitted for Corrosion Science - January 2013*.

[Miyazato and Hiraishi, 2005] Miyazato, S. and Hiraishi, Y. (2005), Transport properties and steel corrosion in ductile fiber reinforced cement composites, *Proceedings of the 11th international conference on fracture*.

[Mohammed et al., 2001] Mohammed, T., Otsuki, N., Hisada, M. and Shibata, T. (2001), Effect of crack width and bar type on corrosion of steel in concrete, *Journal of Materials in Civil Engineering* **13** (3), 194-201.

[Mohammed et al., 2002] Mohammed, T., Otsuki, N., Hamada, H. and Yamaji, T. (2002), Chloride-induced corrosion of steel bars in concrete with presence of gap at steel-concrete interface, *ACI Materials Journal* **99** (2), 149-156.

[Mokhtar et al., 2008] Mokhtar, K.A, Loche, J.-M., Friedmann, H. Amiri, O. and Ammar, A. (2008), *Steel corrosion in reinforced concrete Report no. 2-2 Concrete in Marine Environment*, MEDACHS – Inerreg IIIB Atlantic Space – Project no. 197.

[Molina et al., 1993] Molina, F.J., Alonso, C. and Andrade, C. (1993), Cover cracking as a function of rebar corrosion: Part 2 – Numerical model, *Materials and Structures* **26** (9), 532-548.

[Monfore, 1968] Monfore, G.E. (1968), The electrical resistivity of concrete, *Journal of the PCA Research and Development Laboratories*, 35-48.

[Morse and Williamson, 1977] Morse, D.C. and Williamson, G.R. (1977), *Corrosion behaviour of steel fibrious concrete*, National Technical information Service.

[Moyson, 1995] Moyson, D. (1995), The construction of a steel fibre reinforced concrete segmental lining in London,. *Proceedings of the World Tunnel Congress/STUVA-Tagung'95*, 274–278.

[Nagataki et al, 1997] *Nagataki, S., Otsuki, N., Moriwake, A. and Miyazato, S.* (1997), *Influence of Permeation of Oxygen and Chloride Ions through Joints on Macro-Cell Corrosion*, ACI Special Publication 170-68, 1333-1355.

[Nemegeer et al., 2000] Nemegeer, D., Vanbrabant, J. and Stang, H. (2000), *Final report on durability of steel fibre reinforced concrete*, Brite Euram III.

[Neville, 1996] Neville, A. (1996), *Properties of Concrete*, 4th edition, John Wiley & Sons.

[Nielsen et al., 2010] Nielsen, L.O., Mougaard, J.F., Jacobsen, J.S. and Poulsen, P.N. (2010), A mixed mode for fracture in concrete, *Proceedings of FraMCoS-7 – 7th International Conference on Fracture Mechanics of Concrete and Concrete Structures*.

[Nordstrøm, 2005] Nordstrøm, E., (2005), *Durability of sprayed concrete – steel fibre corrosion in cracks,* Doctoral thesis, Department of Civil and Environmental Engineering, Division of Structural Engineering, Luleå University of Technology, Sweden.

[Nygaard, 2003] Nygaard, P. (2003), *Effect of steel-concrete interface defects on the chloride threshold for reinforcement corrosion*, Master Thesis, Department of Civil Engineering, Technical University of Denmark, Kgs. Lyngby, Denmark.

[Nygaard and Geiker, 2005] Nygaard, P. and Geiker, M.R. (2005), A method for measuring the chloride threshold level required to initiate reinforcement corrosion in concrete, *Materials and Structures* **38** (278), 489-494.

[NZS, 1995] New Zealand Standard (1995),'Concrete structure Part 1 – The Design of Concrete Structures', NZS3101: Part 1.

[Olesen, 2001] Olesen, J.F. (2001), Fictitious Crack Propagation in Fiber-Reinforced Concrete Beams, *Journal of Engineering Mechanics* **127** (3), 272-280.

[Olsen, 2010] Olsen, T. (2010), *Modelling of the Shear Capacity of Reinforced Concrete Beams*, Master Thesis, Department of Civil Engineering, Technical University of Denmark, Kgs. Lyngby, Denmark.

[O'Neil, 1980] *O'Neil, E.F.* (1980), *Study of reinforced concrete beams exposed to marine environment*, ACI Special Publication **65**, 113-132.

[Osterminski et al., 2006] Osterminski, K., Schießl, P., Volkwein, A. and Maye, T.F. (2006), Modelling reinforcement corrosion – usability of a factorial approach for modelling resistivity of concrete, *Materials and Corrosion* **57**, 926-931.

[Otieno et al., 2010] Otieno, M., Alexander, M. and Beushausen, H.-D. (2010), Corrosion in cracked and uncracked concrete – Influence of crack width, concrete quality and crack reopening, *Magazine of Concrete Research* **62** (6), 393-404.

[Ouglova et al., 2006] Ouglova, A., Berthaud, Y., François, M. and Foct, F. (2006), Mechancial properties of an irone oxide formed by corrosion in reinforced concrete structures, *Corrosion Science* **48** (12), 3988-4000.

[Ožbolt et al., 2011] Ožbolt, J., Balabanic, G. and Kušter, M. (2011), 3D Numerical modelling of steel corrosion in concrete structures, *Corrosion Science* **53**, 4166-4177.

[Pease et al., 2006] Pease, B.J., Geiker, M.R., Stang, H., and Weiss, J. (2006), Photogrammetric assessment of flexure induced cracking of reinforced concrete beams under service loads, *Proceedings 2nd International RILEM Symposium Advances in Concrete through Science and Engineering.*

[Pease et al., 2007] Pease, B.J., Skoček, J., Geiker, M.R., Stang, H., and Weiss, J. (2007), The Wedge Splitting Test: Influence of Aggregate Size and Water-to-Cement Ratio, *Proceedings of the RILEM Transport Mechanisms Workshop*.

[Pease et al., 2009] Pease, B.J., Couch, J., Geiker, M., Stang, H., and Weiss, J. (2009), Assessing the portion of the crack length contributing to water sorption using X-ray Absorption Measurements in Concrete Wedge Splitting Specimens, *Proceedings of ConcreteLife '09: second international RILEM workshop on Concrete durability and service life planning.*

[Pease, 2010] Pease, B.J. (2010), *Influence of concrete cracking on ingress and reinforcement corrosion*, Ph.D. Thesis, Department of Civil Engineering,Technical University of Denmark, Kgs. Lyngby, Denmark.

[Pease et al., 2011] Pease, B.J., Geiker, M., Stang, H. and Weiss, J. (2011), The design of an instrumented rebar for assessment of corrosion in cracked concrete, *Materials and Structures* **44** (7), 1259-1271.

[Pease et al., 2012] Pease, B.J., Michel, A. and Stang, H. (2012), Quantifying Movements of Corrosion Products in Reinforced Concrete using X-Ray Attenuation Measurements, *Proceedings of 2nd International Conference on Microdurability*.

[Pease et al., 2012a] Pease, B.J., Michel, A., Thybo A.E.A. and Stang, H. (2012a), Estimation of elastic modulus of reinforcement corrosion products using inverse analysis of digital image correlation measurements for input in corrosion-induced cracking model, *Proceedings of 6th International Conference on Bridge maintenance, safety and management (IABMAS)*.

[Pease et al., 2012b] Pease, B.J., Michel, A., Geiker M. and Stang, H. (2012b), Modelling moisture ingress through simplified concrete crack geometries, *Proceedings of 1st International Congress on Durability of Concrete, ICDC 2012*.

[Pereria et al., 2011] Pereria, E., Fischer, G. and Barros, J. (2011), Image-based detection and analysis of crack propagation in cementitious composites, *Proceedings of International Conference on Advances in Construction Materials through Science and Engineering.*

[Polder et al., 2000] Polder, R., Andrade, C., Elsener, B. Vennesland, O., Gulikers, J. Weidert, R. and Raupach, M. (2000), Test methods for on-site measurement of resistivity of concrete, *Materials and Structures* **33**, 603-611.

[Polder, 2001] Polder, R.B (2001), Test methods for on-site measurement of resistivity of concrete – a RILEM TC-154 technical recommendation, *Construction Building Materials* **15**, 125-135.

[Poursaee and Hansson, 2008] Poursaee, A. and Hansson, C.M. (2008), The influence of longitudinal cracks on the corrosion protection afforded reinforcing steel in high performance concrete, *Cement and Concrete Research* **38** (8-9), 1098-1105.

[Rapoport et al., 2001] Rapoport, J., Aldea, C.-M., Shah, S.P., Ankenman, B. and Karr, A.F. (2001), *Permeability of Cracked Steel Fiber-Reinforced Concrete,* Technical Report no 114, National Institute of Statistical Sciences.

[Rasheeduzzafar et al., 1992] Rasheeduzzafar, Al-Saadoun, S.S., and Al-Gahtani, A.S. (1992), Corrosion cracking in relation to bar diameter, cover and concrete quality, *Journal of Materials in Civil Engineering* **4** (4), 327-342.

[Raupach, 1997] Raupach, M. (1997), Effect of temperature on chloride induced steel corrosion in concrete, *Proceedings of The European Corrosion Congress Event No. 208*.

[Rendell et al., 2002] Rendell, F, Jauberthie, R. and Grantham, M. (2002), *Deteriorated Concrete Inspection – Inspection and physiochemical analysis*, Thomas Telford, London.

[Rehm and Moll, 1964] Rehm, G. and Moll, H.L. (1964), *Versuche zum stadium des einflußes der rissbreite auf die rostbildung an der bewehrung von stahlbeton-bauteilen,* Deutscher Ausschuss für Stahlbeton 169.

[Reza et al., 2001] Reza, F. Batson, G.B., Yarnamuro, J.A. and Lee, J.S. (2001), Volume Electrical Resistivity of Carbon Fiber Cement Composites, *ACI Materials Journal* **98** (1), 25-35.

[Rilem, 1999] Rilem TC 116 PCD (1999), Test for gas permeability of concrete A: Preconditioning of concrete test specimens for the measurement of gas permeability and capillary absorption of water, *Materials and Structures* **32**, 174-179.

[Rilem, 2002] RILEM TC-162 TDF (2002), Test and Design Methods for Steel Fibre Reinforced Concrete, *Materials and Structures* **35**, 579-582.

[Rodriguez and Hooton, 2003] Rodriguez, O.G. and Hooton, R.D. (2003), Influence of Cracks on Chloride Ingress into Concrete, *ACI Materials Journal* **100** (2), 120-126.

[Rosselló et al., 2005] Rosselló, C., Elices, M., and Guinea, G.V. (2005), Fracture of model concrete: 2. Fracture energy and characteristic length, *Cement and Concrete research* **36** (7), 1345-1353.

[Schießl, 1976] *Schießl, P.* (1976), *Zur Frage der zulässigen Rissbreite und der erforderlichen Betondeckung im Stahlbetonbau unter besonderer Berücksichtigung der Karbonatisierung des Betons*, Deutscher Auschuss für Stahlbetong 255.

[Schießl and Raupach, 1997] Schießl, P. and Raupach, M. (1997), Laboratory studies and calculations on the influence of crack width on chloride-induced corrosion of steel in concrete, *ACI Materials Journal* **94** (1), 56-62.

[Schießl and Wölfel, 1986] Schießl, P. and Wölfel, E. (1986), *Konstruktionsregeln zur Beschräcnkung der Rissbreite – Grundlage zur Neufassung DIN 1045, Abschnitt 17.6 (Entwurf 1985)*, Beton- und Stahlbetonbau **81** (1).

[Schnütgen, 1978] Schnütgen, B. (1978), *Materialeigenschaften von Stahlfaserbeton*, In: Berichte des Instituts für Konstruktiven Ingenieurbau, Ruhr-Universität Bochum, Heft 31.

[Scott and Alexander, 2007] Scott, A. and Alexander, M. (2007), The influence of binder type, cracking and cover on corrosion rates of steel in chloride contaminated concrete, *Magazine of Concrete Research* **59** (7), 495-505.

[Shah et al., 1995] Shah, S.P., Swartz, S.E and Ouyang, C. (1995), *Fracture Mechanics of Concrete*, John Wiley & Sons, Inc.

[Skoček and Stang, 2010] Skoček, J., and Stang, H. (2010), Application of optical deformation analysis system on wedge splitting test and its inverse analysis, *Materials and Structures* **43**, 63-72.

[Solgaard et al., 2009] Solgaard, A.O.S., Michel, A., Stang, H., Geiker, M.R., Küter, A. and Edvardsen, C. (2009), Modelling the influence of steel fibres on the electrical resistivity of cementitious composites, *Proceedings of the 3rd International PhD Workshop on Modelling the Durability of Reinforced Concrete*.

[Solgaard et al., 2013] Solgaard, A.O.S., Michel, A. and Stang, H. (2013), *Photogrammetric Investigations on the Debonding along the Concrete/Steel Interface in Reinforced Concrete Beams*, Technical report from Department of Civil Engineering at the Technical University of Denmark, Kgs. Lyngby, Denmark.

[Song et al., 2008] Song, H.-W., Lee, C.-H., and Ann, K.Y. (2008), Factors influencing chloride transport in concrete structures exposed to marine environment, *Cement and Concrete Composites* **30** (2), 113-121.

[Suda et al., 1993] Suda, K., Misra, S., and Motohashi, K. (1993), Corrosion products of reinforcing bars embedded in concrete, *Corrosion Science* **35** (5-8), 1543-1549.

[Takao et al., 1982] Takao, Y., Chou, T.-W. and Taya, M. (1982), Effective Longitudinal Young's Modulus of Misoriented Short Fiber Composites, *Journal of Applied Mechanics* **49** (3), 536-540.

[Tammo and Thelandersson, 2009] Tammo, K. and Thelandersson, S. (2009), Crack widths near reinforcement bars for beams in bending, *Journal of the FIB* **10** (1), 27-34.

[Tammo et al., 2009] Tammo, K., Lundgren, K. and Theandersson, S. (2009), Nonlinear analysis of crack widths in reinforced concrete, *Magazine of Concrete Research* **61** (1), 23-34.

[Tanaka and Tamamushi, 1964] Tanaka, N. and Tamamushi, R. (1964), Kinetic Parameters of Electrode Reactions, *Electrochimica Acta* **9**, 963-989.

[Tang, 1996] Tang, L., (2005), *Chloride Transport in Concrete – Measurement and Prediction,* Doctoral thesis, Institutionen för Byggnadsmaterial, Chalmers University of Technology, Sweden.

[Torrents et al., 2000] Torrents, J.M., Mason, T.O. and Garboczi, E.J. (2000), Impedance spectra of fiber-reinforced cement-based composites. A modeling approach, *Cement and Concrete Research* **30**, 585-592.

[Torrents et al., 2001] Torrents, J.M., Mason, T.O., Peled, A., Shah, S.P and Garboczi, E.J. (2001), Analysis of the impedance spectra of short conductive fiber-reinforced composites, *Journal of Materials Science* **36**, 4003-4012.

[Tsai et al., 2009] Tsai, C.-T., Li, L.-S., Chang, C.-C. and Hwang, C.-L. (2009), Durability design and application of steel fiber reinforced concrete in Taiwan, *The Arabian Journal for Science and Engineering* **34** (1B), 57-79.

[Tuutti, 1982] Tuutti, K., (1982), *Corrosion of steel in concrete*, Report 4-82. Swedish Cement and Concrete Research Institute, Stockholm, Sweden.

[van Mier, 1997] van Mier, J.G.M. (1997), *Fracture Processes in Concrete Assessment of Material Parameters for Fracture Models*, CRC Press.

[Vu et al., 2005] Vu, K., Stewart, M.G. and Mullard, J. (2005), Corrosion-Induced Cracking: Experimental Data and Predictive Models, *ACI Materials Journal* **102** (5), 719-726.

[Wang et al., 1997] Wang, K., Jansen, D.C., Shah, S.P. and Karr, A.F. (1997), Permeability Study of Cracked Concrete, *Cement and Concrete Research* **27** (3), 381-393.

[Wang and Ueda, 2011] Wang, L. and Ueda, T. (2011), Mesoscale Modelling of the Chloride Diffusion in Cracks and Cracked Concrete, *Journal of Advanced Concrete Technology* **9** (3), 241-249.

[Weiss et al., 2012] Weiss, J., Snyder, K., Bullard, J. and Bentz, D. (2012), Using a Saturation Function to Interpret the Electrical Properties of Partially Saturated Concete, *Journal of Materials in Civil Engineering* **10**, http://dx.doi.org/10.1061/(ASCE)MT.1943-5533.0000549

[Whittington et al., 1981] Whittington, H.W., McCarter, J. and Forde, M.C. (1981), Resistivity Characteristics of Concrete, *Proc. Inst. of Civil Engineers*, 107-117.

[Wimpenny et al., 2009] Wimpenny, D., Angerer, W., Cooper, T. and Bernard, S. (2009), The use of Steel and Synthetic Fibres in Concrete under Extreme Conditions, *Proceedings of the 24th Biennal Conference of Concrete Institute of Australia.*

[Win et al., 2004] Win, P.P., Watanabe, M. and Machida, A. (2004), Penetration Profile of Chloride Ion in Cracked Reinforced Concrete, *Cement and Concrete Research* **34**, 1073-1079.

[Woo et al., 2005] Woo, L.Y., Wansom, S., Ozyurt, N., Mu, B., Shah, S.P. and Mason, T.O. (2005), Characterizing fiber dispersion in cement composites using AC-Impedance Spectroscopy, *Cement and Concrete Composites* **27**, 627-636.

[World Tunneling, 2009] World Tunneling – The magazine for the tunneling professional (2009), Madrid metro branches out*, http://www.world-tunnelling.com/features/madrid-metro-branches-out?SQ_DESIGN_NAME=print_friendly, retrieved 12th of March 2013*.

[Yoon et al., 2000] Yoon, S., Wang, K., Weiss, J. and Shah, S. (2000), Interaction between Loading, Corrosion, and Serviceability of Reinforced Concrete, *ACI Materials Journal* **97** (6), 637-644.

The use of traditional reinforcement bars in combination with steel fibres as one, so-called combined reinforcement system has gained impact within the construction industry over the past years. However, such reinforcement systems are only marginally covered by existing guidelines for structural design and the literature on its properties, mechanical as well as durability, is sparse.
This Ph.D. study focused on the impact of the steel fibres on corrosion initiation and propagation of the reinforcement bars of such reinforcement systems. Experimental studies as well as numerical simulations related to reinforcement corrosion in uncracked as well as cracked concrete are presented in the Ph.D. thesis.

DTU Civil Engineering
Department of Civil Engineering
Technical University of Denmark

Brovej, Building 118
2800 Kgs. Lyngby
Telephone 45 25 17 00

www.byg.dtu.dk

ISBN: 9788778773395
ISSN: 1601-2917